

TECHNISCHE UNIVERSITÄT DORTMUND

Dissertation

**Integral equation-based calculations of
the electronic structure of small
molecules under high pressure**

Der
Fakultät für Chemie und Chemische Biologie
vorgelegt zur Erlangung des akademischen Grades
Doktor der Naturwissenschaften
(*Dr. rer. nat.*)
von

Patrick Jascha Kibies
geb. am 02.09.1986
in Witten

Juli 2019

1. Gutachter: Prof. Dr. Stefan M. Kast
2. Gutachter: Prof. Dr. Roland Winter

Diese Arbeit wurde von Dezember 2014 bis Juli 2019 unter der Anleitung von Prof. Dr. Stefan M. Kast in der Arbeitsgruppe Physikalische Chemie III der Fakultät für Chemie und Chemische Biologie an der Technischen Universität Dortmund angefertigt.

Meinen Eltern

Contents

Acknowledgments	iii
Publications	v
Abstract	vii
Zusammenfassung	ix
Third party contributions	xiii
I. Introduction	1
1. Overview	3
1.1. The role of high pressure research	3
1.2. Cosolvents, osmolytes and piezolytes	5
1.2.1. Trimethylamine-N-oxide	6
1.2.2. Urea	7
1.3. Force field development	8
1.4. The ionic product of water under high pressure conditions	9
1.4.1. Experimental findings and methods	10
1.5. Semi-empirical quantum chemistry within EC-RISM	12
1.5.1. Parametrization of the hpCADD Hamiltonian	13
II. Theory	15
2. Dependence of thermodynamics on solvation structure	17
2.1. Statistical solvation models	18
2.2. The molecular Ornstein-Zernike equation	19
2.3. The reference interaction site model: 1D RISM	20
2.4. Calculating solvent susceptibilities	21
2.5. 3D RISM	22
2.6. Coupling the 3D RISM approach with quantum chemistry: EC-RISM	23
2.6.1. Potential calculation in EC-RISM	24
2.7. Empirical correction of the excess chemical potential	26
2.8. Geometry optimizations within EC-RISM	28

Contents

3. Theory of vibrational spectroscopy	29
3.1. Basics	29
3.1.1. A classical view on vibration	30
3.1.2. A quantum-mechanical view on vibration	30
3.2. Vibrational spectroscopy in the molecular model	31
3.2.1. Separation of coordinates	31
3.3. The vibrational Stark effect	35
3.4. Calculation of vibrational modes in quantum chemistry	36
3.5. Calculation of vibrational frequency shifts with EC-RISM	40
4. Theoretical description of thermodynamics for the water autoprotolysis equilibrium	43
III. Methods	47
5. Introducing high pressure in 3D RISM	49
6. Benchmarking the new electrostatics model	63
7. Force field development	65
7.1. Charge scaling for high pressures	65
7.2. Application of differential evolutionary algorithms in force field development	65
7.3. Force field development for urea	67
7.3.1. Optimization of an urea force field	67
7.4. Force field development for hydronium and hydroxide	69
8. Computational details	73
8.1. Computational details: TMAO	73
8.1.1. Dipole moment	73
8.1.2. Vibrational frequencies	73
8.1.3. EC-RISM geometry optimization	73
8.2. Computational details: Urea	74
8.3. Computational details: Benchmark of the new ESP model	74
8.4. Computational details: Calculating the autoprotolysis equilibrium of water	75
8.5. Computational details: Benchmark of a novel semi-empiric Hamiltonian	76
IV. Results	79
9. Results: Trimethylamine-N-oxide	81
9.1. Dipole moment	81
9.1.1. The dipole moment of TMAO as a function of pressure	81

9.2. Development of a force field for TMAO in aqueous high pressure environments	83
9.3. Vibrational spectroscopy	89
10. Results: Urea	97
10.1. Dipole moment	97
10.1.1. The dipole moment of urea as a function of pressure	97
10.2. The influence of Lennard-Jones parameters on the dipole moment and its pressure-dependence	98
11. Results: Performance of the new electrostatics model	105
12. Results: Hydronium and hydroxide	111
12.1. Force field	111
13. Results: The ionic product of water under high pressure conditions	117
14. Results: hpCADD-Hamiltonian	121
15. Summary and outlook	125
List of Tables	127
List of Figures	129
V. Appendix	131
A. Additional data	133
A.1. TMAO	133
A.1.1. Molecular geometries	133
A.1.2. Vibrational data	135
A.2. Urea	159
A.2.1. Bonded urea parameters	159
A.2.2. Non-bonded urea parameters	159
A.2.3. Force field modifications: Parameters	161
A.2.4. Force field modifications: Radial distribution functions	165
A.3. New electrostatics model	171
A.3.1. Molecule geometries	171
A.4. hpCADD	173
A.4.1. List of substances	173
A.4.2. Raw data	184
A.4.3. Scatter plots	199
B. Conventions	241
B.1. Mathematical nomenclature	241

Contents

B.2. Constants and unit conversions used in this thesis	241
C. Software	243

Acknowledgments

Since nearly all the people concerned here are native German speakers, I'd like to express my gratitude in their mother tongue. Ich bedanke mich herzlich bei Herrn Prof. Dr. Stefan M. Kast, der nicht nur für diese Arbeit, sondern in meinem bisherigen akademischen Leben, mir immer mit Rat und Tat zur Seite stand und auch für persönliche Belange immer ein außergewöhnliches Maß an Verständnis aufgebracht hat. Herrn Prof. Dr. Roland Winter möchte ich für die Übernahme des Zweitgutachtens danken und für das Engagement, das den reibungslosen Ablauf der Forschergruppe erst möglich gemacht hat. Dr. Jochen Heil danke ich dafür, dass er stets ein Mentor und Vorbild im wissenschaftlichen Arbeiten war und maßgeblich zu einer tollen Arbeitsplatzatmosphäre beigetragen hat. Ebenfalls für eine solide Anleitung beim organisierten und wissenschaftlichen Arbeiten danke ich Frau Dr. Franziska Hoffgaard. Herr Dr. Daniel Tomazic gebührt Dank für hilfreiche Hinweise zur Python-Bändigung und zur Bedienung von Mathematica, und auch für viele sinnstiftende Gespräche innerhalb und außerhalb der Wissenschaft. Herrn Dr. Leonhard M. Henkes danke ich für intensive Gespräche, sowohl wissenschaftlicher als auch sozialer Natur. Herrn Martin Urban, der mich dankenswerterweise in seinem Büro aufnahm, danke ich für eine produktive Büroatmosphäre und diverse Lektionen im südhessischen Dialekt, Herrn Dr. Florian Mrugalla danke ich für viele interessante Diskussionen und intensiven Austausch zu methodischen und technischen Themen. Herrn Dr. Roland Frach danke ich dafür, dass er oft kleine Kniffe, komplexe Lösungen, hilfreiche Tipps und schnelle Bewertungen zur Hand hatte und diese auch gern geteilt hat. Herrn Tim Pongratz danke ich für die enge und fruchtbare Zusammenarbeit im Hochdruckgebiet. Herrn Lukas Eberlein danke ich in erster Linie ebenfalls für den Austausch zu Hochdruckthemen und natürlich für seinen durchweg positiven Einfluss auf die Atmosphäre am Arbeitsplatz. Herrn Yannic Alber, Herrn Nicolas Tielker, Frau Julia Jasper, Herrn Lennart Eisel und Herrn Lars Schumann danke ich für die Weiterführung der guten Arbeitsatmosphäre und den Austausch zu technischen und wissenschaftlichen Themen. Frau Anneliese Ahlke danke ich dafür, dass sie immer still und unauffällig den Papiertiger, den eine Hochschule stets füttert, zu zähmen verstand. Ebenso danke ich Frau Andrea Jeworrek dafür, dass sie den Verwaltungskram rund um die Forschergruppe immer souverän und hilfsbereit erledigt hat und genauso zuverlässig Tipps, Tricks und Taten bei der Erledigung von Verwaltungsaufgaben zur Hand hatte.

Meinem engen Kooperationspartner, Herrn Dr. Christoph Hölzl und seinem Doktorvater Herrn Prof. Dr. Dominik Horinek danke ich für eine konstruktive Zusammenarbeit, die alle beschriebenen Kraftfeldentwicklungsprozesse erst möglich gemacht haben. Many thanks to Dr. Sho Imoto, who not only provided *ab initio* molecular dynamics

Acknowledgments

(*aiMD*) reference data but also contributed very sophisticated scientific ideas und natürlich Herrn Prof. Dr. Dominik Marx, der neben der wissenschaftlichen Komponente auch die Darstellung der Ergebnisse perfektioniert hat.

Frau Dr. Heike B. Thomas, Herrn Dr. Matthias Hennemann, Herrn Dr. Stefan Güssregen und Herrn Prof. Dr. Timothy Clark danke ich für die intensive Kooperation im hpCADD-Projekt, dafür dass ich Erlangen zur Bergkirchweih erleben durfte und natürlich für den EMPIRE-Support.

Meinen Eltern Diana und Ralf Kibies danke ich für ständige moralische, materielle, finanzielle und tatkräftige Unterstützung und Anleitung, ohne die ich sicher keine akademische Ausbildung erhalten hätte.

Matthias Müller danke ich dafür, dass er stets nur einen Anruf entfernt ist, was auch immer anliegt.

Ich danke Petra, Florian und Lisa Urbaniak dafür, dass sie Unglaubliches leisten.

Meiner Freundin Dr. Elena Zwar danke ich dafür, dass wir gemeinsam den Weg durchs Chemiestudium beschritten und alle schönen und widrigen Dinge auf und neben diesem Weg gemeinsam durchlebt haben.

Allen Lektoren, insbesondere Elena Zwar, Rolf Meyrahn, Tim Pongratz, Lukas Eberlein, Lennart Eisel und Lars Schumann möchte ich für ihr Engagement danken. Ihr findet einfach (fast) alles.

A ship in port is safe, but that is not what ships are built for. — JOHN A. SHEDD

A human must turn information into intelligence or knowledge. We've tended to forget that no computer will ever ask a new question. — GRACE HOPPER

Publications

Publications on topics of this thesis:

- C. Hölzl, P. Kibies, S. Imoto, R. Frach, S. Suladze, R. Winter, D. Marx, D. Horinek, S. M. Kast, *Design principles for high-pressure force fields: Aqueous TMAO solutions from ambient to kilobar pressures*, *J. Chem. Phys.* **144** (2016), 144104.
- R. Frach *et al.*, *The Chemical Shift Baseline for High-Pressure NMR Spectra of Proteins*, *Angew. Chem. Int. Ed.* **55** (2016), 8757.
- S. Imoto, P. Kibies, C. Rosin, R. Winter, S. M. Kast, D. Marx, *Toward Extreme Biophysics: Deciphering the Infrared Response of Biomolecular Solutions at High Pressures*, *Angew. Chem. Int. Ed.*, **55** (2016), 9534.
- H. B. Thomas, M. Hennemann, P. Kibies, F. Hoffgaard, S. Güssregen, G. Hessler, S. M. Kast, T. Clark, *The hpCADD NDDO Hamiltonian: Parametrization*, *J. Chem. Inf. Model.* **57** (2017), 1907.

Further publications with contributions from the author, which are not part of this thesis:

- H. Nelson, A. Ihrig, R. Kahlau, P. Kibies, S. M. Kast, R. Böhmer, *Deuteron magnetic resonance and dielectric studies of guest reorientation and water dynamics in six clathrate hydrates containing ring-type guests*, *J. Non-Cryst. Solids* **407** (2015), 431.
- J. Engel *et al.* *Targeting Drug Resistance in EGFR with Covalent Inhibitors: A Structure-Based Design Approach*, *J. Med. Chem.* **58** (2015), 6844-6863.

Abstract

The topic of this thesis is the effect of high hydrostatic pressures on small molecules. The high complexity of this topic and the number of methods utilized require highly cooperational work, which was organized and funded within the DFG research unit FOR 1979 and the RESOLV cluster of excellence EXC 2033. The development of a semi-empiric Hamilton operator, which was tested for high-pressure applicability within this thesis, has been funded by the German Bundesministerium für Bildung und Forschung as part of the project called high performance computer-aided drug design (hpCADD).

This thesis has the aim, to model high hydrostatic pressure environments in such a way, that a physically based response of the electronic structure of small molecules can be obtained via quantum chemistry (QC) calculations. Since the embedded cluster reference interaction site model (EC-RISM) approach is in principle capable of introducing pressure information into quantum chemistry on a fully physically motivated basis, efforts have been made to extend the scope of EC-RISM to the high-pressure regime. Therefore, one-dimensional reference interaction site model (1D RISM)^{1,2} calculations were performed in order to obtain high pressure solvent susceptibilities for the three-dimensional reference interaction site model (3D RISM)^{3,4} part of EC-RISM.⁵ During this process two types of solvent susceptibilities were created: On the one hand, the hyper-netted chain (HNC) approximation⁶ was utilized, on the other hand the expertise within the DFG research unit was used to perform highly cooperative work in order to introduce classical force field molecular dynamics (ffMD) information into the solvent susceptibilities.⁷ This first step enables the EC-RISM method to gain insight into the electronic structure of small molecules under high pressure.

The effects of high pressure on bio-polymers, especially proteins, is a long-term topic for science and was examined and published in a large number of studies. When studying deep-sea life, researchers found some small molecules repeatedly. In this way, it was found that trimethylamine-N-oxide (TMAO) has a stabilizing effect on proteins in high pressure environments, which is obviously crucial for a range of deep-sea organisms.⁸⁻¹¹ In order to examine the mutual effects of cosolvents like TMAO and proteins on each other with theoretical methods, it is necessary to use suitable force field parameters. For TMAO there is an important effect of pressure-induced electronic polarization.¹² In order to cover these effects, quantum chemistry (QC) calculations were performed applying EC-RISM. The obtained electrostatic information was used to parameterize a high-pressure force field for TMAO.

Abstract

Another important substance, which was found to have impact on the osmotic pressure and that decreases protein stability is urea.¹³ Most interestingly, during the force field development for urea it was found that the same electrostatic scaling approach used for TMAO has no positive effect on the observables obtained with a new urea force field under high pressure conditions. Furthermore, the influence of Lennard-Jones parameters on the observed molecular dipole moment was studied systematically on urea. Dipole moment derivatives with respect to the Lennard-Jones parameters were calculated to quantify this effect.

To learn more on the physical basis of pressure dependent changes in spectroscopically obtained data, first steps were taken, to calculate the pressure dependent change of vibrational frequencies in the TMAO-molecule.¹⁴

In order to improve the treatment of the electrostatic potential (ESP) in 3D RISM calculations a method was developed, that avoids cut-off artifacts when the ESP is split in long-range and short-range contributions in the context of a renormalization approach.¹⁵ To achieve this goal the idea of a switching approach is adapted. In the direct vicinity of the solute the exact ESP is utilized, while at the 3D RISM grid box edges the ESP is calculated from the atomic partial charges. In between these zones, a buffer zone is placed, where the ESP is scaled linearly by a cubic function to ensure a smooth change from the exact to the point-charge based ESP. The change in the excess chemical potential due to this manipulation can be corrected by a perturbative term.

In order to benchmark the novel high-pressure methodology, the applicability of EC-RISM for the prediction of high-pressure thermodynamic observables was tested. Thus, the shift in the autoprotolysis constant of water as a function of pressure was calculated. In order to test to which extent empirical corrections for ambient conditions are applicable at high pressures, different variants were tested. The results were compared with experimental results. Preliminary simulations showed that pre-existing force fields¹⁶ for hydronium and hydroxide do not represent the solvation structure in water in terms of radial distribution functions sufficiently. To overcome these issues a novel force field was developed, which contains dummy sites and represents the solvation structure far better.

As a part of the project hpCADD, which was funded by the German Bundesministerium für Bildung und Forschung (BMBF), a semi-empirical Hamilton operator was parameterized.¹⁷ This Hamilton operator is intended to be the electrostatic component of a force field still to develop. This ansatz including fast semi empiric quantum chemistry is possibly more accurate than point charge based purely classical force fields, while the impact on computational cost is low. As a part of this thesis this Hamiltonian is tested for its polarizability in terms of EC-RISM calculations at ambient and high pressure conditions. The results are compared to calculations using the second order Møller-Plesset perturbation theory (MP2).

Zusammenfassung

Das Thema der vorliegenden Dissertationsschrift ist der Einfluss hoher hydrostatischer Drücke auf kleine Moleküle in wässrigen Umgebungen. Die hohe Komplexität dieser Thematik und die große Anzahl an Methoden, die zur Forschung in diesem Gebiet eingesetzt wird, erfordert in höchstem Maße kooperative Arbeit, die im Rahmen der DFG Forschergruppe FOR 1979 und dem RESOLV-Exzellenzcluster Exc 2033 sowohl finanzielle Förderung als auch einen organisatorischen Rahmen erhalten hat. Die Entwicklung eines semiempirischen Hamiltonoperators, dessen Anwendbarkeit in Hochdruckumgebungen in dieser Arbeit überprüft wurde, wurde durch das Bundesministerium für Bildung und Forschung im Rahmen des Projektes *high performance computer-aided drug design* (hpCADD) gefördert.

Diese Arbeit verfolgt das Ziel, Umgebungen hoher hydrostatischer Drücke auf solch eine Art und Weise zu modellieren, dass die Druckantwort der Elektronenstruktur kleiner Moleküle in Quantenchemierechnungen beobachtet werden kann. Da das *Embedded Cluster Reference Interaction Site Model* (EC-RISM)⁵ prinzipiell dazu geeignet ist, die Druckinformation auf einer vollständig physikalisch motivierten Grundlage abzubilden, wurden Anstrengungen unternommen, um den Anwendungsbereich von EC-RISM auf hohe Drücke zu erweitern. Zu diesem Zweck wurden Rechnungen im Bild des eindimensionalen *Reference Interaction Site Models* (1D RISM)^{1,2} durchgeführt, um die notwendigen Hochdrucksolvenssuszeptibilitäten zu erhalten. Diese Suszeptibilitäten werden für das dreidimensionale RISM (3D RISM)^{3,4} als Teil von EC-RISM benötigt. Im Rahmen dieses Prozesses wurden zwei Typen von Solvenssuszeptibilitäten erzeugt, einerseits solche, die auf Verteilungsfunktionen aus Moleküldynamik (MD)-Simulationen basieren, und andererseits solche, die vollständig auf der *hyper-netted Chain*-Näherung⁶ beruhen. Die MD-Simulationsdaten wurden aus der Kooperation innerhalb der DFG-Forschergruppe erhalten. Dieser erste Schritt ermöglicht EC-RISM-Rechnungen für Hochdruckbedingungen.

Der Effekt von hohen Drücken auf Biopolymere, besonders Proteine, ist ein Thema, das die Wissenschaft schon lange beschäftigt und wozu schon eine große Anzahl an Studien publiziert wurde. Bei der Untersuchung von Leben in der Tiefsee sind bestimmte kleine Moleküle häufiger in Erscheinung getreten. So wurde der proteinstabilisierende Effekt von Trimethylamin-N-oxid (TMAO) erkannt, welcher offenbar essentiell für einige Tiefseeorganismen ist.⁸⁻¹¹ Um die gegenseitigen Effekte von Cosolvenzien wie TMAO und Proteinen aufeinander mit theoretischen Methoden besser charakterisieren zu können, sind geeignete Kraftfelder erforderlich. Im Falle des TMAO hat sich gezeigt, dass es einen wichtigen Effekt durch druckinduzierte Polarisation gibt.¹² Um diesen Effekt in der Kraftfeldentwicklung abdecken zu können, wurden EC-RISM-Rechnungen

Zusammenfassung

an TMAO unter Hochdruckbedingungen durchgeführt und mit den erhaltenen Informationen ein Kraftfeld parametrisiert.

Eine weitere wichtige Substanz, die einen Einfluss auf den osmotischen Druck und einen destabilisierenden Effekt auf Proteine aufweist, ist Harnstoff.¹³ Interessanterweise wurde während der Kraftfeldentwicklungsprozesses erkannt, dass im Fall des Harnstoffs eine Anpassung der Atomladungen im Gegensatz zu TMAO keinen positiven Effekt bewirkt. Am Harnstoff wurde weiterhin die Abhängigkeit von Observablen aus EC-RISM-Rechnungen von den verwendeten Lennard-Jones-Parametern untersucht. Dazu wurde auch das Dipolmoment nach den Lennard-Jones-Parametern abgeleitet.

Um mehr über die physikalischen Vorgänge zu erfahren, die der Druckabhängigkeit spektroskopischer Daten zu Grunde liegen, wurden erste Schritte unternommen, um die Änderung von Vibrationsfrequenzen des TMAO als Funktion des Druckes mit EC-RISM berechnen zu können.

Um Abschneideartefakte bei der Behandlung des elektrostatischen Potentials (ESP) innerhalb eines Renormierungsansatzes¹⁵ der 3D RISM-Methode zu vermeiden, wurde ein so genannter Switching-Ansatz adaptiert. In der direkten Umgebung des Solvates wird das exakte, wellenfunktionsbasierte ESP verwendet und am Rand des verwendeten Gitters kontinuierlich in ein ESP überführt, das aus Atomladungen konstruiert wird. Die dadurch entstehende Abweichung im chemischen Exzesspotential kann durch einen Störungsausdruck korrigiert werden.

Um die neuartige Herangehensweise für Hochdruckberechnungen mit experimentellen Daten vergleichen zu können und damit die Qualität der erhaltenen thermodynamischen Observablen beurteilen zu können, wurde die druckabhängige Verschiebung der Autoprotolysekonstante von Wasser berechnet. Dabei wurden unterschiedliche Arten der empirischen Korrektur in Ansatz gebracht. Um zu diesem Zweck ein möglichst gut geeignetes Kraftfeld für Hydronium und Hydroxid zur Verfügung zu haben, wurde neben literaturbekannten Daten¹⁶ auch ein selbstparametriertes Kraftfeld verwendet, das besser geeignet ist, um die Solvensstruktur abzubilden. Die Thermodynamik wird jedoch vom literaturbekannten Kraftfeld besser wiedergegeben.

Als ein Anteil des hpCADD-Projektes wurde ein semiempirischer Hamiltonoperator parametrisiert,¹⁷ welcher als elektrostatische Komponente für ein noch zu entwickelndes, polarisierbares Kraftfeld gedacht ist. Diesem Ansatz liegt die Idee zu Grunde, die elektrostatische Kraftfeldkomponente durch sehr schnelle semiempirische Quantenchemie zu ersetzen, was möglicherweise eine hohe Genauigkeit bei hinreichend kleinem Rechenaufwand erlaubt. Im Rahmen dieser Arbeit wurde die Polarisierbarkeit dieses Hamiltonoperators erstmals mit EC-RISM bei Umgebungsdruck und bei 10 kbar getestet und mit Ergebnissen aus der Møller-Plesset-Störungstheorie verglichen.

Third party contributions

The radial distribution functions for generating the high pressure solvent susceptibilities were produced by Dr. Christoph Hözl.

The hpCADD-Hamiltonian was parameterized by Dr. Heike B. Thomas and the group of Prof. Dr. Timothy Clark, Friedrich-Alexander-Universität Erlangen, Computer Chemie Centrum.

The EC-RISM-EMPIRE interface was mainly developed by Dr. Franziska M. Hoffgaard.

The partial molar volume correction for EC-RISM was parameterized by Nicolas Tielker.

The DEA approach for force field optimizations was mainly developed by Dr. Christoph Hözl and modified by the author for hydronium and hydroxide.

The force fields for urea and trimethylamine-N-oxide (TMAO) were parameterized, optimized and tested by Dr. Christoph Hözl. The optimization processes used data created by the author.

The *ab initio* molecular dynamics (*aiMD*) simulations have been performed by Dr. Sho Imoto, Jan Noetzel and the group of Prof. Dr. Dominik Marx.

Part I.
Introduction

1. Overview

The introduction begins with an overview of the structure of this thesis, so the reader obtains a rough overview of where to find which aspect. Whenever it seems appropriate this thesis contains crossreferences to other parts, chapters or sections of this thesis. Readers who prefer to read the electronic version are advised to use the invisible hyperlinks, that are found on crossreferences, citations, in the table of contents, the glossary and DOIs in the bibliography.

This part of the thesis will give a quick glance on the topic of small molecules under high pressure and it will introduce the different problem-sets attacked during the research leading to this thesis. The second part of this thesis beginning on page 17 will cope with the theory needed, beginning with the theory of high pressure solvation modelling including the reference interaction site model (RISM) theory for high pressure. Furthermore, it will introduce the basics of vibrational spectroscopy and first steps for calculating pressure dependent vibrational frequencies with embedded cluster reference interaction site model (EC-RISM). A thermodynamic route is discussed, that enables us to calculate the pressure dependence of chemical equilibria for the case of water autoprotolysis. The third part of this thesis holds information on the methods applied throughout this thesis and gives all computational details and settings, that were used to produce the data shown in the fourth section, which contains the results for every topic. Finally, a short summary and a perspective for future work is given. The appendix holds detailed information, that is too voluminous to be placed in the main matter.

1.1. The role of high pressure research

Modelling of solvation *per se* is a large field in physical, theoretical and computational chemistry and it raises generally the problem of modelling the thermodynamic equilibrium correctly. The influence of solvation on the molecule being in solution (solute) is important for a huge variety of properties like chemical reactivity, spectroscopic features and many more. Not only the presence of a solvating agent (solvent) but also the type of solvent is important for the solute's response. More variables, which in some cases have a great impact on solvation are, among others, temperature and pressure. This work will focus on the influence of pressure on small molecules in aqueous environments. The pressure response of these systems is explored up to 10 kbar, which

1. Overview

covers most of the pressure range, in which water can be found liquid at a temperature of 293.15 K.¹⁸

High pressure plays an important role in science and engineering. It is well known that proteins denature under the influence of extreme conditions, like high and low temperatures, high pressure or high salinities. Microorganisms, which are not adapted to pressure strain, stop growth and reproduction above 400-500 bar.¹⁹ Research on mechanisms enabling life under deep-sea conditions, including remarkably high pressures, can provide insight into the biochemical principles of complex organisms^{11,20,21} as well as understanding of mechanisms causing misfolding of proteins,²² which are related to relevant diseases like Alzheimer's. The role of small molecules like osmolytes lies in the focus of current research. The food industry has developed a broad spectrum of high pressure techniques in food preservation.^{23,24} High pressure processes are used instead of high temperature treatment, in order to sterilize food with less damage to odor, color, texture and consistency.²⁴

Already under atmospheric conditions it is convenient to combine experiments with theoretical methods to gain deeper insight into the physical foundation of measured effects. This need is even increased by applying high pressure in experiments. The need to contain the samples in high pressure cells causes additional difficulties and limitations to the choice of methods as well as to the measurements themselves.

Before theoretical methods can be applied to high pressure problems, it has to be tested whether the methods usually applied for ambient conditions are able to depict high pressure effects correctly. Thus, in this thesis high pressure solvation was introduced using the EC-RISM method,⁵ which *per se* is only dependent on experimentally available solvent properties and Lennard-Jones parameters, atomic charges and the solvent structure. In contrast, the extreme pressure polarizable continuum model (XP-PCM) method,²⁵⁻²⁸ which is a variant of the polarizable continuum model (PCM), uses pressure-dependent empirical scaling of the molecule's cavity in order to obtain the correct pressure response of the potential energy surface.²⁷ As a quantum chemistry based method, which is not in need of pressure-dependent parameterization at all - *ab initio* molecular dynamics (*aiMD*) - is available. This methodology applies explicit solvation and molecular dynamics, while the molecular properties are calculated based on electronic density functional theory (DFT). The high level of physical correctness and reliability of obtained observables comes in trade for immense computational effort, even if modern techniques are used.²⁹ Force field based molecular dynamics simulations can model drastically larger systems on a longer timescale with less effort than *aiMD*. But even this class of methods needs sufficient sampling to obtain accurate results. The equilibration time needed depends on the system and the initial conditions.³⁰

This state of affairs led to the start of a interdisciplinary cooperation project, which combines experimental and theoretical methods in order to learn about molecular properties at high pressure, to calibrate and evaluate the performance of theoretical methods and combine all available methods to obtain the most detailed impression of the physical processes that molecules experience under extreme conditions. The

1.2. Cosolvents, osmolytes and piezolytes

organizational framework of this cooperation was handled by the DFG Forschergruppe FOR 1979 situated in Bochum (Ruhr-Universität Bochum), Dortmund (Technische Universität Dortmund) and Regensburg (Universität Regensburg).

Within this research unit the question, which role electronic polarization due to the influence of high hydrostatic pressure plays for small molecules was to be answered. Therefore, high pressure was introduced in the solvent susceptibilities for quantum chemistry (QC) calculations including high pressure solvation in terms of the EC-RISM methodology. Especially, when it comes to theoretical work on the interaction between small molecules and macromolecules like proteins, methods based on solving the Schrödinger equation are not suitable due to their immense computational cost. Thus classical mechanical force fields have to be applied to model these interactions. Based on the results obtained by the research leading to this thesis, high pressure force fields for trimethylamine-N-oxide (TMAO)¹² and urea have been created and tested by cooperators. These studies indicated, that it is necessary to alter the force field charges of TMAO, in order to obtain accurate high pressure observables, while in urea the same charge modification approach leads to a loss of accuracy in the high pressure regime compared with unmodified ambient pressure charges. Additionally, in the case of TMAO it was observed, that there are blue-shifts of infrared bands, when pressure is increased.¹⁴ In a cooperational combined *ai*MD and EC-RISM study first insights into the physical basis of this blue-shift was obtained.¹⁴ To enable this, a development process for the treatment of vibrational spectroscopy within EC-RISM was begun. In order to improve the accuracy of the electrostatic interaction calculation within the EC-RISM method, a new approach for the treatment of the exact electrostatic potential from the quantum chemistry method applied, has been developed. In order to proof that the EC-RISM method is capable of being predictive for the thermodynamics under high pressure conditions, the change in the pK_W -value as a function of pressure was calculated and compared with experimental data. Once it was proven that the methodology gains good agreement with experimental results, the results of extending the EC-RISM method to a novel semi-empirical quantum mechanics (SQM) Hamiltonian were shown and compared with high-level QC in a more prospective part of this thesis.¹⁷

In the following chapter small molecules having influence on the osmotic pressure and protein denaturation under extreme conditions, the so-called osmolytes or co-solvents, are discussed.

1.2. Cosolvents, osmolytes and piezolytes

Generally substances influencing protein fold stability in aqueous environments are called cosolvents.¹³ Soluble substances influencing the osmosis, *i.e.* through cellular membranes, are called osmolytes. There are two classes of osmolytes: intracellular osmolytes and so-called plasmolytes. The terminus piezolyte is used for substances, that stabilize proteins against pressure induced unfolding.³¹ However this nomenclature is

1. Overview

disputed, since there is evidence, that the so-called piezolytes do not change the volumetric properties of proteins and thus have no direct effect on the pressure stability of proteins.³² This work uses the term piezolyte for pressure stabilizing agents without making assumptions on the physical basis for pressure stabilization. Two prominent examples of molecules found to be active in this context are trimethylamine-N-oxide (TMAO) and urea, both of which will be discussed in this thesis.

1.2.1. Trimethylamine-N-oxide

One of the most prominent examples for a stabilizing cosolvent and osmolyte is TMAO, which will be subject of this work. It is known, that some osmolytes stabilize proteins against unfolding. As already mentioned, this effect plays an important role for extremophilic life forms, like thermophiles and piezophiles.⁸⁻¹¹ The influence of pressure (deep sea environment) on protein stability and the mechanisms enabling lie in high pressure surroundings are a current topic of research. Especially enzymes being functional at low or high temperature are of interest for industrial application, while piezophilic enzymes are still more interesting for mechanistic studies.³³ Tatzelt *et al.* were able to show that the application of 100 mmol l^{-1} reduced the formation of insoluble prion plaques in scrapie infested nerve cells of mice by 50 %, while using higher concentrations of TMAO revealed toxic effects.³⁴ The $\text{p}K_{\text{a}}$ -value of TMAO is 4.56.³⁵

Due to its importance for deep-sea life in the course of this thesis theoretical work will be shown, that includes the pressure dependence of TMAO's dipole moment, contributions to the force field development for a novel, pressure dependent, TMAO force field and first approaches to a embedded cluster reference interaction site model (EC-RISM)-based analysis of vibrational spectroscopy. Figure 1.1 shows two-dimensional and three-dimensional representations of the molecular structure of TMAO.

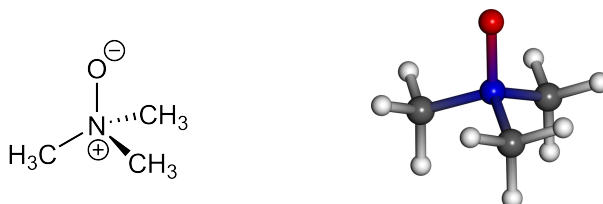


Figure 1.1.: 2D-(left) and 3D-structure(right) of N,N,N-trimethylamine-N-oxide

The results on TMAO, including pressure dependent dipole moments, a short outline of pressure dependent force field electrostatics and vibrational spectroscopy can be found in the results part of this thesis in chapter 9 beginning on page 81.

1.2.2. Urea

Urea is a relatively small organic molecule, which is known as the first ever organic compound being synthesized from inorganic educts by Friedrich Wöhler. Besides to its immense range of industrial applications, including agriculture, it is an important denaturing agent in protein science.¹³ The exact mode of action of urea in protein denaturation is a current research topic and discussed controversially in the literature.¹³ The molecular structure of urea is shown in Figure 1.2.

The hypothesis of urea disturbing the water structure in aqueous solutions is funded in the 1960s. Frank and Franks described the solubility enhancing effect on hydrocarbons in water by a statistical model based on the idea, that urea breaks up the hydrogen bond network of water.³⁶ Contradictory to this hypothesis, it was found, that urea as a single solute has no structure breaking effect on water.³⁷

In the light of protein unfolding it is discussed, that water structure weakens the hydrophobic effect, which has been shown to be the origin of the stability of folded proteins.³⁸ Furthermore a direct interaction between urea and proteins is discussed. Hydrogen bonds between urea and the protein backbone compete with the intra-protein hydrogen bonds stabilizing the folded state in this model.³⁹



Figure 1.2.: 2D (left) and 3D (right) structure of urea. The red bead represents oxygen (O), the black bead carbon (C), the blue beads nitrogen (N) and the white beads hydrogen (H).

Some marine vertebrates use mixtures of urea and TMAO as osmolytes for maintaining osmotic pressure within their cells without having to apply high concentrations of inorganic salts. It has been shown, that the protein destabilizing effect of urea is counteracted by a TMAO concentration being twice the urea concentration.^{10,35} Furthermore it was shown, that the individual effect of urea and TMAO on temperature unfolding of proteins is not changed in mixtures. Basically both agents have the same numerical effect when used alone, both on the unfolding temperature and the chemical potentials, leading to the conclusion, that both osmolytes interact with the protein independently.³⁵ In order to understand the interactions in complex systems comprised of proteins, TMAO and urea in aqueous solutions, it is necessary to prove whether or not ambient pressure optimized force fields are able to resemble the pressure response of urea in the scope of thermodynamic observables. Like in the case of TMAO the electrostatic properties of urea are examined with regard to the dipole moment. The results on urea, including the dipole moment dependency of pressure

1. Overview

and Lennard-Jones parameters can be found in the results section 10 beginning on page 97.

The following chapter illustrates the need for and the problems of force field development regarding high pressure environments.

1.3. Force field development

Since the usually applied empirical force fields for molecular mechanics and molecular dynamics (MD) simulations are parameterized in order to model properties of substances at ambient conditions, the question arises, whether there is any adaptation needed concerning simulations performed under extreme conditions. Despite the applicability of standard force fields for high-pressure conditions being unproven, there is a vast number of published data applying ambient force fields for pressurized molecules.^{12,40-42} It was even noticed, that the pressure response of different ambient pressure force fields varies.⁴¹ Validation of the obtained data is difficult, since there is nearly no experimental data and quantum chemistry (QC) calculations at high pressure conditions cannot be done by simply varying the calculation method, since the pressure is not an input to the Hamilton operator *per se*. In the picture of continuum solvation models for QC calculations, it is possible to introduce pressure by scaling the cavity^{25,26} which is built up by the solute, but this approach lacks a physical basis. Another possibility to obtain the correct pressure response of a wave-function method is to apply *ab initio* molecular dynamics (*aiMD*),⁴³ since there the pressure-dependent interactions are modelled in a realistic manner, since the solvent is treated explicitly by electronic density functional theory. Due to the immense computational cost this methodology requires it lacks applicability for large systems and for large numbers of systems.

The need for dynamic data obtained from force field based molecular dynamics simulations, especially when it comes to modelling osmolyte-protein-interactions, can only be satisfied, if force fields suitable for high pressure environments are available. In order to examine the need of high pressure adjustments to existing force fields, within the framework of the DFG research unit FOR 1979, force fields for TMAO, urea, hydronium and hydroxide have been parameterized in multiple cooperative works. A general overview for the force field development is given in the Methods part of this thesis (see Chapter 7). The results can be found in the Results section.

Force field development is a somewhat involved procedure, since the parameter space is large, especially when optimizing flexible all atom force fields for large biomolecules. Usually hierarchical approaches are chosen and as many experimental parameters as possible have to be taken into account to avoid local optimization and overfitting. In most cases pre-existing force fields are optimized rather than starting a completely new optimization process. Possible strategies for both - new force fields from scratch and the optimization and extension of new force fields - can be found in literature.^{12,16,44-48}

1.4. The ionic product of water under high pressure conditions

These approaches use reference data from spectroscopy, crystallographic information, thermodynamic measurements and also theoretically obtained data from *ab initio* single point calculations and optimizations, as well as wave function based molecular dynamics simulations.

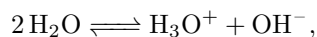
Not only solute polarization as such is interesting under high pressure conditions, but also the pressure influence on thermodynamic properties and chemical reactions. The following chapter introduces the autoprotolysis of water as an well-characterized example of a pressure-influenced chemical equilibrium.

1.4. The ionic product of water under high pressure conditions

While it is common knowledge in chemistry, that the pK_W -value of pure water at 298.15 K and 1 bar is close to 14, the pressure-dependence of autoprotolysis is less familiar among chemists. In order to determine the K_W -value under extreme conditions both direct measurements⁴⁹ and empirically parameterized equations of state⁵⁰⁻⁵² were applied throughout literature. Due to the autoprotolysis of water, hydronium and hydroxide are present wherever water plays a role as a solvent. These ions play an important role not only in chemical surface processes like catalysis but also in geology.⁵³ In some of these areas high pressures are involved, especially when it comes to deep-sea life, where pressures up to 1 kbar occur or geology, where even higher pressures are present. Since the charging of droplets was observed, for instance in waterfalls, much theoretical work on the adsorption of hydroxide to the water/vapor, water/air, water/solid and water/hydrophobic liquid interface has been published.⁵⁴⁻⁵⁸

The relevance of autoprotolysis on the one hand and the availability of experimental high-pressure data on the other hand, makes the aqueous autoprotolysis an ideal benchmark case for the embedded cluster reference interaction site model (EC-RISM) approach.

This chapter will show the calculation of the ionic product of water, resulting from autoprotolysis as a function of pressure. Furthermore, an approach for obtaining force field parameters for the autoprotolysis products hydronium and hydroxide will be presented. The simplest reaction to describe water autoprotolysis is



where the chemical equilibrium is far on the left hand side. Under pressure the autoprotolysis equilibrium shifts towards the right hand side, which was observed in early experiments on this matter. Data from these experiments are shown later on, see Table 1.1 on page 11.⁴⁹

1. Overview

1.4.1. Experimental findings and methods

Since the lack of experimental data under extreme conditions was more severe in the middle of the 20th century, it was desirable to calculate equilibria and other thermodynamic data under high pressure. Equations of state were thus parameterized to calculate different properties, relying on comparatively few data points for parameterization. For instance Owen and Brinkley⁵⁹ started with the well-known equation

$$RT \left(\frac{\partial \ln K}{\partial p} \right)_{T,m} = -\Delta \bar{V}^\circ, \quad (1.1)$$

where R is the universal gas constant, T the temperature, K the thermodynamic equilibrium constant, p the pressure and m the mass.

Assuming that the compressibility of the solute is not pressure-dependent, the pressure-dependent partial molar volume is given as

$$\bar{V}^\circ(p) = \bar{V}^\circ(1 \text{ bar}) - \kappa^\circ(p - 1 \text{ bar}). \quad (1.2)$$

Where

$$\kappa^\circ = - \left(\frac{\partial \bar{V}^\circ}{\partial p} \right)_{T,m} \quad (1.3)$$

is the molal compressibility. Inserting this into equation (1.1), integration yields

$$RT \ln \left(\frac{K(p)}{K(1 \text{ bar})} \right) = -\Delta \bar{V}^\circ(p - 1 \text{ bar}) + \frac{1}{2} \Delta \kappa^\circ (p - 1 \text{ bar})^2. \quad (1.4)$$

In order to include more effects, especially at very high pressures, Gibson developed an empirical equation connecting pressure and density, based on the Tait equation, resulting in a classical equation of state⁶⁰

$$- \Delta_p v = C \ln \left(\frac{B + p}{B} \right), \quad (1.5)$$

with $\Delta_p v$ being the difference of the specific volume $v = 1/\rho$ upon compression from vacuum to the pressure p ; B and C are positive constants. B is a measure for an effective cohesion pressure. Applying Tamman's hypothesis,⁶¹ stating that the solvent in a solution acts like the pure solvent under an external pressure p_e , the Tait equation can be written to calculate the apparent solute volume

$$\phi_1 = v_W - C \ln \left(\frac{B + p_e + p}{B + p} \right). \quad (1.6)$$

Applying the state of the art from the early 1960s it was impossible to determine the ionic product of water calorimetrically. Even the usual way to measure ionization phenomena in aqueous solutions conductometrically was not feasible, since the low

1.4. The ionic product of water under high pressure conditions

concentrations of autoprotolysis products require a level of water purity, which cannot be maintained in high pressure apparatus. For potentiometrical measurements the normal hydrogen electrode would be the reference electrode to be favored, but again: high pressure prohibits the use of gaseous hydrogen. So Hamann described a potentiometrical method using glass electrodes in a pressure range from 1 atm to 2000 atm.⁴⁹ Using his technique, he measured the relative changes of K_W as a function of pressure, applying the approximation

$$E(p) - E(1 \text{ atm}) \approx -\frac{RT}{F} \ln(K_W(p)/K_W(1 \text{ atm})), \quad (1.7)$$

with the electromotoric force E and the Faraday constant F .

The results from this publication are shown in Table 1.1. In this context, in this thesis

$$\Delta pK_W(p) = pK_W(p) - pK_W(1 \text{ bar}) \quad (1.8)$$

is the difference between the pK_W -value at the pressure p to atmospheric pressure, which in modern publications is 1 bar and in older publication 1 atm.

In order to avoid the difficulties arising from the changes in the density upon pressurization, in high pressure contexts the molarity is replaced by molality.¹ The results of an early equation of state are shown in the same table. Both data sets show the same trend, but they do not agree in slope and curvature.

Table 1.1.: Experimental relative changes of K_W as a function of the pressure p measured by Hamann⁴⁹ and early predictions by Owen and Brinkley.⁵⁹ Values in brackets denote the corresponding change $\Delta pK_W(p)$ with respect to atmospheric pressure.

p / atm	$K_W(p)/K_W(1 \text{ atm})$ ⁴⁹	$K_W(p)/K_W(1 \text{ atm})$ ⁵⁹
1	1.00 (0.000)	1.000 (0.000)
250	1.23 (-0.090)	1.261 (-0.101)
500	1.49 (-0.173)	1.574 (-0.197)
1000	2.14 (-0.330)	1.943 (-0.288)
1250	2.58 (-0.412)	2.380 (-0.377)
1500	2.97 (-0.473)	2.893 (-0.461)
1750	3.53 (-0.548)	3.492 (-0.543)
2000	4.01 (-0.603)	5.000 (-0.699)

Later experimental and theoretical works lead to a variety of equations of state to model the pressure-dependence of the autoprotolysis, two examples are shown in Table 1.2.^{51,52} The modern equation of state by Bandura *et al.* is used as the source for reference data in this work.⁵² Here we see, that the different equations of state deviate for higher pressures, while the agreement is good for medium pressures.

¹Being a certain amount of substance in one kilogram of solution, which – assuming no changes in equilibria occur – is pressure-independent.

1. Overview

Table 1.2.: pK_W -values under high-pressure conditions calculated with different equations of state. Values in brackets denote the change with respect to 1 bar. The right column shows the reference data used in this work.

p/bar	pK_W^{51}	pK_W^{52}
1	13.99 (0.00)	13.99 (0.00)
100	13.95 (-0.04)	13.96 (-0.03)
500	13.82 (-0.17)	13.82 (-0.17)
1000	13.66 (-0.33)	13.67 (-0.32)
2000	13.40 (-0.59)	13.39 (-0.60)
3000	13.18 (-0.81)	13.15 (-0.84)
4000	13.00 (-0.99)	12.93 (-1.06)
5000	12.83 (-1.16)	12.74 (-1.25)
7500	12.49 (-1.50)	12.30 (-1.69)
10000	12.21 (-1.78)	11.95 (-2.04)

In order to calculate the thermodynamic equilibrium underlying the autoprotolysis requires some thermodynamical considerations, which are introduced in the theory section of this thesis in chapter 4 beginning on page 43.

In order to be able to treat small molecules quicker within the scope of EC-RISM, self-consistent calculations applying a novel semi-empirical Hamilton operator, which was designed to obtain electrostatic information on drug-like molecules, was tested. An introduction on this Hamilton operator and the motivation for its creation and use are given in the following chapter.

1.5. Semi-empirical quantum chemistry within EC-RISM

Semi-empirical quantum mechanics (SQM) methods are applied in case of classical non-polarizable force fields being insufficient for the description of some binding phenomena, where neither electronic density functional theory (DFT) methods nor *ab initio* calculations are feasible due to their immense computational cost. Especially some non-covalent binding modes, like the σ -hole-effect⁶² or halogen bonds,⁶³ which both are strongly dependent on polarization effects, can be treated in this fashion,⁶⁴ while point-charge based force fields fail. In order to find a suitable approach for the electrostatic part of a polarizable force field that is still to be developed, the high performance computer-aided drug design (hpCADD) project funded by the Bundesministerium für Bildung und Forschung (BMBF), was established.¹⁷ The hpCADD-approach is based on solving the molecular wave function in the neglect of differential diatomic overlap (NDDO) picture in order to obtain the molecular electrostatic properties including the polarization due to the environment.¹⁷ It was not the aim of this project to obtain a Hamiltonian suitable for the calculation of energies or geometries, since these

observables will be obtained from the classical part of the force field, which is still to be developed.

1.5.1. Parametrization of the hpCADD Hamiltonian

The methods and procedures described in this section were already published.¹⁷ The molecular geometries used throughout the parameterization and benchmarking process were performed with Gaussian 09 Rev. E.01,⁶⁵ applying the MP2/aug-cc-pVDZ level of theory/basis set combination. On the same level the dipole moment vector components were calculated and compared with the Hamiltonian to parameterize. Furthermore, the standard deviation, mean signed and unsigned deviations and the maximum and minimum deviations between the high level model and the Hamiltonian candidate on the ParaSurf (AM1) isodensity surface, obtained with the atomic multipole method, were minimized. As an experimental input, vertical ionization potentials from literature were used and, like initial parameters, taken from the NDDO Hamiltonian^{66,67}, except the one electron ionization potential of the hydrogen 1s-orbital, which was taken from experimental data⁶⁸ in order to fix the ionization energies. The derived parameters for multipole integrals were calculated as on the original mutual neglect of diatomic overlap (MNDO) approach.⁶⁶ As a result there are 12 parameters per atom type at maximum. The parameter optimization was performed using the eigenvector following approach⁶⁹ on numerical gradients obtained with the EMPIRE SQM package.^{70,71} Although in the current parameterization d-orbitals were left out, due to computational effort, there is no particular reason, why possible future hpCADD releases should not contain them.

In the original publication of the new Hamiltonian, only vacuum electrostatic properties were benchmarked, but not the solvent induced polarization and even less the effects of pressure. Analysis of both - the fully converged EC-RISM cycle with the novel hpCADD Hamiltonian as the quantum chemistry part, and calculating 10 kbar fully converged EC-RISM solvation - yields insight into the polarization response upon solvation in a very polar solvent - water - which can additionally be amplified by pressure application. With this data available on the one hand it is possible to compare the absolute polarization response with MP2/aug-cc-pVDZ and on the other hand to compare the change in polarization due to pressure increase.

Part II.

Theory

2. Dependence of thermodynamics on solvation structure

In order to calculate thermodynamic properties it is necessary to know the connection between microscopic and macroscopic properties of substances. In the 1950s, Kirkwood and Buff developed a theory, which is capable of covering these two scales.⁷² The central molecular property is the site-site radial distribution function $g_{\alpha\gamma}(r)$ where $r = |\mathbf{r}_\alpha - \mathbf{r}_\gamma|$ is the distance between the sites α and γ . The potential of mean force (PMF) w between two sites is easily obtained by

$$w_{\alpha\gamma}(r) = -k_{\text{B}}T \ln(g_{\alpha\gamma}(r)) \quad (2.1)$$

with the Boltzmann constant k_{B} and the temperature T . It can be understood as the amount of work, which is needed to bring the particles α and γ from infinite separation to the distance r , giving the effective interaction in solution between both particles. The gradient of the PMF is equivalent to the average force that particle j exerts on particle i and *vice versa*. Integration over the site-site total correlation function

$$h_{\alpha\gamma}(\mathbf{r}) = g_{\alpha\gamma}(\mathbf{r}) - 1 \quad (2.2)$$

yields the Kirkwood-Buff integral

$$G_{\alpha\gamma} = \int_V h_{\alpha\gamma}(\mathbf{r}) d\mathbf{r}. \quad (2.3)$$

Exemplary the partial molar volume of the component α in a two-component system comprised of α and γ is obtained from

$$\bar{V}_m(\alpha) = \frac{1 + \rho_j(G_{\gamma\gamma} - G_{\alpha\gamma})}{\rho_\alpha + \rho_\gamma + \rho_\alpha\rho_\gamma(G_{\alpha\alpha} + G_{\gamma\gamma} - 2G_{\alpha\gamma})}, \quad (2.4)$$

where ρ_i is the density of i .⁷³ There are many more relations to calculate *e. g.* chemical potentials, osmotic pressures, or compressibilities. Calculating pair distribution functions can be achieved by molecular dynamics simulations, by Monte Carlo approaches or by statistical solvent models, directly yielding equilibrium distributions.

2.1. Statistical solvation models

The class of statistical solvent models is based on classical density functional theory (DFT), which, similar to electronic DFT, connects free energy by a unique functional $A[\rho] = A^{\text{id}} + A^{\text{ex}}[\rho]$ with the density of the fluid:⁷⁴

$$A^{\text{ex}}[\rho] = A^{\text{ex}}[\rho_0] - \beta^{-1} \left(\int \Delta\rho(\mathbf{r}) \frac{\delta A^{\text{ex}}[\rho_0]}{\delta\rho(\mathbf{r})} d\mathbf{r} + \int_0^1 d\lambda (1-\lambda) \iiint \Delta\rho(\mathbf{r}) \rho(\mathbf{r}') c(\mathbf{r}, \mathbf{r}'; \lambda) d\mathbf{r} d\mathbf{r}' \right), \quad (2.5)$$

where $A^{\text{ex}}[\rho_0]$ is the unknown excess part of the free energy of the undisturbed reference system and

$$c(\mathbf{r}, \mathbf{r}') = -\beta \frac{\delta^2 A^{\text{ex}}[\rho]}{\delta\rho(\mathbf{r})\delta\rho(\mathbf{r}')} \quad (2.6)$$

is the direct second order correlation function. The integral over the coupling parameter λ is a thermodynamic integration in order to scale from no interaction between solute and solvent ($\lambda = 0$) to full interaction ($\lambda = 1$). The three dimensional pair distribution function $g(\mathbf{r}_\alpha, \mathbf{r}_\gamma)$ connects the local density $\rho(\mathbf{r}, \lambda = 1)$ with the bulk density ρ :

$$\rho(\mathbf{r}, \lambda = 1) = \rho g(\mathbf{r}_\alpha = 0, \mathbf{r}_\gamma). \quad (2.7)$$

The local density fluctuation

$$\Delta\rho(\mathbf{r}_\gamma) = \rho(\mathbf{r}, \lambda = 1) - \rho(\mathbf{r}, \lambda = 0) = \rho g(\mathbf{r}_\alpha = 0, \mathbf{r}_\gamma) - \rho \stackrel{!}{=} \rho h(\mathbf{r}_\alpha = 0, \mathbf{r}_\gamma) \quad (2.8)$$

results in the definition of the total correlation function $h(r) = g(r) - 1$.⁷⁴

Following the assumption that introducing an interacting particle has nearly no impact on the direct correlation function, the Helmholtz free energy functional in the hypernetted chain (HNC) approximation can be simplified to gain

$$A[\rho] = A^{\text{id}} + A^{\text{ex}}[\rho_0] - \mu^{\text{ex}} \int \Delta\rho(\mathbf{r}) d\mathbf{r} - \frac{1}{2} \beta^{-1} \iiint \Delta\rho(\mathbf{r}) \Delta\rho(\mathbf{r}') c_0(\mathbf{r}, \mathbf{r}') d\mathbf{r} d\mathbf{r}'. \quad (2.9)$$

Introducing this functional in the grand canonical potential

$$\Omega[\rho] = A[\rho] + \int U(\mathbf{r}) \rho(\mathbf{r}) d\mathbf{r} - \mu \int \rho(\mathbf{r}) d\mathbf{r} \quad (2.10)$$

the density

$$\rho(\mathbf{r}) = \rho_0 \exp \left[-\beta U(\mathbf{r}) + \int \Delta\rho(\mathbf{r}') c_0(\mathbf{r}, \mathbf{r}') d\mathbf{r}' \right] \quad (2.11)$$

is found to minimize the grand canonical potential in a variational approach with the total interaction potential $U(\mathbf{r})$. For a uniform fluid under the assumptions that the

2.2. The molecular Ornstein-Zernike equation

solute particle α is one of the solvent particles γ , the number of particles is constant and the interaction potential $U(\mathbf{r})$ can be described by an additive pair potential $u_{\alpha\gamma}(r_{\alpha\gamma})$, which is only dependent on the distance $r_{\alpha\gamma}$ between both interacting particles, the HNC closure can be obtained:⁶

$$g(\mathbf{r}_{\alpha\gamma}) = \exp \left[-\beta u_{\alpha\gamma}(\mathbf{r}_{\alpha\gamma}) + \rho \int c_{\mathbf{r}_{\alpha\gamma}}(r_{\alpha\gamma}) h(\mathbf{r}_{\alpha\gamma}) d\mathbf{r}_{\gamma'} \right]. \quad (2.12)$$

Terms missing due to the assumptions leading to the HNC closure can be absorbed in a so-called bridge function B , which is not available in a closed analytical form, but can be accounted for numerically, when using explicit solvent simulation derived radial distribution functions.

The HNC closure can be further simplified by a partial series expansion (PSE) approach, leading to the k-th order PSE closure

$$h_{\gamma}(\mathbf{r}) = \begin{cases} \exp(-\beta u_{\gamma}(\mathbf{r}) + h_{\gamma}(\mathbf{r}) - c_{\gamma}(\mathbf{r})) - 1 & \forall -\beta u(\mathbf{r}) - c_{\gamma}(\mathbf{r}) \leq 0 \\ \sum_k \frac{(-\beta u_{\gamma}(\mathbf{r}) + h_{\gamma}(\mathbf{r}) - c_{\gamma}(\mathbf{r}))^k}{k!} & \forall -\beta u(\mathbf{r}) - c_{\gamma}(\mathbf{r}) > 0, \end{cases} \quad (2.13)$$

which replaces the evaluation of the HNC-closure by a Taylor series approximation.⁷⁵ The first order PSE closure is also known as the Kovalenko-Hirata closure.⁷⁶

The closure alone can not be solved, since both, the total correlation function h and the direct correlation function c are not known. The Ornstein-Zernike integral equation

$$h(\mathbf{r}_{\alpha\gamma}) = c(\mathbf{r}_{\alpha\gamma}) + \rho \int c(\mathbf{r}_{\alpha\gamma}) h(\mathbf{r}_{\gamma\gamma'}) d\mathbf{r}' \quad (2.14)$$

can be used as the missing equation to construct a closed system of equations.⁷⁷ The obtained system of equations is applicable for solvation phenomena regarding spherical particles.

2.2. The molecular Ornstein-Zernike equation

For the treatment of molecular solutions, the Ornstein-Zernike theory⁷⁷ has to be extended in two scopes: On the one hand it is necessary to extend the pure solvent method (vv) to solute-solvent (uv) applications and on the other hand it has to be enabled to handle non-spherical anisotropic species. The Ornstein-Zernike equation can be extended to a system of equations

$$\begin{pmatrix} h_{vv} & h_{uv} \\ h_{uv} & h_{uu} \end{pmatrix} - \begin{pmatrix} c_{vv} & c_{uv} \\ c_{uv} & c_{uu} \end{pmatrix} = \begin{pmatrix} c_{vv} & c_{uv} \\ c_{uv} & c_{uu} \end{pmatrix} * \left[\begin{pmatrix} \rho_v & 0 \\ 0 & 0 \end{pmatrix} \cdot \begin{pmatrix} h_{vv} & h_{uv} \\ h_{uv} & h_{uu} \end{pmatrix} \right] \quad (2.15)$$

copying with the vv, uv and uu cases; the *-symbol means convolution. This system of equations can be split up in three integral equations

$$h_{vv} = c_{vv} + (c_{vv} * p_v h_{vv}), \quad (2.16)$$

2. Dependence of thermodynamics on solvation structure

$$h_{uv} = c_{uv} + (c_{uv} * p_v h_{vv}), \quad (2.17)$$

and

$$h_{uu} = c_{uu} + (c_{uv} * p_v h_{uv}). \quad (2.18)$$

This work uses mainly the uv-case in order to calculate molecular properties in solvation and the vv case for determining the solvent susceptibilities, which will be described in following chapters.

In order to treat molecular systems, which usually are not spherically symmetric, more sophisticated methods are necessary. The Ornstein-Zernike equation can be generalized for anisotropic fluids resulting in the molecular Ornstein-Zernike equation⁷⁸

$$h(\mathbf{r}_{\alpha\gamma}, \mathbf{\Omega}_\alpha, \mathbf{\Omega}_\gamma) = c(\mathbf{r}_{\alpha\gamma}, \mathbf{\Omega}_\alpha, \mathbf{\Omega}_\gamma) + \frac{\rho}{8\pi^2} \iint c(\mathbf{r}_{\alpha\gamma}, \mathbf{\Omega}_\alpha, \mathbf{\Omega}_\gamma) h(\mathbf{r}_{\gamma\gamma'}, \mathbf{\Omega}_\alpha, \mathbf{\Omega}_{\gamma'}) d\mathbf{r}_{\gamma'} d\mathbf{\Omega}_{\gamma'} \quad (2.19)$$

that - besides the distance of molecules - recognizes the orientation of the molecules by their Eulerian angles $\mathbf{\Omega}$.

2.3. The reference interaction site model: 1D RISM

Since the system of equations consisting of closure and molecular Ornstein-Zernike equation is difficult and expensive to solve numerically, further approximations have to be applied, leading to an approach called the reference interaction site model (RISM).^{1,2} The basic idea is not to describe the molecules as a single particle, but to use interaction sites, which *e.g.* are the atom positions. In this picture the direct correlation function is approximated as a sum of site-site direct correlation functions

$$c \approx \sum_{\alpha} \sum_{\gamma} c_{\alpha\gamma}(|\mathbf{r}_{\alpha\gamma}|). \quad (2.20)$$

This approach neglects the molecular orientation by averaging.¹

Applying this approach to the integral equations (2.16) and (2.17) leads to the 1D RISM integral equations

$$\rho_v \mathbf{h}_{vv} = \boldsymbol{\omega}_v * \mathbf{c}_{vv} * \boldsymbol{\chi}_{vv} \quad (2.21)$$

and

$$\rho_v \mathbf{h}_{uv} = \boldsymbol{\omega}_u * \mathbf{c}_{uv} * \boldsymbol{\chi}_{vv} \quad (2.22)$$

with the solvent susceptibility

$$\boldsymbol{\chi}_{vv} = \rho_v \boldsymbol{\omega}_v + \rho_v^2 \mathbf{h}_{vv} \quad (2.23)$$

and the intramolecular correlation matrix $\boldsymbol{\omega}$ comprised of the elements

$$\omega_{\alpha\gamma} = \frac{\delta |r_{\alpha\gamma} - l_{\alpha\gamma}|}{4\pi l_{\alpha\gamma}^2}, \quad (2.24)$$

2.4. Calculating solvent susceptibilities

where $l_{\alpha\gamma}$ are the intramolecular site-site distances, representing the three-dimensional structure of the molecule.

This approach enables calculations of radial distribution functions for pure solvents and for solute-solvent systems. In the latter case the solvent susceptibility has to be precomputed in a 1D RISM(vv) calculation. As a result the radial (1D) total correlation functions for every site-site pair are obtained. Since it was observed that the dielectric constant of 1D RISM calculated solvents differs considerably from experimental results, empirical corrections like the DRISM method were developed.^{79,80} For the calculation of solvent susceptibilities in this work, the DRISM formalism was applied.

2.4. Calculating solvent susceptibilities

For every RISM(uv) calculation, regardless of it being one- or three-dimensional, a precalculated solvent susceptibility is needed. In order to perform the necessary 1D DRISM calculations, some input data is required. As a prerequisite the molecular geometry, partial atomic charges and Lennard-Jones parameters are needed for the construction of the pairwise interaction potential. Furthermore, the dielectric constant ϵ and the bulk density ρ are needed¹. With these ingredients in place it is possible to obtain solvent susceptibilities constructed by applying the HNC approximation.

In order to introduce non-zero bridge function contributions, it is possible to use MD simulation based radial distribution functions as a basis for calculating the solvent susceptibilities. For the sake of performance the 1D RISM calculations are performed on a logarithmically scaled grid, where the grid point distance gets larger with growing distance from the center. On the other hand, radial distribution functions usually are obtained on equidistant grids. In order to transform the distribution function from one grid to the other and to filter out high frequency noise, a smoothing spline interpolation is used. Due to the limited box size in MD simulations, the obtained distribution functions usually are rather short-ranged because of the minimum image convention. In order to obtain a sufficient radial range, a smooth cubic switching function is applied to switch from the simulation-based distribution function in the vicinity of the box center to the HNC 1D RISM-based distribution function in the distant range of the grid. Following this approach the bridge function becomes

$$B_{\alpha\gamma}(r) = f(r) [\ln(g_{\alpha\gamma}^{\text{MD}}(r)) + \beta u_{\alpha\gamma}(r) - h_{\alpha\gamma}(r) + c_{\alpha\gamma}(r)], \quad (2.25)$$

where $f(r)$ is the cubic switching function dependent on the simulation box size.⁷

¹In fact these two inputs are carrying the pressure information introduced in the solvent susceptibility

2. Dependence of thermodynamics on solvation structure

2.5. 3D RISM

In principle it is possible to substitute the radial correlation functions in the 1D RISM theory by the spatial ones, which leads to the 3D RISM method, where

$$c(\boldsymbol{\Omega}, \mathbf{r}) \approx \sum_{\gamma} c_{\gamma}(\mathbf{r}) \quad (2.26)$$

can be written. Again there is a system of integral equations

$$\rho_{\gamma, \infty} h_{\gamma}(\mathbf{r}) = \sum_{\gamma'} c_{\gamma'} * \chi_{\gamma\gamma'}(\mathbf{r}), \quad (2.27)$$

where $\rho_{\gamma, \infty}$ is the non-perturbed bulk site density.^{3,4} The second equation in this system again is the closure function

$$h_{\gamma}(\mathbf{r}) = \exp(-\beta u_{\gamma}(\mathbf{r}) + h_{\gamma}(\mathbf{r}) - c_{\gamma}(\mathbf{r}) + B_{\gamma}(\mathbf{r})) - 1. \quad (2.28)$$

Besides the functions already known from 1D RISM theory, $B_{\gamma}(\mathbf{r})$ is the so-called bridge function, which is omitted in case of the HNC-closure. Non-zero bridge functions lead to the need to ensure path independence of the excess chemical potential.

In the 3D-RISM theory, there are analytical expressions for the chemical excess potential μ^{ex} , which is part of the total chemical potential of a component i , given by

$$\mu_i = \left(\frac{\partial G}{\partial n_i} \right)_{p,T} = \mu^{\text{id}} + \mu^{\text{ex}}. \quad (2.29)$$

The calculation of the excess chemical potential is closure dependent. In case of the HNC closure it is

$$\mu_{\text{HNC}}^{\text{ex}} = \frac{1}{\beta} \sum_{\gamma} \rho_{\gamma} \int \left(\frac{1}{2} h_{\gamma}^2(\mathbf{r}) - c_{\gamma}(\mathbf{r}) - \frac{1}{2} h_{\gamma}(\mathbf{r}) c_{\gamma}(\mathbf{r}) \right) \text{d}\mathbf{r}. \quad (2.30)$$

The expression becomes

$$\mu_{\text{PSE}}^{\text{ex}} = \mu_{\text{HNC}}^{\text{ex}} - \frac{1}{\beta} \sum_{\gamma} \rho_{\gamma} \int \frac{\Theta(h_{\gamma}(\mathbf{r})) (h_{\gamma}(\mathbf{r}) - \beta u_{\gamma}(\mathbf{r}) - c_{\gamma}(\mathbf{r}))^{k+1}}{(k+1)!} \text{d}\mathbf{r} \quad (2.31)$$

in the case of the k^{th} order PSE closure.⁷⁵ Θ is the Heaviside step function.

The pairwise interaction potential $u_{\gamma}(\mathbf{r})$ can be split into two additive contributions: a short range part $u_{\gamma}(\mathbf{r})^S$ and a long range contribution $u_{\gamma}(\mathbf{r})^L$. The electrostatic contribution to this potential can be described by the total electrostatic potential

$$u^c(\mathbf{r}) = u^{c, \text{PC}}(\mathbf{r}) + \Delta u^c(\mathbf{r}) \quad (2.32)$$

resulting in a renormalization approach. The first term $u^{c-pc}(\mathbf{r})$ is the electrostatic potential derived from atomic partial charges, usually created by an ESP fitting procedure in EC-RISM calculations. The second part of this equation is the difference between the exact potential and the point charge based one and thus is expected to be short-ranged.¹⁵ In a standard Ewald summation⁸¹ approach the electrostatic potential is further split into two contributions: A short range term and a long range term. The latter contribution is smooth and can thus be treated easily in reciprocal space.

2.6. Coupling the 3D RISM approach with quantum chemistry: EC-RISM

The embedded cluster reference interaction site model (EC-RISM) method⁵ couples quantum chemical calculations with the 3D RISM in a self consistent approach to model granular solvents in quantum chemical calculations. Basically, this is achieved by a mutual electrostatic polarization of solute(u) and solvent(v). Starting with a vacuum quantum chemistry (QC) calculation of the solute, the electrostatic potential is obtained based on the molecular wave function. In order to model the solute's polarizing effect on the solvent, the electrostatic potential has to be handed over to the three-dimensional reference interaction site model (3D RISM) solver. There are two basic methods to achieve that: First an electrostatic potential (ESP) fit method can be used to represent the ESP by point charges at the solute's atom positions (partial charges), second it is possible to use the whole ESP *per se*. The solute's polarization by the solvent is achieved by creating a grid of point charges. This embedding point charge cluster is calculated from the radial distribution function $g(\mathbf{r})$ and the site charges q_γ to obtain the charge density

$$\rho_\gamma^q(\mathbf{r}) = \sum_\gamma q_\gamma \rho_{\gamma,\infty} g_\gamma(\mathbf{r}) \quad (2.33)$$

which then is discretized on a grid leading to the point charges

$$q_\gamma(\mathbf{r}_i) \Delta V \quad (2.34)$$

with the grid cell volume $\Delta V = \Delta x \Delta y \Delta z$.

In the EC-RISM-picture the Gibbs energy in solution for a molecule - described by its set of atom coordinates $\{\mathbf{r}\}$ - can approximately be stated as

$$G(\{\mathbf{r}\}) \approx E_{\text{solv}}(\{\mathbf{r}\}) + \mu^{\text{ex}}(\{\mathbf{r}\}), \quad (2.35)$$

where $E_{\text{solv}}(\{\mathbf{r}\})$ is the electronic energy in solvation derived from QC and $\mu^{\text{ex}}(\{\mathbf{r}\})$ the excess chemical potential from 3D RISM.

Since the treatment of the electrostatic potential in 3D RISM method is quite intricate, it will be explained separately in the following section.

2. Dependence of thermodynamics on solvation structure

2.6.1. Potential calculation in EC-RISM

In the 3D RISM approach, the effect of the solute on the solvent is represented by the potential energy

$$u(\mathbf{r}) = u^{\text{LJ}}(\mathbf{r}) + u_\phi(\mathbf{r}), \quad (2.36)$$

which is comprised of the Lennard-Jones potential energy

$$u^{\text{LJ}}(\mathbf{r}) = \sum_{\alpha} \sum_{\gamma} 4\epsilon_{\alpha\gamma} \left(\left(\frac{\sigma_{\alpha\gamma}}{r(\mathbf{r}_{\alpha}, \mathbf{r}_{\gamma})} \right)^{12} - \left(\frac{\sigma_{\alpha\gamma}}{r(\mathbf{r}_{\alpha}, \mathbf{r}_{\gamma})} \right)^6 \right) \quad (2.37)$$

and the electrostatic potential energy

$$u_\phi(\mathbf{r}) = \sum_{\gamma} \phi(\mathbf{r}) q_{\gamma}. \quad (2.38)$$

Here $\epsilon_{\alpha\gamma}$ and $\sigma_{\alpha\gamma}$ are the mixed Lennard-Jones parameters for the solute-solvent site pair $(\alpha\gamma)$ and q_{γ} is the partial charge of the solvent site γ . As mentioned before, the electrostatic potential can be obtained from atomic partial charges or directly from the molecular wave function of the solute. Here the distance

$$r(\mathbf{r}_{\alpha}, \mathbf{r}_{\gamma}) = |\mathbf{r}_{\gamma} - \mathbf{r}_{\alpha}| \quad (2.39)$$

is the Euclidean distance between the solute site γ and the solvent-site representation at the grid point position \mathbf{r}_{α} .

For numerical reasons the electrostatic potential is handled with a Ewald sum approach splitting up the Coulomb potential into two contributing terms. The Ewald idea is based on splitting long range potentials into a short range part, which can easily be handled in real space and a long range part, which should be as smooth as possible allowing for efficient reciprocal space treatment. This split is achieved by a renormalization approach¹⁵, utilizing the Coulomb interaction energy based on the ESP fit derived charges

$$u^{\text{q}}(\mathbf{r}_{\alpha}\mathbf{r}) = \sum_{\alpha} \sum_{\gamma} \frac{q_{\alpha}q_{\gamma}}{4\pi\epsilon_0 r(\mathbf{r}_{\alpha}, \mathbf{r})}. \quad (2.40)$$

To obtain the splitting, the error function erf and its complement function erfc are used due to their smoothness. So the point charge based potential is split up into a short ranged contribution

$$u_{\text{S}}^{\text{q}}(\mathbf{r}_{\alpha}\mathbf{r}) = \text{erfc} \left(\frac{r(\mathbf{r}_{\alpha}, \mathbf{r}_{\gamma})}{r_p} \right) u^{\text{q}}(\mathbf{r}_{\alpha}\mathbf{r}) \quad (2.41)$$

and a long range contribution

$$u_{\text{L}}^{\text{q}}(\mathbf{r}_{\alpha}\mathbf{r}) = \text{erf} \left(\frac{r(\mathbf{r}_{\alpha}, \mathbf{r}_{\gamma})}{r_p} \right) u^{\text{q}}(\mathbf{r}_{\alpha}\mathbf{r}). \quad (2.42)$$

2.6. Coupling the 3D RISM approach with quantum chemistry: EC-RISM

The error function erf and its complement erfc are convenient for this task, since they are smooth and sum up to 1 at every position. The parameter r_p determines the slope of the scaling. The exact quantum mechanically derived electrostatic interaction energy and the Lennard-Jones interaction energy comprise the total short range interaction energy

$$u^S(\mathbf{r}) = u^{\text{LJ}}(\mathbf{r}) + u^{\text{QC}}(\mathbf{r}) + (u_{\text{S}}^{\text{q}}(\mathbf{r}) - u^{\text{q}}(\mathbf{r})). \quad (2.43)$$

The long range interaction energy is

$$u^{\text{L}}(\mathbf{r}) = u_{\text{L}}^{\text{q}}(\mathbf{r}) \quad (2.44)$$

the long range point charge based Coulomb interaction, which effectively does not contribute to the total interaction energy due to the construction of the renormalization ansatz. This is exact, as long as the calculation grid is sufficiently large to make the difference

$$\Delta u^{\text{C}} = u_{\phi}^{\text{C}}(\mathbf{r}) - u^{\text{q}}(\mathbf{r}) \quad (2.45)$$

vanish at the grid border.

In order to overcome this issue, a new technique, involving gradual switching of the potential evaluation from the exact one in the vicinity of the molecule to the point charge based one at the box edges, is introduced. The cubic switching function

$$s(r; r_{\min}, r_{\max}) = \begin{cases} 1 & \forall r < r_{\min} \\ s_0 + r s_1 + r^2 s_2 + r^3 s_3 & \forall r_{\min} \leq r \leq r_{\max} \\ 0 & \forall r > r_{\max} \end{cases} \quad (2.46)$$

with

$$s_0 = (3r_{\min} r_{\max}^2 - r_{\max}^3) f_s(r_{\min}, r_{\max}), \quad (2.47)$$

$$s_1 = -6 r_{\min} r_{\max} f_s(r_{\min}, r_{\max}), \quad (2.48)$$

$$s_2 = 3(r_{\min} + r_{\max}) f_s(r_{\min}, r_{\max}), \quad (2.49)$$

$$s_3 = -2f_s(r_{\min}, r_{\max}), \quad (2.50)$$

and

$$f_s(r_{\min}, r_{\max}) = (r_{\min} - r_{\max})^3 \quad (2.51)$$

smoothly scales from the QC ESP to the point charge based one. The maximum switching radius is chosen to ensure that the cubic RISM box touches the switching sphere in one point per side (see figure 2.1),ⁱⁱ r_{\min} is per default 2 Å smaller, resulting in 2 Å of switching radial buffer length. This approach has so far only been tested for cubic calculation boxes.

The error in the excess chemical potential of solvation resulting from manipulating the exact ESP

$$\Delta_s \mu^{\text{ex}} = \int_V d\mathbf{r} g(\mathbf{r}) \rho_{\gamma} \Delta_s u(\mathbf{r}) \quad (2.52)$$

ⁱⁱSo the outer switching sphere with $r = r_{\max}$ is the inscribed sphere of the box.

2. Dependence of thermodynamics on solvation structure

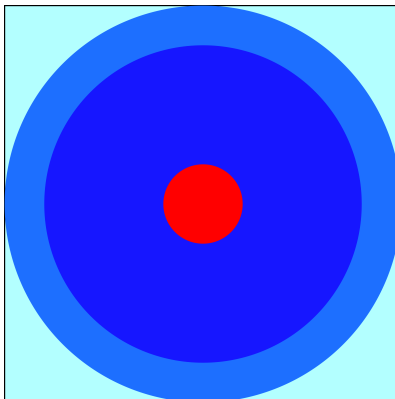


Figure 2.1.: 2D drawing of the switching scheme. Color code: red - solute, dark blue - exact ESP, middle blue - switching zone, light blue - point charge ESP.

can optionally be calculated by the first order perturbation term above, where $\Delta_s u(\mathbf{r}) = (1 - s(r; r_{\min}, r_{\max})) (u^{\text{QC}}(\mathbf{r}) - u^{\text{q}}(\mathbf{r}))$ is the difference between the QC potential and the switched one.

With this novel toolset, in principle three ways to treat the electrostatic potential are available:

1. No switching is applied,
2. switching is applied, the bias is neglected and
3. switching is applied and the bias is corrected by the perturbation term.

Test results achieved with the different ESP methods are shown in Chapter 11 on page 105.

2.7. Empirical correction of the excess chemical potential

Dr. Daniel Tomazic and Nicolas Tielker developed and parameterized an empirical correction for EC-RISM based excess chemical potentials based on ideas originally from other works.⁸²⁻⁸⁴ This approach targets the observation, that 3D RISM calculations usually yield too high values for the excess chemical potentials. It is based on a linear correction, that utilizes different solute features. The primary approach being agnostic against pressure changes is

$$\mu_{\text{corr}}^{\text{ex}} = \mu^{\text{ex}} + c_V V_m + c_q q, \quad (2.53)$$

2.7. Empirical correction of the excess chemical potential

where μ^{ex} is the excess chemical potential from 3D RISM, V_m is the partial molar volume calculated from 3D RISM, q is the net charge of the solute. The variables, c_V and c_q are free parameters from a linear fit model.⁸² The number of parameters actually used in the model is dependent on the solvent. The MNSOL database was used as a dataset of experimental values for parameterizing the model.⁸⁵⁻⁸⁷ In later models the parameter c_μ was fixed at a value of 1 for water.⁸⁸ In order to correct pressure-dependent deviations of excess chemical potential, a pressure-dependent version of the partial molar volume (PMV) correction was parameterized by Nicolas Tielker leading to the extended expression⁸⁹

$$\mu_{\text{corr}}^{\text{ex}} = \mu^{\text{ex}} + c_V V_m + c_q q + c_p (p - 0.001 \text{ kbar}) V_m. \quad (2.54)$$

The subtraction of 1 bar from the actual pressure lets the pressure term become zero for ambient conditions. The parameters used here can be seen in Table 2.1.

Table 2.1.: Parameters for the PMV correction.

c_V	-0.10251020096004647	kcal $\text{\AA}^3 \text{ mol}^{-1}$
c_p	-0.010303222025028758	kcal $\text{\AA}^3 (\text{mol kbar})^{-1}$
c_q	-15.728	kcal $(\text{mol } e^{-1})$

Table 2.2.: Isothermal compressibilities used for calculating the partial molar volumes.

p / bar	$\kappa / 10^{-9} \text{Pa}^{-1}$
1	0.71408832874721480
100	0.70704887902181690
500	0.63338790460350860
1000	0.56945234877521090
2000	0.47497141900066110
3000	0.40861242939881230
4000	0.35948713401276210
5000	0.32165984272410670
7500	0.25661835034262714
10000	0.21521762952542384

The partial molar volume utilized here was calculated from the EC-RISM calculations via the total correlation function $h(\mathbf{r})$. The isothermal compressibilities used here are given in Table 2.2. The compressibilities

$$\kappa = \left(k_B T \rho \left(1 - \rho \sum_{\alpha} \sum_{\gamma} \hat{c}_{\alpha\gamma}(k=0) \right) \right)^{-1} \quad (2.55)$$

are calculated by summing up the $k=0$ elements of the reciprocal space direct correlation functions of water.⁹⁰ They were calculated by Tim Pongratz from 1D RISM-vv based correlation functions of pure water.

2.8. Geometry optimizations within EC-RISM

A prerequisite for geometry optimizations within EC-RISM is the presence of a suitable local minimum on the Gibbs energy surface with respect to the molecular geometry. Within the 3D RISM method, the excess chemical potential is built up additively by contributions from every solute site α and can be calculated as well as its gradient for the PSE- k closure.^{5,75,91-93} The excess chemical potential gradient

$$\frac{\partial \mu^{\text{ex}}}{\partial \mathbf{R}_\alpha} = \sum_\gamma \rho_\gamma \int d\mathbf{r} g_\gamma(\mathbf{r}) \frac{\partial u_\gamma(\mathbf{r}, \mathbf{R}_\alpha)}{\partial \mathbf{R}_\alpha} \quad (2.56)$$

with respect to a single interaction site coordinate \mathbf{R}_α can be written as a sum over the contributions of the solvent sites γ . The other component of the total gradient is the gradient of the electronic solute energy

$$\frac{\partial E_{\text{sol}}}{\partial \mathbf{R}_\alpha} \approx \frac{\partial}{\partial \mathbf{R}_\alpha} \langle \psi_{\text{sol}} | \hat{H} | \psi_{\text{sol}} \rangle, \quad (2.57)$$

which neglects the contribution of the change in the Coulomb potential to the total gradient. The gradient

$$\frac{\partial G}{\partial \mathbf{R}_\alpha} = \frac{\partial E_{\text{sol}}}{\partial \mathbf{R}_\alpha} + \frac{\partial E_{\text{ex}}}{\partial \mathbf{R}_\alpha} \quad (2.58)$$

is constructed as a sum over the solvent site γ contributions.

When this gradient is obtained from the final iteration of an EC-RISM calculation, it can be used as an input for a gradient-based optimization algorithm.¹²

3. Theory of vibrational spectroscopy

Absorption and emission of electromagnetic radiation due to vibrational state transitions in electronically non-excited molecules occur in the wave length range of infrared light.⁹⁴ There are two general types of vibrational spectroscopy: The standard IR spectroscopy, which is able to observe vibrations causing changes in the molecular dipole moment, and Raman spectroscopy, where the sample is illuminated with a strong monochromatic visible light source. The Raman effect leads to scattered light with changed wave-numbers $\tilde{\nu}$. Here, next to the excitation line in the scattered light, the Stokes- ($\tilde{\nu}_{\text{Raman}} < \tilde{\nu}_{\text{exc.}}$) and anti-Stokes-lines ($\tilde{\nu}_{\text{Raman}} > \tilde{\nu}_{\text{exc.}}$) can be observed. The symbol $\tilde{\nu}$ denotes the wave number. Raman spectroscopy observes bands resulting from vibrational modes changing the polarizability of the analyte. The shift of the Stokes- and anti-Stokes-lines with respect to the excitation line gives the wavenumber of the vibrational transition.⁹⁴

With the aim of elucidation the origin of pressure-induced vibrational band shifts in TMAO, a basis for calculating IR spectroscopic information with EC-RISM was built. The procedures performed in order to analyze pressure-dependent infrared spectroscopy do not require the full overview given here, a comprehensive introduction to the basic methods of vibrational analysis is given for the sake of completeness.

3.1. Basics

For a detailed analysis of molecular vibration it is necessary to model and simplify the real system in a fashion that vibrational information becomes computable. The following chapter explains the model of Wilson, Decius and Cross.⁹⁴ Their model describes atoms as point masses. The atomic interactions are modelled by a set of potential functions. Atoms may be considered as polarizable and it is defined that molecules may have a permanent molecular dipole moment, but are not required to. The forces applied to atoms are transmitted by mass-less, approximately Hookean springs. This simple model is able to describe single conformations but it already collapses when rotatable bonds in the sense of a multiple-minima dihedral potential are present. In principle it is necessary to treat these simple mechanical models quantum mechanically, since only quantum mechanics (QM) provide the discretization of energy

3. Theory of vibrational spectroscopy

levels. On the other hand the use of classical approximations gives satisfactory results. In this picture the quantum-mechanical character of the atom is neglected.ⁱ

3.1.1. A classical view on vibration

Classical electrodynamics state that acceleration of charges leads to emission of electromagnetic radiation, as can be seen from 4th Maxwell equation

$$\nabla \times \mathbf{B} = \mu_0 \mathbf{j} + \mu_0 \varepsilon_0 \frac{\partial \mathbf{E}}{\partial t}, \quad (3.1)$$

which is also known as the Ampère-Maxwell law. It constitutes the correlation between the magnetic flux density \mathbf{B} , the electric field strength \mathbf{E} and the electric current \mathbf{j} . The equation shows that time dependent changes of the electric current density or the temporal derivative of the electric field strength result in an oscillating magnetic field, consequently leading to electromagnetic waves.

This law explains why rotating molecules with a non-vanishing molecular dipole moment emit electromagnetic radiation with the frequency of the rotation. Thus it is possible to explain why atoms, having a non-zero permanent molecular dipole moment, emit radiation upon rotation and why rotation can be excited by radiation (e.g. in microwave ovens). This effect is used in rotational spectroscopy and superposed with vibrational effects.ⁱⁱ An infrared (IR) spectrum of a diatomic molecule will show vibration, rotation and their coupling. With an increasing number of atoms, these effects will become more complex.

3.1.2. A quantum-mechanical view on vibration

In the picture of quantum mechanics, there are discrete transitions between vibrational states in harmonic and anharmonic oscillators, which is the only way to explain why there are discrete transitions seen in experimental spectra, since classical mechanics allow continuous changes. Furthermore, in the quantum mechanical point of view only emission and absorption of radiation caused by the transition between allowed states are obtained. These allowed transitions can be determined by the so-called selection rules. The selection rules for the harmonic oscillator allow only transitions changing the quantum number by exactly 1.⁹⁴

ⁱThis argumentation is taken from [94], which was written in the 1950s. Back in those days it was not possible to treat molecular systems with quantum chemistry. Nowadays forces and force constants can be obtained from wave function calculations with molecular quantum mechanics for fairly large systems.

ⁱⁱThis may alter the dipole moments during rotation.

3.2. Vibrational spectroscopy in the molecular model

3.2.1. Separation of coordinates

Starting from the expression of the kinetic and potential energies as function of atom coordinates and velocities, the construction of normal coordinates will be demonstrated. Furthermore, the construction of translatory, rotatory and vibrational wave functions will be shown. For each the general approach of Wilson, Decius and Cross⁹⁴ will be applied. Especially the choice of coordinates is crucial. Appropriate coordinates allow the approximate separation of translational, rotational and vibrational movement.

The first step is to determine the coordinates of the center of gravity X , Y and Z . Additionally we define a system of coordinates x , y and z , which can rotate around the center of gravity. The angle of rotation is given by the three Eulerian angles θ , ϕ and χ . Furthermore, there are $3N - 6$ so-called normal coordinates to determine the atomic positions inside the rotating coordinate system.

Let \mathbf{r}_α be the position of the particle α with respect to the center of gravity and the origin of the coordinate system O . This vector consists of the components x_α , y_α and z_α . The position of O is fixed in space and is given by the vector \mathbf{R} . The equilibrium position of the particle α with the mass m_α is given by \mathbf{a}_α . Following from these definitions, the displacement vector is

$$\boldsymbol{\rho} = \mathbf{r}_\alpha - \mathbf{a}_\alpha. \quad (3.2)$$

The angular velocity of the rotating coordinate system $\boldsymbol{\omega}$ is introduced, thus the velocity vector for each particle α , \mathbf{v}_α with the components \dot{x}_α , \dot{y}_α and \dot{z}_α , including the motion of the center of mass, can be calculated by

$$\mathbf{v}_{\mathbf{R},\alpha} = \dot{\mathbf{R}} + \boldsymbol{\omega} \times \mathbf{r}_\alpha + \mathbf{v}_\alpha. \quad (3.3)$$

The kinetic energy then follows from the equation

$$\begin{aligned} 2T = & \dot{\mathbf{R}}^2 \sum_{\alpha} m_{\alpha} + \sum_{\alpha} (\boldsymbol{\omega} \times \mathbf{r}_{\alpha})^2 + \sum_{\alpha} m_{\alpha} v_{\alpha}^2 + 2\dot{\mathbf{R}} \cdot \boldsymbol{\omega} \times \sum_{\alpha} m_{\alpha} \mathbf{r}_{\alpha} \\ & + 2\dot{\mathbf{R}} \cdot \sum_{\alpha} m_{\alpha} \mathbf{v}_{\alpha} + 2\boldsymbol{\omega} \cdot \sum_{\alpha} (m_{\alpha} \mathbf{r}_{\alpha} \times \mathbf{v}_{\alpha}). \end{aligned} \quad (3.4)$$

Since the point O is chosen to be the center of gravity, we obtain

$$\sum_{\alpha} m_{\alpha} \mathbf{r}_{\alpha} = 0 \quad (3.5)$$

and

$$\sum_{\alpha} m_{\alpha} \mathbf{v}_{\alpha} = 0. \quad (3.6)$$

3. Theory of vibrational spectroscopy

Furthermore, the system shall not show an angular momentum with respect to the axes of rotation, which can be achieved approximately by applying the condition

$$\sum_{\alpha} m_{\alpha} \mathbf{a}_{\alpha} \times \mathbf{v}_{\alpha} = 0. \quad (3.7)$$

Inserting this condition and the substitution of \mathbf{r}_{α} by $a_{\alpha} + \boldsymbol{\rho}_{\alpha}$ in the last term of equation (3.4) leads to the expression

$$2T = \dot{R}^2 \sum_{\alpha} m_{\alpha} + \sum_{\alpha} m_{\alpha} (\boldsymbol{\omega} \times \mathbf{r}_{\alpha})^2 + \sum_{\alpha} m_{\alpha} v_{\alpha}^2 + 2\boldsymbol{\omega} \cdot \sum_{\alpha} m_{\alpha} (\boldsymbol{\rho}_{\alpha} \times \mathbf{v}_{\alpha}). \quad (3.8)$$

In the following argumentation we neglect the first term of (3.8) since it is the kinetic energy of translation, which does not appear in the field-free space in terms of vibrational analysis. The second term is the energy of rotation, the third the energy of vibration and the fourth the Coriolis energy resulting from rotation-vibration coupling. Expanding the equation yields

$$\begin{aligned} 2T &= I_{xx}\omega_x^2 + I_{yy}\omega_y^2 + I_{zz}\omega_z^2 - 2I_{xy}\omega_x\omega_y - 2I_{yz}\omega_y\omega_z - 2I_{zx}\omega_z\omega_x \\ &+ \sum_{\alpha} v_{\alpha}^2 + 2\omega_x \sum_{\alpha} (\boldsymbol{\rho}_{\alpha} \times \mathbf{v}_{\alpha})_x + 2\omega_y \sum_{\alpha} (\boldsymbol{\rho}_{\alpha} \times \mathbf{v}_{\alpha})_y \\ &+ 2\omega_z \sum_{\alpha} (\boldsymbol{\rho}_{\alpha} \times \mathbf{v}_{\alpha})_z. \end{aligned} \quad (3.9)$$

Here I_{xx}, I_{yy} and I_{zz} are the moments of inertia with respect to the axes x, y, z of the moving system of coordinates and I_{xy}, I_{yz} and I_{zx} are the corresponding products of inertia as functions of the particle positions. The components ω_x, ω_y and ω_z comprising the angular velocity result in the components of angular momentum

$$j_x = \sum_{\alpha=1}^N m_{\alpha} (y_{\alpha} \dot{z}_{\alpha} - z_{\alpha} \dot{y}_{\alpha}) \quad (3.10)$$

$$j_y = \sum_{\alpha=1}^N m_{\alpha} (z_{\alpha} \dot{x}_{\alpha} - x_{\alpha} \dot{z}_{\alpha}) \quad (3.11)$$

$$j_z = \sum_{\alpha=1}^N m_{\alpha} (x_{\alpha} \dot{y}_{\alpha} - y_{\alpha} \dot{x}_{\alpha}). \quad (3.12)$$

In case of small displacements it is an appropriate approximation to substitute the actual particle positions by the corresponding equilibrium positions $\rho_{\alpha x}, \rho_{\alpha y}, \rho_{\alpha z}$:

$$j_x \approx \sum_{\alpha=1}^N m_{\alpha} (\rho_{\alpha y} \dot{z}_{\alpha} - \rho_{\alpha z} \dot{y}_{\alpha}) \quad (3.13)$$

$$j_y \approx \sum_{\alpha=1}^N m_{\alpha} (\rho_{\alpha z} \dot{x}_{\alpha} - \rho_{\alpha x} \dot{z}_{\alpha}) \quad (3.14)$$

3.2. Vibrational spectroscopy in the molecular model

$$j_z \approx \sum_{\alpha=1}^N m_{\alpha} (\rho_{\alpha x} \dot{y}_{\alpha} - \rho_{\alpha y} \dot{x}_{\alpha}) \quad (3.15)$$

The kinetic energy can be stated as a function of the atom displacements

$$2T = \sum_{\alpha=1}^N m_{\alpha} \left[\left(\frac{d\Delta x_{\alpha}}{dt} \right)^2 + \left(\frac{d\Delta y_{\alpha}}{dt} \right)^2 + \left(\frac{d\Delta z_{\alpha}}{dt} \right)^2 \right]. \quad (3.16)$$

For a shorter notation we now replace the Cartesian coordinates with the mass weighted Cartesian coordinates

$$q_1 = \sqrt{m_1} \Delta x_1, q_2 = \sqrt{m_1} \Delta y_1, \dots, q_4 = \sqrt{m_2} \Delta x_2, \dots \quad (3.17)$$

and write the kinetic energy as

$$2T = \sum_{i=1}^{3N} \dot{q}_i^2. \quad (3.18)$$

The potential energy can be written in form of a power series as a function of q_i

$$\begin{aligned} 2V &= 2V_0 + 2 \sum_{i=1}^{3N} \left(\frac{\partial V}{\partial q_i} \right)_0 q_i + \sum_{i,j=1}^{3N} \left(\frac{\partial^2 V}{\partial q_i \partial q_j} \right) + \dots \\ &= 2V_0 + 2 \sum_{i=1}^{3N} f_i q_i + \sum_{i,j=1}^{3N} f_{ij} q_i q_j + \dots \end{aligned} \quad (3.19)$$

Defining that the arbitrary zero point of the potential energy represents the case where all atoms are in their equilibrium positions, the V_0 term vanishes. Additionally, the first derivative of the potential energy has to be zero in the equilibrium case:

$$\left(\frac{\partial V}{\partial q_i} \right)_0 = f_i = 0. \quad (3.20)$$

In the case of small displacements the power series terms starting with the power of three are negligible, resulting in the approximate potential energy term

$$2V = \sum_{i,j=1}^{3N} f_{ij} q_i q_j \quad (3.21)$$

with

$$f_{ij} = f_{ji} = \left(\frac{\partial^2 V}{\partial q_i \partial q_j} \right). \quad (3.22)$$

Applying the Lagrange formalism the Newtonian equations of motion collapse to

$$\frac{d}{dt} \frac{\partial T}{\partial \dot{q}_j} + \frac{\partial V}{\partial q_j} = 0, \quad (3.23)$$

3. Theory of vibrational spectroscopy

since V is only dependent of the particle positions and T is a function of the velocities only. Inserting the expressions developed above we obtain a system of equations:

$$\ddot{q}_j + \sum_{i=1}^{3N} f_{ij} q_i = 0 \text{ with } j = 1, 2, \dots, 3N, \quad (3.24)$$

with a solution

$$q_i = A_i \cos(\lambda^{\frac{1}{2}} t + \epsilon). \quad (3.25)$$

Here A_{ij} , λ and ϵ are suitable constants. Inserting gives:

$$\sum_{i=1}^{3N} (f_{ij} - \delta_{ij} \lambda) = 0 \text{ with } j = 1, 2, \dots, 3N. \quad (3.26)$$

δ_{ij} is the Kronecker symbol. Non-trivial solutions for λ can be found by solving the secular equation. These solutions are the coefficients for the unknown amplitudes A_i . In case λ is set to a value λ_k , leading to a vanishing secular determinant, the amplitudes A_{ik} can be determined relatively. From the $3N$ solutions for multi-atomic non-linear molecules six are zero, giving the well known $3N - 6$ modes of vibration. It is seen that the vibrational problem in molecules has a set of solutions with the harmonic amplitudes

$$A_{ik} = K_k l_{ik}, \quad (3.27)$$

where

$$l_{ik} = \frac{A'_{ik}}{\sqrt{\sum_i (A'_{ik})^2}} \quad (3.28)$$

which are obtained from an arbitrary solution A'_{ik} and K_k are constants including the the initial coordinates and velocities. The frequencies

$$\nu = \frac{\lambda_k^{\frac{1}{2}}}{2\pi} \quad (3.29)$$

are obtained from the corresponding force constant k in the harmonic oscillator model.

A solution of the secular equation fulfilling all these criteria is called normal mode of vibration, with the corresponding frequency being called eigenfrequency. Eigenfrequencies of different modes are not necessarily different. In case two different modes show the same eigenfrequency, these modes are called degenerate. If there is only a single mode of vibration with a specific frequency, the atoms move on straight lines when this mode is excited. Degenerate modes sometimes superpose with different phases, leading to elliptic motion. Superposition of non-degenerate modes does not lead to a new normal mode and shows complex motions. In order to describe the molecular vibration in terms of normal modes, the so-called normal coordinates will be introduced here. They can be described by the following system of equations

$$Q_k = \sum_{i=1}^{3N} l''_{ki} q_i \quad (3.30)$$

3.3. The vibrational Stark effect

using the mass-weighted displacement coordinates known from Equation (3.17). The coefficients l''_{ki} have to be chosen in such a fashion, that the kinetic energy is

$$2T = \sum_{k=1}^{3N} \dot{Q}_k^2 \quad (3.31)$$

and the potential energy is

$$2V = \sum_{k=1}^{3N} \lambda'_k Q_k^2. \quad (3.32)$$

This way the potential energy becomes free of cross products. The inverse transformation of normal coordinates in mass-weighted Cartesian ones can be achieved by the application of

$$q_i = \sum_{k=1}^{3N} l'_{ik} Q_k \text{ with } i = 1, 2, \dots, 3N. \quad (3.33)$$

Inserting transformation and inverse transformation into each other results in

$$\sum_{i=1}^{3N} l''_{ki} l'_{il} = \delta_{kl} \text{ and } \sum_{j=1}^{3N} l'_{ki} l''_{kj} = \delta_{ij}. \quad (3.34)$$

In normal coordinates the equations of motion of our systems are written as

$$\frac{d}{dt} \frac{\partial T}{\partial \dot{Q}_k} + \frac{\partial V}{\partial Q_k} = \ddot{Q}_k + \lambda'_k Q_k = 0 \text{ with } k = 1, 2, \dots, 3N, \quad (3.35)$$

with the solution

$$Q_k = K'_k \cos \left(\lambda_k'^{\frac{1}{2}} + \epsilon'_k \right), \quad (3.36)$$

where K'_k and ϵ'_k are arbitrary constants. In mass-weighted atomic displacement coordinates the known solution can be written as

$$q_i = \sum_{k=1}^3 N l'_{ik} K'_k \cos \left(\lambda_k'^{\frac{1}{2}} + \epsilon'_k \right). \quad (3.37)$$

Comparison of the equations' structures shows that

$$l'_{ik} = l_{ik} \text{ and } \lambda'_k = \lambda_k. \quad (3.38)$$

Thus the phase and the frequency of vibration become computable.

3.3. The vibrational Stark effect

Generally vibrational Stark effect (VSE) describes the shift of IR spectroscopic bands in electric fields.⁹⁵ The field resulting in Stark shifts can be induced either by external

3. Theory of vibrational spectroscopy

application, like placing the sample inside a plate capacitor during measurement, or by causes within the sample. On the one hand it is possible, that intramolecular interaction leads to locally confined electric fields, on the other hand the polarizing effect of the solvent may have influence on the solute. It was observed that more polar solvents cause stronger Stark shifts towards lower frequencies.⁹⁶ Since the dielectric constant of water increases significantly with pressure, one may expect red-shifts due to the VSE upon pressurization. In order to examine these effects, a closer look at the VSE is necessary.

The change of the vibrational frequency $\Delta\nu$ can be calculated in terms of the difference in the electric field ΔF by

$$hc\Delta\nu = -\Delta\mu\Delta F, \quad (3.39)$$

where h is the Planck constant, c the speed of light in vacuum, and $\Delta\mu$ the difference between the dipole moments of the ground state and the excited state.⁹⁶ As the negative sign on the right hand side indicates, a larger electric field leads to lower frequencies, suggesting that a more polar solvent generally leads to a red shift in vibrational spectra. For simple aromatic nitriles it was shown, that there is a good correlation between the polarity of the solvent and the C-N-stretch frequency.⁹⁶

Assuming that pressurization solely affects the solvent induced polarization, the VSE is not able to explain pressure induced blue shifts, which have been proven to occur for instance in TMAO¹⁴.

3.4. Calculation of vibrational modes in quantum chemistry

This section describes the way the quantum chemistry package Gaussian⁹⁷ treats vibrational problems and is kept close to an essay of Joseph W. Ochterski.⁹⁸

Now that the principle way to calculate frequencies is known, we have to take a closer look on how modern quantum chemistry (QC) programs deal with vibrational problems. The QC program used throughout this thesis is Gaussian⁹⁷ in different versions. Frequency analysis from QC usually starts with the Cartesian Hessian matrix \mathbf{F}_{CART} , which is comprised of the elements

$$F_{\text{CART},i,j} = \frac{\partial^2 V}{\partial x_i \partial x_j} \quad (3.40)$$

holding the 2nd order derivative of the potential energy, presuming the molecule is in an equilibrium geometry. The $3N$ Cartesian displacement coordinates again are denoted by x . The elements of this matrix can be understood as Cartesian displacement force

3.4. Calculation of vibrational modes in quantum chemistry

constants. In order to reduce computational cost, we will now switch to mass-weighted Cartesian coordinates MCART, resulting in the matrix elements

$$F_{\text{MCART},i,j} = \frac{F_{\text{CART},i,j}}{\sqrt{m_i m_j}} \quad (3.41)$$

with m_i being the particle mass belonging to the mass-weighted Cartesian displacement coordinate $q_i = \sqrt{m_i} x_i$. The eigenvalues of this matrix are the fundamental frequencies. Before actually treating the vibration problem, translation and rotation are separated. The molecule is shifted into the center of gravity similar to the way discussed in Section 3.2.1. In the same Section the calculation of moments and products of inertia I_{ij} is discussed, here we construct moment of inertia tensor

$$\mathbf{I} = \begin{pmatrix} I_{xx} & I_{xy} & I_{xz} \\ I_{yx} & I_{yy} & I_{yz} \\ I_{zx} & I_{zy} & I_{zz} \end{pmatrix}. \quad (3.42)$$

Diagonalization of this tensor yields the normalized eigenvectors comprising the matrix \mathbf{X} which is used to separate rotation and translation. The principal moments \mathbf{I} are obtained as the eigenvalues of \mathbf{I} . The next step on the route to normal coordinates is to obtain the coordinates in the rotating and the translating coordinate systems. The translation is described by the three vectors \mathbf{D}_1 , \mathbf{D}_2 and \mathbf{D}_3 , which contain the square root $\sqrt{m_i}$ of the atom masses multiplied with the unit vector on the corresponding axis. For a diatomic molecule these vectors are

$$\mathbf{D}_1 = \begin{pmatrix} \sqrt{m_1} \\ 0 \\ 0 \\ \sqrt{m_2} \\ 0 \\ 0 \end{pmatrix}, \quad (3.43)$$

$$\mathbf{D}_2 = \begin{pmatrix} 0 \\ \sqrt{m_1} \\ 0 \\ 0 \\ \sqrt{m_2} \\ 0 \end{pmatrix} \quad (3.44)$$

and

$$\mathbf{D}_3 = \begin{pmatrix} 0 \\ 0 \\ \sqrt{m_1} \\ 0 \\ 0 \\ \sqrt{m_2} \end{pmatrix}. \quad (3.45)$$

3. Theory of vibrational spectroscopy

When it comes to obtaining the rotational coordinates, we define the vector components

$$D_{4ji} = \frac{((P_y)_i X_{j3} - (P_z)_i X_{j2})}{\sqrt{m_i}}, \quad (3.46)$$

$$D_{5ji} = \frac{((P_z)_i X_{j1} - (P_x)_i X_{j3})}{\sqrt{m_i}} \quad (3.47)$$

and

$$D_{6ji} = \frac{((P_x)_i X_{j2} - (P_y)_i X_{j1})}{\sqrt{m_i}}. \quad (3.48)$$

Here the index $j = x, y, z$ runs over the principal axes, i denotes the atoms and P is the dot product of the atoms' coordinate with respect to the center of mass and the corresponding row-vector of \mathbf{X} . The vectors are squaredⁱⁱⁱ. If the resulting value is close to zero, the vector does not describe an actual normal mode^{iv} and the vector is canceled before continuing the vibrational analysis. Non-canceled vectors are normalized by dividing them by the square root of the square calculated before. In this place it is preferable to compare the number of obtained normal modes with the number expected for the molecular geometry as a sanity check. In order to obtain the vibrational vectors, which are orthogonal to the rotational and vibrational vectors the Schmidt-Gram algorithm is applied.⁹⁹ This approach yields a transformation matrix \mathbf{D} , which converts the mass-weighted internal coordinates \mathbf{q} into the internal coordinates

$$\mathbf{S} = \mathbf{D}\mathbf{q}. \quad (3.49)$$

These internal coordinates are independent of rotational and translational movement. In order to analyze vibration in internal coordinates, additionally the force constants, given as the Cartesian Hessian \mathbf{f}_{MWC} , need to be converted into the internal Hessian

$$\mathbf{f}_{\text{INT}} = \mathbf{D}^\dagger \mathbf{f}_{\text{MWC}} \mathbf{D}. \quad (3.50)$$

From the internal Hessian, the matrix containing the vibrational force constants is separated and diagonalized, yielding an eigenvalue $\lambda = 4\pi^2\nu^2$ for every vibrational mode, and as many eigenvectors. The matrix \mathbf{L} is comprised of these eigenvectors, thus we state

$$\mathbf{L}^\dagger \mathbf{f}_{\text{INT}} \mathbf{L} = \mathbf{\Lambda} \quad (3.51)$$

with the diagonal matrix of the eigenvalues $\mathbf{\Lambda}$. The wave number

$$\tilde{\nu} = \sqrt{\frac{\lambda_i}{4\pi^2 c^2}} \quad (3.52)$$

of the mode i is now straightforwardly obtained. The remaining information, the reduced mass for every mode, the force constants and the Cartesian displacement

ⁱⁱⁱThis term means, that the dot product of the vector with itself is calculated.

^{iv}Which means, that the molecule is linear or even a single atom.

3.4. Calculation of vibrational modes in quantum chemistry

vectors are calculated separately as illustrated in the following description. In order to obtain the Cartesian normal modes we use the relation

$$\mathbf{L}^\dagger \mathbf{D}^\dagger \mathbf{f}_{\text{MWC}} \mathbf{D} \mathbf{L} = \mathbf{A} = \mathbf{I}_{\text{MWC}}^\dagger \mathbf{f} \mathbf{I}_{\text{MWC}} \quad (3.53)$$

with $\mathbf{I}_{\text{MWC}} = \mathbf{D} \mathbf{L}$. Instead of the mass-weighted matrix \mathbf{I}_{MWC} the analogon in Cartesian coordinates

$$\mathbf{l}_{\text{CART}} = \mathbf{M} \mathbf{D} \mathbf{L} \quad (3.54)$$

can be used, where the matrix \mathbf{M} is a diagonal matrix holding the square root of the reciprocal mass for every Cartesian atom coordinate i , thus having the elements

$$M_{ii} = \frac{1}{\sqrt{m_i}}. \quad (3.55)$$

The elements of \mathbf{l}_{CART} are obtained directly by

$$l_{\text{CART},ki} = \sum_j^3 N \left(\frac{D_{kj} L_{ji}}{\sqrt{m_k}} \right). \quad (3.56)$$

The column vectors of the resulting matrix are the Cartesian normal modes, which still need normalization by multiplication with

$$\mathcal{N}_i = \sqrt{\left(\sum_k^{3N} l_{\text{CART},ki}^2 \right)^{-1}}. \quad (3.57)$$

In order to calculate the normal modes we take the usual definition of the reduced mass for diatomic molecules

$$\frac{1}{\mu} = \frac{1}{m_1} + \frac{1}{m_2} \quad (3.58)$$

into account. For polyatomic molecules this relation collapses, since the unit displacement of every atom has to be considered. Therefore, we obtain the reduced mass

$$\mu_i = \left(\sum_k^{3N} \frac{l_{\text{MWC},ki}^2}{m_k} \right)^{-1} = \left(\sum_k^{3N} \left(\frac{l_{\text{MWC},ki}}{\sqrt{m_k}} \right)^2 \right)^{-1} = \left(\sum_k^{3N} l_{\text{CART},ki}^2 \right)^{-1} = \mathcal{N}^2 \quad (3.59)$$

for every mode i .

This concludes the description of the vibrational analysis by Gaussian as used in this thesis.⁹⁸ The next section will introduce the extension by EC-RISM in order to introduce pressure information into the vibrational analysis.

3.5. Calculation of vibrational frequency shifts with EC-RISM

In order to elucidate the origin of pressure-dependent changes to vibrational spectra obtained experimentally, a method to calculate spectra including pressure is needed. In this section, a first attempt to apply EC-RISM to such problems is applied. Before coming to a detailed description of the workflow applied, a short verbal summary of the method and its limitations is given. Since the second order derivative of the excess chemical potential $\frac{\partial^2 \mu^{\text{ex}}}{\partial x_i \partial x_j}$ is not analytically known, there is no possibility to calculate the total Hessian directly from EC-RISM results. Therefore, the approach demonstrated here bases on

1. calculating the normal modes of vibration utilizing PCM solvation,
2. displacing the atoms along the normal mode vectors starting from the equilibrium position,
3. performing EC-RISM calculations on every obtained structure at 1 bar and the pressure in question and finally
4. determining the relative change of force constant either by numerical derivatives or by fitting a parabola, which is derived analytically.

A severe limitation of this simple approach is, that EC-RISM covers the thermodynamic equilibrium, which is not achieved on the timescale of molecular vibration, so the effects of solvent relaxation are expected to be overestimated.

The well known Cartesian force constant matrix (see eq. (3.40)), also known as Hessian, is extracted from the Gaussian PCM calculation output. In order to get the correct mass-weighting the diagonal mass-matrix,

$$\mathbf{M} = \begin{pmatrix} m_1 & 0 & \cdots & 0 \\ 0 & m_2 & \ddots & \vdots \\ \vdots & \ddots & \ddots & 0 \\ 0 & \cdots & 0 & m_N \end{pmatrix} \quad (3.60)$$

holding the masses for every coordinate is constructed and the square root is applied to every element leading to the matrix

$$\mathbf{M}^{\frac{1}{2}} = \begin{pmatrix} \sqrt{m_1} & 0 & \cdots & 0 \\ 0 & \sqrt{m_2} & \ddots & \vdots \\ \vdots & \ddots & \ddots & 0 \\ 0 & \cdots & 0 & \sqrt{m_N} \end{pmatrix}. \quad (3.61)$$

3.5. Calculation of vibrational frequency shifts with EC-RISM

The mass-weighted Hessian

$$F_{\text{MCART}} = \mathbf{M}^{\frac{1}{2}} \mathbf{F}_{\text{CART}} \mathbf{M}^{\frac{1}{2}} \quad (3.62)$$

is calculated and its eigenvalues and eigenvectors are determined. The eigenvectors represent the mass-weighted Cartesian displacements for every normal mode. In order to retain the actual displacement of every atom, the matrix comprised of the eigenvectors \mathbf{Q} is multiplied with the inverse of $\mathbf{M}^{\frac{1}{2}}$ to obtain the Cartesian displacement matrix

$$\mathbf{X} = \mathbf{Q} \cdot \left(\mathbf{M}^{\frac{1}{2}} \right)^{-1}. \quad (3.63)$$

Every displacement vector is normalized to obtain the vectors for unit displacement. The resulting Cartesian unit displacements obtained are scaled by the amplitudes $-A_{\text{max}}$, $-A_{\frac{1}{2}}$, $-A_{\frac{1}{2}}$, A_{max} and added to the respective equilibrium geometry.

This method leads to the four displaced geometries per normal mode, which are necessary to calculate second order derivatives. For every displaced geometry and the equilibrium structure an EC-RISM calculation is performed. The resulting energies (Gibbs energy in solution, chemical excess potential of solvation, and electronic energy in solution) can now be derived numerically with the five point stencil method, or by fitting a parabola and deriving the second order polynomial in order to obtain pressure dependent force constants in the EC-RISM picture. The second order five-point-stencil derivative is given by the equation

$$k_i(E) = \frac{-E(\mathbf{x} - 2d\mathbf{q}_i) + 16E(\mathbf{x} - d\mathbf{q}_i) - 30E(\mathbf{x}) + 16E(\mathbf{x} + d\mathbf{q}_i) - E(\mathbf{x} + 2d\mathbf{q}_i)}{12d^2}, \quad (3.64)$$

where $k_i(E)$ is the force constant of the normal mode i determined from a measure of energy E , which is one of G_{sol} , E_{sol} or μ^{ex} , d is the displacement step chosen, and \mathbf{q}_i is the set of Cartesian displacement vectors for the mode i while \mathbf{x} is the equilibrium geometry.

Instead of calculating the finite approximation of the second order derivative, it is possible to fit a second order polynomial to the datapoints obtained from EC-RISM calculations, which then can be derived analytically. Both methods have been tested for TMAO. The results are shown in section 9.3. Detailed plots of the raw data and the fitted polynomials can be found in Appendix (see Section A.1.2 on page 147).

Once having obtained the force constants from EC-RISM calculations, they are used in order to scale the polarizable continuum model (PCM)-based frequency in order to obtain pressure dependent frequencies. The well-known expression for the eigenfrequency of a harmonic oscillator is

$$\nu(k, \mu) = \frac{\sqrt{\frac{k}{\mu}}}{2\pi}. \quad (3.65)$$

3. Theory of vibrational spectroscopy

Thus, the frequency ratio due to the pressure dependent change in frequency with respect to 1 bar becomes

$$f(p) = \sqrt{\frac{k(p)}{k(1 \text{ bar})}} = \frac{\nu(p)}{\nu(1 \text{ bar})}. \quad (3.66)$$

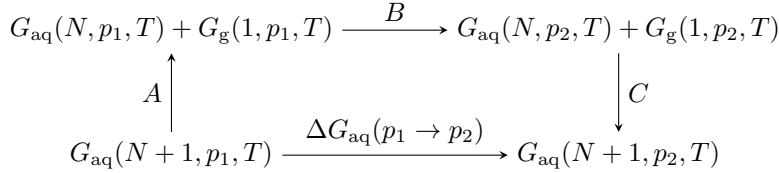
Using the force constants from EC-RISM calculations within this equation, a scaling factor is obtained, that can be used, in order to scale the PCM based 1 bar frequencies or wave numbers:

$$\nu(p) = f(p)\nu^{\text{PCM}}. \quad (3.67)$$

4. Theoretical description of thermodynamics for the water autoprotolysis equilibrium

Calculating the pressure induced shift of a chemical equilibrium basically means to calculate the change of the reaction Gibbs energy as a function of pressure. In order to do so it is necessary to know, how to sort out the pressure-dependence of the Gibbs energy of a single solute species. Since in the autoprotolysis reaction the solvent is one of the reactants, we have to account for the change of its Gibbs energy as a function of pressure as well.

The change in Gibbs energy of a solute in solution $\Delta G(p_1 \rightarrow p_2)$ for the transition between two different pressures p_1 and p_2 can be described by the following thermodynamic cycle. While the direct reaction path in solution is depicted in the bottom of the scheme, the path via A , B and C means the way to bring one particle from the solution into gas phase, change the pressure and bring this particle back to solution. This way it becomes clear, why ideal gas contributions are important when changing the standard conditions in liquid phase.



The legs denoted A , B and C are given by

$$\begin{aligned}
 A = & + [N\mu_{\text{aq}}^{\text{v}}(p_1, T) + \mu_{\text{g}}^{\text{u, id}}(p_1, T) + E_{\text{g}}^{\text{u}}(T) - TS_{\text{g}}(T)] \\
 & - [N\mu_{\text{sol}}^{\text{v}}(p_1, T) + \mu_{\text{sol}}^{\text{u}}(p_1, T) + E_{\text{sol}}^{\text{u}}(p_1, T) - TS_{\text{sol}}^{\text{u}}(p_1, T)], \quad (4.1)
 \end{aligned}$$

$$B = N\mu_{\text{aq}}^{\text{v}}(p_2, T) - N\mu_{\text{aq}}^{\text{v}}(p_1, T) + \mu_{\text{g}}^{\text{u, id}}(p_2, T) - \mu_{\text{g}}^{\text{u, id}}(p_1, T) \quad (4.2)$$

and

$$\begin{aligned}
 C = & - [N\mu_{\text{aq}}^{\text{v}}(p_2, T) + \mu_{\text{g}}^{\text{u, id}}(p_2, T) + E_{\text{g}}^{\text{u}}(T) - TS_{\text{g}}(T)] \\
 & + [N\mu_{\text{sol}}^{\text{v}}(p_2, T) + \mu_{\text{sol}}^{\text{u}}(p_2, T) + E_{\text{sol}}^{\text{u}}(p_2, T) - TS_{\text{sol}}^{\text{u}}(p_2, T)]. \quad (4.3)
 \end{aligned}$$

4. Theoretical description of thermodynamics for the water autoprotolysis equilibrium

The annotation u means the observable of the solute, v marks solvent-related quantities, the index aq means a quantity in solution, while g denotes the gas phase. Considering, that every chemical potential μ is the sum of an ideal part μ^{id} and an excess part μ^{ex} , A , B and C can be summed up to

$$\Delta G_{\text{aq}}(p_1 \rightarrow p_2) \stackrel{N \rightarrow \infty}{=} E_{\text{sol}}^{\text{u}}(p_2, T) - E_{\text{sol}}^{\text{u}}(p_1, T) - T(S_{\text{sol}}^{\text{u}}(p_2, T) - S_{\text{sol}}^{\text{u}}(p_1, T)) + \mu_{\text{sol}}^{\text{u,ex}}(p_2, T) - \mu_{\text{sol}}^{\text{u,ex}}(p_1, T) + \mu_{\text{sol}}^{\text{u,id}}(p_2, T) - \mu_{\text{sol}}^{\text{u,id}}(p_1, T), \quad (4.4)$$

assuming the thermodynamic limit of an infinite number of particles. The missing difference in ideal chemical potentials can be written as the integral over the ideal part of the solute's partial molar volume.

The total partial molar volume

$$V^{\text{u}} = V^{\text{u,id}} + V^{\text{u,ex}} = \kappa RT + \int (1 - g(r)) dr = \kappa RT(1 - \rho C^{\text{uv}}) \quad (4.5)$$

is comprised of an ideal part and an excess contribution.^{100,101} Since the 3D RISM approach recognizes the excess part only, it is necessary, to introduce the ideal part

$$V^{\text{u,id}}(p) = \kappa(p)RT \quad (4.6)$$

separately, gaining the difference in ideal chemical potentials

$$\mu_{\text{sol}}^{\text{u,id}}(p_2, T) - \mu_{\text{sol}}^{\text{u,id}}(p_1, T) = \int_{p_1}^{p_2} \bar{V}(p, T)^{\text{u,id}} dp. \quad (4.7)$$

Following equation 4.5 this can be achieved by integrating the isothermal compressibilities of the solvent.

$$\int_{p_1}^{p_2} \bar{V}^{\text{u,id}}(p, T) dp = RT \int_{p_1}^{p_2} \kappa^{\text{v}} dp. \quad (4.8)$$

Neglecting the entropic contribution, assuming constant temperature and collecting the observables calculable with EC-RISM in the EC-RISM based Gibbs energy

$$G_{\text{sol}}^{\text{u}}(p) = E_{\text{sol}}^{\text{u}}(p) + \mu_{\text{sol}}^{\text{u,ex}}(p) \quad (4.9)$$

allows for the compact notation

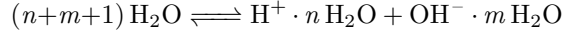
$$\Delta G_{\text{aq}}(p_1 \rightarrow p_2) = G_{\text{sol}}^{\text{u}}(p_2) - G_{\text{sol}}^{\text{u}}(p_1) + RT \int_{p_1}^{p_2} \kappa^{\text{v}} dp. \quad (4.10)$$

The isothermal compressibility function used in this case is

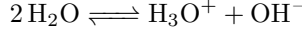
$$\kappa(p) = \frac{d\rho(p)}{dp} \rho^{-1}(p), \quad (4.11)$$

where the density $\rho(p)$ is represented by the equation of state by Floriano *et al.* (compare Equation (5.2)).¹⁰²

In order to cover the most general case the reaction



it would be necessary to model larger ion-water clusters and probably it would become necessary to construct partition functions considering multiple different solvation patterns for the proton and hydroxide. As a proof of concept here the simpler reaction



was assumed to be sufficient. Thus, the Gibbs energy of reaction can be written as

$$\Delta_{\text{R}}G = G(\text{H}_3\text{O}^+) + G(\text{OH}^-) - 2G(\text{H}_2\text{O}). \quad (4.12)$$

In order to model the autoprotolysis of water correctly, there have been approaches applying water clusters and water-ion clusters with or without the use of continuum electrostatics based solvation models.^{103,104} Defining the pure water phase as a reference state and using the experimental atmospheric pressure $\text{p}K_{\text{W}}$ -value as an offset allows for calculating the pressure-dependent $\text{p}K_{\text{W}}$ -value without quantum chemical calculations of water. This is equivalent to the use of experimentally based chemical potentials. The change of the Gibbs energy of water in this case can be fully captured by integrating its partial molar volume obtaining the change in the chemical potential

$$\Delta\mu^{\text{H}_2\text{O}}(p_1 \rightarrow p_2) = \int_{p_1}^{p_2} \bar{V}(p) dp. \quad (4.13)$$

Bringing together all the terms above, for the total reaction we obtain a pressure shift of the reaction Gibbs energy of water autoprotolysis

$$\begin{aligned} \Delta\Delta_{\text{R}}G(p_1 \rightarrow p_2) &= \left(G_{\text{sol}}^{\text{H}_3\text{O}^+}(p_2) - G_{\text{sol}}^{\text{H}_3\text{O}^+}(p_1) \right) + \left(G_{\text{sol}}^{\text{OH}^-}(p_2) - G_{\text{sol}}^{\text{OH}^-}(p_1) \right) \\ &+ 2 \int_{p_1}^{p_2} RT \kappa^{\text{H}_2\text{O}} dp - 2 \int_{p_1}^{p_2} V_m^{\text{H}_2\text{O}} dp. \end{aligned} \quad (4.14)$$

The $\text{p}K_{\text{W}}$ -value can be calculated from Gibbs reaction energies by

$$\text{p}K_{\text{W}} = \frac{\Delta_{\text{R}}G}{RT \ln 10}. \quad (4.15)$$

Therefore

$$\Delta\text{p}K_{\text{W}}(p_1 \rightarrow p_2) = \frac{\Delta\Delta_{\text{R}}G(p_1 \rightarrow p_2)}{RT \ln 10} \quad (4.16)$$

is the pressure-dependent change of the negative decadic logarithm of the autoprotolysis constant. The value for each pressure is obtained by adding the experimental value at 1 bar to the difference mentioned above

$$\text{p}K_{\text{W}}(p) = \text{p}K_{\text{W}}^{\text{exp}}(1 \text{ bar}) + \Delta_p \text{p}K_{\text{W}}. \quad (4.17)$$

Part III.
Methods

5. Introducing high pressure in 3D RISM

All pressure-dependent solvent information can be introduced into the 3D RISM integral equation (see eq. (2.27) on page 22) by adjusting the bulk densities $\rho_{\gamma,\infty}$ and the solvent susceptibility χ . The pressure-dependent density can easily be obtained from empirical equations of state.¹⁰² The solvent susceptibility can be calculated in different ways, usually involving 1D RISM calculations.

Dielectrically consistent 1D RISM calculations applying the HNC-approximation can straightforwardly be used to obtain the site-site pair distribution functions, which can be transformed into solvent susceptibilities. The change of the solvent's dielectric constant upon pressurization was shown to be crucial for examining high pressure solvation phenomena in the 1940s. Owen and Brinkley published an empirical equation of state for the dielectric constants of different solvents at high pressure in 1943.¹⁰⁵ In the following decades, this class of equation was continuously refined. Floriano and Nascimento finally published equations of state for the density and the dielectric constant of water.¹⁰² Both quantities are calculated applying these equations in this thesis. The dielectric constant is given by

$$\varepsilon_r(p) = \varepsilon_r(298 \text{ K}, 10 \text{ MPa}) + a_0 \ln \left(\frac{a_1 + p}{a_1 + 10 \text{ MPa}} \right), \quad (5.1)$$

where p is the pressure in MPa, $\varepsilon_r(298 \text{ K}, 10 \text{ MPa})$ the dielectric constant at 10 MPa and 298 K, a_0 is a unit-less parameter and a_1 a parameter in MPa. At $T = 298 \text{ K}$ the parameters $\varepsilon_r(298 \text{ K}, 10 \text{ MPa}) = 78.85$, $a_0 = 141113$ and $a_1 = 341.5902 \text{ MPa}$ were determined.¹⁰² The matching equation of state representing the density of water is

$$\rho(p) = \rho(298 \text{ K}, 0.1 \text{ MPa}) + a_0 \ln \left(\frac{a_1 + p}{a_1 + 0.1 \text{ MPa}} \right) \text{ g cm}^{-3} \quad (5.2)$$

with $\rho(298 \text{ K}, 0.1 \text{ MPa}) = 0.997 \text{ g cm}^{-3}$, $a_0 = 0.214 \text{ g cm}^{-3}$ and $a_1 = 476.693 \text{ MPa}$.¹⁰²

In order to perform these calculations, the pressure-dependent dielectric constants have to be known and can be obtained from empirical equations of state as well.¹⁰² Both, densities and dielectric constants from the equation of state for the pressures used in this work are shown in Table 5.1.

Instead of neglecting the bridge function $B(r)$ in the HNC approximation, it is possible to extract $B(r)$ from pair distribution functions g^{MD} of the pure solvent, determined

5. Introducing high pressure in 3D RISM

by classical force field molecular dynamics (ffMD) simulations at the corresponding pressure.⁷ The resulting bridge function

$$B(r) = sw(r) (\ln(g^{\text{MD}}(r)) + \beta u(r) - h(r) + c(r)) \quad (5.3)$$

is scaled by a cubic switching function $sw(r)$. The original pair distribution function from the simulation is transferred to the logarithmic 1D RISM grid and smoothed by a cubic spline.¹⁰⁶ The resulting function is applied as a constraint to the 1D RISM solver. A comparison between the original function and the spline in the area of the first solvation shell is shown in Figures 5.2 to 5.6. In order to extrapolate distances, which are larger than the range of the simulation based radial distribution functions, the HNC approximation is applied.

Table 5.1.: Pressure-dependent densities ρ and dielectric constants ϵ of water, which were used to generate high pressure solvent susceptibilities. The values were calculated with the equations of state taken from Floriano *et al.*¹⁰²

p/bar	ϵ	$\rho/\text{\AA}^{-3}$
1	78.4	0.03333
100	78.9	0.03348
500	80.4	0.03404
1000	82.1	0.03460
2000	84.9	0.03583
3000	87.3	0.03682
4000	89.4	0.03769
5000	91.2	0.03846
7500	94.8	0.04009
10000	97.7	0.04142

In order to introduce bridge function contributions into the solvent susceptibilities, radial distribution functions were extracted from a molecular dynamics (MD) simulation of 17440 SPC/E¹⁰⁷ water molecules, covering 20 ns of simulated time in 195 samples with a bin width of 0.02 \AA . The simulation and radial distribution functions extraction was performed by Dr. Christoph Hölzl. The distribution functions are shown in Figure 5.1. Especially in the oxygen-oxygen distribution function it can be seen that with rising pressure the second solvation shell peak is virtually pushed into the first solvation shell.

The pressures used in this work are 1 bar, 100 bar, 500 bar, 1 kbar, 2 kbar, 3 kbar, 4 kbar, 5 kbar, 7.5 kbar and 10 kbar. The 1D RISM calculations with the modified SPC/E water^{5,107,108} for the solvent susceptibilities used throughout this work were performed on a one-dimensional logarithmic grid consisting of 512 points ranging from $5.98 \cdot 10^{-3} \text{\AA}$ to 164.02 \AA . The geometry of the water model and the Lennard-Jones-parameters used are shown in Table 5.2. The temperature was set to 298.15 K. In case of HNC approximated susceptibilities convergence was assumed, when the maximum

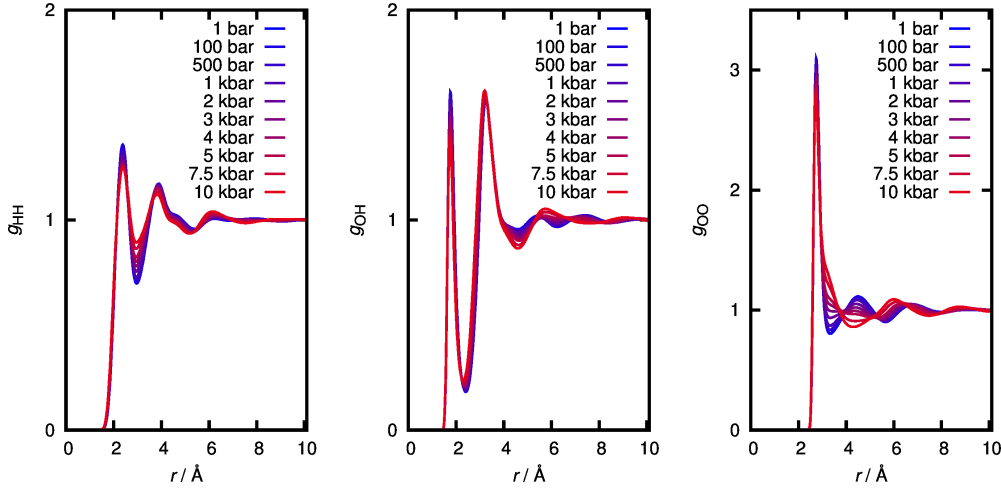


Figure 5.1.: Radial distribution functions of the water sites in dependence of the pressure as obtained from the MD simulations. The hydrogen-hydrogen (HH) RDF are shown left, the oxygen-hydrogen (OH) RDF are shown in the center, and the oxygen-oxygen (OO) RDF are shown in the right panel.

Table 5.2.: Geometry and non-bonded parameters of the modified SPC/E water model.^{5,107,108}

Atom	$x/\text{\AA}$	$y/\text{\AA}$	$z/\text{\AA}$	q/e	$\sigma/\text{\AA}$	ϵ/zJ
O	0.000	0.000	0.000	-0.8476	3.1660	1.0797
H	-0.815	0.000	0.579	0.4238	1.0000	0.3891
H	0.815	0.000	0.579	0.4238	1.0000	0.3891

norm of the difference of the direct correlation function of two successive iterations fell below 10^{-7} . For the MD derived bridge function based susceptibilities the original radial distribution functions obtained from MD simulations with a bin width of 0.02 \AA , were smoothed by a cubic spline. The smoothing factor was built up in order to reflect the number of bins and the statistical uncertainty resulting from 195 samples of 20 ns of simulated time in a system comprised of 17440 water molecules. The achievable convergence criterion was 0.00025 with respect to the direct correlation function's difference maximum norm.¹²

5. Introducing high pressure in 3D RISM

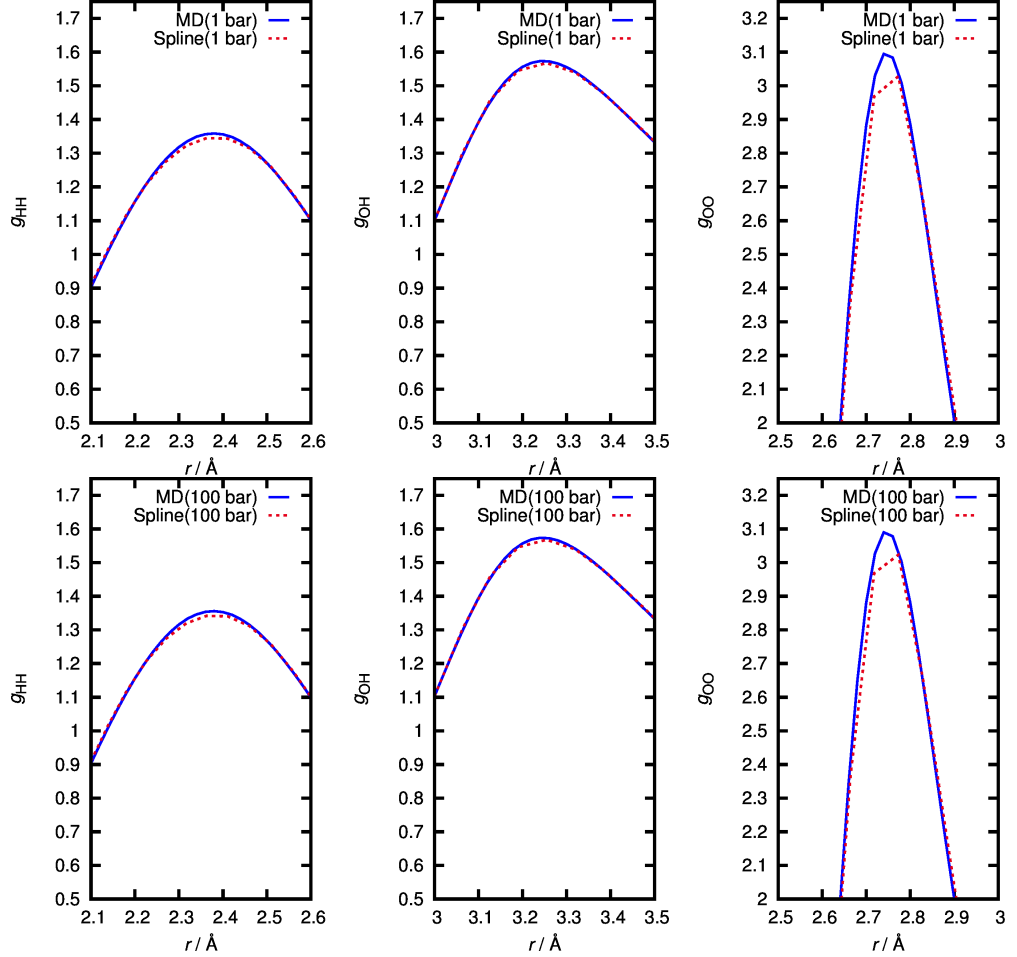


Figure 5.2.: Radial distribution functions of the water sites in dependence of the pressure as obtained from the MD simulations. The hydrogen-hydrogen (HH) RDF are shown left, the oxygen-hydrogen (OH) RDF are shown in the center, and the oxygen-oxygen (OO) RDF are shown in the right panel. The range around the first maximum is compared with the corresponding function smoothed by the cubic spline. Distribution functions for 1 bar (top) and 100 bar (bottom) are shown.

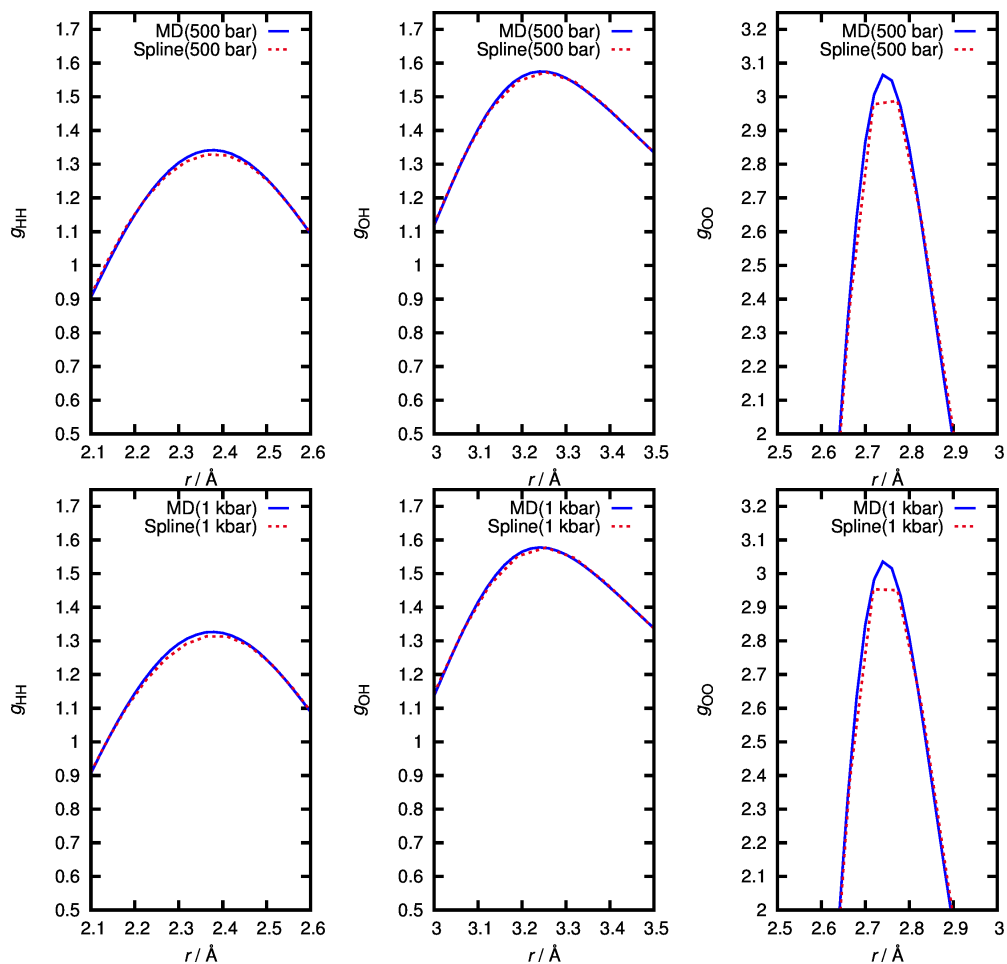


Figure 5.3.: Radial distribution functions of the water sites in dependence of the pressure as obtained from the MD simulations. The hydrogen-hydrogen (HH) RDF are shown left, the oxygen-hydrogen (OH) RDF are shown in the center, and the oxygen-oxygen (OO) RDF are shown in the right panel. The range around the first maximum is compared with the corresponding function smoothed by the cubic spline. Distribution functions for 500 bar (top) and 1 kbar (bottom) are shown.

5. Introducing high pressure in 3D RISM

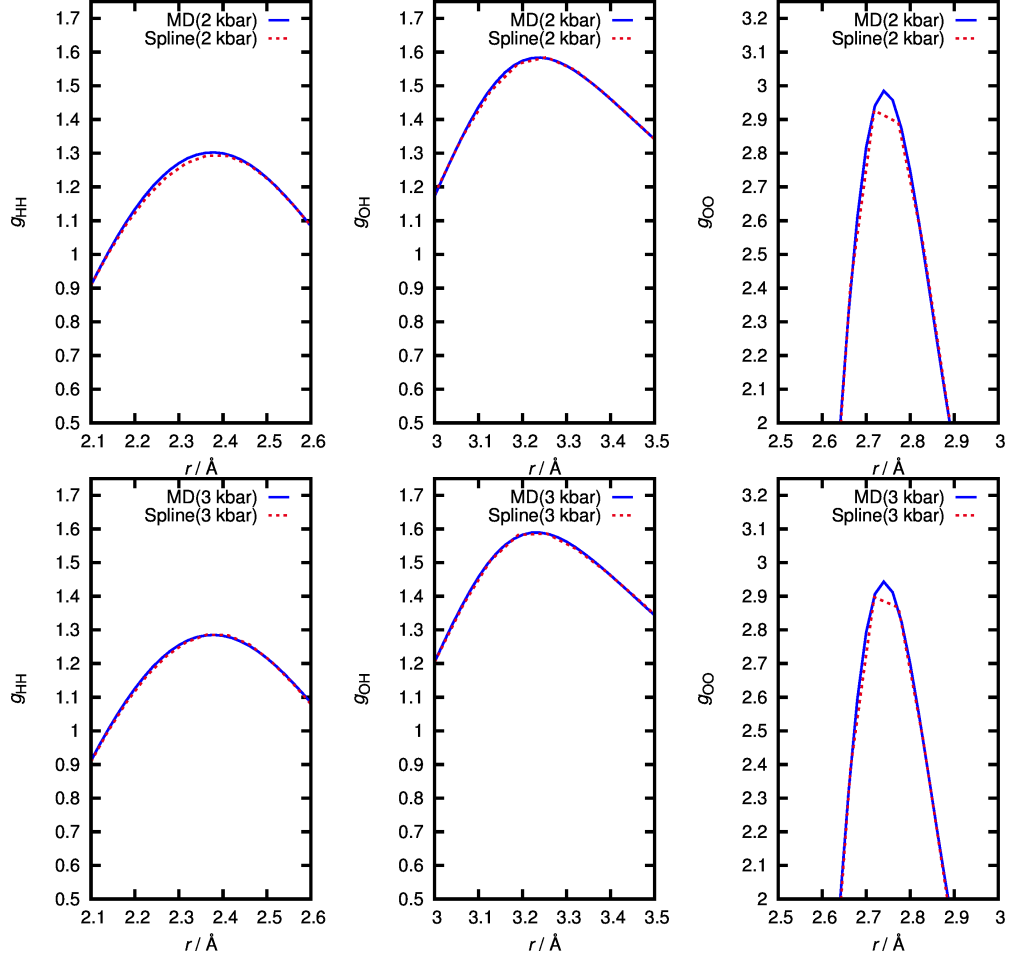


Figure 5.4.: Radial distribution functions of the water sites in dependence of the pressure as obtained from the MD simulations. The hydrogen-hydrogen (HH) RDF are shown left, the oxygen-hydrogen (OH) RDF are shown in the center, and the oxygen-oxygen (OO) RDF are shown in the right panel. The range around the first maximum is compared with the corresponding function smoothed by the cubic spline. Distribution functions for 2 kbar (top) and 3 kbar (bottom) are shown.

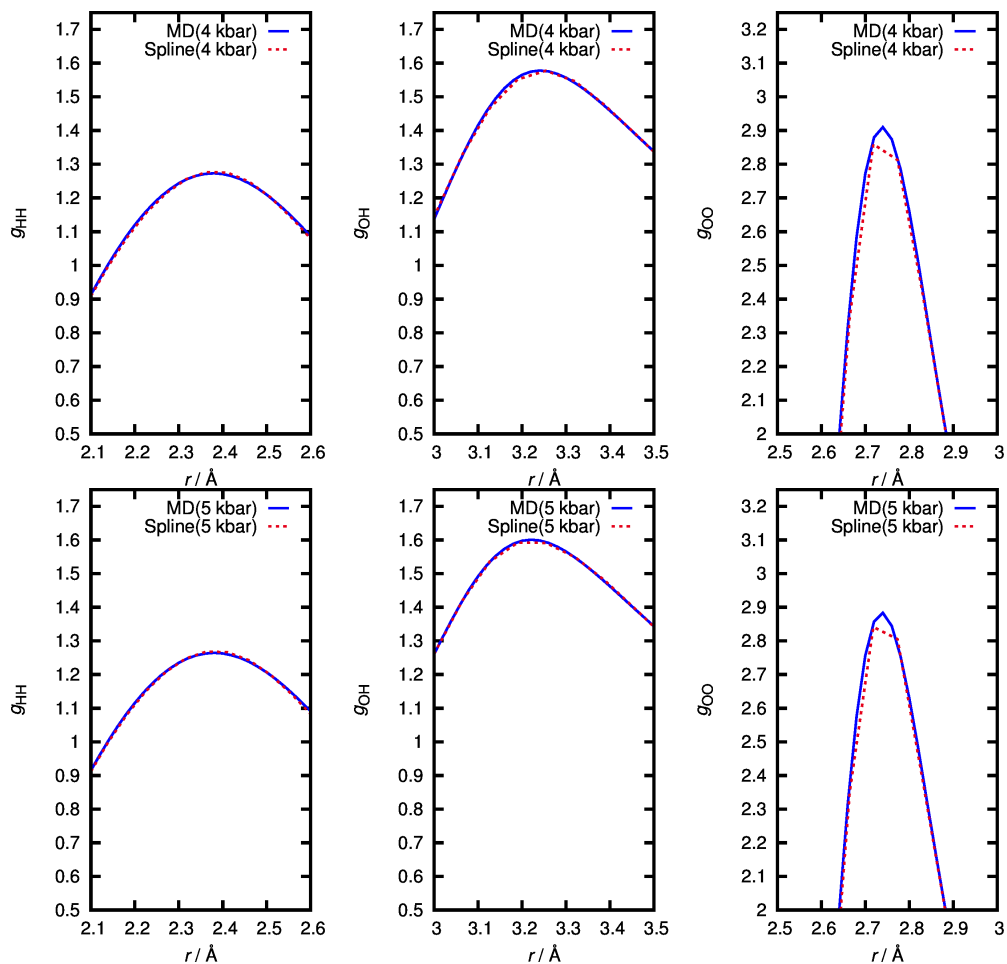


Figure 5.5.: Radial distribution functions of the water sites in dependence of the pressure as obtained from the MD simulations. The hydrogen-hydrogen (HH) RDF are shown left, the oxygen-hydrogen (OH) RDF are shown in the center, and the oxygen-oxygen (OO) RDF are shown in the right panel. The range around the first maximum is compared with the corresponding function smoothed by the cubic spline. Distribution functions for 4 kbar (top) and 5 kbar (bottom) are shown.

5. Introducing high pressure in 3D RISM

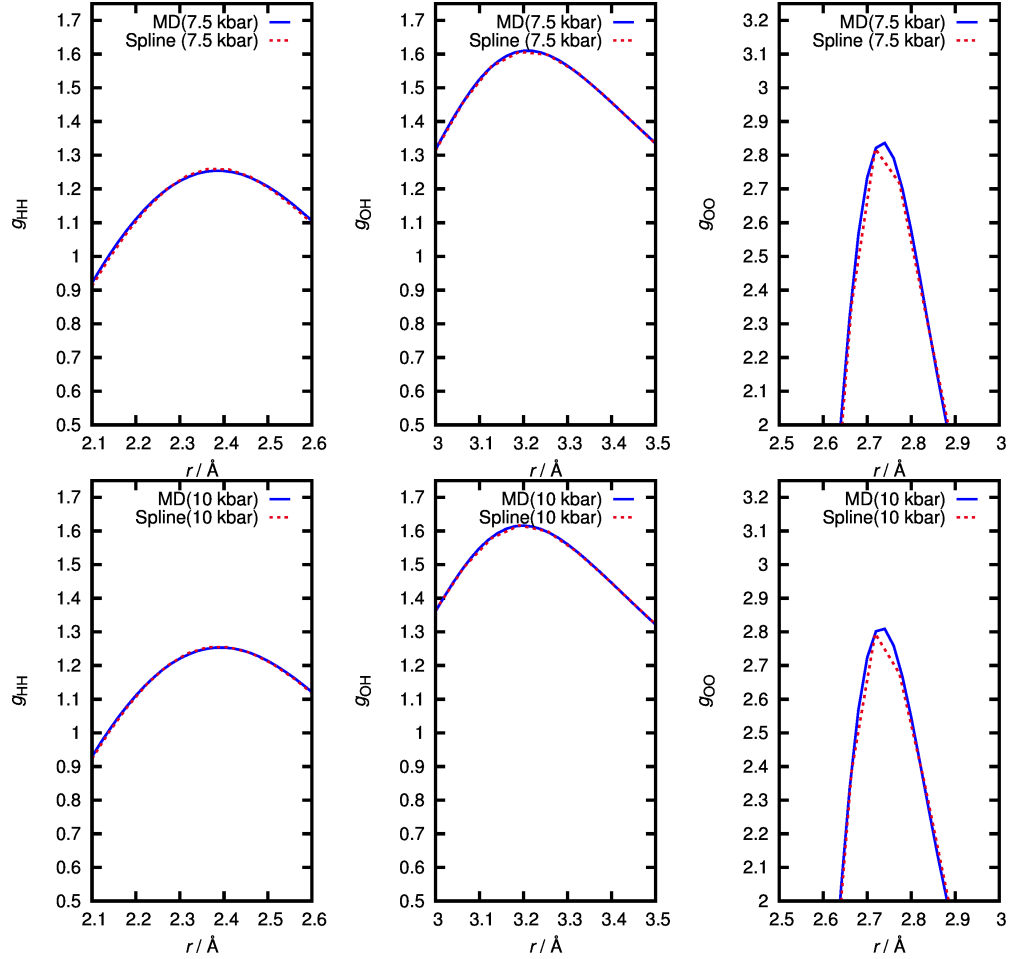


Figure 5.6.: Radial distribution functions of the water sites in dependence of the pressure as obtained from the MD simulations. The hydrogen-hydrogen (HH) RDF are shown left, the oxygen-hydrogen (OH) RDF are shown in the center, and the oxygen-oxygen (OO) RDF are shown in the right panel. The range around the first maximum is compared with the corresponding function smoothed by the cubic spline. Distribution functions for 7.5 kbar (top) and 10 kbar (bottom) are shown.

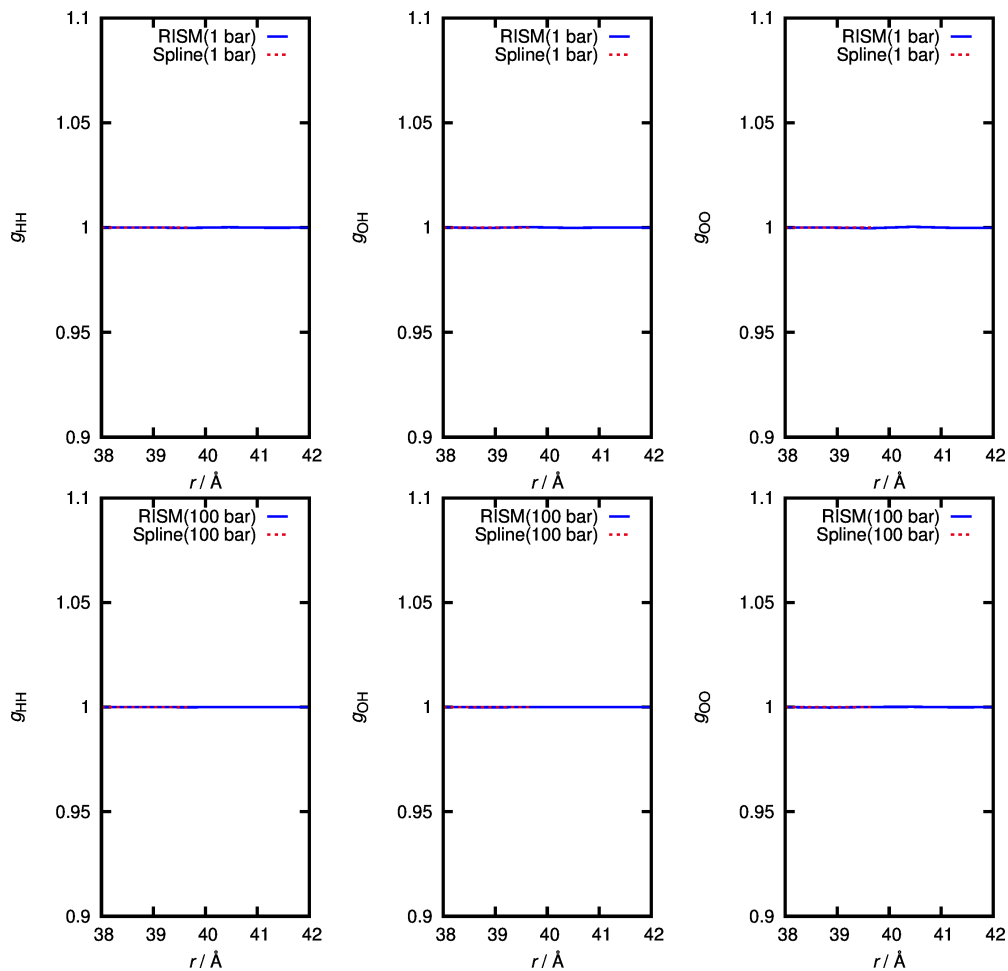


Figure 5.7.: Radial distribution functions of the water sites in dependence of the pressure as obtained from the MD simulations. The hydrogen-hydrogen (HH) RDF are shown left, the oxygen-hydrogen (OH) RDF are shown in the center, and the oxygen-oxygen (OO) RDF are shown in the right panel. Comparison of the switching region between the spline-smoothed distribution function and the resulting extrapolated distribution function for 1 bar (top) and 100 bar (bottom).

5. Introducing high pressure in 3D RISM

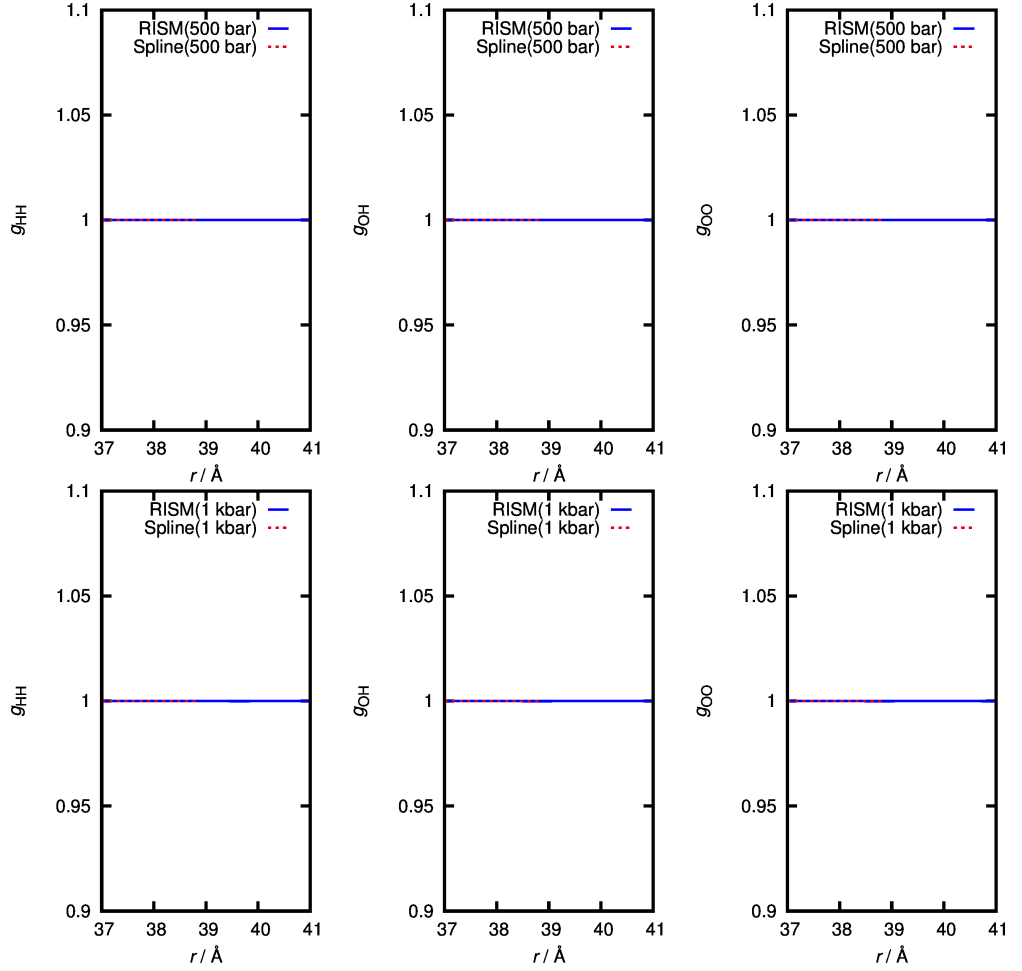


Figure 5.8.: Radial distribution functions of the water sites in dependence of the pressure as obtained from the MD simulations. The hydrogen-hydrogen (HH) RDF are shown left, the oxygen-hydrogen (OH) RDF are shown in the center, and the oxygen-oxygen (OO) RDF are shown in the right panel. Comparison of the switching region between the spline-smoothed distribution function and the resulting extrapolated distribution function for 500 bar (top) and 1 kbar (bottom).

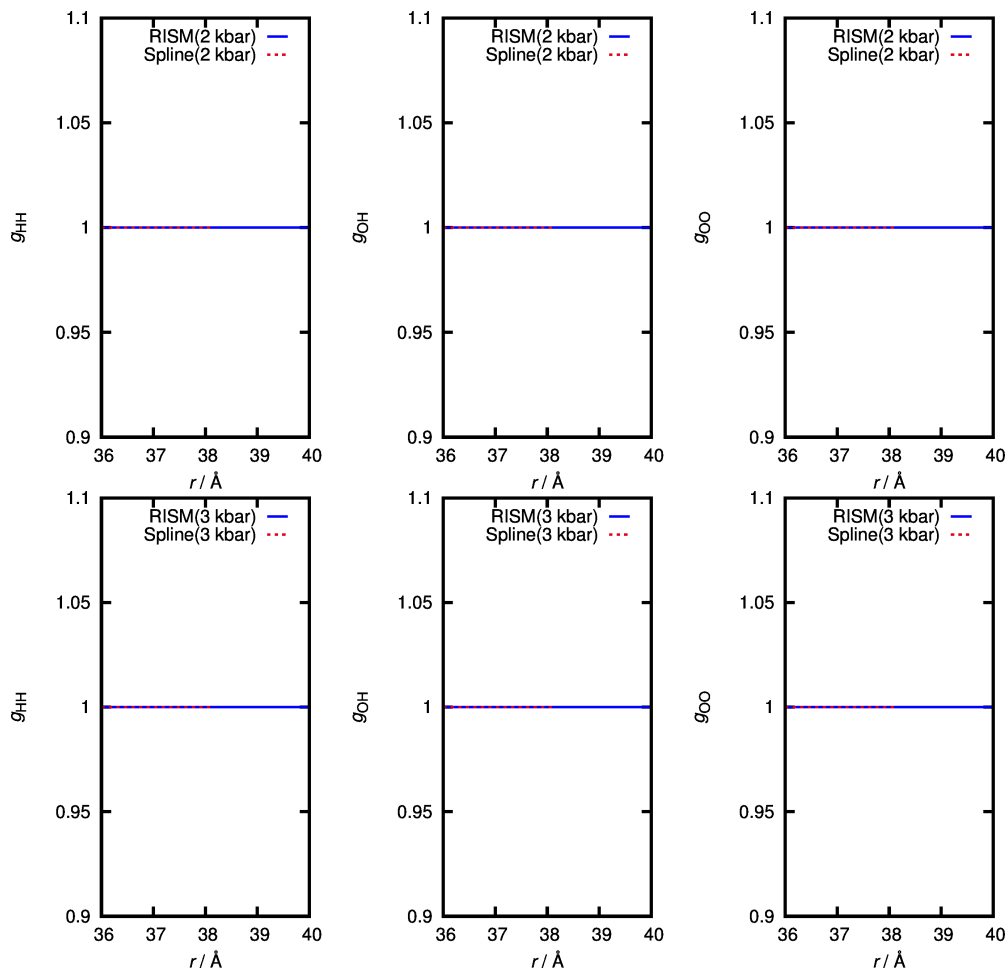


Figure 5.9.: Radial distribution functions of the water sites in dependence of the pressure as obtained from the MD simulations. The hydrogen-hydrogen (HH) RDF are shown left, the oxygen-hydrogen (OH) RDF are shown in the center, and the oxygen-oxygen (OO) RDF are shown in the right panel. Comparison of the switching region between the spline-smoothed distribution function and the resulting extrapolated distribution function for 2 kbar (top) and 3 kbar (bottom).

5. Introducing high pressure in 3D RISM

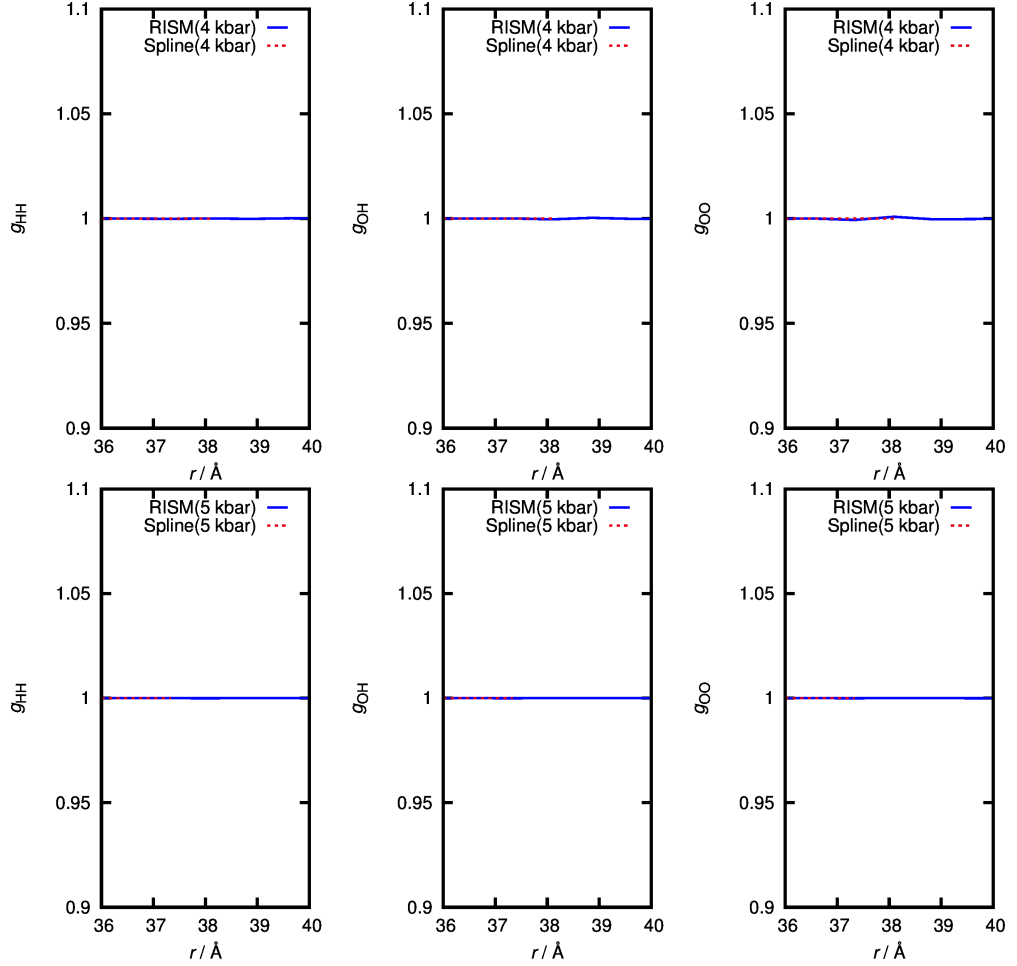


Figure 5.10.: Radial distribution functions of the water sites in dependence of the pressure as obtained from the MD simulations. The hydrogen-hydrogen (HH) RDF are shown left, the oxygen-hydrogen (OH) RDF are shown in the center, and the oxygen-oxygen (OO) RDF are shown in the right panel. Comparison of the switching region between the spline-smoothed distribution function and the resulting extrapolated distribution function for 4 kbar (top) and 5 kbar (bottom).

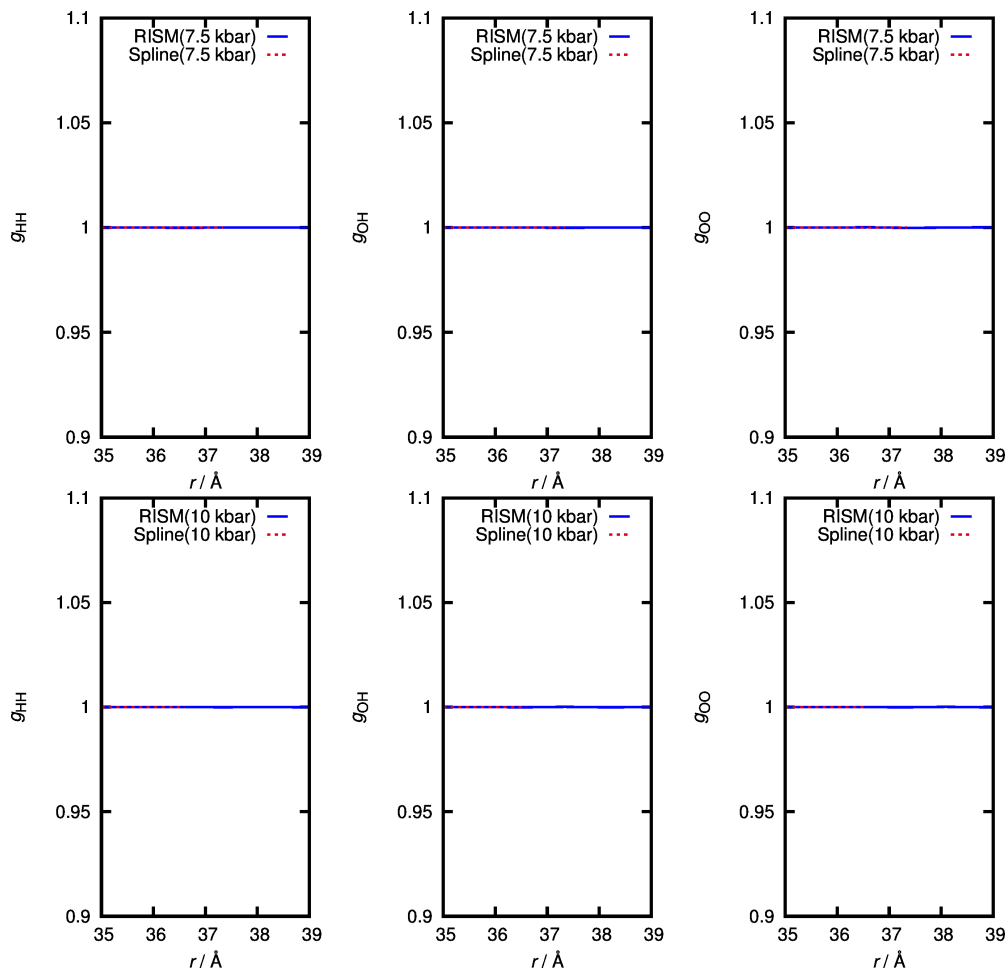


Figure 5.11.: Radial distribution functions of the water sites in dependence of the pressure as obtained from the MD simulations. The hydrogen-hydrogen (HH) RDF are shown left, the oxygen-hydrogen (OH) RDF are shown in the center, and the oxygen-oxygen (OO) RDF are shown in the right panel. Comparison of the switching region between the spline-smoothened distribution function and the resulting extrapolated distribution function for 7.5 kbar (top) and 10 kbar (bottom).

6. Benchmarking the new electrostatics model

As benchmark systems two species were chosen, alanine in three different protonation states, which are anionic, cationic and zwitter-ionic (see Figure 6.1) and molecular nitrogen. The Cartesian coordinates of the species can be found in Appendix A.3.1 on page 171. Alanine represents the class of proteinogenic amino acids, which are biologically relevant and where the protonation state plays an highly important role for the biological function. Nitrogen (N_2) is interesting, because it is a small linear molecule without a permanent dipole moment. It's electrostatic behavior in isotropic surroundings can not be described by atomic partial charges at all, thus the full ESP is necessary. A further test set was created by moving the nitrogen molecule by 1 Å along the bond axis off center, in order to check the sensitivity of the ESP models to asymmetric solute placement.

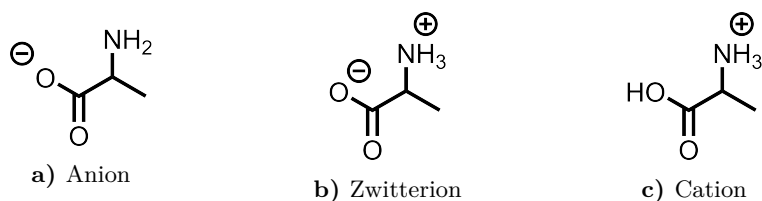


Figure 6.1.: Two dimensional representations of the three different alanine species.

Table 6.1.: Number of grid points and the resulting box lengths used in the 3D RISM calculations to benchmark the new ESP model.

n	$L / \text{Å}$
48	14.4
64	19.2
80	24
96	28.8
112	33.6
128	38.4
192	57.6

6. Benchmarking the new electrostatics model

This test-setup aims to the elucidation of the grid-size dependence of thermodynamic observables from EC-RISM. Thus the grid sizes listed in Table 6.1 were chosen and calculations were performed for all electrostatic models implemented, which are: no switching, switching without perturbative correction and switching with perturbative correction of chemical excess potentials. These calculations were performed for all test molecules. The computational details can be found in Section 8.3 on page 74. The results are presented in the Chapter 11 on page 105.

7. Force field development

7.1. Charge scaling for high pressures

In the case of trimethylamine-N-oxide (TMAO) it was shown, that it is necessary to adapt the atomic charges of the force field in order to obtain correct results for electrostatically dominated observables, like coordination numbers.¹² Since the absolute charges obtained from EC-RISM are different from the force field charges, it is not possible to just use the EC-RISM charges in the force field. In order to cover the pressure effect in electrostatics nonetheless, a charge scaling approach has been constructed. This ansatz is able to cover the relative, pressure dependent change in dipole moment and the ratios of the charges *per se*.¹² The high pressure charge

$$q_i^{\text{HP}}(p) = q_i^{\text{amb}} + \alpha q_{\text{ref}}^{\text{amb}} \frac{\Delta q_i^{\text{EC-RISM}}(p)}{\Delta q_{\text{ref}}^{\text{EC-RISM}}(p)}, \quad (7.1)$$

is calculated based on the atomic charge q_i^{amb} . $\Delta q_{\text{ref}}^{\text{EC-RISM}}(p)$ is the difference between the high pressure charge and the ambient pressure charge from EC-RISM, while $\Delta q_{\text{ref}}^{\text{EC-RISM}}(p)$ is this difference for the reference atom. The linear fit parameter α ensures the correct dipole moment scaling. Strict charge neutrality, which can be violated due to numerical noise, is ensured by additively modifying the oxygen charge.¹²

7.2. Application of differential evolutionary algorithms in force field development

Optimizing force fields usually means to modify a large number of parameters in order to gain good results on a comparatively low number of observables. Additionally, there usually is a non-linear dependency between force field parameters and observables. This leads to the task, to find a global optimum for all observables introduced in dependency of the whole parameter set. The first step is to compress the overall force field candidate performance into a single scalar value. In the context of evolutionary and genetic algorithms, the function coping with that task is called a fitness function, when it shall be maximized or a cost function, when the aim is to minimize this value. All approaches introduced in this thesis have in common, that their aim is to minimize the deviation between force field based values and reference data, so it seems fruitful to use cost functions here. Furthermore, for most force field parameters there is a

7. Force field development

range of plausible values¹ for every parameter. One possible method to solve this type of problem is the differential evolutionary approach, which was introduced by Storn and Price.¹⁰⁹ This method will be described qualitatively in this section.

In order to initialize the optimization process a number of candidates is created randomly and ideally equally distributed over the search space defined by the parameter ranges. The number of parameter sets is called population size and remains constant over the whole optimization process. Instead of starting from randomly chosen parameter sets, it is also possible to utilize final populations of previous runs or to seed known parameter sets into the process. Optionally the pre-known sets can be modified by adding normally distributed modifications.¹⁰⁹

The idea of differential evolution is, to calculate the difference between two randomly chosen parameter vectors \mathbf{a} and \mathbf{b} and add the result to a third one \mathbf{c} , so the resulting candidate is

$$\mathbf{d} = f \cdot (\mathbf{b} - \mathbf{a}) + \mathbf{c}, \quad (7.2)$$

which is called mutation, where f is a weighting factor. Additionally, so-called crossover steps are performed, which by random chooses a member of the current population to replace a number of parameters of the candidate vector by parameters from the previous population. The probability of crossover is an input parameter of the algorithm.¹⁰⁹

After the mutation and crossover the fitness of the resulting parameter is tested. When the resulting fitness is better than the one of the vector \mathbf{c} mutated firsthand, the new parameter set becomes a member of the next generation, otherwise \mathbf{c} will become a next-generation member.¹⁰⁹

Differential evolution was applied by Dr. Christoph Hölzl in order to optimize urea force-field parameters. A modified version of his DEA-script was used by the author to optimize the non-bonded parameters and the position of a Coulomb dummy site within the molecules for hydronium and hydroxide. The details and results will be discussed in the appropriate sections.

7.3. Force field development for urea

7.3.1. Optimization of an urea force field

Geometry and bonded parameters

The force field development described in the following chapter was performed by Dr. Christoph Hölzl. The development process is depicted here briefly for the sake of completeness. The bond lengths and the dihedral angle parameters for urea were

¹Negative radii or positive atomic charges, that are larger than the charge of the nucleus are extreme examples of implausible parameters.

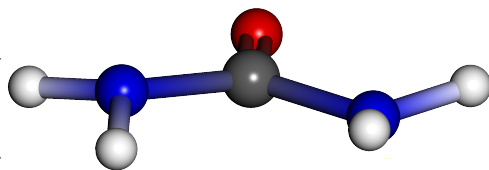


Figure 7.1.: 3D structure of the B3LYP/6-311+G(d,p) optimized urea molecule. The aqueous solution was modelled by PCM. The out-of-plane positions of the hydrogen atoms with respect to the N-C-N-plane can be seen here.

Table 7.1.: Cartesian coordinates of the B3LYP/6-311+G(d,p) optimized urea molecule. Water was presented by PCM.

No.	Type	Element	$x/\text{\AA}$	$y/\text{\AA}$	$z/\text{\AA}$
1	n	N	-5.018548289978	1.580397660980	-0.079180097529
2	c	C	-3.775055284607	2.143894547729	-0.018401674379
3	n	N	-2.721665907762	1.279046837960	-0.118460690540
4	o	O	-3.612364415590	3.365832280003	0.119127870290
5	hn	H	-5.135019222112	0.625298053403	-0.406616679365
6	hn	H	-5.798244033836	2.212489078593	-0.231161753831
7	hn	H	-2.865505017771	0.278599918435	-0.011269172048
8	hn	H	-1.810187828342	1.639401622897	0.145982197403

obtained from the General AMBER Force Field (GAFF)^{47,110}, while the bond angle parameters were taken from the Kirkwood-Buff Force Field (KBFF).¹¹¹ All simulations were performed with GROMACS 2016.3.¹¹²⁻¹¹⁸ The force field parameters of urea can be found in the appendix A.2.1 beginning on page 159. Water was represented by the the TIP4P/2005 model.¹¹⁹

The Cartesian coordinates of the optimized geometry are given in Table 7.1. This geometry was obtained by B3LYP/6-311+G(d,p) optimization and PCM modelling water. Tight convergence criteria were applied for both, the SCF cycle and the geometry optimization. The integral grid for DFT was set to ultrafine, symmetry was not considered. The optimization was carried out with Gaussian 03 Rev. D.02.⁹⁷ This geometry was used for all EC-RISM calculations on urea. Remarkably, in contrast to the force field models DFT calculations unveil, that the hydrogen atoms are bent slightly out of the O-C-N plane as can be seen in Figure 7.1.

7. Force field development

Urea V1

The urea force field development process as described here was carried out completely by Dr. Christoph Hölzl (UR). Throughout the optimization process the differential evolutionary algorithm (DEA) by Storn and Price¹⁰⁹ was applied as implemented in the Python library `inspyred`.¹²⁰ The cost function for the DEA was evaluated from the results of three different MD simulations. First a trajectory of 2 ns was used to calculate the first solvation shell coordination number up to the distance determined by the first minimum in radial distribution functions obtained from *ab initio* molecular dynamics (*aiMD*). Furthermore the Luzar/Chandler criterion was applied to determine the number of hydrogen bonds accepted/donated by hydrogen, nitrogen and oxygen of urea. The second simulation resembled a urea solution of about 2 mol l⁻¹. The resulting density was compared with data from literature. The third simulation was carried out on a solution of circa 8 mol l⁻¹, which was compared with the in-house densities from the FOR 1978. The cost function

$$\begin{aligned}
 f(q_O, q_N, q_H, s_\sigma) = & \sum_{i=O,N,C,H} C_{1i} \left| \frac{N^{\text{ff}}(i) - N^{\text{aiMD}}(i)}{N^{\text{aiMD}}(i)} \right| \\
 & + \sum_{i=O,N,H} C_{2i} \left| \frac{n^{\text{ff}}(i) - n^{\text{aiMD}}(i)}{n^{\text{aiMD}}(i)} \right| \\
 & + \sum_{i=1}^2 C_{3i} \left| \frac{\rho^{\text{ff}}(i) - \rho^{\text{exp}}(i)}{\rho^{\text{exp}}(i)} \right|
 \end{aligned} \tag{7.3}$$

evaluates the first shell coordination numbers

$$N(i) = \rho_{\text{WAT}} \int_0^{r_{\text{min}}^{\text{aiMD}}(i)} 4\pi r^2 g_{i-\text{OW}}(r) dr, \tag{7.4}$$

which are the numbers of hydrogen bonds n and the densities ρ of the 2 mol l⁻¹ and the 8 mol l⁻¹ solution. The weighting coefficients are given by the matrix

$$C = \begin{bmatrix} 1 & 1 & 1 & 1 \\ 1 & 0.5 & 1 & \\ 25 & 25 & & \end{bmatrix}. \tag{7.5}$$

The population size was set to 100 and the optimization process was terminated after 750 force field candidate evaluations. The resulting non-bonded force field parameters are shown in Table A.45 in the appendix A.2.2 on page 160.

Urea V2

The only change introduced into urea V2 force field is the change of the Lennard-Jones parameters ϵ for oxygen and nitrogen to the mean value of the AMBER and KBFF force field parameters. The resulting parameters are shown in Table A.46 in Appendix A.2.2 on page 160.

Urea V3

In contrast to the V1 and V2 force field some changes were introduced. Most importantly now the hydrogen in *cis*-position is treated separately from *trans*-positioned hydrogen in terms of the atomic charges. The cost function

$$\begin{aligned}
f(q_{\text{O}}, q_{\text{N}}, q_{\text{H}^{\text{cis}}}, q_{\text{H}^{\text{trans}}}, s_{\sigma}) = & \sum_{i=\text{O},\text{N},\text{C},\text{H}^{\text{cis}},\text{H}^{\text{trans}}} C_{1i} \left| \frac{N^{\text{ff}}(i) - N^{\text{aiMD}}(i)}{N^{\text{aiMD}}(i)} \right| \\
& + \sum_{i=\text{O},\text{H}^{\text{cis}},\text{H}^{\text{trans}}} C_{2i} \left| \frac{n^{\text{ff}}(i) - n^{\text{aiMD}}(i)}{n^{\text{aiMD}}(i)} \right| \\
& + \sum_{i=1}^2 C_{3i} \left| \frac{\rho^{\text{ff}}(i) - \rho^{\text{exp}}(i)}{\rho^{\text{exp}}(i)} \right|
\end{aligned} \tag{7.6}$$

with the coefficient matrix

$$C = \begin{bmatrix} 1 & 1 & 1 & 0.5 & 0.5 \\ 1 & 0.5 & 0.5 & & \\ 25 & 25 & & & \end{bmatrix} \tag{7.7}$$

was modified to include the *cis*-/*trans*-hydrogen. The resulting parameters are shown in Table A.47 in appendix A.2.2 on page 160.

7.4. Force field development for hydronium and hydroxide

For the exact prediction of thermodynamic data for hydronium and hydroxide in aqueous solution, suitable Lennard-Jones parameters are crucial for the construction of the cavity and to compute dispersion in 3D RISM calculations. Force fields for ionized water species in bulk solution are rare. Furthermore, the thermodynamics in RISM calculations are heavily dependent on the quality of solute(*u*)-solvent(*v*) pair distribution functions (*uv*-PDF). For instance, in the RISM picture, thermodynamic data are obtained by integrating over site-site distribution functions.

In spite of the importance of the autoprotolysis products of water, *e.g.* for the quick proton and hydroxide transfer in aqueous phases or direct interactions with biomolecules like proteins, implicit and explicit solvation models neglect those species. Especially classical non-polarizable force field simulations use water models comprised of H₂O only. Many studies on the behavior of hydronium and hydroxide at the water surface^{55,57} and water interfaces with other phases like solid polymers^{121,122} or hydrophobic media⁵⁴ have been published.ⁱⁱ

ⁱⁱThe literature given here is only a small fraction of what was published.

7. Force field development

Recently a new force field was developed, which performs well in reproducing the solvation thermodynamics of hydronium and hydroxide in free energy MD simulations at atmospheric pressure¹⁶. Own tests revealed that the solvation structure in terms of uv-radial distribution functions cannot be calculated correctly with this force field in reference to *ai*MD simulation based data, which was recognized visually in Figure 12.3a and 12.3b in the Results part on page 114. In the case of hydronium, the difference between *ai*MD and ffMD with the latter force field can be seen mainly in the oxygen-hydrogen distribution function, while in the case of hydroxide the hydrogen centered distribution functions are affected.

Starting from the perspective to change as few parameters as possible, the geometry was adapted from a pre-existing force field by Bonthuis *et al.*¹⁶ Since a rigid body force field was desired, there is no need of optimization of internal degrees of freedom, so it could be constrained to the non-bonding interactions being represented by the atomic charges and the Lennard-Jones-Parameters. In order to optimize these parameters, the differential evolutionary algorithm (DEA) by Storn and Price¹⁰⁹ was applied in a Python script made by Dr. Christoph Hölzl, using the DEA library from *inspyred*.¹²⁰ This script was modified by the author in order to fit the problem. The population size for runs was set to 50 individual force field candidates, while 100 evaluations were performed per run, meaning that the initial run creates 50 randomly chosen force field candidates. The performance of each candidate was tested and 50 more evaluation steps were performed with cross-over or mutation steps. The cross-over rate was set to 1.0, while the mutation rate was 0.2.

The simulation boxes for hydronium were comprised of 1182 SPC/E¹⁰⁷ water molecules and eight hydronium ions resulting in a cubic box with 3.32056 nm of edge length. In case of hydroxide the box is comprised of 966 SPC/E molecules and eight hydronium ions in a cubic box with an edge length of 3.10554 nm. Both types of ions were held in place by a harmonic position restraint with a force constant of 100 MJ mol⁻¹ nm⁻². The 50 best performing force fields from these evaluations comprise the final population, which was inserted as the start population for the next run. This cycle was repeated 10 times. In order to obtain the radial distribution function (RDF), first a short equilibration simulation was performed for 100000 time steps, 2 fs each, initiated with randomly chosen velocities at a temperature of 300 K, which was maintained by a stochastic velocity scaling approach¹²³ with a time constant of 1 ps. The equations of motion were solved applying a leap-frog integrator.¹²⁴ Van-der-Waals interactions were treated with a cutoff, the neighbor list with buffering was constructed in the Verlet cutoff scheme with a cutoff of 10 Å, while the neighbor list was updated every 20 timesteps, applying the grid method for reconstructing the neighbor list. Coulomb interactions were calculated in the particle mesh Ewald formalism,¹²⁵ where 4th-order interpolation was applied on a Fourier grid spacing of 0.12 nm. The real-space Coulomb cutoff was set to 1 Å. The final coordinates and velocities of the equilibration simulation were passed to the production run, applying the same settings for 1500000 timesteps. Thus, the equilibration and production simulations were performed in the *NVT* ensemble. All simulations and preparation steps were performed with the GROMACS 2016.3 suite.¹¹⁶

7.4. Force field development for hydronium and hydroxide

Additionally, to get a quick idea of the radial distribution functions at 10 kbar, simulations were performed in the NpT ensemble. Simulations for 10 kbar were performed with the same settings, except for the pressure being maintained by a Berendsen barostat¹²⁶ set to 10 kbar, applying a time constant of 1 ps and a compressibility of $1.1697134721242294 \cdot 10^{-5} \text{ bar}^{-1}$. Equilibration time was extended to 10000000 timesteps, since the pressure had to be introduced. For the production run the same settings were applied, the simulation time was 1500000 timesteps.

The box setup, minimizations, equilibration runs, simulations and extraction of the radial distribution functions were performed with the GROMACS 2016.3 package. Equilibration, simulation and evaluation was automatically performed by the DEA script. Coordination numbers were calculated with the script `coordination_number.py`, which was written in Python 2.7 by Christoph Hölzl. This script calculates the coordination number

$$N(i, j; r_{\max}) = \rho_j \int_0^{r_{\max}} 4\pi r^2 g_{ij}(r) dr \quad (7.8)$$

where ρ_j is the number density of the solvent site j , r_{\max} is the radius, up to which the coordination number is calculated and i is the corresponding solute site.

The so-called cost function

$$f = \sum_i C(i) \left| \frac{N_i(\text{ffMD}) - N_i(\text{aiMD})}{N_i(\text{aiMD})} \right| \quad (7.9)$$

of the DEA was calculated from the weighted deviation of the coordination numbers N for different solvation shells obtained with the force field candidate in comparison to the coordination numbers calculated from *ab initio* MD simulations performed by Dr. Sho Imoto. Every contribution was scaled with a weighting factor $C(i)$. The cost function parameters are shown in Table 7.2 and 7.3.

Table 7.2.: Cost function parameters for hydroxide.

i	range	r_{\max}/nm	$N(\text{aiMD})$	$C(i)$
OW-Ox	max1	0.265	1.3651282325	4
OW-Ox	min1	0.375	6.08135571979	2
OW-Hx	min1	0.245	0.646921326355	0
OW-Hx	max2	0.295	2.62348186819	0
OW-Hx	min2	0.345	5.57196208255	0
HW-Ox	max1	0.165	0.691236483387	6
HW-Ox	min1	0.255	2.21074506305	3
HW-Ox	max2	0.315	3.86055437716	3
HW-Hx	max1	0.205	0.757601583256	0
HW-Hx	min1	0.255	2.30798624207	0

7. Force field development

Table 7.3.: Cost function parameters for hydronium.

i	range	r_{\max}/nm	$N(ai\text{MD})$	$C(i)$
OW-Oy	max1	0.255	1.355362521630	1
OW-Oy	min1	0.295	3.022305413130	1
OW-Oy	max2	0.425	9.652672773550	1
OW-Hy	max1	0.155	0.526975131109	8
OW-Hy	min1	0.225	0.967488932975	8
OW-Hy	max2	0.305	2.174832624270	8
HW-Oy	min1	0.245	0.148757238624	2
HW-Oy	max1	0.305	1.935308739030	2
HW-Oy	min2	0.355	4.463830670310	2
HW-Hy	max1	0.205	0.413951596103	0
HW-Hy	min1	0.255	1.062972459810	0
HW-Hy	max2	0.365	4.612991400610	0

8. Computational details

8.1. Computational details: TMAO

8.1.1. Dipole moment

The EC-RISM calculations to obtain the dipole moment were performed on the HF/6-311+G** level of theory during iteration and on the B3LYP/6-311+G** level for the final evaluation after convergence, which was assumed, when the change of the Gibbs energy between two consecutive steps fell below $0.01 \text{ kcal mol}^{-1}$. The QC calculations were performed with Gaussian 03 Rev. D.02.¹²⁷ The partial charges to polarize the solvent were obtained with the CHelpG¹²⁸ method without dipole moment constraint. Symmetry was not taken into account. The box size for 3D RISM calculations was determined automatically in a fashion, that ensures a minimum solvent buffer of 25 Å during iteration and of 30 Å for the final evaluation. This lead to $88 \times 90 \times 88$ grid points during iteration and to $106 \times 106 \times 104$ grid points during the final calculation. The grid point distance was 0.3 Å in every principal axis direction. As a closure for the 3D RISM integral equation system the PSE-3 closure was utilized. The 3D RISM calculation was assumed converged as soon as the maximum norm of the difference of the direct correlation function dropped below 10^{-6} . The Lennard-Jones parameters of TMAO were taken from the V3 force field. The geometry of TMAO was optimized on the B3LYP/6-311+G** level. PCM with the default settings for water was used.

8.1.2. Vibrational frequencies

The calculations for the vibrational modes were performed basically with the same settings. The need for higher spatial resolution required a grid size of 240^3 grid points with a distance of 0.1 Å. The requirement to resolve small energy differences lead to the decision to change the EC-RISM convergence threshold to $0.0001 \text{ kcal mol}^{-1}$.

8.1.3. EC-RISM geometry optimization

In order to perform EC-RISM geometry optimizations, the EC-RISM method was extended by an optimization method by Dr. Roland Frach. The gradient calculated in the fashion outlined in section 2.8 is handed over to a limited memory variant of the Broyden-Fletcher-Goldfarb-Shanno (BFGS) algorithm.¹²⁹ The same EC-RISM

8. Computational details

settings as for the regular singlepoint calculations on TMAO were applied. As a convergence criterion for the geometry optimization a Gibbs energy difference of smaller than $0.005 \text{ kcal mol}^{-1}$ was applied. In order to avoid clashes between solute atoms or the solute being torn apart, a damping factor of 0.5 was introduced in the first iteration, mixing in the previous geometry. The damping factor was decreased from iteration to iteration applying the power of 4.

8.2. Computational details: Urea

In the same fashion as for TMAO EC-RISM calculations were performed for urea in order to obtain the dipole moment as a function of pressure. The 3D-RISM box had a dimension of $90 \times 88 \times 84$ grid points during iteration and of $106 \times 104 \times 100$ in the final RISM calculation, resulting in a solvent buffer of 25 \AA and 30 \AA respectively. The grid spacing was 0.3 \AA in every principal axis direction in both cases. The very same simulation based RDF derived χ_{SIM} and the HNC based χ_{HNC} were used as solvent susceptibilities as in the TMAO case. The calculations were performed with an electrostatic potential calculated from the atomic partial charges. The PSE-3 equation was used as a closure relation. Convergence of the 3D RISM iteration was assumed, when the residual maximum norm of two consecutive iterations became smaller than 10^{-6} , while the EC-RISM cycle converged as soon as the change in solvation Gibbs energy fell below $0.01 \text{ kcal mol}^{-1}$. The quantum chemistry part was performed on the B3LYP/6-311+G(d,p) level for the final evaluation. During the EC-RISM iteration cycle B3LYP was replaced by Hartree-Fock theory. The resulting pressure-dependent dipole moments are given in Table 10.1 and in Figure 10.1 in the Results part of this thesis. The Lennard-Jones parameters for the RISM calculations were taken from the urea V3 force field (see Section 7.3.1).

8.3. Computational details: Benchmark of the new ESP model

The EC-RISM calculations for all benchmark data were calculated utilizing a symmetry reduced, DRISM HNC based solvent susceptibility of water at 298.15 K and 1 bar of pressure. The B3LYP/6-311+(G,p) QC calculations were performed with Gaussian 09 Rev. E.01⁶⁵ for final iteration and were replaced by Hartree-Fock calculations during iteration. The EC-RISM calculation was assumed converged as soon as the change in Gibbs energy became smaller than $0.01 \text{ kcal mol}^{-1}$. Symmetry handling was turned off in Gaussian. The calculation grid with 0.3 \AA grid point distance was constructed cubically by a different number of points in the directions of the principal axes which can be found in Table 6.1 on page 63. The molecules were automatically centered, so the center of gravity is in the box's origin, except in case of the shifted N_2 . As a closure relation the second order PSE closure was applied. As an ESP fit the CHElpG¹²⁸ was

8.4. Computational details: Calculating the autoprotolysis equilibrium of water

used. It was distinguished between cases with and without dipole moment constraint. The handling of the ESP in 3D RISM was performed in three modes: without switching, with switching but without chemical potential perturbation and with both. As a convergence criterion for the 3D RISM integral equation, a maximum norm of 10^{-6} of the difference of the direct correlation function between two consecutive iterations was chosen.

8.4. Computational details: Calculating the autoprotolysis equilibrium of water

The EC-RISM energies were calculated applying force field based geometries and quantum chemically optimized geometries given in Tables 8.1 to 8.4. The geometry optimizations were performed with Gaussian 09 Rev. E.01⁶⁵ applying the MP2/6-311+G(d,p) method using tight convergence criteria for the SCF cycle and the optimization under aqueous PCM solvation.

Table 8.1.: Quantum chemically optimized geometry of hydronium.

	$x/\text{\AA}$	$y/\text{\AA}$	$z/\text{\AA}$
O	-0.046474031351	0.232857539185	0.044111486660
H	0.587961215464	-0.099710000991	0.706854992186
H	0.335239448094	0.144468718741	-0.849972086619
H	-0.876726632208	-0.277616256934	0.099005607773

All EC-RISM calculations were performed using Gaussian 09 Rev. E.01⁶⁵, applying the MP2/6-311+G(d,p) level of theory for final evaluation and the HF/6-311+G(d,p) during iteration. Electrostatics were covered by using the full electrostatic potential from QM, while dipole moment constraint ESP derived **CHelpG**¹²⁸ charges were used for renormalization purposes. The potential switching scheme with a 2 \AA buffer was applied and the resulting perturbation energy was added into the excess chemical potential. As solvent files for each pressure HNC 1D DRISM calculated solvent susceptibilities (compare Chapter 5) were used.¹² The choice of the HNC based solvent susceptibilities for these calculations is founded in the availability of the PMV correction for these solvent models. Furthermore it has been seen, that HNC based

Table 8.2.: Quantum chemically optimized geometry of hydroxide.

	$x/\text{\AA}$	$y/\text{\AA}$	$z/\text{\AA}$
O	-0.481465838742	0.000000000000	0.000000000000
H	0.481465838742	0.000000000000	0.000000000000

8. Computational details

Table 8.3.: Force field geometry of hydronium.

	$x/\text{\AA}$	$y/\text{\AA}$	$z/\text{\AA}$
O	-0.04300	0.20600	0.04000
H	0.58500	-0.23900	0.64600
H	0.34400	-0.00700	-0.83500
H	-0.79900	-0.40600	0.06600

Table 8.4.: Force field geometry of hydroxide.

	$x/\text{\AA}$	$y/\text{\AA}$	$z/\text{\AA}$
O	-0.166666666667	0.000000000000	0.000000000000
H	0.833333333333	0.000000000000	0.000000000000

solvent susceptibilities usually show monotonous trends for pressure dependent observables and it was seen, that the pressure dependence of pressure induced band shifts in nuclear magnetic resonance spectroscopy can be calculated with this type of solvent susceptibilities more accurately.¹³⁰ The grid dimension was 128^3 grid points with a grid point distance of 0.3 \AA on the principal axes. Symmetry reduction was not applied in Gaussian, the embedding point charge cluster was compressed applying the `qcompress` utility.¹³¹ 3D RISM calculations were assumed converged as soon as the maximum norm of the direct correlation function difference between two consecutive iterations fell below 0.000001 . The EC-RISM calculation was assumed converged in case the change in Gibbs energy in solution became smaller than $0.01 \text{ kcal mol}^{-1}$.

8.5. Computational details: Benchmark of a novel semi-empiric Hamiltonian

Reference calculations were performed on the `MP2/aug-cc-pVDZ` level for iteration and the final evaluation in the EC-RISM cycle. The cubic 3D RISM grid was chosen to maintain a minimum solvent buffer of 25 \AA around the molecule, while the grid point distance was set to 0.3 \AA . As a closure the PSE-3 equation was used. The 3D RISM calculation was assumed converged, when the maximum residual norm of the direct correlation function became smaller than 0.000001 . The full electrostatic potential from the QC codes was treated utilizing the switching scheme introduced earlier in this work (see Section 2.6.1), applying a switching buffer of 2 \AA and adding the perturbative switching offset. In the MP2 case the atomic charges were constrained to meet the dipole moment directly evaluated from the wave function. Since EMPIRE does not evaluate the wave function based dipole moment, for the hpCADD Hamiltonian the dipole moment resulting from the ESP fit was used. The 3D RISM settings were equal

8.5. Computational details: Benchmark of a novel semi-empiric Hamiltonian

for both pressures and QC methods. The EC-RISM cycle was assumed converged as soon as the change in the Gibbs energy in solution between two consecutive iterations became smaller than $0.01 \text{ kcal mol}^{-1}$.

Part IV.

Results

9. Results: Trimethylamine-N-oxide

9.1. Dipole moment

9.1.1. The dipole moment of TMAO as a function of pressure

Quantum chemical calculations usually show the trend to reveal increasing dipole moments with higher pressures. Different methods, EC-RISM and DFT based MD simulations, prove this trend for TMAO as well. Previously published data can be found in Table 9.1 and Figure 9.1.¹²

In order to determine the pressure-dependence of the dipole moment, MD simulations based on electronic DFT (*ab initio* MD, *aiMD*) were performed and evaluated by Dr. Sho Imoto. The author of this thesis calculated the pressure-dependent solvent susceptibilities of water based on classical force field MD simulations performed by Dr. Christoph Hölzl. Both, simulated and HNC-based solvent susceptibilities were used to determine the dipole moment and the partial charges of TMAO as a function of pressure. The results of these calculations can be seen in Table 9.1 and Figure 9.1. Comparing the dipole moment shift between 1 bar and 10 kbar of *aiMD* (0.32 D), EC-RISM-HNC calculations (0.14 D) and EC-RISM-SIM calculations (0.54 D), it can be seen that HNC underestimates the pressure induced shift, while solvent susceptibilities accounting for simulated bridge functions tend to overestimate the pressure induced polarization.

Table 9.1.: Dipole moment of TMAO as a function of pressure.¹²

p/bar	$\mu(\chi_{\text{SIM}})/\text{D}$	$\mu(\chi_{\text{HNC}})/\text{D}$	$\mu(\text{aiMD})/\text{D}$
1	7.9037	8.3178	8.55
100	7.9277	8.3206	-
500	8.1099	8.3312	-
1000	8.2163	8.3433	-
2000	8.2658	8.3644	-
3000	8.3121	8.3820	-
4000	8.3105	8.3974	-
5000	8.4227	8.4385	-
7500	8.4236	8.4385	-
10000	8.4400	8.4608	8.87

9. Results: Trimethylamine-N-oxide

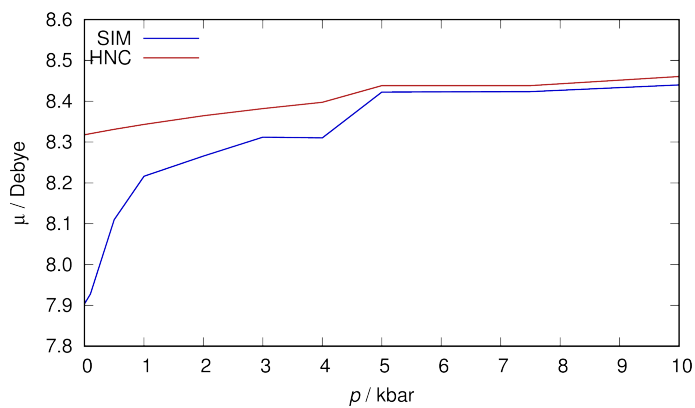


Figure 9.1.: Dipole moment of TMAO as a function of pressure obtained from EC-RISM calculations.¹²

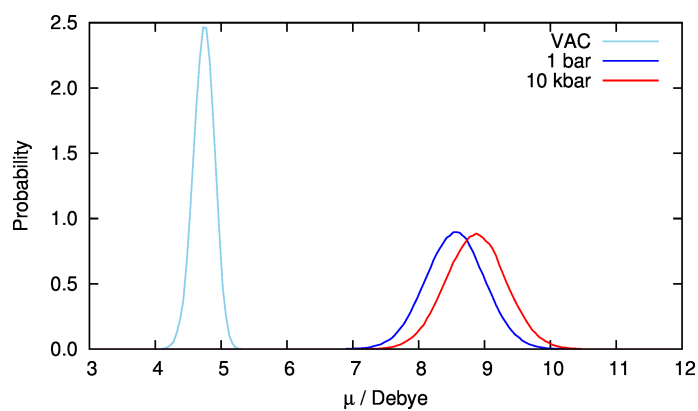


Figure 9.2.: Dipole moment of TMAO obtained from *aiMD* calculations *in vacuo*, at 1 bar and at 10kbar. Data generated by Dr. Sho Imoto.¹²

9.2. Development of a force field for TMAO in aqueous high pressure environments

The development process described in this section was the result of a cooperation within the Deutsche Forschungsgemeinschaft (DFG) research group FOR 1979. Three workgroups were part of this cooperation: The group of Prof. Dr. Dominik Marx at the Ruhr-Universität Bochum, the group of Prof. Dr. Dominik Horinek, Universität Regensburg and the group of Prof. Dr. Stefan M. Kast, Technische Universität Dortmund. Especially Dr. Sho Imoto (Bochum), Dr. Christoph Hölzl (Regensburg) and the author (Dortmund) were involved in this process. The results have already been published.¹²

In order to test and modify an existing ambient force field for TMAO¹³² at extreme pressures *aiMD* simulations of aqueous TMAO solutions at 1 bar and at 10 kbar were performed by Dr. Sho Imoto. Similar, but considerably larger, systems were treated with *ffMD* by Dr. Christoph Hölzl to compare a well-defined set of observables with *aiMD* results as well as experimental data. For performing single-point QC calculations the EC-RISM method was applied in order to gain the pressure-dependent dipole moment (see Section 9.1.1) and the corresponding ESP-derived partial charges.

EC-RISM geometry optimizations were applied to TMAO at 1 bar and at 10 kbar revealing that there is no relevant structural change in TMAO visible, neither between 1 bar and 10 kbar, nor between EC-RISM and PCM at the B3LYP/6-311+G(d,p) level of theory. The obtained N-O bond length was 1.384 Å. One has to keep in mind that both solvation models, PCM and EC-RISM, are not able to reproduce the electron transfer due to explicit hydrogen bonding. So it is no surprise, that in contrast *aiMD* results show a small increase of the N-O bond length between 1 bar (1.418 ± 0.001 Å) and 10 kbar (1.421 ± 0.001 Å).¹² The geometries are shown in the Appendix A.1.1 on page 133.

As a starting point for the optimization, a TMAO force field known to perform well at ambient conditions for a variety of observables was necessary. Existing force fields were benchmarked: One by Kast *et al.*¹³² (referred to as V1 from here on) and the same force field modified by Schneck *et al.*¹³³ (referred to as V2 from here on). The novel force field introduced here, which has already been published, is referred to as V3.¹² The high-pressure variant of this force field is called V3-HP.

High pressure densities of aqueous TMAO solutions calculated with the V1 force field do not match experimental results,¹³⁴ as can easily be seen in Figure 9.3. Since the density is a property of certain interest, when it comes to analyzing high pressure environments, further force field optimization is required.¹² The novel optimization approach used the ambient pressure density as a function of concentration and the activity coefficient derivative y_{TT} (see Figure 9.4) as optimization targets.¹² The resulting force field is named V3 from here on. Its performance on the observables improved significantly compared to the V2 force field (see Figures 9.3 and 9.4).

9. Results: Trimethylamine-N-oxide

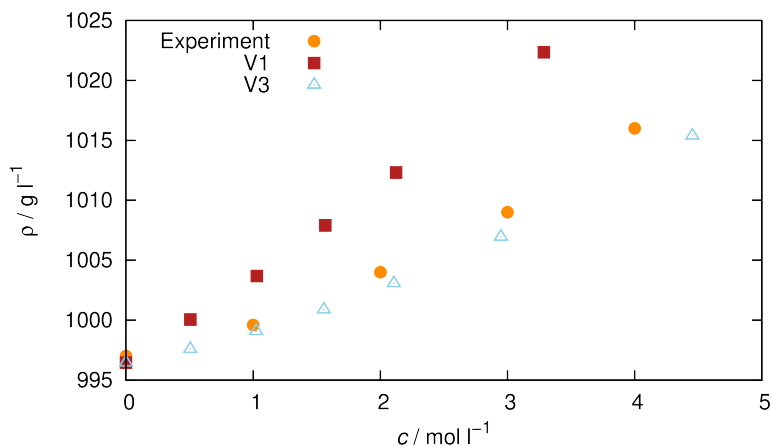


Figure 9.3.: Density of aqueous TMAO solutions as a function of the molar TMAO concentration obtained with the V1 and the novel V3 force field in comparison to experimental data.¹³⁴

When it comes to simulations at high pressure conditions applying the V3 force field, it can be seen that there are deficiencies in observables, which are heavily depending on electrostatic solute properties. This can clearly be seen in the probabilities of certain numbers of H-bonds accepted by TMAO (see Figure 9.5), which are not accurately represented. In order to obtain the correct pressure response for electrostatically dominated observables the charge scaling scheme described in Section 7.1 was applied. This approach was performed with both sets of solvent susceptibilities (with MD based bridge function contributions and HNC based ones). It is clearly seen, that the HNC-based solvent susceptibility-derived charges do improve the hydrogen statistics in comparison with the non-modified ambient pressure force field. The best match between force field and high pressure *aiMD* is achieved with the charge scaling based on MD simulation derived solvent susceptibilities, though.

Intramolecularly the force field is partially constrained, since the C-H distances along the covalent bonds are fixed. The geometry and the remaining intramolecular potential parameters are taken directly from the V1 force field omitting the 1-3 Urey-Bradley potential.¹²

Furthermore it can be clearly seen, that the hydrogen bonds' statistical response to pressure is reproduced by charge scaled V3 force field (V3-HP) dramatically better than by V3 alone. It has to be noted, that the effect of charge scaling is too small when the charge scaling approach is performed by using the HNC based solvent susceptibilities to compute the dipole moments and atomic charges, whereas use of the susceptibilities including the simulation derived bridge functions leads to a great improvement with respect to the *aiMD* results. The overall pressure response of the hydration pattern

9.2. Development of a force field for TMAO in aqueous high pressure environments

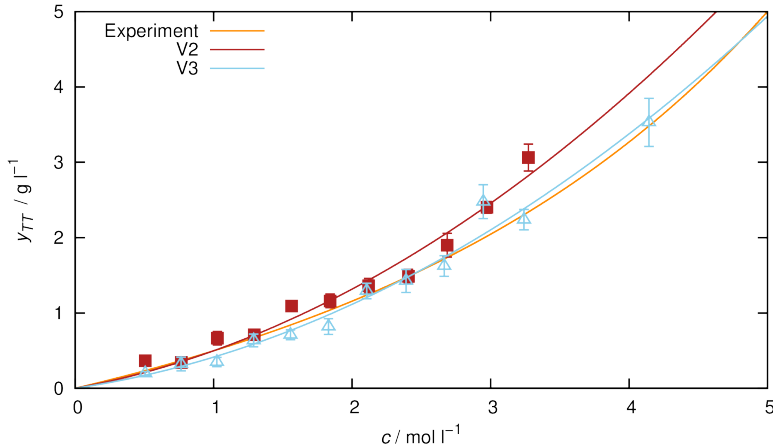


Figure 9.4.: The activity coefficient derivative y_{TT} as a function of concentration. The experimental reference was calculated from osmometry results.¹³⁵

can be seen in Figure 9.7. There the solvation pattern is split up in a hydrophilic and a hydrophobic region utilizing a simple geometric criterion: The hydrophilic region is closer than 3.25 \AA to the TMAO oxygen and closer than 4.5 \AA to at least one TMAO carbon atom, while the hydrophobic region is closer than 4.5 \AA to at least one of the carbon atoms, but farther away than 3.25 \AA from the oxygen atom.

In order to further investigate the performance of the novel force field, ffMD and *ai*MD result-based solvation structures are compared. The radial distribution functions $g(r)$ (see Figure 9.6) of the water sites around the oxygen atom of TMAO gained by ffMD simulations agree outstandingly well with the *ai*MD results. The differences between EC-RISM and the simulation methods are explained by the different water models applied (modified SPC/E^{5,107,108} in the EC-RISM case, TIP4P/2005¹¹⁹ in the MD simulation), while the Lennard-Jones parameters utilized for TMAO were the same. Comparing Figures 9.7b and 9.7c gives a qualitative impression of the structural similarities of the solvation patterns. *NB*: The difference in smoothness between both methods results from the far better statistics in the ffMD case, due to the immense computational cost of long trajectories and/or large systems for *ai*MD simulations.

As mentioned before, the density of the solution is an important observable in high pressure environments, since it is directly correlated to compressibilities and partial molar volumes. In Figure 9.8 the densities of water and aqueous TMAO solutions are compared. Experimental results were available from ambient pressure up to 700 bar. A second order polynomial fit was performed to extrapolate up to 10 kbar. The V3-HP(10 kbar) force field yields a deviation as small as 0.005 g cm^{-3} (0.4%), which is in the range of the accuracy of TIP4P/2005¹¹⁹ water deviating by 0.003 g cm^{-3} (0.25%).

9. Results: Trimethylamine-N-oxide

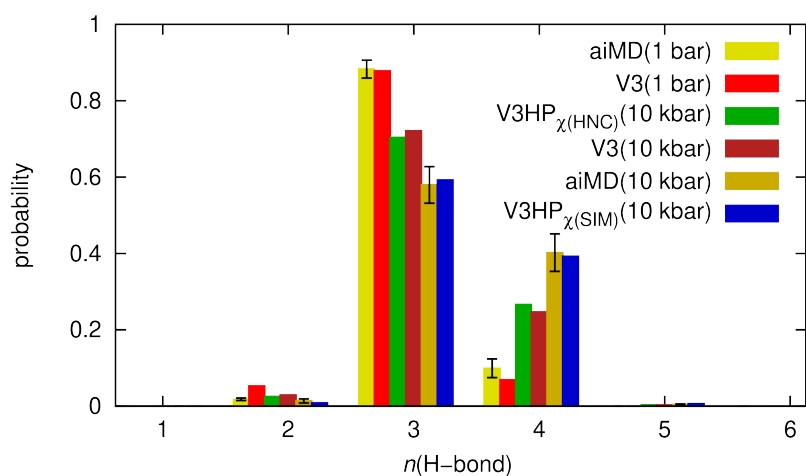


Figure 9.5.: Histogram of the probabilities to find a certain number of hydrogen bonds accepted by TMAO for the V3 and the V3-HP force field at 1 bar and at 10 bar in comparison to *aiMD* results.¹²

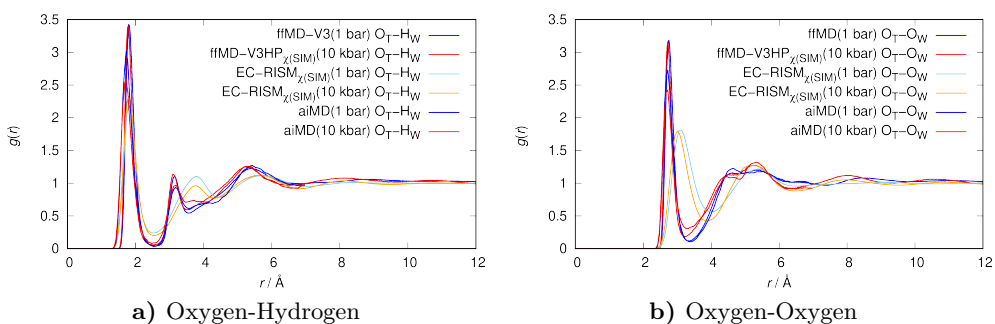


Figure 9.6.: Radial distribution functions of water hydrogen (left) and water oxygen (right) around TMAO oxygen with the different methods. Deviations between EC-RISM and the other methods can be explained by the different water models.

9.2. Development of a force field for TMAO in aqueous high pressure environments

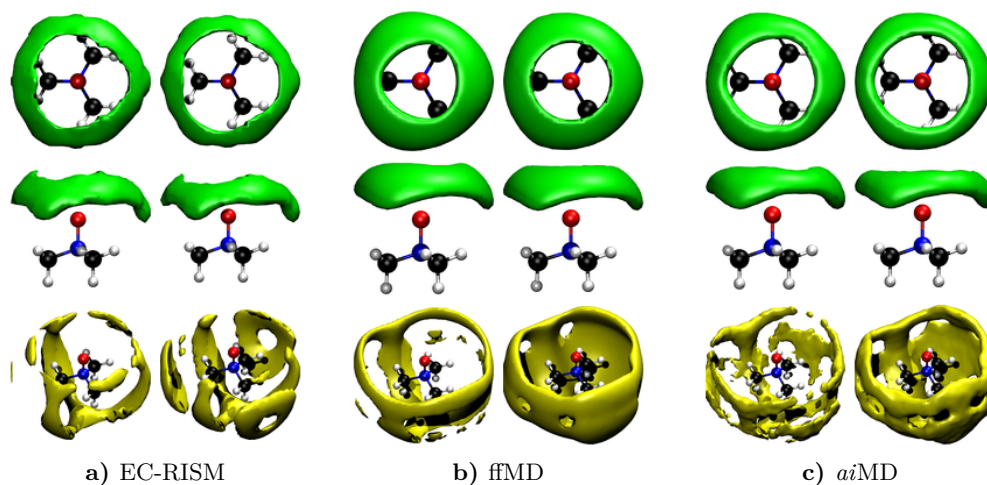


Figure 9.7.: Three dimensional structure of TMAO and the spatial distribution functions of water oxygen as isosurfaces (isovalues 0.0648 \AA^{-3} (1 bar) and 0.0800 \AA^{-3} (10 kbar) for the dynamics, which is twice the bulk density and 2 in terms of the g function for EC-RISM). The left column in every panel represents the 1 bar distribution, while the right columns show 10 kbar results. Green isosurfaces represent hydrophilic and yellow ones hydrophobic solvation.

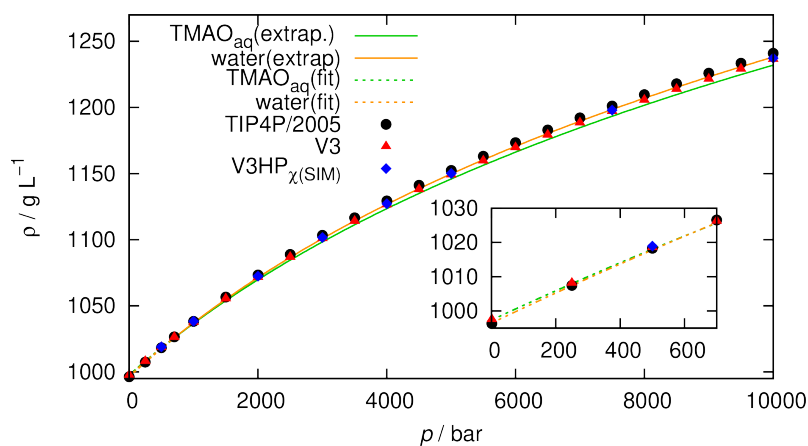


Figure 9.8.: Density of water and of aqueous 0.5 mmol cm^{-3} TMAO solution. Experimental data is shown in comparison to data from ffMD.¹²

9.3. Vibrational spectroscopy

This section presents the results of a combined experimental, *ai*MD and EC-RISM approach to elucidate the origin of pressure-dependent IR band shifts observed in TMAO.¹⁴

The theory of vibrational spectroscopy at high pressure conditions is interesting, because Fourier transform infrared spectroscopy is one of the spectroscopic techniques available at pressures up to 10 kbar and even higher. Since structural changes and changes to the solvation patterns go along with variations in vibrational properties of molecules, IR spectroscopy at high pressure is a powerful tool to gain insight into pressure-dependent intramolecular and intermolecular effects. As an experimental finding, spectra of 0.5 mmol cm^{-3} TMAO in aqueous solution were measured by Dr. Christopher Rosin (Physikalische Chemie 1, Prof. Dr. Roland Winter, Technische Universität Dortmund). The relevant peaks, background corrected and isolated from non-TMAO peaks can be seen in Figure 9.9. All four shifts show a slight but significant blueshift upon pressurization, which contradicts the simple picture of the vibrational Stark effect, that would suggest a red shift due to the higher dielectric constant of water at high pressures (see Section 3.3).

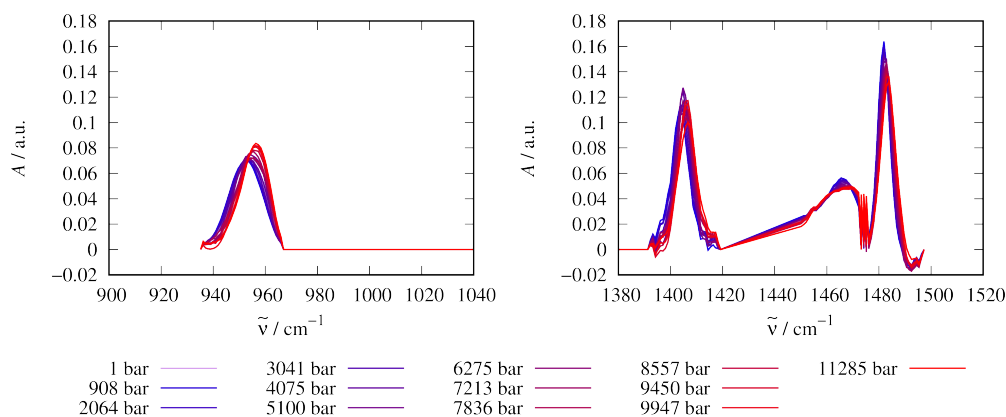


Figure 9.9.: Experimental peaks of the modes calculated from FTIR measurement. The peaks were background corrected and isolated from non-relevant peaks. The measurements were performed by Dr. Christopher Rosin.¹⁴

The complete set of vibrational frequencies and intensities of TMAO obtained from a B3LYP/6-311+G(d,p) calculation is shown in Table 9.2. In order to obtain the correct modes, the frequencies and intensities were considered. For every frequency modes with a high intensity was chosen, resulting in Mode 10 for high frequency methyl deformation (CH_3 -def. high), mode 11 and 12 as degenerate modes for the medium frequency methyl deformation (CH_3 -def. middle), mode 17 and 18 for the low frequency methyl deformation (CH_3 -def low) and last but not least mode 25 for the nitrogen-oxygen

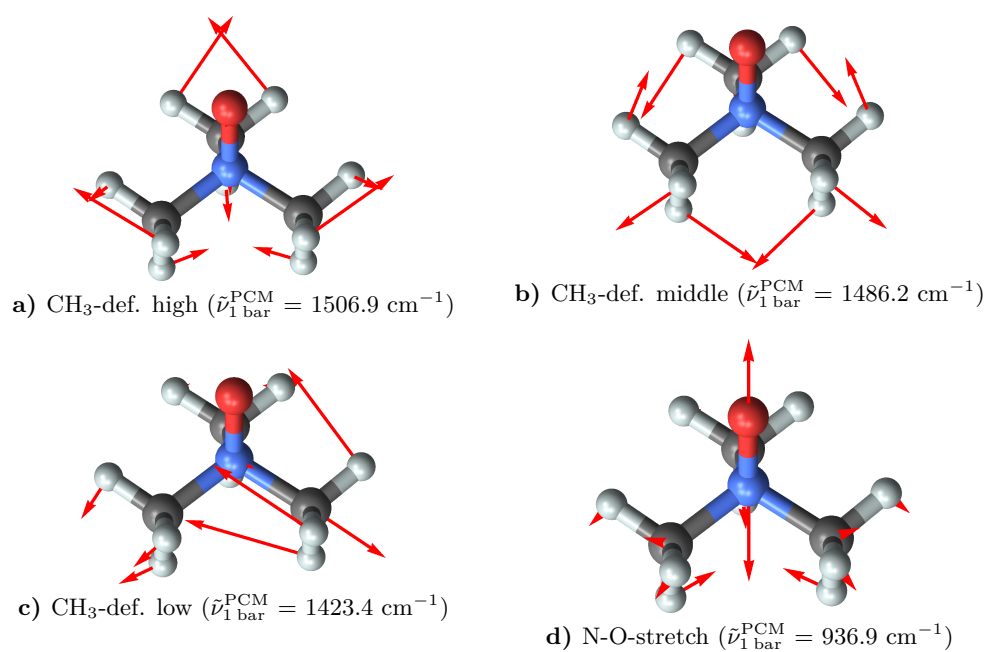


Figure 9.10.: Representative normal modes of TMAO, the red arrows depict the Cartesian atomic displacement upon unit distortion of the normal mode.

9. Results: Trimethylamine-N-oxide

stretch (NO-stretch). Degenerate modes were considered by averaging. The normal mode vectors obtained from the same calculation for every relevant type of mode are shown in Figure 9.10.

In order to elucidate the origin of those shifts, *ai*MD simulations and EC-RISM calculations were performed. The *ai*MD method is able to predict accurate IR-spectra $\alpha(\tilde{\nu})n(\tilde{\nu})$ from trajectories by calculating the Fourier transform of the dipole auto-correlation function

$$\alpha(\tilde{\nu})n(\tilde{\nu}) = \frac{2\pi^2 c \tilde{\nu}^2}{3\varepsilon_0 V k_B T} \int_{-\infty}^{\infty} dt \langle \mathbf{M}(0)\mathbf{M}(t) \rangle \exp(-2\pi i c \tilde{\nu} t), \quad (9.1)$$

where \mathbf{M} is the dipole moment, V is the sample volume, T is the temperature, c is the speed of light in vacuum and ε_0 is the electric permittivity of the vacuum. In contrast, the EC-RISM method lacks for an analytical second derivative of the free energy in solvation. Thus it is not possible to directly obtain vibrational information. The methodology applied to calculate pressure-dependent vibrational information is outlined in Section 3.5. Due to the explicit solvation picture the *ai*MD methodology provides, it is possible to examine solvation structure-dependent properties, in this case spectroscopic information. In contrast, the EC-RISM approach indeed applies approximations to the solvation structure and it neglects the solute-solvate electron transfer, but is able to split energetic contributions into an electronic energy term and a solvation free energy term. The complementary advantages make *ai*MD and EC-RISM the ideal combination of methods to elucidate complex vibrational problems. Since there were clear signs, that the number of hydrogen bonds accepted by TMAO rises from three to four upon compression to 10 kbar¹², it was obvious to investigate this phenomenon by spectroscopy.

Firsthand EC-RISM overestimates the pressure effect on the vibrational spectrum of TMAO, which is mainly founded in the fact that for every distorted structure the solvation pattern in thermodynamic equilibrium is calculated. Due to the fast vibration it seems plausible, that the solvation structure is not able to relax in this timescale. This may lead to an overpronunciation of solvation effects. Nonetheless it is easy to separately observe the pressure effect on frequencies calculated by the full Gibbs energy in solution compared to the pure intramolecular contribution from pressure-dependent polarization. EC-RISM calculations were performed on the well-established B3LYP/6-311+G(d,p) level without applying the exact electrostatic potential. The normal modes examined for this work were obtained applying the PCM as a solvation model on the same level of theory in QC. For every experimental band considered here representative normal modes are shown in Figure 9.10. Please note that the CH₃-def. middle and the CH₃-def. low modes are both comprised of two degenerate vibrational modes. Due to their similarity only one mode each is shown in Figure 9.10. All frequency calculations are based on averaging the force constants of normal modes were performed.

The EC-RISM force constants obtained with the method of finite differences are shown in Table 9.3, the force constants from fitted second order polynomials can be seen in

Table 9.2.: IR frequencies and intensities from B3LYP/6-311+G(d,p) with PCM ambient pressure water. The analyzed modes are marked with yellow highlighting.

Mode	$\bar{\nu}/\text{cm}^{-1}$	I/km mol $^{-1}$
1	3165.2	6.82
2	3165.0	6.82
3	3159.5	0.00
4	3148.2	18.63
5	3139.4	0.74
6	3139.2	0.75
7	3057.7	16.82
8	3047.1	8.87
9	3047.0	8.85
10	1506.9	25.57
11	1486.2	29.01
12	1486.2	28.97
13	1475.3	0.62
14	1475.2	0.61
15	1462.4	0.42
16	1458.8	0.00
17	1423.4	1.73
18	1423.3	1.71
19	1279.2	0.39
20	1279.2	0.39
21	1241.1	27.50
22	1130.8	1.59
23	1130.6	1.60
24	1067.0	0.00
25	936.9	40.77
26	930.4	3.75
27	930.2	3.74
28	755.6	6.65
29	493.7	18.41
30	493.4	18.32
31	454.8	15.65
32	372.7	11.41
33	371.7	11.50
34	295.4	0.11
35	295.0	0.11
36	223.9	0.00

9. Results: Trimethylamine-N-oxide

Table 9.5. When comparing the resulting force constants of both evaluation methods, it is seen, that the finite difference based force constants tend to show non-monotonous behavior with respect to pressure. Since sometimes EC-RISM calculations on distorted geometries obtain lower energies than the optimized central structure, it is plausible, that the finite differences approach fails, when the parabola is not centered within the differentiation interval. The fitting procedure in contrast is able to modify the linear component to recenter the parabola. Thus the fitting method is able to gain the curvature (and therefore the force constants) even if the minimum is not centered in the range of calculated distortions.

Table 9.3.: Raw force constants obtained from finite differences of the Gibbs energies in solution from EC-RISM calculations.

Mode	$k(1 \text{ bar}) / \text{kg s}^{-2}$	$k(100 \text{ bar}) / \text{kg s}^{-2}$	$k(5 \text{ kbar}) / \text{kg s}^{-2}$	$k(10 \text{ kbar}) / \text{kg s}^{-2}$
CH ₃ -def. high	141.036	141.072	141.674	141.315
CH ₃ -def. middle (a)	138.481	138.188	139.460	139.423
CH ₃ -def. middle (b)	156.428	158.162	169.455	171.835
CH ₃ -def. low (a)	144.075	144.090	146.291	146.364
CH ₃ -def. low (b)	155.179	156.099	164.977	165.749
N-O-stretch	293.557	294.563	305.467	305.715

Table 9.4.: Raw force constants obtained from finite differences of the Electronic energies in solution from EC-RISM calculations.

Mode	$k(1 \text{ bar}) / \text{kg s}^{-2}$	$k(100 \text{ bar}) / \text{kg s}^{-2}$	$k(5 \text{ kbar}) / \text{kg s}^{-2}$	$k(10 \text{ kbar}) / \text{kg s}^{-2}$
CH ₃ -def. high	139.89	139.448	139.21	139.003
CH ₃ -def. middle (a)	138.309	138.002	137.806	138.218
CH ₃ -def. middle (b)	149.013	148.42	149.472	150.6
CH ₃ -def. low (a)	133.095	132.631	131.786	132.304
CH ₃ -def. low (b)	125.97	124.958	120.264	121.167
N-O-stretch	214.927	214.3	210.315	211.08

Table 9.5.: Raw force constants obtained from polynomials fitted on Gibbs energies in solution from EC-RISM calculations.

Mode	$k(1 \text{ bar}) / \text{kg s}^{-2}$	$k(100 \text{ bar}) / \text{kg s}^{-2}$	$k(5 \text{ kbar}) / \text{kg s}^{-2}$	$k(10 \text{ kbar}) / \text{kg s}^{-2}$
CH ₃ -def. high	141.968	142.545	144.830	145.629
CH ₃ -def. middle (a)	148.629	149.540	155.490	156.309
CH ₃ -def. middle (b)	142.779	143.469	147.453	148.231
CH ₃ -def. low (a)	149.011	150.043	155.705	156.771
CH ₃ -def. low (b)	138.260	138.312	139.183	139.421
N-O-stretch	277.772	279.330	289.725	291.012

Following this argumentation the frequency shifts were calculated applying the fitting

Table 9.6.: Raw force constants obtained from polynomials fitted on electronic energies in solution from EC-RISM calculations.

Mode	$k(1 \text{ bar}) / \text{kg s}^{-2}$	$k(100 \text{ bar}) / \text{kg s}^{-2}$	$k(5 \text{ kbar}) / \text{kg s}^{-2}$	$k(10 \text{ kbar}) / \text{kg s}^{-2}$
CH ₃ -def. high	150.818	150.967	153.287	153.456
CH ₃ -def. middle (a)	137.931	137.781	136.626	137.026
CH ₃ -def. middle (b)	144.004	144.067	145.035	145.295
CH ₃ -def. low (a)	142.638	142.572	143.312	143.662
CH ₃ -def. low (b)	140.114	140.136	141.033	141.074
N-O-stretch	239.472	239.634	243.072	243.659

ansatz only. The shifted frequencies

$$\tilde{\nu}(p) = \tilde{\nu}_{1 \text{ bar}}^{\text{PCM}} \cdot \sqrt{\frac{f(p)}{f(1 \text{ bar})}} \quad (9.2)$$

calculated with EC-RISM are shown in Table 9.7, where $\tilde{\nu}^{\text{G}}$ denotes frequencies and shifts obtained from the Gibbs energy in solution and $\tilde{\nu}^{\text{E}}$ means the same quantities obtained from the electronic energy only. The frequencies and shifts calculated with 3D RISM on a fixed point charge force field are shown in Table 9.8. The fixed-charge force field was comprised of the Lennard-Jones parameters from the V3 force field and the charges were obtained from the converged EC-RISM calculation of the undistorted molecule geometry. Therefore, the effects of electronic re-polarization were neglected, while the solvent structure was still able to relax completely. This analysis allows to show, that molecular polarization has a tremendous effect on the pressure induced frequency shifts in TMAO, even if the fully relaxed solvent is used.

The full EC-RISM shifts are highly overestimated. In stark contrast, the full equilibrium solvation picture without repolarizing the solute leads to much smaller shifts, indicating that the electrostatic polarization plays a major role for pressure-dependent band shifts. In order to further elucidate these effects, it is necessary to develop a novel theory allowing for calculations of the non-relaxed solvation environment.

aiMD results have shown, that the average number of H-bonds to TMAO rises with pressure,¹² which suggests an effect on vibrational properties as well. The IR spectra of three- and fourfold coordinated TMAO were calculated separately from the trajectories. The results show, that the fourfold coordinate species shows a redshift of approximately 10 cm^{-1} in comparison to the threefold coordinate species. On the other hand the threefold coordinated species shows a similar blueshift upon compression from 1 bar to 10 kbar, which basically means, that in the 10 kbar spectrum the fourfold coordinated structure takes the place of the threefold hydrogen-bonded structure at 1 bar. This finding correlates very well with the observed normalized skewnesses of the N-O-peak in the experimental spectra (changes by -0.107 in *aiMD* and by -0.187 in experiment).¹⁴ Most interestingly, the skewness of the pure three- and fourfold peaks remains nearly unchanged upon compression.¹⁴ This finding exper-

9. Results: Trimethylamine-N-oxide

Table 9.7.: EC-RISM calculated frequencies and frequency shifts from the total Gibbs energy in solution and from the intramolecular part at different pressures in comparison to the PCM values.¹⁴

p/bar	Mode	rel. Intensity(PCM)	$\tilde{\nu}_{1\text{bar}}^{\text{PCM}}/\text{cm}^{-1}$	$\tilde{\nu}^{\text{G}}(p)/\text{cm}^{-1}$	$\Delta_p\tilde{\nu}^{\text{G}}/\text{cm}^{-1}$	$\tilde{\nu}^{\text{E}}(p)/\text{cm}^{-1}$	$\Delta_p\tilde{\nu}^{\text{E}}/\text{cm}^{-1}$
100	N-O-stretch	1.00	936.9	939.5	2.6	937.2	0.3
	CH ₃ -def. low	0.04	1423.4	1426.0	2.6	1423.3	-0.1
	CH ₃ -def. middle	0.71	1486.2	1490.2	4.0	1485.9	-0.3
	CH ₃ -def. high	0.63	1506.9	1509.9	3.0	1507.6	0.7
5000	N-O-stretch	1.00	936.9	956.8	19.9	943.9	7.0
	CH ₃ -def. low	0.04	1423.4	1441.6	18.2	1427.4	4.0
	CH ₃ -def. middle	0.71	1486.2	1515.2	29.0	1485.3	-0.9
	CH ₃ -def. high	0.63	1506.9	1522.0	15.1	1519.2	12.3
10000	N-O-stretch	1.00	936.9	959.0	22.1	945.0	8.1
	CH ₃ -def. low	0.04	1423.4	1444.7	21.3	1428.4	5.0
	CH ₃ -def. middle	0.71	1486.2	1519.2	33.0	1487.1	0.9
	CH ₃ -def. high	0.63	1506.9	1526.2	19.3	1520.0	13.1

Table 9.8.: 3D RISM calculated frequencies and frequency shifts on the distorted geometries with fixed charges from EC-RISM of the minimum energy geometry.¹⁴

p/bar	Mode	Intensity	$\tilde{\nu}_{1\text{bar}}^{\text{PCM}}/\text{cm}^{-1}$	$\tilde{\nu}^{\text{G}}(p)/\text{cm}^{-1}$	$\Delta_p\tilde{\nu}^{\text{G}}/\text{cm}^{-1}$
10000	N-O-stretch	1.00	936.9	938.2	2.3
	CH ₃ -def. low	0.04	1423.4	1424.9	1.5
	CH ₃ -def. middle	0.71	1486.2	1488.1	1.9
	CH ₃ -def. high	0.63	1506.9	1507.2	0.3

imentally supports the result, that the hydrogen bonding of water to TMAO increases upon compression.¹⁴

10. Results: Urea

10.1. Dipole moment

10.1.1. The dipole moment of urea as a function of pressure

In order to obtain the pressure dependent dipole moments of urea, EC-RISM calculations were performed for the available pressures (for computational details see Section 8.2 on page 74) were performed and the wave-function based dipole moment was extracted from the final EC-RISM iteration. Again solvent susceptibilities applying the HNC approximations were used as well as susceptibilities recognizing MD simulation based bridge functions. The resulting dipole moments can be seen in Table 10.1 and Figure 10.1. As Lennard-Jones parameters for urea, the newly parameterized urea-V3 force field was applied.

Table 10.1.: Dipole moment of urea as a function of pressure. Values in brackets are the differences to 1 bar.

p/bar	$\mu(\chi_{\text{SIM}})/\text{D}$	$\mu(\chi_{\text{HNC}})/\text{D}$	$ai\text{MD}$
1	6.6812 (0.0000)	7.0610 (0.0000)	7.3283 (0.0000)
100	6.7013 (0.0201)	7.0630 (0.0020)	–
500	6.8410 (0.1598)	7.0702 (0.0092)	–
1000	6.9241 (0.2429)	7.0785 (0.0175)	–
2000	6.9622 (0.2810)	7.0930 (0.0320)	–
3000	6.9994 (0.3182)	7.1053 (0.0443)	–
4000	6.9865 (0.3053)	7.1161 (0.0551)	–
5000	7.0839 (0.4027)	7.1256 (0.0646)	–
7500	7.0822 (0.4010)	7.1458 (0.0848)	–
10000	7.1030 (0.4218)	7.1621 (0.1011)	7.5521 (0.2238)

When comparing the obtained dipole moments with the *aiMD* reference values, it is seen that *aiMD* simulations gain stronger polarized urea molecules than EC-RISM with both types of solvent susceptibilities. As the dipole moment differences with respect to 1 bar per method show, the simulation based solvent susceptibilities lead to an overestimation of the pressure dependence of the dipole moment, whereas the HNC model underestimates it.

10. Results: Urea

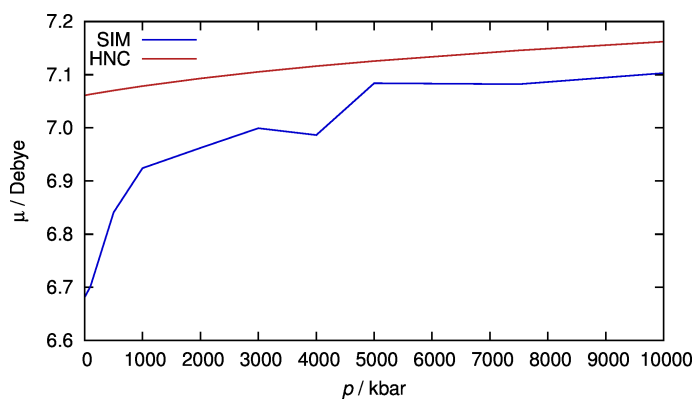


Figure 10.1.: Pressure-dependent dipole moment of urea

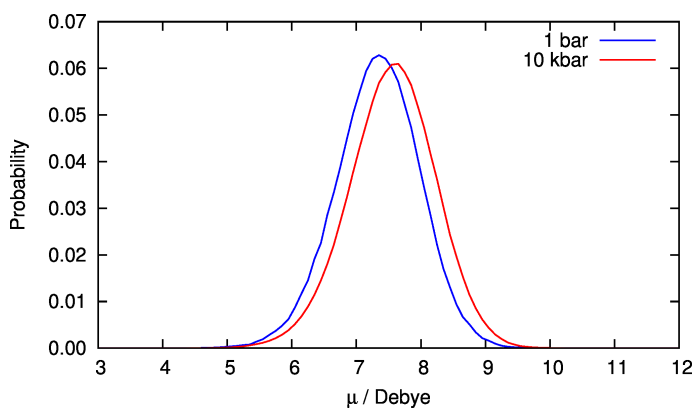


Figure 10.2.: Dipole moment histogram for 1 bar and 10 kbar from *aiMD*. Data by Jan Noetzel.

10.2. The influence of Lennard-Jones parameters on the dipole moment and its pressure-dependence

In order to investigate the influence of the Lennard-Jones parameters used for 3D RISM calculations on the pressure-dependent dipole moments obtained in EC-RISM calculations numerical derivatives of the dipole moment

$$\frac{\partial \mu}{\partial x} = \frac{\mu(x + \Delta x) - \mu(x - \Delta x)}{2\Delta x} \quad (10.1)$$

with respect to the Lennard-Jones parameters $x \in \{\sigma, \epsilon\}$ for each atom type were calculated. The same settings as utilized in the original urea V3 force field were used.

10.2. The influence of Lennard-Jones parameters on the dipole moment and its pressure-dependence

The resulting dipole moments are shown in Table 10.2, the dipole moment derivatives calculated from these results can be seen in Table 10.3.

Table 10.2.: Raw dipole moments from parameter variation at 1 bar and 10 kbar.

parameter	Δx	unit	$\mu^{1 \text{ bar}}/\text{D}$	$\mu^{10 \text{ kbar}}/\text{D}$
$\epsilon(\text{C})$	-0.1	zJ	6.6809	7.1031
$\epsilon(\text{C})$	+0.1	zJ	6.6814	7.1030
$\epsilon(\text{H})$	-0.1	zJ	6.7096	7.1389
$\epsilon(\text{H})$	+0.1	zJ	6.6714	7.0914
$\epsilon(\text{N})$	-0.1	zJ	6.6861	7.1090
$\epsilon(\text{N})$	+0.1	zJ	6.6765	7.0974
$\epsilon(\text{O})$	-0.1	zJ	6.7040	7.1319
$\epsilon(\text{O})$	+0.1	zJ	6.6610	7.0775
$\sigma(\text{C})$	-0.1	Å	6.6836	7.1060
$\sigma(\text{C})$	+0.1	Å	6.6780	7.0992
$\sigma(\text{H})$	-0.1	Å	6.6912	7.1148
$\sigma(\text{H})$	+0.1	Å	6.6701	7.0901
$\sigma(\text{N})$	-0.1	Å	6.6902	7.1127
$\sigma(\text{N})$	+0.1	Å	6.6656	7.0855
$\sigma(\text{O})$	-0.1	Å	6.8337	7.2921
$\sigma(\text{O})$	+0.1	Å	6.5450	6.9339

As it can easily be seen, the Lennard-Jones parameters on the urea oxygen atom have the largest influence on the calculated dipole moment, showing that allowing proximity of water to urea oxygen increases the dipole moment heavily. Based on the resulting dipole moment derivatives, two different approaches were attempted. The first approach was to construct a system of equations, that ensures that the resulting dipole moments remain unchanged, when up to four Lennard-Jones parameters are manually changed at a time.

As freely variable parameters the σ and ϵ parameters of oxygen and nitrogen were chosen and two models were built up, one for σ and one for ϵ . In order to predict the change in the dipole moments the function

$$\Delta\mu(\Delta x, \mathbf{M}_{\{\sigma, \epsilon\}}) = \sum_i \Delta x_i M_i \tag{10.2}$$

has been built up, where \mathbf{M} is the vector containing all dipole moment derivatives

10. Results: Urea

Table 10.3.: Raw dipole moment derivatives from parameter variation at 1 bar and 10 kbar.

parameter	unit	$\partial\mu^{1 \text{ bar}}/\partial x$	$\partial\mu^{10 \text{ kbar}}/\partial x$
$\epsilon(\text{C})$	D/zJ	0.0025	-0.0005
$\epsilon(\text{H})$	D/zJ	-0.1910	-0.2375
$\epsilon(\text{N})$	D/zJ	-0.0480	-0.0580
$\epsilon(\text{O})$	D/zJ	-0.2150	-0.2720
$\sigma(\text{C})$	D/Å	-0.0280	-0.0340
$\sigma(\text{H})$	D/Å	-0.1055	-0.1235
$\sigma(\text{N})$	D/Å	-0.1230	-0.1360
$\sigma(\text{O})$	D/Å	-1.4435	-1.7910

needed¹. In that fashion a system of equations

$$\begin{aligned}\Delta\mu(\Delta x, \mathbf{M}_\sigma(1\text{bar})) &= 0 \\ \Delta\mu(\Delta x, \mathbf{M}_\sigma(10\text{kbar})) &= 0\end{aligned}\quad (10.3)$$

was constructed and solved for $\Delta\epsilon_{\text{H}}$ and $\Delta\epsilon_{\text{C}}$ resulting in the equations

$$\Delta\epsilon_{\text{H}}(\Delta\epsilon_{\text{N}}, \Delta\epsilon_{\text{O}}) = -0.245194\Delta\epsilon_{\text{N}} - 1.14255\Delta\epsilon_{\text{O}} \quad (10.4)$$

and

$$\Delta\epsilon_{\text{C}}(\Delta\epsilon_{\text{N}}, \Delta\epsilon_{\text{O}}) = 0.467174\Delta\epsilon_{\text{N}} - 1.29053\Delta\epsilon_{\text{O}} \quad (10.5)$$

The same procedure has been performed for the σ parameters, which resulted in the equations

$$\Delta\sigma_{\text{H}}(\Delta\sigma_{\text{N}}, \Delta\sigma_{\text{O}}) = -2.89922\Delta\sigma_{\text{N}} + 8.28682\Delta\sigma_{\text{O}} \quad (10.6)$$

and

$$\Delta\epsilon_{\text{C}}(\Delta\sigma_{\text{N}}, \Delta\sigma_{\text{O}}) = 6.53101\Delta\sigma_{\text{N}} - 82.7771\Delta\sigma_{\text{O}}. \quad (10.7)$$

Using this approach, the parameters were varied manually in a fashion to ensure, that all obtained parameters were greater or equal zero. Ten different force field candidates were constructed that way. The parameters can be seen in the Appendix A.2.3 on page 161. The dipole moments resulting from these calculations can be seen in Table 10.4. Please note, that V3-Mod1 is a force field candidate, which was not created with the dipole moment constraints, but was created completely manually as a first guess. The modification V3-Mod3 is created to completely remove the Lennard-Jones Interaction from hydrogen, thus it is plausible, that the dipole moment cannot be kept near the original force field in this particular case. The other force field modifications show good agreements with the dipole moments obtained with urea V3.

¹Which means all σ or all ϵ derivatives.

10.2. The influence of Lennard-Jones parameters on the dipole moment and its pressure-dependence

As another approach the knowledge on the pressure dependence of the dipole moment derivatives was used, in order to meet the pressure difference of the dipole moment from aiMD simulations at 1 bar and at 10 kbar. In this case a minimization

$$\begin{aligned} \Delta x = \operatorname{argmin}(| & (\mu_{10 \text{ kbar}}^{\text{EC-RISM}} + \Delta\mu_{10 \text{ kbar}}(\Delta\mathbf{x})) \\ & - (\mu_{1 \text{ bar}}^{\text{EC-RISM}} + \Delta\mu_{1 \text{ bar}}(\Delta\mathbf{x})) \\ & - (\mu_{10 \text{ kbar}}^{\text{aiMD}} - \mu_{1 \text{ bar}}^{\text{aiMD}})|) \end{aligned} \quad (10.8)$$

was performed. Where $\Delta\mathbf{x}$ is the vector of the variation needed in the Lennard-Jones parameters to meet the aiMD based dipole moment difference, representing the degrees of freedom for the minimization. This ansatz leads to a residual of $3.44 \cdot 10^{-12}$ D. The resulting parameter changes are shown in Table 10.5.

The resulting dipole moments from EC-RISM calculations with the modified Lennard-Jones parameters are shown in Table 10.6. As it can be seen easily, the difference of the dipole moments improved, the deviation of the absolute dipole moments increased. In order to avoid this effect, it might be possible to augment the parameter optimization by introducing the deviation of the total dipole moment deviation in future work. Furthermore it might be helpful, to repeat the whole process of creating dipole moment derivatives in a parameter range near the destination force field. It is also imaginable to perform this kind of optimization with differential evolution or other optimization ansatzes.

In order to investigate the influence of the solvation patterns, that is exerted by the Lennard-Jones parameters, the spatial distribution pair functions of the solvent sites were integrated radially with the Lebedev-Laikov method,¹³⁶ to gain a logarithmic radial grid with 392 points ranging from $5.976 \cdot 10^{-3}$ Å to 14.879 Å centered on urea's oxygen. The radial distribution functions are shown in Appendix A.2.4 on page 165. In order to get a numerical impression of the impact on the solvation structure the coordination numbers were calculated for the first hydration shell, which was assumed to reach up to 2.4 Å for hydrogen and to 4.1 Å for oxygen. The coordination numbers obtained are shown in Table 10.7.

This method is not yet verified by ffMD simulations, which should be the next step in order to further investigate potential applications of EC-RISM for force field development purposes.

10. Results: Urea

Table 10.4.: Dipole moments calculated with the modified Lennard-Jones parameters and simulation based solvent susceptibilities.

Mod	1 bar	10 kbar
V3	6.6812	7.1030
Mod1	6.0652	6.3410
Mod2	6.7129	7.1438
Mod3	7.4500	8.0663
Mod4	6.8668	7.3373
Mod5	6.6861	7.1096
Mod6	6.6806	7.1019
Mod7	6.6906	7.1150
Mod8	6.6941	7.1178
Mod9	6.5179	6.8977
Mod10	6.6600	7.0757

Table 10.5.: Suggested changes in Lennard-Jones-Parameters, in order to achieve the same difference in dipole moments between 1 bar and 10 kbar.

parameter		unit
$\Delta\epsilon(\text{C})$	0.00468318	zJ
$\Delta\epsilon(\text{H})$	0.07258890	zJ
$\Delta\epsilon(\text{N})$	0.01561050	zJ
$\Delta\epsilon(\text{O})$	0.08898000	zJ
$\Delta\sigma(\text{C})$	0.00936632	Å
$\Delta\sigma(\text{H})$	0.02809900	Å
$\Delta\sigma(\text{N})$	0.02029370	Å
$\Delta\sigma(\text{O})$	0.54246600	Å

Table 10.6.: Resulting dipole moments with V3, the analytically modified V3^{an} and *aiMD*. *aiMD*-data by Jan Noetzel.

p/bar	$\mu(\text{V3})/\text{D}$	$\mu(\text{V3}^{\text{an}})/\text{D}$	$\mu(\text{aiMD})/\text{D}$
1	6.6812	6.0661	7.3283
10 k	7.1030	6.3410	7.5521
$\Delta\mu$	0.4218	0.2749	0.2239

10.2. The influence of Lennard-Jones parameters on the dipole moment and its pressure-dependence

Table 10.7.: Coordination numbers of hydrogen and oxygen around urea's oxygen atom at 1 bar and 10 kbar.

Force field	$N_{\text{H}}(1 \text{ bar})$	$N_{\text{H}}(10 \text{ kbar})$	$N_{\text{O}}(1 \text{ bar})$	$N_{\text{O}}(10 \text{ kbar})$
V3	2.55243	3.40952	8.47033	9.47623
V3 Mod 1	2.56230	3.41195	8.47033	9.47623
V3 Mod 2	2.29621	3.05504	8.1093	9.35302
V3 Mod 3	3.20340	4.06711	8.19724	9.12449
V3 Mod 4	2.76879	3.61217	8.32509	9.24185
V3 Mod 5	2.57205	3.42073	8.45584	9.45243
V3 Mod 6	2.55464	3.40598	8.49092	9.50844
V3 Mod 7	2.55243	3.40952	8.53176	9.57259
V3 Mod 8	2.53889	3.38601	8.56329	9.63258
V3 Mod 9	2.29621	3.05504	8.10930	9.35302
V3 Mod 10	2.48171	3.30508	8.49596	9.61812

11. Results: Performance of the new electrostatics model

In order to demonstrate the performance of the new electrostatics method alanine was used as a test case and treated as a cation, a zwitter-ion and an anion with the EC-RISM method, using various grid dimensions. Furthermore nitrogen (N_2) was treated, on the one hand centered in the RISM box, on the other hand off-center by 1 Å along the bond axis. The thermodynamic observables of all potential calculation methods converge for large grids, as one would expect (see figures 11.1 to 11.4).

In some cases however, small grid sizes show a mismatch of thermodynamic observables for small grid sizes, especially, when no dipole moment constraint is applied when fitting the point charges (compare figure 11.2, where the blue dashed line represents the case utilizing neither potential switching nor dipole moment constraint). This result leads to the conclusion that application of either of dipole moment constraint or the switching scheme is sufficient to sort out the cutoff bias, which is indicated by the fact, that all other lines nearly cannot be distinguished due to the similarity of the results. This also indicates, that the switching scheme addresses the correct source of error. Furthermore, in Table 11.1 shows, that the differences between the methods are comparably small on the largest grid tested, and that the greatest overall difference between the switched and the non-switched electrostatics model is the largest for the alanine zwitter-ionic species, when not constraining the dipole moment of the partial charges. Even in this case the pure application of the dipole moment constraint improves the results drastically.

The computational details for these calculations are given in Chapter 6 on page 63.

11. Results: Performance of the new electrostatics model

Table 11.1.: Differences in the resulting thermodynamic data between the method given in every line and the potential switching approach including the perturbation energy term, calculated on the largest grid. “SWP” denotes potential switching including the perturbation term, “SW” the switching approach neglecting the perturbation term and “plain” the switching-less approach. The column “dipole constraint” states whether or not the ESP fit in the QC calculation was constraint to match the wave-function based dipole moment. Ala+- denotes the alanine zwitter-ion, “(s)” denotes the positional shifting of the solute within the box.

Species	ESP mode	dipole constraint	$\Delta\mu_0^{\text{ex}}/\text{kcal mol}^{-1}$	$\Delta\mu^{\text{ex}}/\text{kcal mol}^{-1}$	$\Delta E_{\text{sol}}/\text{kcal mol}^{-1}$	$\Delta G_{\text{sol}}/\text{kcal mol}^{-1}$
Ala+-	SWP	yes	0.000000	0.000000	0.000000	0.000000
Ala+-	SWP	no	0.000245	0.001411	-0.000482	0.000929
Ala+-	SW	yes	0.000004	-0.000011	0.000000	-0.000011
Ala+-	SW	no	0.000109	0.000758	-0.000482	0.000276
Ala+-	Plain	yes	-0.000341	0.000451	-0.000220	0.000231
Ala+-	Plain	no	-0.080788	-0.513538	0.225197	-0.288341
Ala+	SWP	yes	0.000000	0.000000	0.000000	0.000000
Ala+	SWP	no	0.000083	0.000618	-0.000157	0.000461
Ala+	SW	yes	-0.000024	0.000046	-0.000004	0.000042
Ala+	SW	no	0.000014	0.000258	-0.000159	0.000099
Ala+	Plain	yes	0.000166	0.000532	-0.000001	0.000531
Ala+	Plain	no	-0.025143	-0.159655	0.074876	-0.084779
Ala-	SWP	yes	0.000000	0.000000	0.000000	0.000000
Ala-	SWP	no	0.000837	0.002062	-0.000786	0.001276
Ala-	SW	yes	0.000838	0.001834	-0.000747	0.001087
Ala-	SW	no	0.000722	0.001831	-0.000786	0.001046
Ala-	Plain	yes	0.000002	-0.000001	0.000000	-0.000001
Ala-	Plain	no	0.017642	-0.065131	0.023059	-0.042072
N ₂	SWP	yes	0.000000	0.000000	0.000000	0.000000
N ₂	SWP	no	0.000000	0.000000	-0.000000	0.000000
N ₂	SW	yes	-0.000051	-0.000058	0.000000	-0.000058
N ₂	SW	no	-0.000051	-0.000058	0.000000	-0.000058
N ₂	Plain	yes	-0.000021	-0.000029	-0.000001	-0.000029
N ₂	Plain	no	-0.000026	-0.000029	-0.000001	-0.000029
N ₂ (s)	SWP	yes	0.000000	0.000000	0.000000	0.000000
N ₂ (s)	SWP	no	-0.000000	0.000000	0.000000	0.000000
N ₂ (s)	SW	yes	-0.000051	-0.000058	0.000000	-0.000058
N ₂ (s)	SW	no	-0.000051	-0.000058	0.000000	-0.000058
N ₂ (s)	Plain	yes	-0.000027	-0.000030	0.000001	-0.000029
N ₂ (s)	Plain	no	-0.000027	-0.000031	0.000001	-0.000030

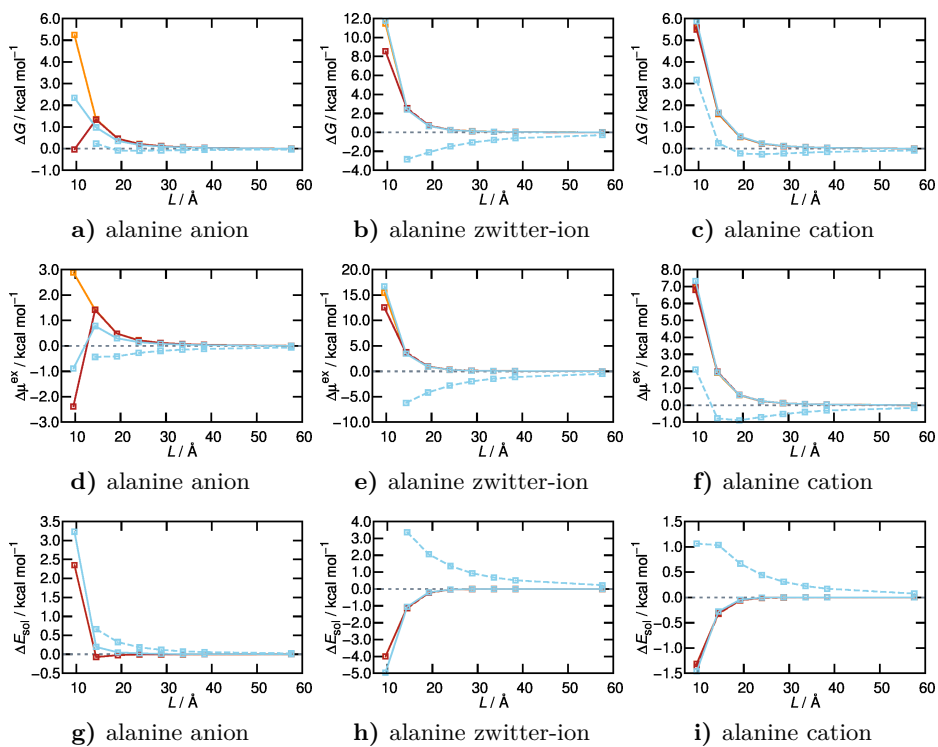


Figure 11.1.: Difference of the Gibbs energy (top row), excess chemical potential (middle row) and solute electronic energy (bottom row) in solution as a function of grid size with respect to the largest grid for the three different alanine species. Blue lines show data calculated without potential switching, red lines show data with potential switching and orange lines show data with potential switching and perturbation energy term. Solid lines represent data calculated with dipole moment constraint, dashed lines indicate non-constrained partial charges.

11. Results: Performance of the new electrostatics model

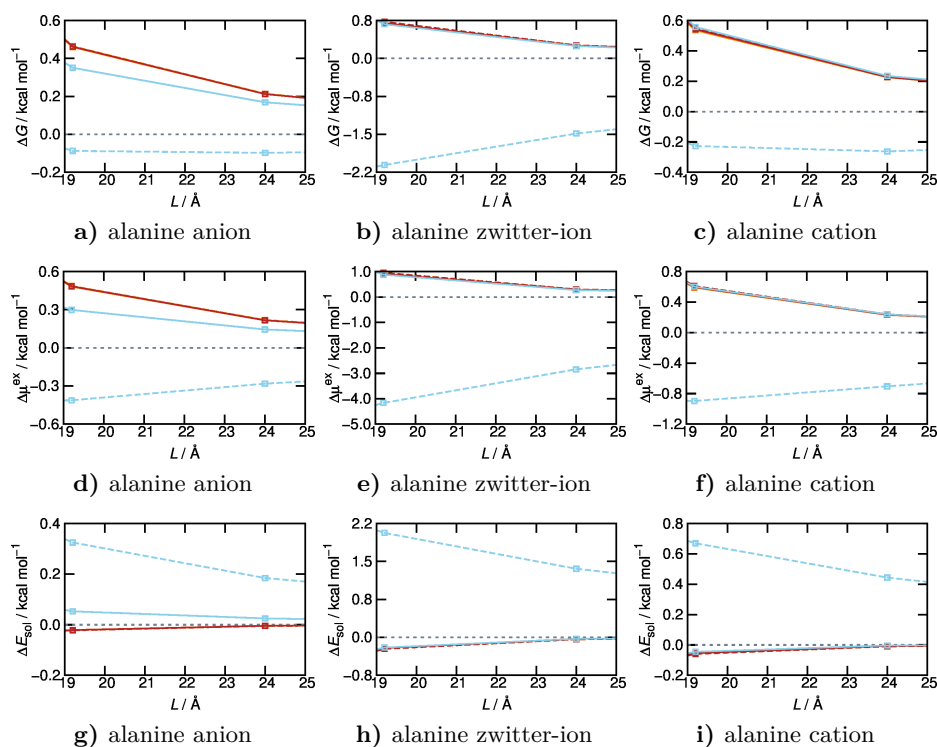


Figure 11.2: Detailed plot of the difference of the Gibbs energy (top row), excess chemical potential (middle row) and solute electronic energy (bottom row) in solution as a function of grid size with respect to the largest grid size for the three different alanine species. Blue lines show data calculated without potential switching, red lines show data with potential switching and orange lines show data with potential switching and perturbation energy term. Solid lines represent data calculated with dipole moment constraint, dashed lines indicate non-constrained partial charges.

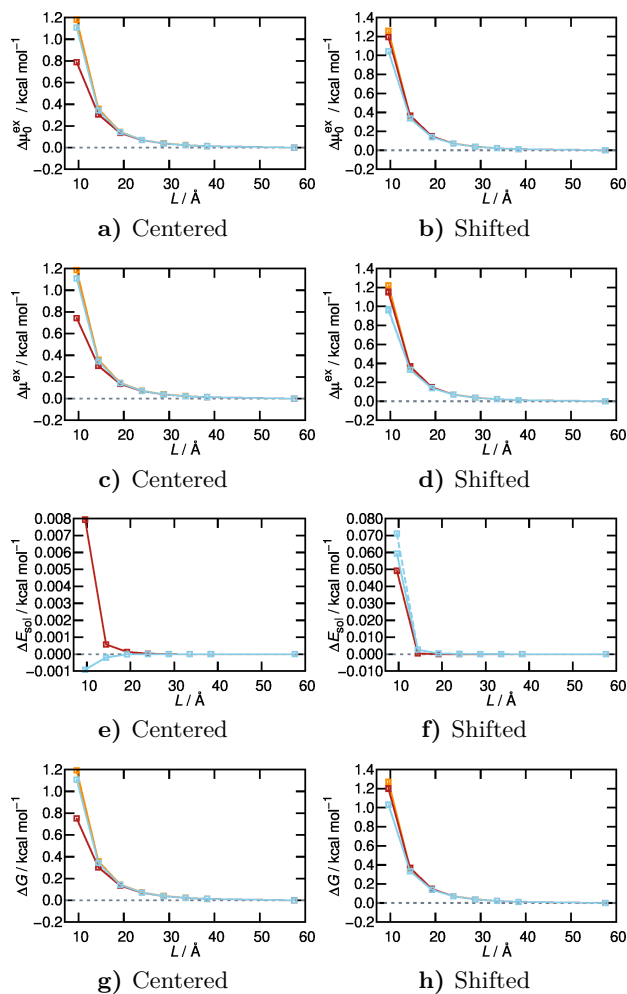


Figure 11.3.: Difference of the excess chemical potential in vacuo (first row) as well as in solution (second row), the electronic energy and the Gibbs energy in solution as a function of grid size with respect to the largest grid for molecular nitrogen centered in the box (left) and shifted by 1 Å along the bond axis (right). Blue lines show data calculated without potential switching, red lines show data with potential switching and orange lines show data with potential switching and perturbation energy term. Solid lines represent data calculated with dipole moment constraint, dashed lines indicate non-constrained partial charges.

11. Results: Performance of the new electrostatics model

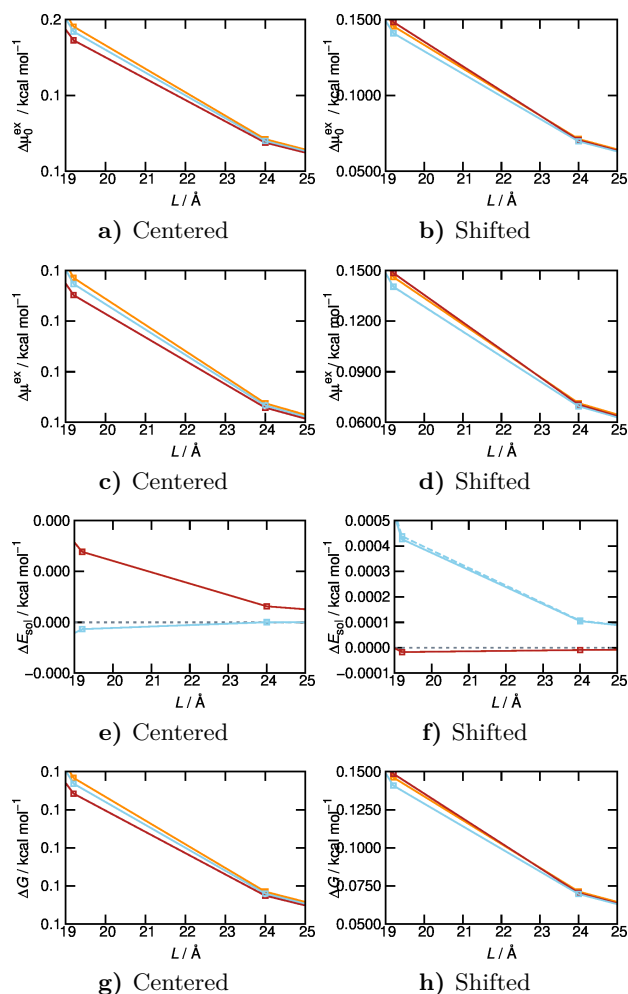


Figure 11.4.: Detailed view on the middle section of the differences of the excess chemical potential *in vacuo* (first row) as well as in solution (second row), the electronic energy and the Gibbs energy in solution as a function of grid size with respect to the largest grid for molecular nitrogen centered in the box (left) and shifted by 1 \AA along the bond axis (right). Blue lines show data calculated without potential switching, red lines show data with potential switching and orange lines show data with potential switching and perturbation energy term. Solid lines represent data calculated with dipole moment constraint, dashed lines indicate non-constrained partial charges.

12. Results: Hydronium and hydroxide

12.1. Force field

In this section the results of the parameterization process for the new hydronium and hydroxide force fields are presented. During the optimization process it became clear that the solvation pattern cannot be obtained with a simple force field model without implementation of additional dummy sites. Introduction of simple point charge dummy sites in order to represent the oxygen’s lone electron pairs brought a substantial improvement to solvation structure representation. The location of the dummy site with respect to the atoms can be seen in the Figures 12.1 and 12.2, the resulting non-bonding parameters are shown in Table 12.1. The Cartesian geometries of the ions are given in Tables 12.3 and 12.4.

The force field parameters resulting from the optimization process are shown in Table 12.1. The parameters of the reference force field by Bonthuis *et al.* are shown in Table 12.2.¹⁶ Highly remarkable is the lack of non-bonded interaction on the hydroxide hydrogen atom in the latter force field.

Table 12.1.: Final non-bonding force field parameters for hydronium and hydroxide for the force field candidate with dummy interaction sites. Here H^+ labels hydrogen atoms, O^+ the oxygen atom and Du^+ the dummy center of the hydronium ion. The sites of hydroxide are H^- , O^- and Du^- accordingly.

	H^+	O^+	Du^+	H^-	O^-	Du^-
σ/nm	0.0345	0.2669	0	0.0980	0.3528	0
$\epsilon\text{kJ mol}^{-1}$	0.0485	0.7590	0	0.0058	0.4588	0
q/e	0.6767	-1.2311	0.2010	0.1811	0.4900	-1.6711

The resulting RDF of water sites with respect to the ions’ hydrogen and oxygen atoms, obtained directly from the optimization process at 1 bar in comparison to the *aiMD* based RDF are shown in the Figures 12.3a and 12.3b. The reader has to keep in mind, that the RDF resulting from *aiMD* is noisy due to the comparably small system and the short simulation time. For hydronium, the most remarkable improvement with respect to the force field by Bonthuis *et al.*¹⁶ is the vanishing of the additional first solvation shell peak in the O^+-H -RDF.¹ For hydronium the obvious differences can

¹This notation denotes the ion’s atom with the ion charge, the second atom is part of the water.

Table 12.2.: Non-bonding force field parameters for hydronium and hydroxide by Bonthuis *et al.*¹⁶ H⁺ denotes hydrogen, O⁺ the oxygen of hydronium, while the hydroxide sites are marked H⁻ and O⁻.

	H ⁺	O ⁺	H ⁻	O ⁻
σ/nm	0	0.31	0	0.381
$\epsilon/\text{kJ mol}^{-1}$	0	0.8	0	0.05
q/e	0.8	-1.4	0	-1

Table 12.3.: Geometry of the hydronium ion with dummy site taken from the minimized simulation box.

	x/nm	y/nm	z/nm
O	0.808	0.798	0.852
H	0.894	0.812	0.897
H	0.790	0.704	0.873
H	0.747	0.843	0.913
Du	0.807	0.804	0.828

be seen in the hydrogen centered functions, which can be explained by the lack of Lennard-Jones parameters and of a charge on the hydroxide hydrogen.

Table 12.4.: Geometry of the hydroxide ion with dummy site taken from the minimized simulation box.

	x/nm	y/nm	z/nm
O	0.761	0.774	0.777
H	0.801	0.729	0.697
Du	0.757	0.778	0.785

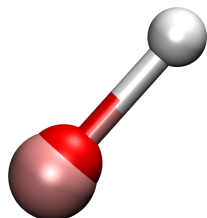


Figure 12.1.: Three-dimensional depiction of the hydroxide model geometry. Hydrogen atoms are shown in white, oxygen in red and dummies in light-red.

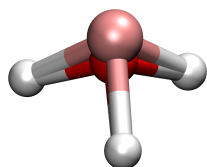


Figure 12.2.: Three-dimensional depiction of the hydronium model geometry. Hydrogen atoms are shown in white, oxygen in red and dummies in light-red.

12. Results: Hydronium and hydroxide

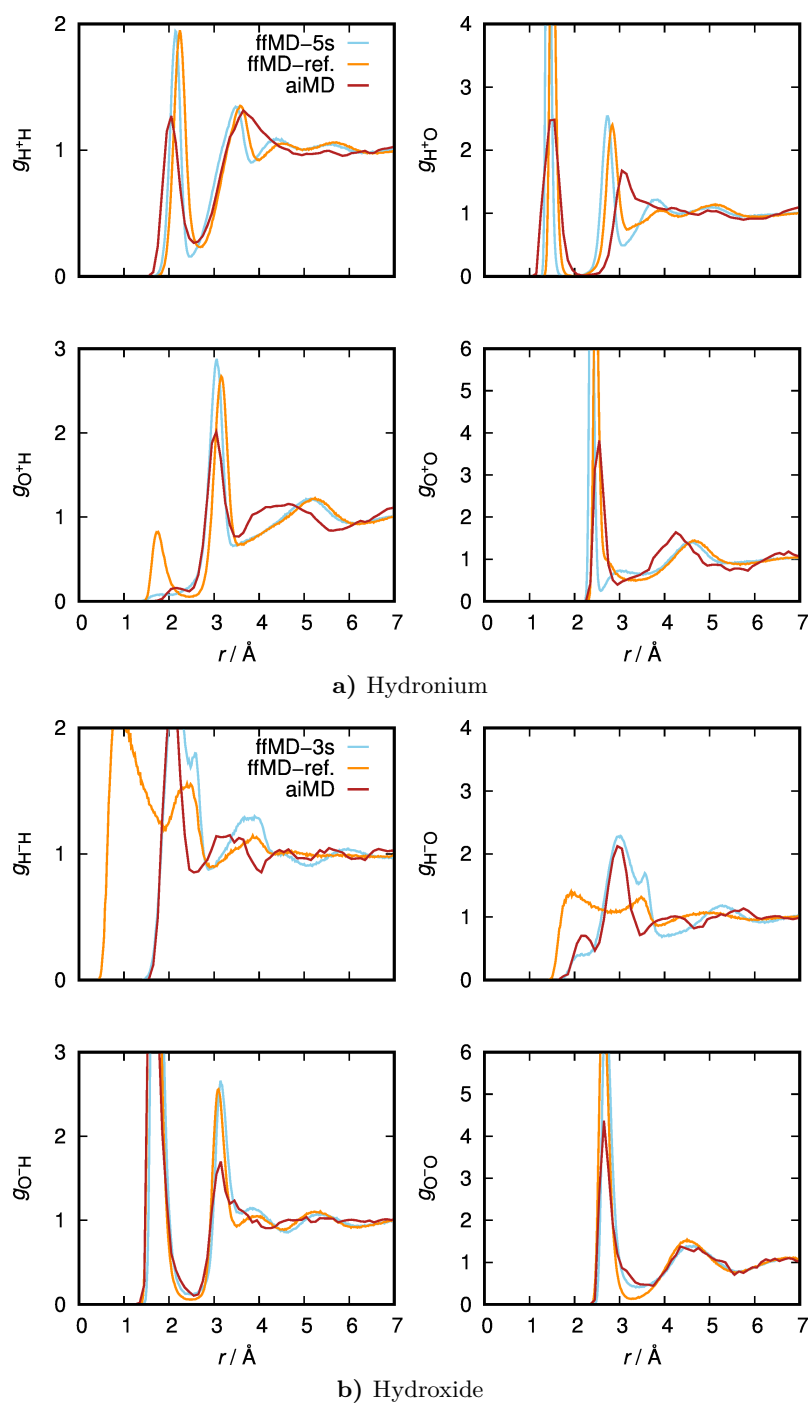


Figure 12.3.: Radial distribution functions of water around hydronium (top) and hydroxide (bottom) at 1 bar. The simulation was performed with the self-parameterized force field (blue lines), with the force field of Bonthuis *et al.* (orange lines). The reference stems from *aiMD* simulations (red lines). The panels show the hydrogen-hydrogen RDF (top left), the hydrogen-oxygen function (top right), the oxygen-hydrogen RDF (bottom left) and the oxygen-oxygen function (bottom right).

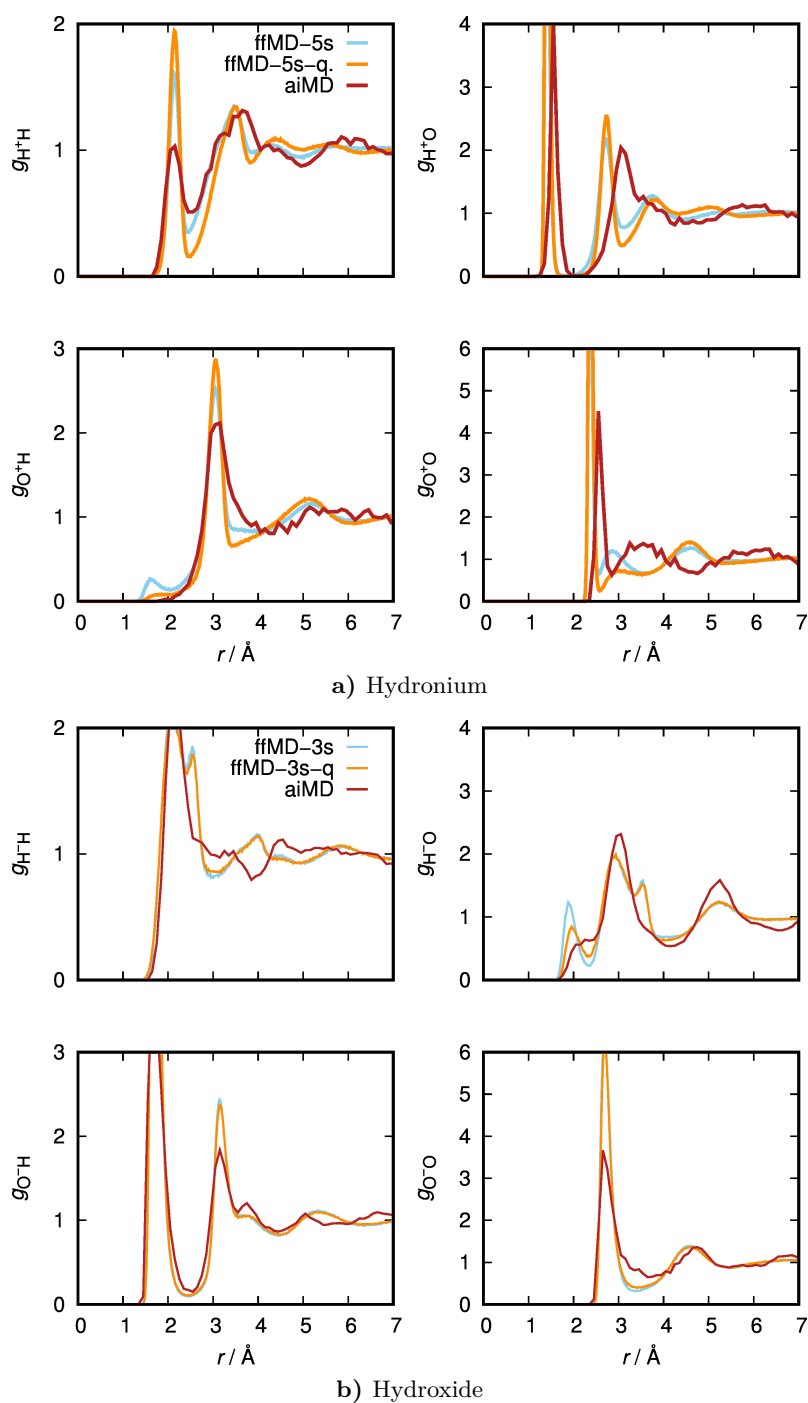


Figure 12.4.: Radial distribution functions of water around hydronium (top) and hydroxide (bottom) at 10 kbar. The simulation was performed with the self-parameterized force field (blue lines) and with the same force field with scaled high pressure charges (orange lines). The reference stems from *aiMD* simulations (red lines). The panels show the hydrogen-hydrogen RDF (top left), the hydrogen-oxygen function (top right), the oxygen-hydrogen RDF (bottom left) and the oxygen-oxygen function (bottom right).

12. Results: Hydronium and hydroxide

In order to test the force fields' structural response to high pressure, simulations were performed with the original optimized force field and with a modified candidate at 10 kbar. The modification was performed in the same fashion as for TMAO in order to obtain the correct dipole moment. The dipole moments were taken from EC-RISM calculations on the same level as for TMAO, with χ_{SIM} as solvent susceptibilities. The dipole moments obtained can be seen in Table 12.5. Again reference data were produced by Dr. Sho Imoto using *aiMD*. The high pressure RDF can be seen in Figures 12.4a and 12.4b. For both ions there are only small changes in solvation structure visible. The most remarkable changes can be seen in the direct vicinity of the molecule in the $\text{O}^+ - \text{H}$ and the $\text{H}^- - \text{O}$ functions.

Table 12.5.: Dipole moments of hydronium and hydroxide at 1 bar and 10 kbar.

p/bar	$\mu(\text{H}_3\text{O}^+)$	$\mu(\text{OH}^-)$
1	2.4226	2.9273
10000	2.5208	3.0873

Table 12.6.: High pressure charges for hydronium and hydroxide. O^+ , H^+ , Du^+ are the oxygen, hydrogen and dummy site of hydronium, while O^- , H^- and Du^- are the respective sites of hydroxide.

Site	q/e
O^+	-1.18573
H^+	0.683616
Du^+	0.134883
O^-	0.144415
H^-	0.556603
Du^-	-1.70102

In order to test the performance of the new force field, it was used alongside the Bonthuis *et al.*¹⁶ force field to calculate the pressure-dependent change of water autoprotolysis. In that way the thermodynamics of the simplest plausible autoprotolysis reaction were analyzed. The method and the results are shown in the following section.

13. Results: The ionic product of water under high pressure conditions

For the two different force field variants, which are the one by Bonthuis *et al.*,¹⁶ referred to as "ref", and the DEA-optimized one, referred to as 3s for hydroxide and 5s for hydronium, the pK_W -values were calculated using different levels of PMV correction. There are none (raw), not dependent on the pressure (Corr) and pressure-dependent pCorr). These values are presented in Tables 13.1 to 13.4. The same data is plotted in Figure 13.1.

Table 13.1.: Table of pK_W -values calculated with the 3s/5s force field on force field based geometries. "ref" denotes the equation of state based reference data, "Corr" marks pressure independently PMV-corrected data, "pCorr" pressure dependently corrected data and "raw" data without any correction at all. Δ denotes the difference between each pressure and 1 bar.

p/bar	pK_W^{exp}	ΔpK_W^{exp}	pK_W^{Corr}	$\Delta pK_W^{\text{Corr}}$	pK_W^{pCorr}	$\Delta pK_W^{\text{pCorr}}$	pK_W^{raw}	ΔpK_W^{raw}
1	13.9949	0.0000	13.9949	0.0000	13.9949	0.0000	13.9949	0.0000
100	13.9600	-0.0348	13.9316	-0.0633	13.9459	-0.0490	14.0009	0.0060
500	13.8254	-0.1694	13.6123	-0.3826	13.6669	-0.3280	14.0298	0.0350
1000	13.6694	-0.3255	13.3234	-0.6715	13.3997	-0.5952	14.0744	0.0795
2000	13.3900	-0.6048	12.9320	-1.0629	12.9864	-1.0085	14.1801	0.1852
3000	13.1448	-0.8500	12.6958	-1.2990	12.6729	-1.3220	14.2961	0.3012
4000	12.9258	-1.0691	12.5521	-1.4427	12.4178	-1.5770	14.4146	0.4197
5000	12.7275	-1.2673	12.4663	-1.5286	12.1983	-1.7966	14.5312	0.5364
7500	12.2998	-1.6951	12.3884	-1.6065	11.7278	-2.2671	14.8019	0.8071
10000	11.9418	-2.0531	12.4013	-1.5935	11.3012	-2.6937	15.0367	1.0418
RMS:	—	—	0.3340	—	0.4421	—	1.6147	—
MSE:	—	—	-0.1757	—	-0.3964	—	1.2757	—

It can immediately be seen that not correcting the chemical excess potential does not lead to correct thermodynamic pressure-dependence. Furthermore it can be seen that the original Bonthuis *et al.* force field performs nearly perfectly in calculations of the autoprotolysis equilibrium, which proves that the parameterization with the aim of exact thermodynamics was successful. On the other hand the self parameterized force field, which performs far better in reproducing solvation structure in terms of radial

13. Results: The ionic product of water under high pressure conditions

Table 13.2.: Table of pK_W -values calculated with the 3s/5s force field on quantum mechanically optimized geometries. "ref" denotes the equation of state based reference data, "Corr" marks pressure independently PMV-corrected data, "pCorr" pressure dependently corrected data and "raw" data without any correction at all. Δ denotes the difference between each pressure and 1 bar.

p/bar	pK_W^{ref}	ΔpK_W^{ref}	pK_W^{Corr}	$\Delta pK_W^{\text{Corr}}$	pK_W^{pCorr}	$\Delta pK_W^{\text{pCorr}}$	pK_W^{raw}	ΔpK_W^{raw}
1	13.9949	0.0000	13.9949	0.0000	13.9949	0.0000	13.9949	0.0000
100	13.9600	-0.0348	13.9336	-0.0613	13.9455	-0.0494	14.0023	0.0074
500	13.8254	-0.1694	13.6383	-0.3566	13.6821	-0.3128	14.0369	0.0420
1000	13.6694	-0.3255	13.3709	-0.6240	13.4271	-0.5677	14.0874	0.0926
2000	13.3900	-0.6048	13.0141	-0.9808	13.0331	-0.9618	14.2042	0.2094
3000	13.1448	-0.8500	12.8048	-1.1901	12.7339	-1.2610	14.3298	0.3349
4000	12.9258	-1.0691	12.6829	-1.3120	12.4900	-1.5049	14.4568	0.4619
5000	12.7275	-1.2673	12.6152	-1.3797	12.2791	-1.7157	14.5809	0.5860
7500	12.2998	-1.6951	12.5716	-1.4233	11.8235	-2.1714	14.8663	0.8714
10000	11.9418	-2.0531	12.6094	-1.3854	11.4059	-2.5889	15.1124	1.1176
RMS:	—	—	0.3288	—	0.3772	—	1.6569	—
MSE:	—	—	-0.0715	—	-0.3405	—	1.3103	—

distribution functions, performs still well, albeit the Bonthuis *et al.* force field delivers better results. These results underline the fact that force field development always means finding a compromise between different features, and that a good performance in one field does not necessarily mean supremacy for every observable with every method.

Table 13.3.: Table of pK_W -values calculated with the reference force field by Bonthuis *et al.* on force field based geometries. "exp" denotes the equation of state based reference data, "Corr" marks pressure independently PMV-corrected data, "pCorr" pressure dependently corrected data and "raw" data without any correction at all. Δ denotes the difference between each pressure and 1 bar.

p/bar	pK_W^{exp}	ΔpK_W^{exp}	pK_W^{Corr}	$\Delta pK_W^{\text{Corr}}$	pK_W^{pCorr}	$\Delta pK_W^{\text{pCorr}}$	pK_W^{raw}	ΔpK_W^{raw}
1	13.9949	0.0000	13.9949	0.0000	13.9949	0.0000	13.9949	0.0000
100	13.9600	-0.0348	13.9439	-0.0509	13.9301	-0.0648	14.0022	0.0073
500	13.8254	-0.1694	13.8689	-0.1260	13.7936	-0.2013	14.0366	0.0418
1000	13.6694	-0.3255	13.7908	-0.2041	13.6271	-0.3678	14.0897	0.0948
2000	13.3900	-0.6048	13.7275	-0.2674	13.3625	-0.6324	14.2159	0.2211
3000	13.1448	-0.8500	13.7382	-0.2567	13.1525	-0.8424	14.3548	0.3599
4000	12.9258	-1.0691	13.7898	-0.2051	12.9728	-1.0221	14.4975	0.5026
5000	12.7275	-1.2673	13.8638	-0.1310	12.8095	-1.1854	14.6385	0.6436
7500	12.2998	-1.6951	14.0893	0.0944	12.4293	-1.5656	14.9696	0.9748
10000	11.9418	-2.0531	14.3239	0.3290	12.0521	-1.9428	15.2633	1.2684
RMS:	—	—	1.1253	—	0.0686	—	1.7208	—
MSE:	—	—	0.8057	—	0.0272	—	1.3537	—

Table 13.4.: Table of pK_W -values calculated with the reference force field by Bonthuis *et al.* on quantumm chemically optimized geometries. "exp" denotes the equation of state based reference data, "Corr" marks pressure independently PMV-corrected data, "pCorr" pressure dependently corrected data and "unCorr" data without any correction at all. Δ denotes the difference between each pressure and 1 bar.

p/bar	pK_W^{exp}	ΔpK_W^{exp}	pK_W^{Corr}	$\Delta pK_W^{\text{Corr}}$	pK_W^{pCorr}	$\Delta pK_W^{\text{pCorr}}$	pK_W^{raw}	ΔpK_W^{raw}
1	13.9949	0.0000	13.9949	0.0000	13.9949	0.0000	13.9949	0.0000
100	13.9600	-0.0348	13.9447	-0.0502	13.9286	-0.0663	14.0026	0.0077
500	13.8254	-0.1694	13.8906	-0.1043	13.8048	-0.1901	14.0412	0.0463
1000	13.6694	-0.3255	13.8314	-0.1635	13.6481	-0.3468	14.0991	0.1042
2000	13.3900	-0.6048	13.7986	-0.1963	13.3987	-0.5962	14.2339	0.2390
3000	13.1448	-0.8500	13.8336	-0.1613	13.2005	-0.7944	14.3809	0.3860
4000	12.9258	-1.0691	13.9054	-0.0895	13.0302	-0.9647	14.5309	0.5360
5000	12.7275	-1.2673	13.9967	0.0018	12.8746	-1.1203	14.6789	0.6840
7500	12.2998	-1.6951	14.2567	0.2618	12.5091	-1.4858	15.0258	1.0309
10000	11.9418	-2.0531	14.5178	0.5230	12.1421	-1.8528	15.3329	1.3380
RMS:	—	—	1.2341	—	0.1162	—	1.7571	—
MSE:	—	—	0.8990	—	0.0725	—	1.3824	—

13. Results: The ionic product of water under high pressure conditions

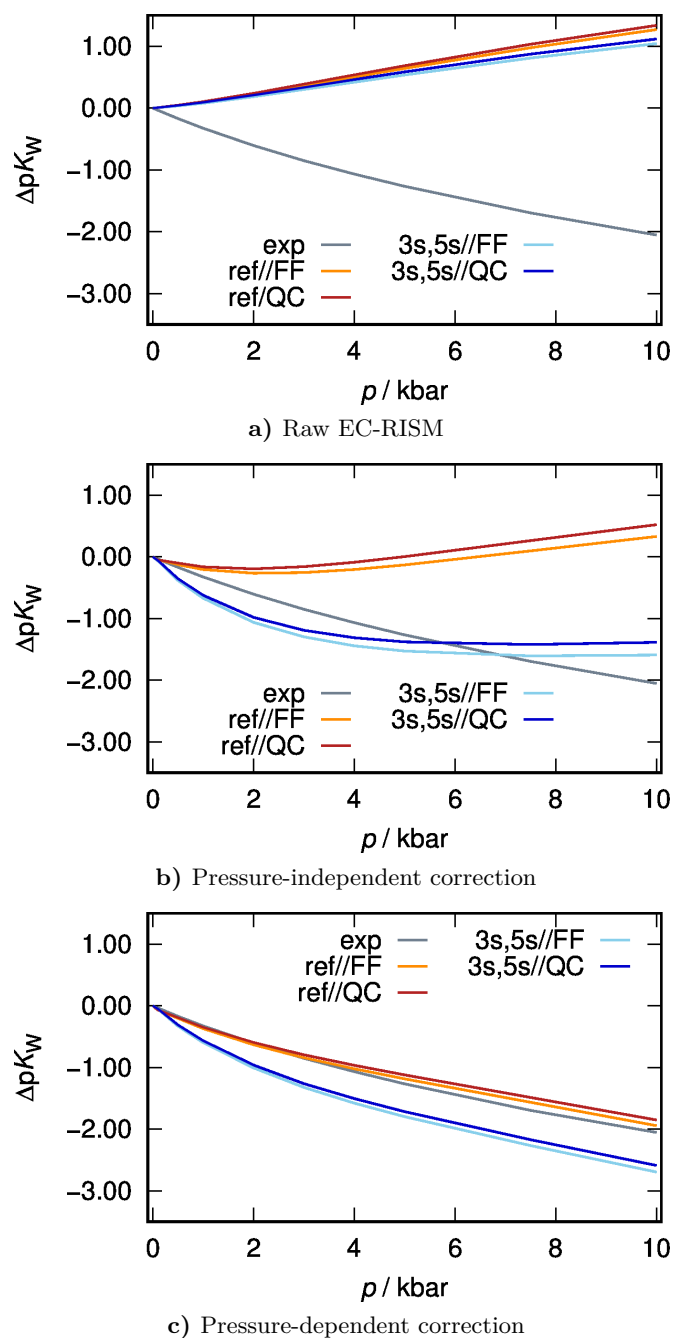


Figure 13.1.: Plots of calculated ΔpK_W for different force fields and molecule geometries without PMV-correction (top), with pressure independent PMV-correction (center) and with the pressure dependent PMV correction (bottom) in comparison to experimental values.

14. Results: hpCADD-Hamiltonian

Whereas the overall results for 3D RISM calculations on electrostatic potentials from vacuum hpCADD-calculations were satisfactory (compare ref. [17]), even though the novel ansatz for the treatment of the electrostatic potential was not available then. In case of fully converged EC-RISM calculations, there are some deficiencies regarding the resulting dipole moments and chemical excess potentials. Comparing mean signed errors (MSE) and root mean squared deviations (RMSD) for the dipole moment (see Figures 14.1 and 14.2) it can be observed, that high pressure (and along with it a more polarizing environment) leads to larger deviations than atmospheric conditions, which may suggest, that the impact of external polarization is overestimated by hpCADD. Remarkably, the group of nitriles shows that a massive underestimation of the dipole moment on the one hand leads to a good prediction of the excess chemical potential on the other hand. This discrepancy can only be explained by a deviation in the electrostatic potentials calculated with hpCADD or MP2 respectively. A more detailed look at the resulting excess chemical potential descriptors (see Figures 14.3 and 14.4) unveils, that the error for polarized calculations is much larger than the error obtained from non-polarized calculations, which has been published before.¹⁷ This polarization effect is not limited to electrostatic effects of the solvent environment, but may have also a drastic effect on intermolecular interaction due to mutual polarization.

14. Results: hpCADD-Hamiltonian

Table 14.1.: Root mean square deviation (RMSD) and mean signed error (MSE) between hpCADD and MP2 at 1 bar for every substance class. Data is shown for the excess chemical potential (μ^{ex}) and the total molecular dipole moment μ .

Class	RMSD(μ^{ex})/kcal mol ⁻¹	RMSD(μ)/D	MSE(μ^{ex})/kcal mol ⁻¹	MSE(μ)/D
Alkanes	2.390	0.376	-1.009	-0.017
Alcohols	5.401	1.155	5.349	-1.012
Amides	12.685	2.458	-3.874	1.079
Bromides	2.791	1.180	2.283	-1.019
Ketones & aldehydes	5.527	0.803	5.313	-0.717
Chlorides	2.493	0.642	1.941	-0.505
Carboxylic acids	8.344	1.016	8.264	0.820
Esters	9.525	4.317	-1.982	2.156
Ethers	4.658	1.190	4.481	-1.026
Fluorides	2.789	0.821	2.029	-0.455
Conjugated systems	20.973	3.031	-14.545	0.786
Nitriles	2.841	4.269	-0.155	-4.129
Sulfones	7.489	0.692	-4.729	-0.310
Thioethers	3.662	2.013	2.587	-1.441
Thiones	3.332	1.816	2.417	-0.988
Total	8.549	2.263	-7.35 · 10 ⁻⁵	-0.138

Table 14.2.: Root mean square deviation (RMSD) and mean signed error (MSE) between hpCADD and MP2 at 10 kbar for every substance class. Data is shown for the excess chemical potential (μ^{ex}) and the total molecular dipole moment μ .

Class	RMSD(μ^{ex})/kcal mol ⁻¹	RMSD(μ)/D	MSE(μ^{ex})/kcal mol ⁻¹	MSE(μ)/D
Alkanes	6.141	0.505	-0.627	0.096
Alcohols	6.486	1.216	6.337	-0.951
Amides	17.683	2.827	-5.318	1.239
Bromides	3.340	1.270	2.628	-1.067
Ketones & aldehydes	7.187	0.891	6.771	-0.751
Chlorides	3.124	0.690	2.294	-0.507
Carboxylic acids	10.679	1.104	10.593	0.920
Esters	15.906	5.420	-4.094	2.765
Ethers	17.873	1.385	10.850	-1.197
Fluorides	3.580	0.893	2.4615	-0.469
Conjugated systems	31.071	3.449	-21.353	0.614
Nitriles	4.411	4.300	-1.207	-4.125
Sulfones	10.653	0.841	-8.470	0.226
Thioethers	5.760	2.504	3.0471	-1.609
Thiones	2.866	2.107	2.625	-1.506
Total	13.288	2.680	-0.288	-0.045

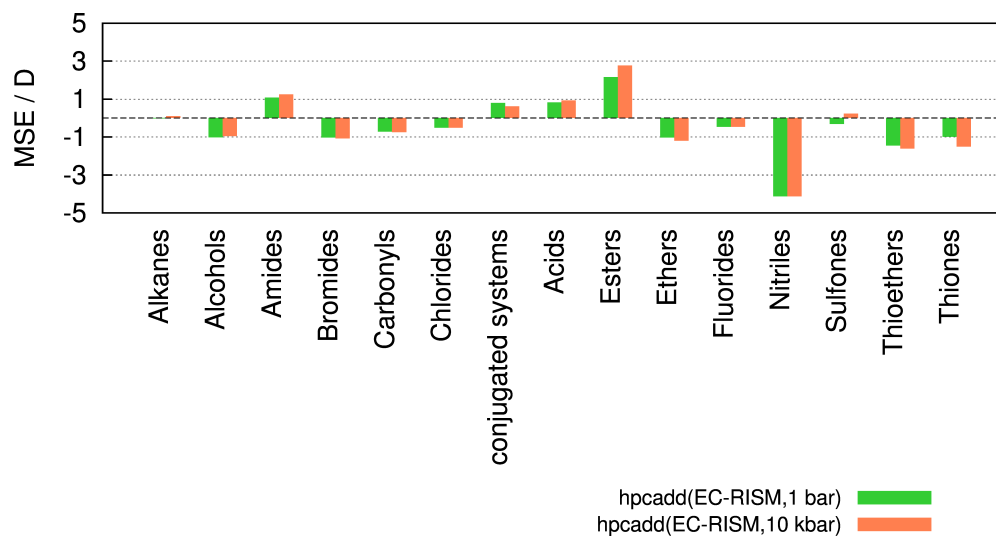


Figure 14.1.: Mean signed Errors (MSE) of the dipole moments calculated with EC-RISM using hpCADD with respect to the MP2 reference calculations.

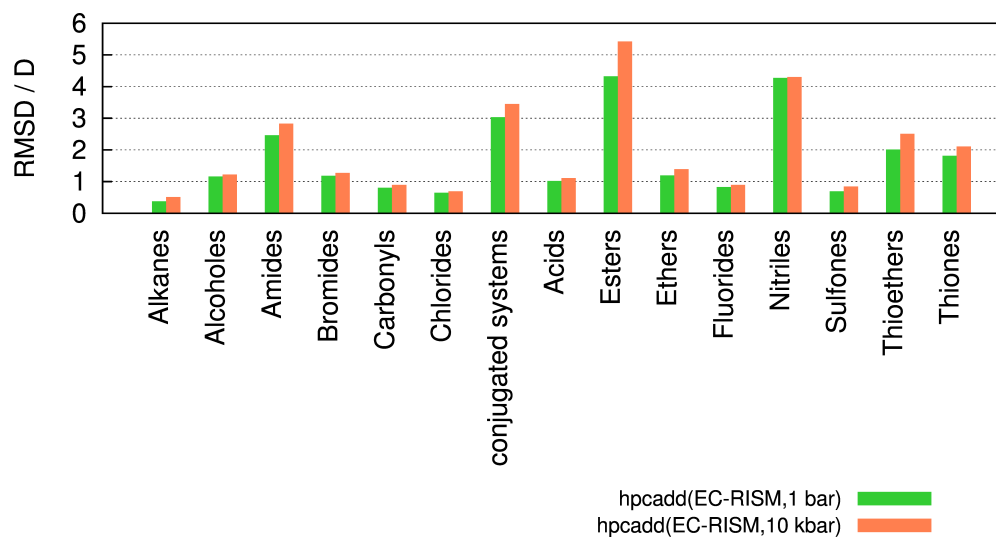


Figure 14.2.: Root mean square errors (RMSE) of the dipole moments calculated with EC-RISM using hpCADD with respect to the MP2 reference calculations.

14. Results: hpCADD-Hamiltonian

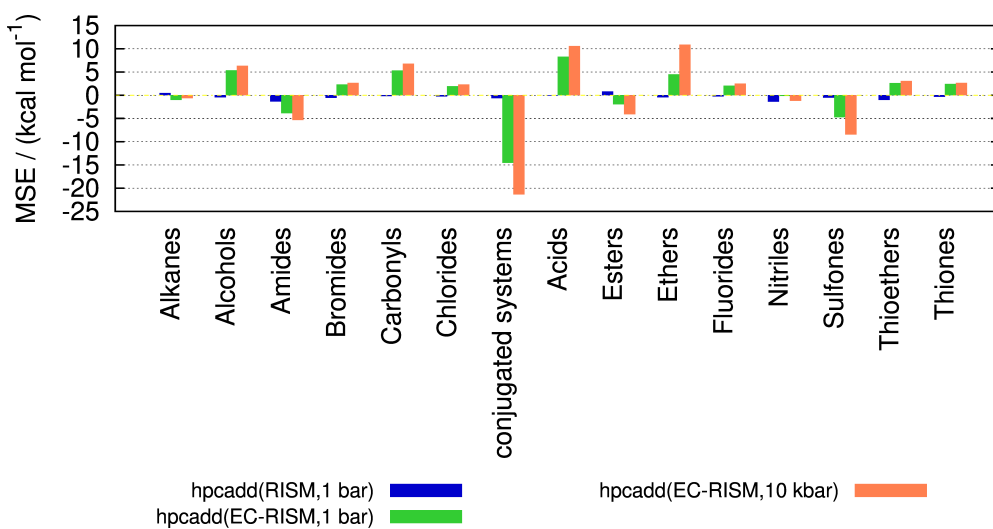


Figure 14.3.: Mean signed Errors (MSE) of the excess chemical potentials calculated with EC-RISM using hpCADD with respect to the MP2 reference calculations. RISM 1 bar data is taken from [17].

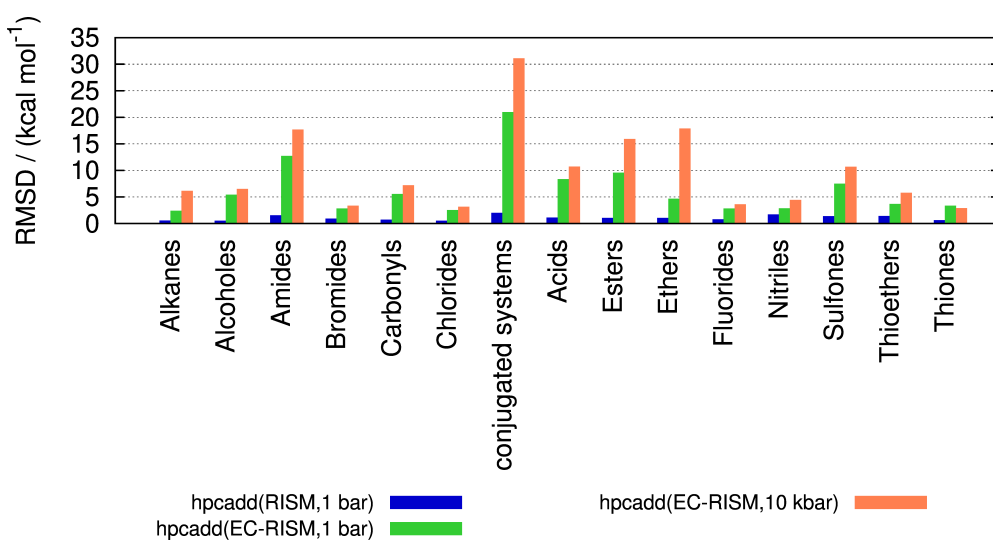


Figure 14.4.: Root mean square errors (RMSE) of the excess chemical potentials calculated with EC-RISM using hpCADD with respect to the MP2 reference calculations. RISM 1 bar data is taken from [17].

15. Summary and outlook

To begin of the scientific journey culminating in this thesis, questions on the effects of pressure induced polarization of small molecules were asked. In order to answer these questions a set of new methods has been developed in a course of highly cooperative and interdisciplinary scientific work.

The first step was to introduce high pressure into the three-dimensional reference interaction site model (3D RISM), by calculating suitable high pressure solvent susceptibilities, some of which are based on data from classical force field molecular dynamics (ffMD) simulations by Dr. Christoph Hölzl. These solvent susceptibilities were used for calculating the dipole moment response of trimethylamine-N-oxide (TMAO) and urea on pressure. The obtained information then was used by Dr. Christoph Hölzl to generate pressure-dependent force field charges for both molecules. Data generated with these force fields were compared with experimental results from literature and from the DFG research unit 1979 as well as with *ab initio* molecular dynamics (*aiMD*) data, which was generated by Dr. Sho Imoto and Jan Noetzel. Comparison revealed, that pressure dependent charges are required for the accurate determination of high pressure observables from high ffMD simulations on TMAO. For urea in contrast, the results turn out to deteriorate when introducing modified charges.

In case of urea some efforts were taken, in order to examine, to which extent coordination numbers and dipole moments are influenced by the variation of Lennard-Jones parameters. This helps to gain an idea of the sensitivity of the embedded cluster reference interaction site model (EC-RISM) methodology to different Lennard-Jones parameters and may help to improve force fields using the quick EC-RISM approach.

In order to gain insight into the physical basis of pressure dependent shifts of vibrational spectroscopic bands of TMAO, initial work to develop a framework for the calculation of vibrational problems with EC-RISM was established up to the point, that equilibrium solvation for normal-mode displaced molecular geometries is assumed. This picture allows for the prediction of the correct shift direction of the experimentally observed bands, while the shift is largely overestimated. These results were used together with *aiMD* based predictions by Dr. Sho Imoto to elucidate the origin of these shifts.

The handling of exact electrostatic potentials within the EC-RISM method was improved by developing, testing and establishing a new numerical approach to avoid cut-off artifacts in Coulomb potential renormalization, which is a prerequisite for the high level of accuracy needed for the prediction of thermodynamic equilibria.

15. Summary and outlook

For testing the accuracy of high pressure EC-RISM calculations, the ultimate goal was to accurately predict the pressure dependent shift of the water autoprotolysis equilibrium. To do so, it became necessary to recapitulate the role of the solute's Lennard-Jones parameters. Since the force field by Bonthuis *et al.* was not suitable to reproduce the radial distribution functions of water sites around hydronium and hydroxide obtained by *aiMD*, efforts were taken to extend the existing force field by charged dummy sites. Furthermore the Lennard-Jones parameters were optimized. Both problems were simultaneously tackled by the application of differential evolution. The EC-RISM results for hydronium and hydroxide were obtained under usage of the new electrostatics model and an empirical correction by Nicolas Tielker, which compensates errors on excess chemical potential depending on the partial molar volume, the solute charge and the pressure. The newly modelled force field performs better on solvation structure than the reference. Furthermore it performs good on calculating the shift of the autoprotolysis equilibrium. Nonetheless the original Bonthuis force field performs even better in that case. Regardless of the force field used, it was shown that neglecting the empirical correction leads to failure. This way a *modus operandi* for calculating the pressure dependence of chemical equilibria was found.

The polarizability of a novel semi-empirical Hamiltonian created by the high performance computer-aided drug design (hpCADD) project funded by the Bundesministerium für Bildung und Forschung (BMBF) was tested for its polarizability by EC-RISM calculations at 1 bar and 10 kbar. The test revealed, that still some work has to be performed in order to make the Hamiltonian fit for the use in polarizable force field ansatzes.

As a conclusion it can be stated, that the EC-RISM method was successfully extended to the scope of high hydrostatic pressure in terms of electronic properties and thermodynamics. Furthermore a starting-point for the treatment of high-pressure vibrational spectroscopy was found.

Usually scientific work does answer questions but leaves some new questions behind. This thesis is no exception in this manner. Future work has to address the topic of high pressure electrostatics in force field development, and should answer the question, in which cases pressure adaptation of atomic charges is necessary. Furthermore a model to correctly represent the non-equilibrium solvation situation during molecular vibration has to be developed and is a current topic in the DFG research unit. In conclusion it can be stated, that this thesis documents the basis of high pressure EC-RISM calculations and applications, but there are still many open tasks.

Bibliography

- ¹D. Chandler and H. C. Andersen, “Optimized cluster expansions for classical fluids. II. theory of molecular liquids”, *J. Chem. Phys.* **57**, 1930–1937 (1972).
- ²F. Hirata and P. J. Rossky, “An extended RISM equation for molecular polar fluids”, *Chem. Phys. Letters* **83**, 329–334 (1981).
- ³D. Beglov and B. Roux, “An integral equation to describe the solvation of polar molecules in liquid water”, *J. Phys. Chem. B* **101**, 7821–7826 (1997).
- ⁴A. Kovalenko and F. Hirata, “Three-dimensional density profiles of water in contact with a solute of arbitrary shape: a RISM approach”, *Chem. Phys. Letters* **290**, 237–244 (1998) [10.1016/S0009-2614\(98\)00471-0](https://doi.org/10.1016/S0009-2614(98)00471-0).
- ⁵T. Kloss, J. Heil, and S. M. Kast, “Quantum chemistry in solution by combining 3d integral equation theory with a cluster embedding approach”, *J. Phys. Chem. B* **112**, 4337–4343 (2008) [10.1021/jp710680m](https://doi.org/10.1021/jp710680m).
- ⁶K. Hiroike, “A new approach to the theory of classical fluids. II: multicomponent systems”, *Prog. Theor. Phys.* **24**, 317–330 (1960) [10.1143/PTP.24.317](https://doi.org/10.1143/PTP.24.317).
- ⁷S. M. Kast, K. F. Schmidt, and B. Schilling, “Integral equation theory for correcting truncation errors in molecular simulations”, *Chemical physics letters* **367**, 398–404 (2003).
- ⁸P. H. Yancey, M. D. Rhea, K. Kemp, and D. M. Bailey, “Trimethylamine oxide, betaine and other osmolytes in deep-sea animals: depth trends and effects on enzymes under hydrostatic pressure”, *Cell. Mol. Biol.* **50**, 1–6 (2004).
- ⁹P. H. Yancey, “Organic osmolytes as compatible, metabolic and counteracting cytoprotectants in high osmolarity and other stresses”, *J. Exp. Biol.* **208**, 2819–2830 (2005) [10.1242/jeb.01730](https://doi.org/10.1242/jeb.01730).
- ¹⁰P. H. Yancey, M. E. Clark, S. C. Hand, R. D. Bowlus, and G. N. Somero, “Living with water stress: evolution of osmolyte systems”, *Science* **217**, 1214–1222 (1982) [10.1126/science.7112124](https://doi.org/10.1126/science.7112124).
- ¹¹P. H. Yancey, M. E. Geringer, J. C. Drazen, A. A. Rowden, and A. Jamieson, “Marine fish may be biochemically constrained from inhabiting the deepest ocean depths”, *Proc. Natl. Acad. Sci. U. S. A.* **111**, 4461–4465 (2014) [10.1073/pnas.1322003111](https://doi.org/10.1073/pnas.1322003111).
- ¹²C. Hölzl, P. Kibies, S. Imoto, R. Frach, S. Suladze, R. Winter, D. Marx, D. Horinek, and S. M. Kast, “Design principles for high-pressure force fields: aqueous TMAO solutions from ambient to kilobar pressures”, *J. Chem. Phys.* **144**, 144104 (2016) [10.1063/1.4944991](https://doi.org/10.1063/1.4944991).

Bibliography

- ¹³D. R. Canchi and A. E. García, “Cosolvent effects on protein stability”, *Annu. Rev. Phys. Chem.* **64**, 273–293 (2013) 10.1146/annurev-physchem-040412-110156.
- ¹⁴S. Imoto, P. Kibies, C. Rosin, R. Winter, S. M. Kast, and D. Marx, “Toward extreme biophysics: deciphering the infrared response of biomolecular solutions at high pressures”, *Angew. Chem., Int. Ed.* **55**, 9534–9538 (2016) 10.1002/anie.201602757.
- ¹⁵F. Hoffgaard, J. Heil, and S. M. Kast, “Three-dimensional RISM integral equation theory for polarizable solute models”, *J. Chem. Theory Comput.* **9**, 4718–4726 (2013) 10.1021/ct400699q.
- ¹⁶D. J. Bonthuis, S. I. Mamatkulov, and R. R. Netz, “Optimization of classical non-polarizable force fields for OH and h3o+”, *J. Chem. Phys.* **144**, 104503 (2016) 10.1063/1.4942771.
- ¹⁷H. B. Thomas, M. Hennemann, P. Kibies, F. Hoffgaard, S. Güssregen, G. Hessler, S. M. Kast, and T. Clark, “The hpCADD NDDO hamiltonian: parametrization”, *J. Chem. Inf. Model.* **57**, 1907–1922 (2017) 10.1021/acs.jcim.7b00080.
- ¹⁸“Revised release on the pressure along the melting and sublimation curves of ordinary water substance”, *IAPWS R14-08* (2011).
- ¹⁹M. Gross and R. Jaenicke, “Proteins under pressure”, *Eur. J. Biochem.* **221**, 617–630 (1994) 10.1111/j.1432-1033.1994.tb18774.x.
- ²⁰A. L. Samerotte, J. C. Drazen, G. L. Brand, B. A. Seibel, and P. H. Yancey, “Correlation of trimethylamine oxide and habitat depth within and among species of teleost fish: an analysis of causation”, *Physiol. Biochem. Zool.* **80**, 197–208 (2007) 10.1086/510566.
- ²¹A. B. Downing, G. T. Wallace, and P. H. Yancey, “Organic osmolytes of amphipods from littoral to hadal zones: increases with depth in trimethylamine n-oxide, scyllo-inositol and other potential pressure counteractants”, *Deep Sea Res. Part I Oceanogr. Res. Pap.* **138**, 1–10 (2018) 10.1016/j.dsr.2018.05.008.
- ²²P. K. Nandi, A. Bera, and P.-Y. Sizaret, “Osmolyte trimethylamine n-oxide converts recombinant -helical prion protein to its soluble -structured form at high temperature”, *J. Mol. Biol.* **362**, 810–820 (2006) 10.1016/j.jmb.2006.07.060.
- ²³M. F. Patterson, M. Quinn, R. Simpson, and A. Gilmour, “Sensitivity of vegetative pathogens to high hydrostatic pressure treatment in phosphate-buffered saline and foods”, *J. Food Prot.* **58**, 524–529 (1995) 10.4315/0362-028X-58.5.524.
- ²⁴I. Oey, M. Lille, A. Van Loey, and M. Hendrickx, “Effect of high-pressure processing on colour, texture and flavour of fruit- and vegetable-based food products: a review”, *Trends Food Sci. Technol.* **19**, 320–328 (2008) 10.1016/j.tifs.2008.04.001.
- ²⁵R. Cammi, V. Verdolino, B. Mennucci, and J. Tomasi, “Towards the elaboration of a QM method to describe molecular solutes under the effect of a very high pressure”, *Chem. Phys.* **344**, 135–141 (2008) 10.1016/j.chemphys.2007.12.010.

- ²⁶R. Cammi, C. Cappelli, B. Mennucci, and J. Tomasi, “Calculation and analysis of the harmonic vibrational frequencies in molecules at extreme pressure: methodology and diborane as a test case”, *J. Chem. Phys.* **137**, 154112 (2012) 10.1063/1.4757285.
- ²⁷R. Cammi, “A new extension of the polarizable continuum model: toward a quantum chemical description of chemical reactions at extreme high pressure”, *J. Comput. Chem.* **36**, 2246–2259 (2015) 10.1002/jcc.24206.
- ²⁸R. Fukuda, M. Ehara, and R. Cammi, “Modeling molecular systems at extreme pressure by an extension of the polarizable continuum model (PCM) based on the symmetry-adapted cluster-configuration interaction (SAC–CI) method: confined electronic excited states of furan as a test case”, *J. Chem. Theory Comput.* **11**, 2063–2076 (2015) 10.1021/ct5011517.
- ²⁹T. D. Kühne, “Ab-initio molecular dynamics”, *Wiley Interdiscip. Rev. Comput. Mol. Sci.* **4**, 391–406 (2014) 10.1002/wcms.1176.
- ³⁰M. P. Allen and D. J. Tildesley, *Computer simulation of liquids* (Clarendon Press ; Oxford University Press, Oxford [England] : New York, 1987), 385 pp.
- ³¹D. Martin, D. Bartlett, and M. Roberts, “Solute accumulation in the deep-sea bacterium photobacterium profundum”, *Extremophiles* **6**, 507–514 (2002) 10.1007/s00792-002-0288-1.
- ³²C. M. Papini, P. P. Pandharipande, C. A. Royer, and G. I. Makhatadze, “Putting the piezolyte hypothesis under pressure”, *Biophys. J.* **113**, 974–977 (2017) 10.1016/j.bpj.2017.07.012.
- ³³E. Ohmae, Y. Miyashita, and C. Kato, “Thermodynamic and functional characteristics of deep-sea enzymes revealed by pressure effects”, *Extremophiles* **17**, 701–709 (2013) 10.1007/s00792-013-0556-2.
- ³⁴J. Tatzelt, S. B. Prusiner, and W. J. Welch, “Chemical chaperones interfere with the formation of scrapie prion protein.”, *EMBO J.* **15**, 6363–6373 (1996) 10.1002/j.1460-2075.1996.tb01027.x.
- ³⁵T.-Y. Lin and S. N. Timasheff, “Why do some organisms use a urea-methylamine mixture as osmolyte? thermodynamic compensation of urea and trimethylamine n-oxide interactions with protein”, *Biochemistry* **33**, 12695–12701 (1994) 10.1021/bi00208a021.
- ³⁶H. S. Frank and F. Franks, “Structural approach to the solvent power of water for hydrocarbons; urea as a structure breaker”, *J. Chem. Phys.* **48**, 4746–4757 (1968) 10.1063/1.1668057.
- ³⁷D. Horinek and R. R. Netz, “Can simulations quantitatively predict peptide transfer free energies to urea solutions? thermodynamic concepts and force field limitations”, *J. Phys. Chem. A* **115**, 6125–6136 (2011) 10.1021/jp1110086.
- ³⁸K. A. Dill, “Dominant forces in protein folding”, *Biochemistry* **29**, 7133–7155 (1990) 10.1021/bi00483a001.

Bibliography

- ³⁹M. Auton and D. W. Bolen, “Predicting the energetics of osmolyte-induced protein folding/unfolding”, *Proc. Natl. Acad. Sci. U. S. A.* **102**, 15065–15068 (2005) 10.1073/pnas.0507053102.
- ⁴⁰E. Paci and M. Marchi, “Intrinsic compressibility and volume compression in solvated proteins by molecular dynamics simulation at high pressure.”, *Proc. Natl. Acad. Sci. U. S. A.* **93**, 11609–11614 (1996) 10.1073/pnas.93.21.11609.
- ⁴¹T. Hansson, C. Oostenbrink, and W. van Gunsteren, “Molecular dynamics simulations”, *Curr. Opin. Struct. Biol.* **12**, 190–196 (2002) 10.1016/S0959-440X(02)00308-1.
- ⁴²N. Smolin, V. P. Voloshin, A. V. Anikeenko, A. Geiger, R. Winter, and N. N. Medvedev, “TMAO and urea in the hydration shell of the protein SNase”, *Phys. Chem. Chem. Phys.* **19**, 6345–6357 (2017) 10.1039/C6CP07903B.
- ⁴³D. Marx and J. Hutter, *Ab initio molecular dynamics: basic theory and advanced methods* (Cambridge University Press, 2009).
- ⁴⁴H. Sun, “Ab initio calculations and force field development for computer simulation of polysilanes”, *Macromolecules* **28**, 701–712 (1995) 10.1021/ma00107a006.
- ⁴⁵W. L. Jorgensen, D. S. Maxwell, and J. Tirado-Rives, “Development and testing of the OPLS all-atom force field on conformational energetics and properties of organic liquids”, *J. Am. Chem. Soc.* **118**, 11225–11236 (1996) 10.1021/ja9621760.
- ⁴⁶N. Foloppe and A. D. M. Jr, “All-atom empirical force field for nucleic acids: i. parameter optimization based on small molecule and condensed phase macromolecular target data”, *J. Comput. Chem.* **21**, 86–104 (2000) 10.1002/(SICI)1096-987X(20000130)21:2<86::AID-JCC2>3.0.CO;2-G.
- ⁴⁷J. Wang, R. M. Wolf, J. W. Caldwell, P. A. Kollman, and D. A. Case, “Development and testing of a general amber force field”, *J. Comput. Chem.* **25**, 1157–1174 (2004).
- ⁴⁸V. Hornak, R. Abel, A. Okur, B. Strockbine, A. Roitberg, and C. Simmerling, “Comparison of multiple amber force fields and development of improved protein backbone parameters”, *Proteins: Struct., Funct., Bioinf.* **65**, 712–725 (2006) 10.1002/prot.21123.
- ⁴⁹Hamann, “The ionization of water at high pressures”, *Journal of physical chemistry* (1952) **67**, 2233 (1963).
- ⁵⁰W. B. Holzappel, “Effect of pressure and temperature on the conductivity and ionic dissociation of water up to 100 kbar and 1000c”, *J. Chem. Phys.* **50**, 4424 (1969) 10.1063/1.1670914.
- ⁵¹W. L. Marshall and E. U. Franck, “Ion product of water substance, 0–1000c, 1–10,000 bars new international formulation and its background”, *J. Phys. Chem. Ref. Data* **10**, 295–304 (1981) 10.1063/1.555643.
- ⁵²A. V. Bandura and S. N. Lvov, “The ionization constant of water over wide ranges of temperature and density”, *J. Phys. Chem. Ref. Data* **35**, 15–30 (2006) 10.1063/1.1928231.

- ⁵³K. Hermansson, P. A. Bopp, D. Spångberg, L. Pejov, I. Bakó, and P. D. Mitev, “The vibrating hydroxide ion in water”, *Chem. Phys. Letters* **514**, 1–15 (2011) 10.1016/j.cplett.2011.07.042.
- ⁵⁴R. Vácha, D. Horinek, M. L. Berkowitz, and P. Jungwirth, “Hydronium and hydroxide at the interface between water and hydrophobic media”, *Physical Chemistry Chem. Phys.* **10**, 4975 (2008) 10.1039/b806432f.
- ⁵⁵L. X. Dang, “Solvation of the hydronium ion at the water liquid/vapor interface”, *J. Chem. Phys.* **119**, 6351–6353 (2003) 10.1063/1.1599274.
- ⁵⁶R. Zimmermann, U. Freudenberg, R. Schweiß, D. Küttner, and C. Werner, “Hydroxide and hydronium ion adsorption — a survey”, *Curr. Opin. Colloid Interface Sci.* **15**, 196–202 (2010) 10.1016/j.cocis.2010.01.002.
- ⁵⁷C. J. Mundy, I.-F. W. Kuo, M. E. Tuckerman, H.-S. Lee, and D. J. Tobias, “Hydroxide anion at the air–water interface”, *Chem. Phys. Letters* **481**, 2–8 (2009) 10.1016/j.cplett.2009.09.003.
- ⁵⁸B. Winter, M. Faubel, R. Vácha, and P. Jungwirth, “Behavior of hydroxide at the water/vapor interface”, *Chem. Phys. Letters* **474**, 241–247 (2009) 10.1016/j.cplett.2009.04.053.
- ⁵⁹B. B. Owen and S. R. Brinkley, “Calculation of the effect of pressure upon ionic equilibria in pure water and in salt solutions.”, *Chem. Rev.* **29**, 461–474 (1941) 10.1021/cr60094a003.
- ⁶⁰R. E. Gibson, “On the effect of pressure on the solubility of solids in liquids”, *Am. J. Sci.* **35A**, 49 (1938).
- ⁶¹G. Tammann, “Kap. III Abhängigkeit des Volumens der Lösungen vom Druck”, in *ÜBER DIE BEZIEHUNGEN ZWISCHEN DEN INNEREN KRÄFTEN UND EIGENSCHAFTEN DER LÖSUNGEN; EIN BEITRAG ZUR THEORIE HOMOGENER SYSTEME* (1907), pp. 36–46.
- ⁶²M. Hennemann, J. S. Murray, P. Politzer, K. E. Riley, and T. Clark, “Polarization-induced -holes and hydrogen bonding”, *J. Mol. Model.* **18**, 2461–2469 (2012) 10.1007/s00894-011-1263-5.
- ⁶³T. Clark, J. S. Murray, and P. Politzer, “Role of polarization in halogen bonds”, *Aust. J. Chem.* **67**, 451 (2014) 10.1071/CH13531.
- ⁶⁴A. Horn, J.-H. Lin, and T. Clark, “Multipole electrostatic model for MNDO-like techniques with minimal valence spd-basis sets”, *Theor. Chem. Acc.* **114**, 159–168 (2005) 10.1007/s00214-005-0657-9.
- ⁶⁵M. J. Frisch, G. W. Trucks, H. B. Schlegel, G. E. Scuseria, M. A. Robb, J. R. Cheeseman, G. Scalmani, V. Barone, B. Mennucci, G. A. Petersson, H. Nakatsuji, M. Caricato, X. Li, H. P. Hratchian, A. F. Izmaylov, J. Bloino, G. Zheng, J. L. Sonnenberg, M. Hada, M. Ehara, K. Toyota, R. Fukuda, J. Hasegawa, M. Ishida, T. Nakajima, Y. Honda, O. Kitao, H. Nakai, T. Vreven, J. A. Montgomery Jr., J. E. Peralta, F. Ogliaro, M. Bearpark, J. J. Heyd, E. Brothers, K. N. Kudin, V. N. Staroverov, R. Kobayashi, J. Normand, K. Raghavachari, A. Rendell, J. C. Burant,

Bibliography

- S. S. Iyengar, J. Tomasi, M. Cossi, N. Rega, J. M. Millam, M. Klene, J. E. Knox, J. B. Cross, V. Bakken, C. Adamo, J. Jaramillo, R. Gomperts, R. E. Stratmann, O. Yazyev, A. J. Austin, R. Cammi, C. Pomelli, J. W. Ochterski, R. L. Martin, K. Morokuma, V. G. Zakrzewski, G. A. Voth, P. Salvador, J. J. Dannenberg, S. Dapprich, A. D. Daniels, Ö. Farkas, J. B. Foresman, J. V. Ortiz, J. Cioslowski, and D. J. Fox, *Gaussian 09 revision e.01*, Gaussian Inc. Wallingford CT 2009 (Gaussian Inc., Wallingford CT, 2016).
- ⁶⁶M. J. S. Dewar and W. Thiel, “Ground states of molecules. 39. MNDO results for molecules containing hydrogen, carbon, nitrogen, and oxygen”, *J. Am. Chem. Soc.* **99**, 4907–4917 (1977) 10.1021/ja00457a005.
- ⁶⁷M. J. S. Dewar, E. G. Zoebisch, E. F. Healy, and J. J. P. Stewart, “Development and use of quantum mechanical molecular models. 76. AM1: a new general purpose quantum mechanical molecular model”, *J. Am. Chem. Soc.* **107**, 3902–3909 (1985) 10.1021/ja00299a024.
- ⁶⁸L. Fiedler, J. Gao, and D. G. Truhlar, “Polarized molecular orbital model chemistry. 1. ab initio foundations”, *J. Chem. Theory Comput.* **7**, 852–856 (2011) 10.1021/ct1006373.
- ⁶⁹J. Baker, “An algorithm for the location of transition states”, *J. Comput. Chem.* **7**, 385–395 (1986) 10.1002/jcc.540070402.
- ⁷⁰M. Hennemann and T. Clark, “EMPIRE: a highly parallel semiempirical molecular orbital program: 1: self-consistent field calculations”, *J. Mol. Model.* **20** (2014) 10.1007/s00894-014-2331-4.
- ⁷¹J. T. Margraf, M. Hennemann, B. Meyer, and T. Clark, “EMPIRE: a highly parallel semiempirical molecular orbital program: 2: periodic boundary conditions”, *J. Mol. Model.* **21** (2015) 10.1007/s00894-015-2692-3.
- ⁷²J. G. Kirkwood and F. P. Buff, “The statistical mechanical theory of solutions. i”, *J. Chem. Phys.* **19**, 774 (1951) 10.1063/1.1748352.
- ⁷³K. E. Newman, “Kirkwood–buff solution theory: derivation and applications”, *Chem. Soc. Rev.* **23**, 31–40 (1994) 10.1039/CS9942300031.
- ⁷⁴J.-P. Hansen and I. R. McDonald, *Theory of simple liquids*, 3rd ed, OCLC: ocm62290613 (Elsevier / Academic Press, Amsterdam ; Boston, 2007), 416 pp.
- ⁷⁵S. M. Kast and T. Kloss, “Closed-form expressions of the chemical potential for integral equation closures with certain bridge functions”, *J. Chem. Phys.* **129**, 236101 (2008) 10.1063/1.3041709.
- ⁷⁶A. Kovalenko and F. Hirata, “Self-consistent description of a metal-water interface by the kohn-sham density functional theory and the three-dimensional reference interaction site model”, *J. Chem. Phys.* **110**, 10095 (1999).
- ⁷⁷L. S. Ornstein and F. Zernike, “Accidental deviations of density and opalescence at the critical point of a single substance”, in *Proc. akad. sci.(amsterdam)*, Vol. 17 (1914), p. 793.

- ⁷⁸L. Blum, “Invariant expansion. II. the Ornstein-Zernike equation for nonspherical molecules and an extended solution to the mean spherical model”, *J. Chem. Phys.* **57**, 1862–1869 (1972) 10.1063/1.1678503.
- ⁷⁹J. S. Perkyns and B. M. Pettit, “A dielectrically consistent interaction site theory for solvent—electrolyte mixtures”, *Chem. Phys. Letters* **190**, 626–630 (1992) 10.1016/0009-2614(92)85201-K.
- ⁸⁰J. Perkyns and B. M. Pettitt, “A site-site theory for finite concentration saline solutions”, *J. Chem. Phys.* **97**, 7656 (1992) 10.1063/1.463485.
- ⁸¹P. P. Ewald, “Die berechnung optischer und elektrostatischer gitterpotentiale”, *Ann. Phys.* **369**, 253–287 (1921) 10.1002/andp.19213690304.
- ⁸²N. Tielker, D. Tomazic, J. Heil, T. Kloss, S. Ehrhart, S. Güssregen, K. F. Schmidt, and S. M. Kast, “The SAMPL5 challenge for embedded-cluster integral equation theory: solvation free energies, aqueous pK_a, and cyclohexane–water log d”, *J. Comput.-Aided Mol. Des.* **30**, 1035–1044 (2016) 10.1007/s10822-016-9939-7.
- ⁸³E. L. Ratkova, D. S. Palmer, and M. V. Fedorov, “Solvation thermodynamics of organic molecules by the molecular integral equation theory: approaching chemical accuracy”, *Chem. Rev.* **115**, 6312–6356 (2015) 10.1021/cr5000283.
- ⁸⁴V. Sergiievskiy, G. Jeanmairet, M. Levesque, and D. Borgis, “Solvation free-energy pressure corrections in the three dimensional reference interaction site model”, *J. Chem. Phys.* **143**, 184116 (2015) 10.1063/1.4935065.
- ⁸⁵A. V. Marenich, C. P. Kelly, J. D. Thompson, G. D. Hawkins, C. C. Chambers, D. K. Giesen, P. Winget, C. J. Cramer, and D. G. Truhlar, *Minnesota solvation database*, Version 2012 (University of Minnesota, Minneapolis, 2012).
- ⁸⁶A. V. Marenich, R. M. Olson, C. P. Kelly, C. J. Cramer, and D. G. Truhlar, “Self-consistent reaction field model for aqueous and nonaqueous solutions based on accurate polarized partial charges”, *J. Chem. Theory Comput.* **3**, 2011–2033 (2007) 10.1021/ct7001418.
- ⁸⁷C. P. Kelly, C. J. Cramer, and D. G. Truhlar, “SM6: a density functional theory continuum solvation model for calculating aqueous solvation free energies of neutrals, ions, and solutewater clusters”, *J. Chem. Theory Comput.* **1**, 1133–1152 (2005) 10.1021/ct050164b.
- ⁸⁸N. Tielker, L. Eberlein, S. Güssregen, and S. M. Kast, “The SAMPL6 challenge on predicting aqueous pK_a values from EC-RISM theory”, *J. Comput.-Aided Mol. Des.* **32**, 1151–1163 (2018) 10.1007/s10822-018-0140-z.
- ⁸⁹N. Tielker, *Personal communication*, E-mail.
- ⁹⁰T. Imai, M. Kinoshita, and F. Hirata, “Theoretical study for partial molar volume of amino acids in aqueous solution: implication of ideal fluctuation volume”, *J. Chem. Phys.* **112**, 9469–9478 (2000) 10.1063/1.481565.

Bibliography

- ⁹¹S. Gusarov, T. Ziegler, and A. Kovalenko, “Self-consistent combination of the three-dimensional RISM theory of molecular solvation with analytical gradients and the amsterdam density functional package”, *J. Phys. Chem. A* **110**, 6083–6090 (2006) 10.1021/jp054344t.
- ⁹²N. Yoshida and F. Hirata, “A new method to determine electrostatic potential around a macromolecule in solution from molecular wave functions”, *J. Comput. Chem.* **27**, 453–462 (2006) 10.1002/jcc.20356.
- ⁹³T. Miyata and F. Hirata, “Combination of molecular dynamics method and 3d-RISM theory for conformational sampling of large flexible molecules in solution”, *J. Comput. Chem.* **29**, 871–882 (2008) 10.1002/jcc.20844.
- ⁹⁴E. B. Wilson, J. C. Decius, and P. C. Cross, *Molecular vibrations: the theory of infrared and raman vibrational spectra* (Dover Publications, New York, 1980), 388 pp.
- ⁹⁵A. Chattopadhyay and S. G. Boxer, “Vibrational stark effect spectroscopy”, *J. Am. Chem. Soc.* **117**, 1449–1450 (1995) 10.1021/ja00109a038.
- ⁹⁶N. M. Levinson, S. D. Fried, and S. G. Boxer, “Solvent-induced infrared frequency shifts in aromatic nitriles are quantitatively described by the vibrational stark effect”, *J. Phys. Chem. B* **116**, 10470–10476 (2012) 10.1021/jp301054e.
- ⁹⁷M. J. Frisch, G. W. Trucks, H. B. Schlegel, G. E. Scuseria, M. A. Robb, J. R. Cheeseman, G. Scalmani, V. Barone, B. Mennucci, G. A. Petersson, H. Nakatsuji, M. Caricato, X. Li, H. P. Hratchian, A. F. Izmaylov, J. Bloino, G. Zheng, J. L. Sonnenberg, M. Hada, M. Ehara, K. Toyota, R. Fukuda, J. Hasegawa, M. Ishida, T. Nakajima, Y. Honda, O. Kitao, H. Nakai, T. Vreven, J. A. Montgomery Jr., J. E. Peralta, F. Ogliaro, M. Bearpark, J. J. Heyd, E. Brothers, K. N. Kudin, V. N. Staroverov, R. Kobayashi, J. Normand, K. Raghavachari, A. Rendell, J. C. Burant, S. S. Iyengar, J. Tomasi, M. Cossi, N. Rega, J. M. Millam, M. Klene, J. E. Knox, J. B. Cross, V. Bakken, C. Adamo, J. Jaramillo, R. Gomperts, R. E. Stratmann, O. Yazyev, A. J. Austin, R. Cammi, C. Pomelli, J. W. Ochterski, R. L. Martin, K. Morokuma, V. G. Zakrzewski, G. A. Voth, P. Salvador, J. J. Dannenberg, S. Dapprich, A. D. Daniels, Ö. Farkas, J. B. Foresman, J. V. Ortiz, J. Cioslowski, and D. J. Fox, *Gaussian 09 revision d.02*, Gaussian Inc. Wallingford CT 2009 (Gaussian Inc., Wallingford CT, 2004).
- ⁹⁸J. W. Ochterski, *Vibrational analysis in gaussian*, 1999.
- ⁹⁹E. Schmidt, “Über die auflösung linearer gleichungen mit unendlich vielen unbekanntem”, *Rend. Circ. Matem. Palermo* **25**, 53–77 (1908) 10.1007/BF03029116.
- ¹⁰⁰T. Lazaridis, “Inhomogeneous fluid approach to solvation thermodynamics. 1. theory”, *J. Phys. Chem. B* **102**, 3531–3541 (1998) 10.1021/jp9723574.
- ¹⁰¹T. Imai, H. Nomura, M. Kinoshita, and F. Hirata, “Partial molar volume and compressibility of alkalihalide ions in aqueous solution: hydration shell analysis with an integral equation theory of molecular liquids”, *J. Phys. Chem. B* **106**, 7308–7314 (2002) 10.1021/jp014504a.
- ¹⁰²W. B. Floriano and M. A. C. Nascimento, “Dielectric constant and density of water as a function of pressure at constant temperature”, *Braz. J. Phys.* **34**, 38–41 (2004).

- ¹⁰³E. Perlt, M. v. Domaros, B. Kirchner, R. Ludwig, and F. Weinhold, “Predicting the ionic product of water”, *Sci. Rep.* **7**, 10244 (2017) 10.1038/s41598-017-10156-w.
- ¹⁰⁴S. Dhillon and A. L. L. East, “Challenges in predicting $\Delta_{\text{rxn}}G$ in solution: hydronium, hydroxide, and water autoionization”, *Int. J. Quantum Chem.* **118**, e25703 (2018) 10.1002/qua.25703.
- ¹⁰⁵B. B. Owen and S. R. Brinkley, “The effect of pressure upon the dielectric constants of liquids”, *Phys. Rev.* **64**, 32–36 (1943) 10.1103/PhysRev.64.32.
- ¹⁰⁶P. Dierckx, “An algorithm for smoothing, differentiation and integration of experimental data using spline functions”, *Journal of Computational and Applied Mathematics* **1**, 165–184 (1975) 10.1016/0771-050X(75)90034-0.
- ¹⁰⁷H. J. C. Berendsen, J. R. Grigera, and T. P. Straatsma, “The missing term in effective pair potentials”, *J. Phys. Chem.* **91**, 6269–6271 (1987).
- ¹⁰⁸S. M. Kast, J. Heil, S. Güssregen, and K. F. Schmidt, “Prediction of tautomer ratios by embedded-cluster integral equation theory”, *J. Comput.-Aided Mol. Des.* **24**, 343–353 (2010) 10.1007/s10822-010-9340-x.
- ¹⁰⁹R. Storn and K. Price, “Differential evolution – a simple and efficient heuristic for global optimization over continuous spaces”, *J. Global Optim.* **11**, 341–359 (1997) 10.1023/A:1008202821328.
- ¹¹⁰J. Wang, W. Wang, P. A. Kollman, and D. A. Case, “Automatic atom type and bond type perception in molecular mechanical calculations”, *J. Mol. Graph. Model.* **25**, 247–260 (2006) 10.1016/j.jmgl.2005.12.005.
- ¹¹¹S. Weerasinghe and P. E. Smith, “A Kirkwood-Buff derived force field for mixtures of urea and water”, *J. Phys. Chem. B* **107**, 3891–3898 (2003) 10.1021/jp022049s.
- ¹¹²M. J. Abraham, T. Murtola, R. Schulz, S. Páll, J. C. Smith, B. Hess, and E. Lindahl, “GROMACS: high performance molecular simulations through multi-level parallelism from laptops to supercomputers”, *SoftwareX* **1-2**, 19–25 (2015) 10.1016/j.softx.2015.06.001.
- ¹¹³S. Páll, M. J. Abraham, C. Kutzner, B. Hess, and E. Lindahl, “Tackling exascale software challenges in molecular dynamics simulations with GROMACS”, in *Solving software challenges for exascale*, edited by S. Markidis and E. Laure, *Lecture Notes in Computer Science* (2015), pp. 3–27.
- ¹¹⁴S. Pronk, S. Páll, R. Schulz, P. Larsson, P. Bjelkmar, R. Apostolov, M. R. Shirts, J. C. Smith, P. M. Kasson, D. van der Spoel, B. Hess, and E. Lindahl, “GROMACS 4.5: a high-throughput and highly parallel open source molecular simulation toolkit”, *Bioinformatics* **29**, 845–854 (2013) 10.1093/bioinformatics/btt055.
- ¹¹⁵B. Hess, C. Kutzner, D. van der Spoel, and E. Lindahl, “GROMACS 4: algorithms for highly efficient, load-balanced, and scalable molecular simulation”, *J. Chem. Theory Comput.* **4**, 435–447 (2008) 10.1021/ct700301q.
- ¹¹⁶D. Van Der Spoel, E. Lindahl, B. Hess, G. Groenhof, A. E. Mark, and H. J. C. Berendsen, “GROMACS: fast, flexible, and free”, *J. Comput. Chem.* **26**, 1701–1718 (2005) 10.1002/jcc.20291.

Bibliography

- ¹¹⁷E. Lindahl, B. Hess, and D. van der Spoel, “GROMACS 3.0: a package for molecular simulation and trajectory analysis”, *J. Mol. Model.* **7**, 306–317 (2001) 10.1007/s008940100045.
- ¹¹⁸H. J. C. Berendsen, D. van der Spoel, and R. van Drunen, “GROMACS: a message-passing parallel molecular dynamics implementation”, *Comput. Phys. Commun.* **91**, 43–56 (1995) 10.1016/0010-4655(95)00042-E.
- ¹¹⁹J. L. F. Abascal and C. Vega, “A general purpose model for the condensed phases of water: TIP4p/2005”, *J. Chem. Phys.* **123**, 234505 (2005) 10.1063/1.2121687.
- ¹²⁰A. Garrett, *Inspyred: bio-inspired algorithms in python*, GitHub Repository, (2017) <http://aarongarrett.github.io/inspyred/>.
- ¹²¹D. W. M. Hofmann, L. Kuleshova, and B. D’Aguanno, “Molecular dynamics simulation of hydrated nafion with a reactive force field for water”, *J. Mol. Model.* **14**, 225–235 (2008) 10.1007/s00894-007-0265-9.
- ¹²²R. Devanathan, A. Venkatnathan, and M. Dupuis, “Atomistic simulation of nafion membrane. 2. dynamics of water molecules and hydronium ions”, *J. Phys. Chem. B* **111**, 13006–13013 (2007) 10.1021/jp0761057.
- ¹²³G. Bussi, D. Donadio, and M. Parrinello, “Canonical sampling through velocity rescaling”, *J. Chem. Phys.* **126**, 014101 (2007) 10.1063/1.2408420.
- ¹²⁴R. Hockney, S. Goel, and J. Eastwood, “Quiet high-resolution computer models of a plasma”, *Journal of Computational Physics* **14**, 148–158 (1974) 10.1016/0021-9991(74)90010-2.
- ¹²⁵T. Darden, D. York, and L. Pedersen, “Particle mesh ewald: an $n \log(n)$ method for ewald sums in large systems”, *J. Chem. Phys.* **98**, 10089–10092 (1993) 10.1063/1.464397.
- ¹²⁶H. J. C. Berendsen, J. P. M. Postma, W. F. van Gunsteren, A. DiNola, and J. R. Haak, “Molecular dynamics with coupling to an external bath”, *J. Chem. Phys.* **81**, 3684–3690 (1984) 10.1063/1.448118.
- ¹²⁷M. J. Frisch, G. W. Trucks, H. B. Schlegel, G. E. Scuseria, M. A. Robb, J. R. Cheeseman, J. A. Montgomery Jr., T. Vreven, K. N. Kudin, J. C. Burant, J. M. Millam, S. S. Iyengar, J. Tomasi, V. Barone, B. Mennucci, M. Cossi, G. Scalmani, N. Rega, G. A. Petersson, H. Nakatsuji, M. Hada, M. Ehara, K. Toyota, R. Fukuda, J. Hasegawa, M. Ishida, T. Nakajima, Y. Honda, O. Kitao, H. Nakai, M. Klene, X. Li, J. E. Knox, H. P. Hratchian, J. B. Cross, V. Bakken, C. Adamo, J. Jaramillo, R. Gomperts, R. E. Stratmann, O. Yazyev, A. J. Austin, R. Cammi, C. Pomelli, J. W. Ochterski, P. Y. Ayala, K. Morokuma, G. A. Voth, P. Salvador, J. J. Dannenberg, V. G. Zakrzewski, S. Dapprich, A. D. Daniels, M. C. Strain, O. Farkas, D. K. Malick, A. D. Rabuck, K. Raghavachari, J. B. Foresman, J. V. Ortiz, Q. Cui, A. G. Baboul, S. Clifford, J. Cioslowski, B. B. Stefanov, G. Liu, A. Liashenko, P. Piskorz, I. Komaromi, R. L. Martin, D. J. Fox, T. Keith, M. A. Al-Laham, C. Y. Peng, A. Nanayakkara, M. Challacombe, P. M. W. Gill, B. Johnson, W. Chen, M. W. Wong, C. Gonzalez, and J. A. Pople, *Gaussian 03, revision d.02*, Gaussian, Inc., Wallingford, CT, 2004 (2004).

- ¹²⁸L. E. Chirlian and M. M. Francl, “Atomic charges derived from electrostatic potentials: a detailed study”, *J. Comput. Chem.* **8**, 894–905 (1987) 10.1002/jcc.540080616.
- ¹²⁹R. H. Byrd, P. Lu, J. Nocedal, and C. Zhu, “A limited memory algorithm for bound constrained optimization”, *SIAM J. Sci. Comput.* **16**, 1190–1208 (1995) 10.1137/0916069.
- ¹³⁰R. Frach, P. Kibies, S. Böttcher, T. Pongratz, S. Strohfeldt, S. Kurrmann, J. Koehler, M. Hofmann, W. Kremer, H. R. Kalbitzer, O. Reiser, D. Horinek, and S. M. Kast, “The chemical shift baseline for high-pressure NMR spectra of proteins”, *Angew. Chem. Int. Ed.* **55**, 8757–8760 (2016) 10.1002/anie.201602054.
- ¹³¹J. Heil, “Effiziente fluidphasentheorie für protonierungsprozesse in komplexen systemen”, Dissertation (Technische Universität Dortmund, Dortmund, 2016).
- ¹³²K. M. Kast, J. Brickmann, S. M. Kast, and R. S. Berry, “Binary phases of aliphatic n-oxides and water: force field development and molecular dynamics simulation”, *J. Phys. Chem. A* **107**, 5342–5351 (2003).
- ¹³³E. Schneck, D. Horinek, and R. R. Netz, “Insight into the molecular mechanisms of protein stabilizing osmolytes from global force-field variations”, *J. Phys. Chem. B* **117**, 8310–8321 (2013).
- ¹³⁴Q. Zou, B. J. Bennion, V. Daggett, and K. P. Murphy, “The molecular mechanism of stabilization of proteins by TMAO and its ability to counteract the effects of urea”, *J. Am. Chem. Soc.* **124**, 1192–1202 (2002).
- ¹³⁵E. S. Courtenay, M. W. Capp, C. F. Anderson, and M. T. Record, “Vapor pressure osmometry studies of osmolyteprotein interactions: implications for the action of osmoprotectants in vivo and for the interpretation of “osmotic stress” experiments in vitro [†]”, *Biochemistry* **39**, 4455–4471 (2000) 10.1021/bi9928871.
- ¹³⁶V. I. Lebedev and D. N. Laikov, “A quadrature formula for the sphere of the 131st algebraic order of accuracy”, *Dokl. Math.* **59**, 477–481 (1999).
- ¹³⁷O. Tange, “GNU parallel: the command-line power tool”, *USENIX* **36** (2011).
- ¹³⁸L. Wall, ed., *Perl language reference manual: for perl version 5.12.1* (Network Theory Ltd, Bristol, 2010), 724 pp.
- ¹³⁹M. Kohm, *KOMA-script: eine sammlung von klassen und paketen für LaTeX 2: anleitung zu version 3.25*, in collab. with D. A. T. Dante, 6., überarbeitete und erweiterte Auflage für KOMA-Script 3, OCLC: 1031466820 (Lehmanns Media, Berlin, 2018), 728 pp.
- ¹⁴⁰L. 3. Project, *User’s guide for the amsmath package (version 2.1)* (American Mathematical Society, 2018).
- ¹⁴¹M. Hensel, *The mhchem bundle v4.08* (CTAN, 2018).
- ¹⁴²G. Van Rossum and F. L. Drake Jr, *Python tutorial* (Centrum voor Wiskunde en Informatica Amsterdam, The Netherlands, 1995).

Bibliography

¹⁴³W. Humphrey, A. Dalke, and K. Schulten, “VMD – visual molecular dynamics”, *J. Mol. Graph.* **14**, 33–38 (1996).

List of Tables

1.1.	Experimental relative changes of K_W as a function of the pressure p measured by Hamann ⁴⁹ and early predictions by Owen and Brinkley. ⁵⁹ Values in brackets denote the corresponding change $\Delta pK_W(p)$ with respect to atmospheric pressure.	11
1.2.	pK_W -values under high-pressure conditions calculated with different equations of state. Values in brackets denote the change with respect to 1 bar. The right column shows the reference data used in this work.	12
2.1.	Parameters for the partial molar volume (PMV) correction.	27
2.2.	Isothermal compressibilities used for calculating the partial molar volumes.	27
5.1.	Pressure-dependent densities ρ and dielectric constants ϵ of water, which were used to generate high pressure solvent susceptibilities. The values were calculated with the equations of state taken from Floriano <i>et al.</i> ¹⁰²	50
5.2.	Geometry and non-bonded parameters of the modified SPC/E water model. ^{5,107,108}	51
6.1.	Number of grid points and the resulting box lengths used in the 3D RISM calculations to benchmark the new ESP model.	63
7.1.	Cartesian coordinates of the B3LYP/6-311+G(d,p) optimized urea molecule. Water was presented by PCM.	68
7.2.	Cost function parameters for hydroxide.	72
7.3.	Cost function parameters for hydronium.	72
8.1.	Quantum chemically optimized geometry of hydronium.	75
8.2.	Quantum chemically optimized geometry of hydroxide.	75
8.3.	Force field geometry of hydronium.	76
8.4.	Force field geometry of hydroxide.	76
9.1.	Dipole moment of TMAO as a function of pressure. ¹²	81
9.2.	IR frequencies and intensities from B3LYP/6-311+G(d,p) with PCM ambient pressure water. The analyzed modes are marked with yellow highlighting.	92
9.3.	Raw force constants obtained from finite differences of the Gibbs energies in solution from EC-RISM calculations.	93

List of Tables

9.4.	Raw force constants obtained from finite differences of the Electronic energies in solution from EC-RISM calculations.	93
9.5.	Raw force constants obtained from polynomials fitted on Gibbs energies in solution from EC-RISM calculations.	93
9.6.	Raw force constants obtained from polynomials fitted on electronic energies in solution from EC-RISM calculations.	94
9.7.	EC-RISM calculated frequencies and frequency shifts from the total Gibbs energy in solution and from the intramolecular part at different pressures in comparison to the PCM values. ¹⁴	95
9.8.	3D RISM calculated frequencies and frequency shifts on the distorted geometries with fixed charges from EC-RISM of the minimum energy geometry. ¹⁴	95
10.1.	Dipole moment of urea as a function of pressure. Values in brackets are the differences to 1 bar.	97
10.2.	Raw dipole moments from parameter variation at 1 bar and 10 kbar.	99
10.3.	Raw dipole moment derivatives from parameter variation at 1 bar and 10 kbar.	100
10.4.	Dipole moments calculated with the modified Lennard-Jones parameters and simulation based solvent susceptibilities.	102
10.5.	Suggested changes in Lennard-Jones-Parameters, in order to achieve the same difference in dipole moments between 1 bar and 10 kbar.	102
10.6.	Resulting dipole moments with V3, the analytically modified V3 ^{an} and <i>aiMD</i> . <i>aiMD</i> -data by Jan Noetzel.	102
10.7.	Coordination numbers of hydrogen and oxygen around urea's oxygen atom at 1 bar and 10 kbar.	103
11.1.	Differences in the resulting thermodynamic data between the method given in every line and the potential switching approach including the perturbation energy term, calculated on the largest grid. "SWP" denotes potential switching including the perturbation term, "SW" the switching approach neglecting the perturbation term and "plain" the switching-less approach. The column "dipole constraint" states whether or not the ESP fit in the QC calculation was constraint to match the wave-function based dipole moment. Ala+- denotes the alanine zwitterion, "(s)" denotes the positional shifting of the solute within the box.	106
12.1.	Final non-bonding force field parameters for hydronium and hydroxide for the force field candidate with dummy interaction sites. Here H ⁺ labels hydrogen atoms, O ⁺ the oxygen atom and Du ⁺ the dummy center of the hydronium ion. The sites of hydroxide are H ⁻ , O ⁻ and Du ⁻ accordingly.	111
12.2.	Non-bonding force field parameters for hydronium and hydroxide by Bonthuis <i>et al.</i> ¹⁶ H ⁺ denotes hydrogen, O ⁺ the oxygen of hydronium, while the hydroxide sites are marked H ⁻ and O ⁻	112

12.3. Geometry of the hydronium ion with dummy site taken from the minimized simulation box.	112
12.4. Geometry of the hydroxide ion with dummy site taken from the minimized simulation box.	112
12.5. Dipole moments of hydronium and hydroxide at 1 bar and 10 kbar. . . .	116
12.6. High pressure charges for hydronium and hydroxide. O^+ , H^+ , Du^+ are the oxygen, hydrogen and dummy site of hydronium, while O^- , H^- and Du^- are the respective sites of hydroxide.	116
13.1. Table of pK_W -values calculated with the 3s/5s force field on force field based geometries. "ref" denotes the equation of state based reference data, "Corr" marks pressure independently PMV-corrected data, "pCorr" pressure dependently corrected data and "raw" data without any correction at all. Δ denotes the difference between each pressure and 1 bar.	117
13.2. Table of pK_W -values calculated with the 3s/5s force field on quantum mechanically optimized geometries. "ref" denotes the equation of state based reference data, "Corr" marks pressure independently PMV-corrected data, "pCorr" pressure dependently corrected data and "raw" data without any correction at all. Δ denotes the difference between each pressure and 1 bar.	118
13.3. Table of pK_W -values calculated with the reference force field by Bonthuis <i>et al.</i> on force field based geometries. "exp" denotes the equation of state based reference data, "Corr" marks pressure independently PMV-corrected data, "pCorr" pressure dependently corrected data and "raw" data without any correction at all. Δ denotes the difference between each pressure and 1 bar.	119
13.4. Table of pK_W -values calculated with the reference force field by Bonthuis <i>et al.</i> on quantum mechanically optimized geometries. "exp" denotes the equation of state based reference data, "Corr" marks pressure independently PMV-corrected data, "pCorr" pressure dependently corrected data and "unCorr" data without any correction at all. Δ denotes the difference between each pressure and 1 bar.	119
14.1. Root mean square deviation (RMSD) and mean signed error (MSE) between hpCADD and MP2 at 1 bar for every substance class. Data is shown for the excess chemical potential (μ^{ex}) and the total molecular dipole moment μ	122
14.2. Root mean square deviation (RMSD) and mean signed error (MSE) between hpCADD and MP2 at 10 kbar for every substance class. Data is shown for the excess chemical potential (μ^{ex}) and the total molecular dipole moment μ	122
A.1. Cartesian coordinates of TMAO optimized with B3LYP/6-311+G(d,p). Water was modelled with PCM.	133

List of Tables

A.2. Cartesian coordinates of TMAO optimized with B3LYP/6-311+G(d,p). Water was modelled with EC-RISM with 1 bar solvent susceptibilities from MD simulations.	134
A.3. Cartesian coordinates of TMAO optimized with B3LYP/6-311+G(d,p). Water was modelled with EC-RISM with 10 kbar solvent susceptibilities from MD simulations.	134
A.4. Distorted structures for mode 10	135
A.5. Distorted structures for mode 11	136
A.6. Distorted structures for mode 12	137
A.7. Distorted structures for mode 17	138
A.8. Distorted structures for mode 18	139
A.9. Distorted structures for mode 25	140
A.10. Thermodynamic data for mode 10 at 1 bar.	141
A.11. Thermodynamic data for mode 10 at 100 bar.	141
A.12. Thermodynamic data for mode 10 at 5 kbar.	141
A.13. Thermodynamic data for mode 10 at 10 kbar.	142
A.14. Thermodynamic data for mode 11 at 1 bar.	142
A.15. Thermodynamic data for mode 11 at 100 bar.	142
A.16. Thermodynamic data for mode 11 at 5 kbar.	142
A.17. Thermodynamic data for mode 11 at 10 kbar.	142
A.18. Thermodynamic data for mode 12 at 1 bar.	143
A.19. Thermodynamic data for mode 12 at 100 bar.	143
A.20. Thermodynamic data for mode 12 at 5 kbar.	143
A.21. Thermodynamic data for mode 12 at 10 kbar.	143
A.22. Thermodynamic data for mode 17 at 1 bar.	143
A.23. Thermodynamic data for of mode 17 at 100 bar.	144
A.24. Thermodynamic data for mode 17 at 5 kbar.	144
A.25. Thermodynamic data for mode 17 at 10 kbar.	144
A.26. Thermodynamic data for mode 18 at 1 bar.	144
A.27. Thermodynamic data for mode 18 at 100 bar.	144
A.28. Thermodynamic data for mode 18 at 5 kbar.	145
A.29. Thermodynamic data for mode 18 at 10 kbar.	145
A.30. Thermodynamic data for mode 25 at 1 bar.	145
A.31. Thermodynamic data for mode 25 at 100 bar.	145
A.32. Thermodynamic data for mode 25 at 5 kbar.	145
A.33. Thermodynamic data for mode 25 at 10 kbar.	146
A.34. Fit coefficients for TMAO modes at 1 bar obtained from Gibbs energies.	156
A.35. Fit coefficients for TMAO modes at 100 bar obtained from Gibbs energies.	156
A.36. Fit coefficients for TMAO modes at 5 kbar obtained from Gibbs energies.	156
A.37. Fit coefficients for TMAO modes at 10 kbar obtained from Gibbs energies.	156
A.38. Fit coefficients for TMAO modes at 1 bar obtained from electronic en- ergies.	157
A.39. Fit coefficients for TMAO modes at 100 bar obtained from electronic energies.	157

A.40. Fit coefficients for TMAO modes at 5 kbar obtained from electronic energies.	157
A.41. Fit coefficients for TMAO modes at 10 kbar obtained from electronic energies.	158
A.42. Rigid bond lengths of urea.	159
A.43. Harmonic angles of urea.	159
A.44. Dihedrals. $V_d = k(1 + \cos(n\theta - \theta_S))$	159
A.45. Urea V1 non-bonded parameters. Optimized by Dr. Christoph Hözl. . .	160
A.46. Urea V2 non-bonded parameters. Optimized by Dr. Christoph Hözl. . .	160
A.47. Urea V3 non-bonded parameters	160
A.48. Parameters of the modified urea force field V3-Mod1. Values in brackets denote the difference to the original V3 force field	161
A.49. Parameters of the modified urea force field V3-Mod2. Values in brackets denote the difference to the original V3 force field	161
A.50. Parameters of the modified urea force field V3-Mod3. Values in brackets denote the difference to the original V3 force field	162
A.51. Parameters of the modified urea force field V3-Mod4. Values in brackets denote the difference to the original V3 force field	162
A.52. Parameters of the modified urea force field V3-Mod5. Values in brackets denote the difference to the original V3 force field	162
A.53. Parameters of the modified urea force field V3-Mod6. Values in brackets denote the difference to the original V3 force field	163
A.54. Parameters of the modified urea force field V3-Mod7. Values in brackets denote the difference to the original V3 force field	163
A.55. Parameters of the modified urea force field V3-Mod8. Values in brackets denote the difference to the original V3 force field	163
A.56. Parameters of the modified urea force field V3-Mod9. Values in brackets denote the difference to the original V3 force field	164
A.57. Parameters of the modified urea force field V3-Mod10. Values in brackets denote the difference to the original V3 force field	164
A.58. Cartesian coordinates of the optimized alanine anion.	171
A.59. Cartesian coordinates of the optimized alanine zwitterion.	171
A.60. Cartesian coordinates of the optimized alanine cation.	172
A.61. Cartesian coordinates of the optimized nitrogen molecule.	172
A.62. Cartesian coordinates of the shifted optimized nitrogen molecule.	172
A.63. Alkanes	174
A.64. Alcohols	175
A.65. Amides	175
A.66. Bromides	176
A.67. Aldehydes and Ketones	176
A.68. Chlorides	177
A.69. Carboxylic acids	177
A.70. Esters	178
A.71. Ethers	179
A.72. Fluorides	179

List of Tables

A.73.Conjugated systems	180
A.74.Nitriles	181
A.75.Sulfones	181
A.76.Thioethers	182
A.77.Thiols	182
A.78.Thiones	183
A.79.Raw hpCADD EC-RISM results for the group of the Alkanes at 1 bar. .	184
A.80.Raw hpCADD EC-RISM results for the group of the Alcohols at 1 bar. .	184
A.81.Raw hpCADD EC-RISM results for the group of the Amides at 1 bar. .	185
A.82.Raw hpCADD EC-RISM results for the group of the Bromides at 1 bar. .	185
A.83.Raw hpCADD EC-RISM results for the group of the Carbonyls at 1 bar. .	185
A.84.Raw hpCADD EC-RISM results for the group of the Chlorides at 1 bar. .	185
A.85.Raw hpCADD EC-RISM results for the group of the Acids at 1 bar. . .	186
A.86.Raw hpCADD EC-RISM results for the group of the Esters at 1 bar. . .	186
A.87.Raw hpCADD EC-RISM results for the group of the Ethers at 1 bar. . .	186
A.88.Raw hpCADD EC-RISM results for the group of the Fluorides at 1 bar. .	186
A.89.Raw hpCADD EC-RISM results for the group of the conjugated systems at 1 bar.	187
A.90.Raw hpCADD EC-RISM results for the group of the Nitriles at 1 bar. .	187
A.91.Raw hpCADD EC-RISM results for the group of the Sulfones at 1 bar. .	187
A.92.Raw hpCADD EC-RISM results for the group of the Thioethers at 1 bar. .	187
A.93.Raw hpCADD EC-RISM results for the group of the Thiones at 1 bar. .	187
A.94.Raw hpCADD EC-RISM results for the group of the Alkanes at 10 kbar. .	188
A.95.Raw hpCADD EC-RISM results for the group of the Alcohols at 10 kbar. .	188
A.96.Raw hpCADD EC-RISM results for the group of the Amides at 10 kbar. .	188
A.97.Raw hpCADD EC-RISM results for the group of the Bromides at 10 kbar.	189
A.98.Raw hpCADD EC-RISM results for the group of the Carbonyls at 10 kbar.	189
A.99.Raw hpCADD EC-RISM results for the group of the Chlorides at 10 kbar.	189
A.100Raw hpCADD EC-RISM results for the group of the Acids at 10 kbar. .	189
A.101Raw hpCADD EC-RISM results for the group of the Esters at 10 kbar. .	190
A.102Raw hpCADD EC-RISM results for the group of the Ethers at 10 kbar. .	190
A.103Raw hpCADD EC-RISM results for the group of the Fluorides at 10 kbar. .	190
A.104Raw hpCADD EC-RISM results for the group of the conjugated systems at 10 kbar.	191
A.105Raw hpCADD EC-RISM results for the group of the Nitriles at 10 kbar. .	191
A.106Raw hpCADD EC-RISM results for the group of the Sulfones at 10 kbar. .	191
A.107Raw hpCADD EC-RISM results for the group of the Thioethers at 10 kbar.	191
A.108Raw hpCADD EC-RISM results for the group of the Thiones at 10 kbar. .	191
A.109Raw MP2 EC-RISM results for the group of the Carbonyls at 1 bar. . .	192
A.110Raw MP2 EC-RISM results for the group of the Chlorides at 1 bar. . .	192
A.111Raw MP2 EC-RISM results for the group of the Acids at 1 bar.	192

A.112 Raw MP2 EC-RISM results for the group of the Esters at 1 bar. 192

A.113 Raw MP2 EC-RISM results for the group of the Ethers at 1 bar. 193

A.114 Raw MP2 EC-RISM results for the group of the Fluorides at 1 bar. 193

A.115 Raw MP2 EC-RISM results for the group of the conjugated systems at
1 bar. 193

A.116 Raw MP2 EC-RISM results for the group of the Nitriles at 1 bar. 193

A.117 Raw MP2 EC-RISM results for the group of the Sulfones at 1 bar. 194

A.118 Raw MP2 EC-RISM results for the group of the Thioethers at 1 bar. 194

A.119 Raw MP2 EC-RISM results for the group of the Thiones at 1 bar. 194

A.120 Raw MP2 EC-RISM results for the group of the Alkanes at 10 kbar. 194

A.121 Raw MP2 EC-RISM results for the group of the Alcohols at 10 kbar. 195

A.122 Raw MP2 EC-RISM results for the group of the Amides at 10 kbar. 195

A.123 Raw MP2 EC-RISM results for the group of the Bromides at 10 kbar. 195

A.124 Raw MP2 EC-RISM results for the group of the Carbonyls at 10 kbar. 195

A.125 Raw MP2 EC-RISM results for the group of the Chlorides at 10 kbar. 196

A.126 Raw MP2 EC-RISM results for the group of the Acids at 10 kbar. 196

A.127 Raw MP2 EC-RISM results for the group of the Esters at 10 kbar. 196

A.128 Raw MP2 EC-RISM results for the group of the Ethers at 10 kbar. 196

A.129 Raw MP2 EC-RISM results for the group of the Fluorides at 10 kbar. 197

A.130 Raw MP2 EC-RISM results for the group of the conjugated systems at
10 kbar. 197

A.131 Raw MP2 EC-RISM results for the group of the Nitriles at 10 kbar. 197

A.132 Raw MP2 EC-RISM results for the group of the Sulfones at 10 kbar. 197

A.133 Raw MP2 EC-RISM results for the group of the Thioethers at 10 kbar. 198

A.134 Raw MP2 EC-RISM results for the group of the Thiones at 10 kbar. 198

List of Figures

1.1.	2D-(left) and 3D-structure(right) of N,N,N-trimethylamine-N-oxide . . .	6
1.2.	2D (left) and 3D (right) structure of urea. The red bead represents oxygen (O), the black bead carbon (C), the blue beads nitrogen (N) and the white beads hydrogen (H).	7
2.1.	2D drawing of the switching scheme. Color code: red - solute, dark blue - exact ESP, middle blue - switching zone, light blue - point charge ESP.	26
5.1.	Radial distribution functions of the water sites in dependence of the pressure as obtained from the MD simulations. The hydrogen-hydrogen (HH) RDF are shown left, the oxygen-hydrogen (OH) RDF are shown in the center, and the oxygen-oxygen (OO) RDF are shown in the right panel.	51
5.2.	Radial distribution functions of the water sites in dependence of the pressure as obtained from the MD simulations. The hydrogen-hydrogen (HH) RDF are shown left, the oxygen-hydrogen (OH) RDF are shown in the center, and the oxygen-oxygen (OO) RDF are shown in the right panel. The range around the first maximum is compared with the corresponding function smoothed by the cubic spline. Distribution functions for 1 bar (top) and 100 bar (bottom) are shown.	52
5.3.	Radial distribution functions of the water sites in dependence of the pressure as obtained from the MD simulations. The hydrogen-hydrogen (HH) RDF are shown left, the oxygen-hydrogen (OH) RDF are shown in the center, and the oxygen-oxygen (OO) RDF are shown in the right panel. The range around the first maximum is compared with the corresponding function smoothed by the cubic spline. Distribution functions for 500 bar (top) and 1 kbar (bottom) are shown.	53
5.4.	Radial distribution functions of the water sites in dependence of the pressure as obtained from the MD simulations. The hydrogen-hydrogen (HH) RDF are shown left, the oxygen-hydrogen (OH) RDF are shown in the center, and the oxygen-oxygen (OO) RDF are shown in the right panel. The range around the first maximum is compared with the corresponding function smoothed by the cubic spline. Distribution functions for 2 kbar (top) and 3 kbar (bottom) are shown.	54

List of Figures

5.5. Radial distribution functions of the water sites in dependence of the pressure as obtained from the MD simulations. The hydrogen-hydrogen (HH) RDF are shown left, the oxygen-hydrogen (OH) RDF are shown in the center, and the oxygen-oxygen (OO) RDF are shown in the right panel. The range around the first maximum is compared with the corresponding function smoothed by the cubic spline. Distribution functions for 4 kbar (top) and 5 kbar (bottom) are shown. 55

5.6. Radial distribution functions of the water sites in dependence of the pressure as obtained from the MD simulations. The hydrogen-hydrogen (HH) RDF are shown left, the oxygen-hydrogen (OH) RDF are shown in the center, and the oxygen-oxygen (OO) RDF are shown in the right panel. The range around the first maximum is compared with the corresponding function smoothed by the cubic spline. Distribution functions for 7.5 kbar (top) and 10 kbar (bottom) are shown. 56

5.7. Radial distribution functions of the water sites in dependence of the pressure as obtained from the MD simulations. The hydrogen-hydrogen (HH) RDF are shown left, the oxygen-hydrogen (OH) RDF are shown in the center, and the oxygen-oxygen (OO) RDF are shown in the right panel. Comparison of the switching region between the spline-smoothened distribution function and the resulting extrapolated distribution function for 1 bar (top) and 100 bar (bottom). 57

5.8. Radial distribution functions of the water sites in dependence of the pressure as obtained from the MD simulations. The hydrogen-hydrogen (HH) RDF are shown left, the oxygen-hydrogen (OH) RDF are shown in the center, and the oxygen-oxygen (OO) RDF are shown in the right panel. Comparison of the switching region between the spline-smoothened distribution function and the resulting extrapolated distribution function for 500 bar (top) and 1 kbar (bottom). 58

5.9. Radial distribution functions of the water sites in dependence of the pressure as obtained from the MD simulations. The hydrogen-hydrogen (HH) RDF are shown left, the oxygen-hydrogen (OH) RDF are shown in the center, and the oxygen-oxygen (OO) RDF are shown in the right panel. Comparison of the switching region between the spline-smoothened distribution function and the resulting extrapolated distribution function for 2 kbar (top) and 3 kbar (bottom). 59

5.10. Radial distribution functions of the water sites in dependence of the pressure as obtained from the MD simulations. The hydrogen-hydrogen (HH) RDF are shown left, the oxygen-hydrogen (OH) RDF are shown in the center, and the oxygen-oxygen (OO) RDF are shown in the right panel. Comparison of the switching region between the spline-smoothened distribution function and the resulting extrapolated distribution function for 4 kbar (top) and 5 kbar (bottom). 60

5.11. Radial distribution functions of the water sites in dependence of the pressure as obtained from the MD simulations. The hydrogen-hydrogen (HH) RDF are shown left, the oxygen-hydrogen (OH) RDF are shown in the center, and the oxygen-oxygen (OO) RDF are shown in the right panel. Comparison of the switching region between the spline-smoothened distribution function and the resulting extrapolated distribution function for 7.5 kbar (top) and 10 kbar (bottom).	61
6.1. Two dimensional representations of the three different alanine species.	63
7.1. 3D structure of the B3LYP/6-311+G(d,p) optimized urea molecule. The aqueous solution was modelled by PCM. The out-of-plane positions of the hydrogen atoms with respect to the N-C-N-plane can be seen here.	67
9.1. Dipole moment of TMAO as a function of pressure obtained from EC-RISM calculations. ¹²	82
9.2. Dipole moment of TMAO obtained from <i>aiMD</i> calculations <i>in vacuo</i> , at 1 bar and at 10kbar. Data generated by Dr. Sho Imoto. ¹²	82
9.3. Density of aqueous TMAO solutions as a function of the molar TMAO concentration obtained with the V1 and the novel V3 force field in comparison to experimental data. ¹³⁴	84
9.4. The activity coefficient derivative y_{TT} as a function of concentration. The experimental reference was calculated from osmometry results. ¹³⁵	85
9.5. Histogram of the probabilities to find a certain number of hydrogen bonds accepted by TMAO for the V3 and the V3-HP force field at 1 bar and at 10 bar in comparison to <i>aiMD</i> results. ¹²	86
9.6. Radial distribution functions of water hydrogen (left) and water oxygen (right) around TMAO oxygen with the different methods. Deviations between EC-RISM and the other methods can be explained by the different water models.	87
9.7. Three dimensional structure of TMAO and the spatial distribution functions of water oxygen as isosurfaces (isovalues 0.0648 \AA^{-3} (1 bar) and 0.0800 \AA^{-3} (10 kbar) for the dynamics, which is twice the bulk density and 2 in terms of the g function for EC-RISM). The left column in every panel represents the 1 bar distribution, while the right columns show 10 kbar results. Green isosurfaces represent hydrophilic and yellow ones hydrophobic solvation.	87
9.8. Density of water and of aqueous 0.5 mmol cm^{-3} TMAO solution. Experimental data is shown in comparison to data from ffMD. ¹²	88
9.9. Experimental peaks of the modes calculated from FTIR measurement. The peaks were background corrected and isolated from non-relevant peaks. The measurements were performed by Dr. Christopher Rosin. ¹⁴	89
9.10. Representative normal modes of TMAO, the red arrows depict the Cartesian atomic displacement upon unit distortion of the normal mode.	90

List of Figures

10.1. Pressure-dependent dipole moment of urea	98
10.2. Dipole moment histogram for 1 bar and 10 kbar from <i>ai</i> MD. Data by Jan Noetzel.	98
11.1. Difference of the Gibbs energy (top row), excess chemical potential (middle row) and solute electronic energy (bottom row) in solution as a function of grid size with respect to the largest grid for the three different alanine species. Blue lines show data calculated without potential switching, red lines show data with potential switching and orange lines show data with potential switching and perturbation energy term. Solid lines represent data calculated with dipole moment constraint, dashed lines indicate non-constrained partial charges.	107
11.2. Detailed plot of the difference of the Gibbs energy (top row), excess chemical potential (middle row) and solute electronic energy (bottom row) in solution as a function of grid size with respect to the largest grid for the three different alanine species. Blue lines show data calculated without potential switching, red lines show data with potential switching and orange lines show data with potential switching and perturbation energy term. Solid lines represent data calculated with dipole moment constraint, dashed lines indicate non-constrained partial charges.	108
11.3. Difference of the excess chemical potential <i>in vacuo</i> (first row) as well as in solution (second row), the electronic energy and the Gibbs energy in solution as a function of grid size with respect to the largest grid for molecular nitrogen centered in the box (left) and shifted by 1 Å along the bond axis (right). Blue lines show data calculated without potential switching, red lines show data with potential switching and orange lines show data with potential switching and perturbation energy term. Solid lines represent data calculated with dipole moment constraint, dashed lines indicate non-constrained partial charges.	109
11.4. Detailed view on the middle section of the differences of the excess chemical potential <i>in vacuo</i> (first row) as well as in solution (second row), the electronic energy and the Gibbs energy in solution as a function of grid size with respect to the largest grid for molecular nitrogen centered in the box (left) and shifted by 1 Å along the bond axis (right). Blue lines show data calculated without potential switching, red lines show data with potential switching and orange lines show data with potential switching and perturbation energy term. Solid lines represent data calculated with dipole moment constraint, dashed lines indicate non-constrained partial charges.	110
12.1. Three-dimensional depiction of the hydroxide model geometry. Hydrogen atoms are shown in white, oxygen in red and dummies in light-red.	113
12.2. Three-dimensional depiction of the hydronium model geometry. Hydrogen atoms are shown in white, oxygen in red and dummies in light-red.	113

12.3. Radial distribution functions of water around hydronium (top) and hydroxide (bottom) at 1 bar. The simulation was performed with the self-parameterized force field (blue lines), with the force field of Bonthuis <i>et al.</i> (orange lines). The reference stems from <i>ai</i> MD simulations (red lines). The panels show the hydrogen-hydrogen radial distribution function (RDF) (top left), the hydrogen-oxygen function (top right), the oxygen-hydrogen RDF (bottom left) and the oxygen-oxygen function (bottom right).	114
12.4. Radial distribution functions of water around hydronium (top) and hydroxide (bottom) at 10 kbar. The simulation was performed with the self-parameterized force field (blue lines) and with the same force field with scaled high pressure charges (orange lines). The reference stems from <i>ai</i> MD simulations (red lines). The panels show the hydrogen-hydrogen RDF (top left), the hydrogen-oxygen function (top right), the oxygen-hydrogen RDF (bottom left) and the oxygen-oxygen function (bottom right).	115
13.1. Plots of calculated ΔpK_W for different force fields and molecule geometries without PMV-correction (top), with pressure independent PMV-correction (center) and with the pressure dependent PMV correction (bottom) in comparison to experimental values.	120
14.1. Mean signed Errors (MSE) of the dipole moments calculated with EC-RISM using hpCADD with respect to the MP2 reference calculations.	123
14.2. Root mean square errors (RMSE) of the dipole moments calculated with EC-RISM using hpCADD with respect to the MP2 reference calculations.	123
14.3. Mean signed Errors (MSE) of the excess chemical potentials calculated with EC-RISM using hpCADD with respect to the MP2 reference calculations. RISM 1 bar data is taken from [17].	124
14.4. Root mean square errors (RMSE) of the excess chemical potentials calculated with EC-RISM using hpCADD with respect to the MP2 reference calculations. RISM 1 bar data is taken from [17].	124
A.1. Gibbs energy (left column), solute electronic energy (center column) and chemical excess potential (right) column for the analyzed normal modes of vibration at 1 bar. Every plot is normalized on the lowest occurring value.	148
A.2. Gibbs energy (left column), solute electronic energy (center column) and chemical excess potential (right) column for the analyzed normal modes of vibration at 100 bar. Every plot is normalized on the lowest occurring value.	149
A.3. Gibbs energy (left column), solute electronic energy (center column) and chemical excess potential (right) column for the analyzed normal modes of vibration at 5 kbar. Every plot is normalized on the lowest occurring value.	150

List of Figures

A.4. Gibbs energy (left column), solute electronic energy (center column) and chemical excess potential (right) column for the analyzed normal modes of vibration at 1 bar. Every plot is normalized on the lowest occurring value. 151

A.5. Gibbs energy (left) and solute electronic energy (right) from EC-RISM calculations on the distorted TMAO molecule at 1 bar. Calculated data points are shown as orange points, the red lines represent a fitted second order polynomial. 152

A.6. Gibbs energy (left) and solute electronic energy (right) from EC-RISM calculations on the distorted TMAO molecule at 100 bar. Calculated data points are shown as orange points, the red lines represent a fitted second order polynomial. 153

A.7. Gibbs energy (left) and solute electronic energy (right) from EC-RISM calculations on the distorted TMAO molecule at 5 kbar. Calculated data points are shown as orange points, the red lines represent a fitted second order polynomial. 154

A.8. Gibbs energy (left) and solute electronic energy (right) from EC-RISM calculations on the distorted TMAO molecule at 10 kbar. Calculated data points are shown as orange points, the red lines represent a fitted second order polynomial. 155

A.9. Radial distribution functions of the water sites around urea's oxygen, calculated with EC-RISM applying the V3 parameters. 165

A.10. Radial distribution functions of the water sites around urea's oxygen, calculated with EC-RISM applying the V3 Mod 1 parameters. 166

A.11. Radial distribution functions of the water sites around urea's oxygen, calculated with EC-RISM applying the V3 Mod 2 parameters. 166

A.12. Radial distribution functions of the water sites around urea's oxygen, calculated with EC-RISM applying the V3 Mod 3 parameters. 167

A.13. Radial distribution functions of the water sites around urea's oxygen, calculated with EC-RISM applying the V3 Mod 4 parameters. 167

A.14. Radial distribution functions of the water sites around urea's oxygen, calculated with EC-RISM applying the V3 Mod 5 parameters. 168

A.15. Radial distribution functions of the water sites around urea's oxygen, calculated with EC-RISM applying the V3 Mod 6 parameters. 168

A.16. Radial distribution functions of the water sites around urea's oxygen, calculated with EC-RISM applying the V3 Mod 7 parameters. 169

A.17. Radial distribution functions of the water sites around urea's oxygen, calculated with EC-RISM applying the V3 Mod 8 parameters. 169

A.18. Radial distribution functions of the water sites around urea's oxygen, calculated with EC-RISM applying the V3 Mod 9 parameters. 170

A.19. Radial distribution functions of the water sites around urea's oxygen, calculated with EC-RISM applying the V3 Mod 10 parameters. 170

A.20. Scatter plots of the dipole moments of the hpCADD-Hamiltonians vs. the MP2/aug-cc-pVDZ-reference. Data for the group of hydrocarbons is shown, 1 bar on the left, and 10 kbar on the right hand side. 199

A.21.Scatter plots of the dipole moments of the hpCADD-Hamiltonians vs. the MP2/aug-cc-pVDZ-reference. Data for the group of alcohols is shown, 1 bar on the left, and 10 kbar on the right hand side.	200
A.22.Scatter plots of the dipole moments of the hpCADD-Hamiltonians vs. the MP2/aug-cc-pVDZ-reference. Data for all molecules is shown, 1 bar on the left, and 10 kbar on the right hand side.	200
A.23.Scatter plots of the dipole moments of the hpCADD-Hamiltonians vs. the MP2/aug-cc-pVDZ-reference. Data for the group of amides is shown, 1 bar on the left, and 10 kbar on the right hand side.	201
A.24.Scatter plots of the dipole moments of the hpCADD-Hamiltonians vs. the MP2/aug-cc-pVDZ-reference. Data for the group of amines is shown, 1 bar on the left, and 10 kbar on the right hand side.	201
A.25.Scatter plots of the dipole moments of the hpCADD-Hamiltonians vs. the MP2/aug-cc-pVDZ-reference. Data for the group of bromides is shown, 1 bar on the left, and 10 kbar on the right hand side.	202
A.26.Scatter plots of the dipole moments of the hpCADD-Hamiltonians vs. the MP2/aug-cc-pVDZ-reference. Data for the group of aldehydes and ketones is shown, 1 bar on the left, and 10 kbar on the right hand side.	202
A.27.Scatter plots of the dipole moments of the hpCADD-Hamiltonians vs. the MP2/aug-cc-pVDZ-reference. Data for the group of chlorides is shown, 1 bar on the left, and 10 kbar on the right hand side.	203
A.28.Scatter plots of the dipole moments of the hpCADD-Hamiltonians vs. the MP2/aug-cc-pVDZ-reference. Data for the group of carboxylic acids is shown, 1 bar on the left, and 10 kbar on the right hand side.	203
A.29.Scatter plots of the dipole moments of the hpCADD-Hamiltonians vs. the MP2/aug-cc-pVDZ-reference. Data for the group of esters is shown, 1 bar on the left, and 10 kbar on the right hand side.	204
A.30.Scatter plots of the dipole moments of the hpCADD-Hamiltonians vs. the MP2/aug-cc-pVDZ-reference. Data for the group of ethers is shown, 1 bar on the left, and 10 kbar on the right hand side.	204
A.31.Scatter plots of the dipole moments of the hpCADD-Hamiltonians vs. the MP2/aug-cc-pVDZ-reference. Data for the group of fluorides is shown, 1 bar on the left, and 10 kbar on the right hand side.	205
A.32.Scatter plots of the dipole moments of the hpCADD-Hamiltonians vs. the MP2/aug-cc-pVDZ-reference. Data for the group of nitriles is shown, 1 bar on the left, and 10 kbar on the right hand side.	205
A.33.Scatter plots of the dipole moments of the hpCADD-Hamiltonians vs. the MP2/aug-cc-pVDZ-reference. Data for the group of sulfones is shown, 1 bar on the left, and 10 kbar on the right hand side.	206
A.34.Scatter plots of the dipole moments of the hpCADD-Hamiltonians vs. the MP2/aug-cc-pVDZ-reference. Data for the group of thioethers is shown, 1 bar on the left, and 10 kbar on the right hand side.	206
A.35.Scatter plots of the dipole moments of the hpCADD-Hamiltonians vs. the MP2/aug-cc-pVDZ-reference. Data for the group of thiones is shown, 1 bar on the left, and 10 kbar on the right hand side.	207

List of Figures

A.36.Scatter plots of the dipole moment difference between 10 kbar and 1 bar of the hpCADD-Hamiltonians vs. the MP2/aug-cc-pVDZ-reference. Datapoints for the alkanes are shown. 207

A.37.Scatter plots of the dipole moment difference between 10 kbar and 1 bar of the hpCADD-Hamiltonians vs. the MP2/aug-cc-pVDZ-reference. Datapoints for the alcohols are shown. 208

A.38.Scatter plots of the dipole moment difference between 10 kbar and 1 bar of the hpCADD-Hamiltonians vs. the MP2/aug-cc-pVDZ-reference. The whole dataset is shown. 208

A.39.Scatter plots of the dipole moment difference between 10 kbar and 1 bar of the hpCADD-Hamiltonians vs. the MP2/aug-cc-pVDZ-reference. Datapoints for the amides are shown. 209

A.40.Scatter plots of the dipole moment difference between 10 kbar and 1 bar of the hpCADD-Hamiltonians vs. the MP2/aug-cc-pVDZ-reference. Datapoints for the amines are shown. 209

A.41.Scatter plots of the dipole moment difference between 10 kbar and 1 bar of the hpCADD-Hamiltonians vs. the MP2/aug-cc-pVDZ-reference. Datapoints for the bromides are shown. 210

A.42.Scatter plots of the dipole moment difference between 10 kbar and 1 bar of the hpCADD-Hamiltonians vs. the MP2/aug-cc-pVDZ-reference. Datapoints for the aldehydes and ketones are shown. 210

A.43.Scatter plots of the dipole moment difference between 10 kbar and 1 bar of the hpCADD-Hamiltonians vs. the MP2/aug-cc-pVDZ-reference. Datapoints for the chlorides are shown. 211

A.44.Scatter plots of the dipole moment difference between 10 kbar and 1 bar of the hpCADD-Hamiltonians vs. the MP2/aug-cc-pVDZ-reference. Datapoints for the carboxylic acids are shown. 211

A.45.Scatter plots of the dipole moment difference between 10 kbar and 1 bar of the hpCADD-Hamiltonians vs. the MP2/aug-cc-pVDZ-reference. Datapoints for the esters are shown. 212

A.46.Scatter plots of the dipole moment difference between 10 kbar and 1 bar of the hpCADD-Hamiltonians vs. the MP2/aug-cc-pVDZ-reference. Datapoints for the ethers are shown. 212

A.47.Scatter plots of the dipole moment difference between 10 kbar and 1 bar of the hpCADD-Hamiltonians vs. the MP2/aug-cc-pVDZ-reference. Datapoints for the fluorides are shown. 213

A.48.Scatter plots of the dipole moment difference between 10 kbar and 1 bar of the hpCADD-Hamiltonians vs. the MP2/aug-cc-pVDZ-reference. Datapoints for the nitriles are shown. 213

A.49.Scatter plots of the dipole moment difference between 10 kbar and 1 bar of the hpCADD-Hamiltonians vs. the MP2/aug-cc-pVDZ-reference. Datapoints for the sulfones are shown. 214

A.50.Scatter plots of the dipole moment difference between 10 kbar and 1 bar of the hpCADD-Hamiltonians vs. the MP2/aug-cc-pVDZ-reference. Datapoints for the thioethers are shown. 214

A.51.Scatter plots of the dipole moment difference between 10 kbar and 1 bar of the hpCADD-Hamiltonians vs. the MP2/aug-cc-pVDZ-reference. Datapoints for the thiones are shown. 215

A.52.Scatter plot of the difference in solute electronic energy in solution between 10 kbar and 1 bar of the hpCADD-Hamiltonians vs. the MP2/aug-cc-pVDZ-reference. Datapoints for the hydrocarbons are shown. 215

A.53.Scatter plot of the difference in solute electronic energy in solution between 10 kbar and 1 bar of the hpCADD-Hamiltonians vs. the MP2/aug-cc-pVDZ-reference. Datapoints for the alcohols are shown. . . 216

A.54.Scatter plot of the difference in solute electronic energy in solution between 10 kbar and 1 bar of the hpCADD-Hamiltonians vs. the MP2/aug-cc-pVDZ-reference. Datapoints for the whole data set are shown. 216

A.55.Scatter plot of the difference in solute electronic energy in solution between 10 kbar and 1 bar of the hpCADD-Hamiltonians vs. the MP2/aug-cc-pVDZ-reference. Datapoints for the amides are shown. . . 217

A.56.Scatter plot of the difference in solute electronic energy in solution between 10 kbar and 1 bar of the hpCADD-Hamiltonians vs. the MP2/aug-cc-pVDZ-reference. Datapoints for the amines are shown. . . 217

A.57.Scatter plot of the difference in solute electronic energy in solution between 10 kbar and 1 bar of the hpCADD-Hamiltonians vs. the MP2/aug-cc-pVDZ-reference. Datapoints for the bromides are shown. . 218

A.58.Scatter plot of the difference in solute electronic energy in solution between 10 kbar and 1 bar of the hpCADD-Hamiltonians vs. the MP2/aug-cc-pVDZ-reference. Datapoints for aldehydes and ketones are shown. 218

A.59.Scatter plot of the difference in solute electronic energy in solution between 10 kbar and 1 bar of the hpCADD-Hamiltonians vs. the MP2/aug-cc-pVDZ-reference. Datapoints for the chlorides are shown. . 219

A.60.Scatter plot of the difference in solute electronic energy in solution between 10 kbar and 1 bar of the hpCADD-Hamiltonians vs. the MP2/aug-cc-pVDZ-reference. Datapoints for the carboxylic acids are shown. 219

A.61.Scatter plot of the difference in solute electronic energy in solution between 10 kbar and 1 bar of the hpCADD-Hamiltonians vs. the MP2/aug-cc-pVDZ-reference. Datapoints for the ethers are shown. . . 220

A.62.Scatter plot of the difference in solute electronic energy in solution between 10 kbar and 1 bar of the hpCADD-Hamiltonians vs. the MP2/aug-cc-pVDZ-reference. Datapoints for the esters are shown. . . 220

A.63.Scatter plot of the difference in solute electronic energy in solution between 10 kbar and 1 bar of the hpCADD-Hamiltonians vs. the MP2/aug-cc-pVDZ-reference. Datapoints for the fluorides are shown. . 221

A.64.Scatter plot of the difference in solute electronic energy in solution between 10 kbar and 1 bar of the hpCADD-Hamiltonians vs. the MP2/aug-cc-pVDZ-reference. Datapoints for the nitriles are shown. . . 221

List of Figures

A.65.Scatter plot of the difference in solute electronic energy in solution between 10 kbar and 1 bar of the hpCADD-Hamiltonians vs. the MP2/aug-cc-pVDZ-reference. Datapoints for the sulfones are shown. 222

A.66.Scatter plot of the difference in solute electronic energy in solution between 10 kbar and 1 bar of the hpCADD-Hamiltonians vs. the MP2/aug-cc-pVDZ-reference. Datapoints for the thioethers are shown. 222

A.67.Scatter plot of the difference in solute electronic energy in solution between 10 kbar and 1 bar of the hpCADD-Hamiltonians vs. the MP2/aug-cc-pVDZ-reference. Datapoints for the thiones are shown. 223

A.68.Scatter plot of the difference in solutes Gibbs energy in solution between 10 kbar and 1 bar of the hpCADD-Hamiltonians vs. the MP2/aug-cc-pVDZ-reference. Datapoints for the hydrocarbons are shown. 224

A.69.Scatter plot of the difference in solutes Gibbs energy in solution between 10 kbar and 1 bar of the hpCADD-Hamiltonians vs. the MP2/aug-cc-pVDZ-reference. Datapoints for the alcohols are shown. 225

A.70.Scatter plot of the difference in solutes Gibbs energy in solution between 10 kbar and 1 bar of the hpCADD-Hamiltonians vs. the MP2/aug-cc-pVDZ-reference. Datapoints for the whole data set are shown. 225

A.71.Scatter plot of the difference in solutes Gibbs energy in solution between 10 kbar and 1 bar of the hpCADD-Hamiltonians vs. the MP2/aug-cc-pVDZ-reference. Datapoints for the amides are shown. 226

A.72.Scatter plot of the difference in solutes Gibbs energy in solution between 10 kbar and 1 bar of the hpCADD-Hamiltonians vs. the MP2/aug-cc-pVDZ-reference. Datapoints for the amines are shown. 226

A.73.Scatter plot of the difference in solutes Gibbs energy in solution between 10 kbar and 1 bar of the hpCADD-Hamiltonians vs. the MP2/aug-cc-pVDZ-reference. Datapoints for the bromides are shown. 227

A.74.Scatter plot of the difference in solutes Gibbs energy in solution between 10 kbar and 1 bar of the hpCADD-Hamiltonians vs. the MP2/aug-cc-pVDZ-reference. Datapoints for aldehydes and ketones are shown. 227

A.75.Scatter plot of the difference in solutes Gibbs energy in solution between 10 kbar and 1 bar of the hpCADD-Hamiltonians vs. the MP2/aug-cc-pVDZ-reference. Datapoints for the chlorides are shown. 228

A.76.Scatter plot of the difference in solutes Gibbs energy in solution between 10 kbar and 1 bar of the hpCADD-Hamiltonians vs. the MP2/aug-cc-pVDZ-reference. Datapoints for the carboxylic acids are shown. 228

A.77.Scatter plot of the difference in solutes Gibbs energy in solution between 10 kbar and 1 bar of the hpCADD-Hamiltonians vs. the MP2/aug-cc-pVDZ-reference. Datapoints for the ethers are shown. 229

A.78.Scatter plot of the difference in solutes Gibbs energy in solution between 10 kbar and 1 bar of the hpCADD-Hamiltonians vs. the MP2/aug-cc-pVDZ-reference. Datapoints for the esters are shown. 229

A.79.Scatter plot of the difference in solutes Gibbs energy in solution between 10 kbar and 1 bar of the hpCADD-Hamiltonians vs. the MP2/aug-cc-pVDZ-reference. Datapoints for the fluorides are shown. 230

A.80.Scatter plot of the difference in solutes Gibbs energy in solution between 10 kbar and 1 bar of the hpCADD-Hamiltonians vs. the MP2/aug-cc-pVDZ-reference. Datapoints for the nitriles are shown.	230
A.81.Scatter plot of the difference in solutes Gibbs energy in solution between 10 kbar and 1 bar of the hpCADD-Hamiltonians vs. the MP2/aug-cc-pVDZ-reference. Datapoints for the sulfones are shown.	231
A.82.Scatter plot of the difference in solutes Gibbs energy in solution between 10 kbar and 1 bar of the hpCADD-Hamiltonians vs. the MP2/aug-cc-pVDZ-reference. Datapoints for the thioethers are shown.	231
A.83.Scatter plot of the difference in solutes Gibbs energy in solution between 10 kbar and 1 bar of the hpCADD-Hamiltonians vs. the MP2/aug-cc-pVDZ-reference. Datapoints for the thiones are shown.	232
A.84.Scatter plot of the difference in solutes excess chemical potential in solution between 10 kbar and 1 bar of the hpCADD-Hamiltonians vs. the MP2/aug-cc-pVDZ-reference. Datapoints for the hydrocarbons are shown.	232
A.85.Scatter plot of the difference in solutes excess chemical potential in solution between 10 kbar and 1 bar of the hpCADD-Hamiltonians vs. the MP2/aug-cc-pVDZ-reference. Datapoints for the alcohols are shown.	233
A.86.Scatter plot of the difference in solutes excess chemical potential in solution between 10 kbar and 1 bar of the hpCADD-Hamiltonians vs. the MP2/aug-cc-pVDZ-reference. Datapoints for the whole data set are shown.	233
A.87.Scatter plot of the difference in solutes excess chemical potential in solution between 10 kbar and 1 bar of the hpCADD-Hamiltonians vs. the MP2/aug-cc-pVDZ-reference. Datapoints for the amides are shown.	234
A.88.Scatter plot of the difference in solutes excess chemical potential in solution between 10 kbar and 1 bar of the hpCADD-Hamiltonians vs. the MP2/aug-cc-pVDZ-reference. Datapoints for the amines are shown.	234
A.89.Scatter plot of the difference in solutes excess chemical potential in solution between 10 kbar and 1 bar of the hpCADD-Hamiltonians vs. the MP2/aug-cc-pVDZ-reference. Datapoints for the bromides are shown.	235
A.90.Scatter plot of the difference in solutes excess chemical potential in solution between 10 kbar and 1 bar of the hpCADD-Hamiltonians vs. the MP2/aug-cc-pVDZ-reference. Datapoints for aldehydes and ketones are shown.	235
A.91.Scatter plot of the difference in solutes excess chemical potential in solution between 10 kbar and 1 bar of the hpCADD-Hamiltonians vs. the MP2/aug-cc-pVDZ-reference. Datapoints for the chlorides are shown.	236
A.92.Scatter plot of the difference in solutes excess chemical potential in solution between 10 kbar and 1 bar of the hpCADD-Hamiltonians vs. the MP2/aug-cc-pVDZ-reference. Datapoints for the carboxylic acids are shown.	236

List of Figures

- A.93. Scatter plot of the difference in solutes excess chemical potential in solution between 10 kbar and 1 bar of the hpCADD-Hamiltonians vs. the MP2/aug-cc-pVDZ-reference. Datapoints for the ethers are shown. . 237
- A.94. Scatter plot of the difference in solutes excess chemical potential in solution between 10 kbar and 1 bar of the hpCADD-Hamiltonians vs. the MP2/aug-cc-pVDZ-reference. Datapoints for the esters are shown. . 237
- A.95. Scatter plot of the difference in solutes excess chemical potential in solution between 10 kbar and 1 bar of the hpCADD-Hamiltonians vs. the MP2/aug-cc-pVDZ-reference. Datapoints for the fluorides are shown. 238
- A.96. Scatter plot of the difference in solutes excess chemical potential in solution between 10 kbar and 1 bar of the hpCADD-Hamiltonians vs. the MP2/aug-cc-pVDZ-reference. Datapoints for the nitriles are shown. 238
- A.97. Scatter plot of the difference in solutes excess chemical potential in solution between 10 kbar and 1 bar of the hpCADD-Hamiltonians vs. the MP2/aug-cc-pVDZ-reference. Datapoints for the sulfones are shown. 239
- A.98. Scatter plot of the difference in solutes excess chemical potential in solution between 10 kbar and 1 bar of the hpCADD-Hamiltonians vs. the MP2/aug-cc-pVDZ-reference. Datapoints for the thioethers are shown. . 239
- A.99. Scatter plot of the difference in solutes excess chemical potential in solution between 10 kbar and 1 bar of the hpCADD-Hamiltonians vs. the MP2/aug-cc-pVDZ-reference. Datapoints for the thiones are shown. 240

Part V.
Appendix

A. Additional data

A.1. TMAO

A.1.1. Molecular geometries

Table A.1.: Cartesian coordinates of TMAO optimized with B3LYP/6-311+G(d,p).
Water was modelled with PCM.

Atom	$x/\text{\AA}$	$y/\text{\AA}$	$z/\text{\AA}$
O	-0.000407411458	-0.000162256119	-0.038044302128
N	0.000089485816	-0.000017093161	1.345456194689
C	1.413496611272	-0.000023664400	1.849266968249
C	-0.706516479816	1.223742125781	1.850662594411
C	-0.706601650192	-1.223685278235	1.850600824646
H	1.427064789179	-0.000108294276	2.940990271431
H	1.899779654438	0.891190771242	1.457893603882
H	1.899944843922	-0.891042163071	1.457673026432
H	-0.714665011212	1.233983089110	2.942323269945
H	-1.720982590056	1.199933392359	1.457908966708
H	-0.177169923921	2.090891794471	1.461133282618
H	-0.715088162156	-1.233819496585	2.942269121446
H	-0.177024870511	-2.090847509391	1.461370552879
H	-1.720919285304	-1.200035417723	1.457495624793

A. Additional data

Table A.2.: Cartesian coordinates of TMAO optimized with B3LYP/6-311+G(d,p).
Water was modelled with EC-RISM with 1 bar solvent susceptibilities
from MD simulations.

Atom	$x/\text{\AA}$	$y/\text{\AA}$	$z/\text{\AA}$
O	-0.000407419755	-0.000162255523	-0.038045467580
N	0.000089489635	-0.000017093213	1.345457090374
C	1.413496569308	-0.000023663958	1.849266720279
C	-0.706516455070	1.223742080696	1.850662305425
C	-0.706601624757	-1.223685234132	1.850600536582
H	1.427064759387	-0.000108294387	2.940990244667
H	1.899779686492	0.891190780720	1.457893725766
H	1.899944875803	-0.891042172760	1.457673148387
H	-0.714664995522	1.233983063260	2.942323250642
H	-1.720982620252	1.199933418455	1.457909099531
H	-0.177169930609	2.090891832398	1.461133414079
H	-0.715088146563	-1.233819470723	2.942269102082
H	-0.177024877519	-2.090847547174	1.461370684462
H	-1.720919315809	-1.200035443686	1.457495757657

Table A.3.: Cartesian coordinates of TMAO optimized with B3LYP/6-311+G(d,p).
Water was modelled with EC-RISM with 10 kbar solvent susceptibilities
from MD simulations.

Atom	$x/\text{\AA}$	$y/\text{\AA}$	$z/\text{\AA}$
O	-0.000407511449	-0.000162246922	-0.038068102355
N	0.000089531735	-0.000017093746	1.345475905123
C	1.413495152135	-0.000023657239	1.849261687915
C	-0.706515677026	1.223740727725	1.850656489650
C	-0.706600835959	-1.223683896021	1.850594734637
H	1.427063939633	-0.000108296010	2.940989445895
H	1.899780064147	0.891190805580	1.457896201787
H	1.899945251047	-0.891042200832	1.457675625622
H	-0.714664563395	1.233982338175	2.942322595089
H	-1.720982968224	1.199933749813	1.457911786450
H	-0.177170054520	2.090892309433	1.461136083942
H	-0.715087715834	-1.233818745524	2.942268445585
H	-0.177025006333	-2.090848021876	1.461373356119
H	-1.720919668803	-1.200035773076	1.457498445534

A.1.2. Vibrational data

Table A.4.: Distorted structures for mode 10

$\Delta x / \text{\AA}$	atom	$x / \text{\AA}$	$y / \text{\AA}$	$z / \text{\AA}$	
-0.04	O	-0.0004357877386	-0.0001524999218	-0.03818667616	
	N	0.0000186742689	-0.00001520411332	1.343886636	
	C	1.4139415	-0.00002008160878	1.848787203	
	C	-0.706742239	1.22429789	1.849728764	
	C	-0.7068288719	-1.224245072	1.849664366	
	H	1.434429026	-0.00007453818636	2.940821229	
	H	1.890559358	0.90024537	1.466608461	
	H	1.890709334	-0.9001268376	1.466443292	
	H	-0.7177295535	1.241211128	2.941709633	
	H	-1.724404149	1.187473863	1.4666319	
	H	-0.1650786259	2.087319883	1.468251906	
	H	-0.7180897812	-1.241084095	2.941653163	
	H	-0.1649439204	-2.087269883	1.468467195	
	H	-1.724357256	-1.187561868	1.46624172	
	-0.02	O	-0.0004359113718	-0.0001524434369	-0.03820317216
		N	0.00001894645245	-0.00001547157966	1.344568878
C		1.413615035	-0.00001994802089	1.849192558	
C		-0.7065788625	1.224009988	1.850137393	
C		-0.7066642394	-1.223957116	1.850072617	
H		1.43040899	-0.00007396506818	2.941064269	
H		1.895136032	0.8957385339	1.462542737	
H		1.895282868	-0.8956187933	1.462377115	
H		-0.7157007896	1.237734972	2.941952964	
H		-1.722770511	1.193738988	1.462538163	
H		-0.1713125689	2.089052217	1.464176612	
H		-0.71607144	-1.237602525	2.941896196	
H		-0.1711803547	-2.089003159	1.464382324	
H		-1.722723339	-1.193832251	1.462155743	
0.02		O	-0.0004361586382	-0.0001523304671	-0.03823616418
		N	0.00001949081955	-0.00001600651234	1.34593336
	C	1.412962106	-0.00001968084511	1.850003269	
	C	-0.7062521095	1.223434183	1.85095465	
	C	-0.7063349744	-1.223381205	1.85088912	
	H	1.422368917	-0.00007281883182	2.941550349	
	H	1.904289378	0.8867248617	1.454411287	
	H	1.904429935	-0.8866027047	1.45424476	
	H	-0.7116432619	1.23078266	2.942439626	
	H	-1.719503236	1.206269239	1.45435069	
	H	-0.1837804547	2.092516887	1.456026024	
	H	-0.7120347578	-1.230639384	2.942382261	
	H	-0.1836532232	-2.092469712	1.456212583	
	H	-1.719455505	-1.206373017	1.453983788	
	0.04	O	-0.0004362822714	-0.0001522739822	-0.03825266018
		N	0.0000197630031	-0.00001627397868	1.346615601
C		1.412635641	-0.00001954725722	1.850408624	
C		-0.7060887329	1.223146281	1.851363279	
C		-0.7061703419	-1.223093249	1.851297371	
H		1.41834888	-0.00007224571364	2.94179339	
H		1.908866052	0.8822180256	1.450345563	
H		1.909003469	-0.8820946603	1.450178583	
H		-0.709614498	1.227306504	2.942682958	
H		-1.717869598	1.212534365	1.450256954	
H		-0.1900143976	2.094249222	1.45195073	
H		-0.7100164167	-1.227157813	2.942625294	
H		-0.1898896574	-2.094202989	1.452127712	
H		-1.717821589	-1.212643399	1.449897811	

A. Additional data

Table A.5.: Distorted structures for mode 11

$\Delta x / \text{\AA}$	atom	$x / \text{\AA}$	$y / \text{\AA}$	$z / \text{\AA}$
-0.04	O	-0.0005256396802	-0.0003296591726	-0.03821901952
	N	0.000876537405	0.001685404399	1.345250666
	C	1.413360875	0.0009340608799	1.849197656
	C	-0.7056903165	1.224253801	1.850055339
	C	-0.7064637587	-1.223484056	1.851368748
	H	1.429176861	-0.0165084183	2.941010079
	H	1.890968656	0.8933795113	1.450868405
	H	1.901725834	-0.895636062	1.472079445
	H	-0.7286999763	1.229495386	2.941821844
	H	-1.726037176	1.19802056	1.472230055
	H	-0.1703415083	2.084301259	1.45385787
	H	-0.7100932009	-1.229338979	2.942793215
	H	-0.1878203666	-2.094021537	1.454137715
	H	-1.718243559	-1.210253196	1.450570372
-0.02	O	-0.0004808373426	-0.0002410230623	-0.03821934385
	N	0.0004478780205	0.0008348326765	1.345250892
	C	1.413324723	0.0004571232234	1.849397785
	C	-0.7060529012	1.223987943	1.85030068
	C	-0.7064816828	-1.223576608	1.850924808
	H	1.427782907	-0.008290905124	2.941158694
	H	1.895340681	0.8923056046	1.454672709
	H	1.900791118	-0.8933734055	1.465195192
	H	-0.721186001	1.231877101	2.94200907
	H	-1.723587025	1.199012337	1.465337241
	H	-0.17394401	2.087542906	1.456979594
	H	-0.7120731499	-1.231729967	2.942466222
	H	-0.1826185778	-2.092378986	1.457217584
	H	-1.71966649	-1.205177915	1.454320069
0.02	O	-0.0003912326674	-0.00006375084168	-0.03821999249
	N	-0.0004094407485	-0.0008663107685	1.345251345
	C	1.413252418	-0.0004967520894	1.849798042
	C	-0.7067780707	1.223456228	1.850791363
	C	-0.706517531	-1.223761713	1.850036928
	H	1.424994999	0.008144121224	2.941455924
	H	1.90408473	0.890157791	1.462281315
	H	1.898921686	-0.8888480924	1.451426684
	H	-0.7061580505	1.236640531	2.942383521
	H	-1.718686722	1.200995891	1.451551613
	H	-0.1811490135	2.094026199	1.463223041
	H	-0.7160330479	-1.236511942	2.941812235
	H	-0.172215	-2.089093885	1.463377323
	H	-1.722512354	-1.195027353	1.461819463
0.04	O	-0.0003464303298	0.00002488526863	-0.03822031682
	N	-0.000838100133	-0.001716882491	1.345251572
	C	1.413216265	-0.0009736897459	1.849998171
	C	-0.7071406555	1.22319037	1.851036704
	C	-0.7065354551	-1.223854265	1.849592989
	H	1.423601046	0.0163616344	2.941604539
	H	1.908456754	0.8890838843	1.466085619
	H	1.897986969	-0.8865854359	1.44454243
	H	-0.6986440752	1.239022247	2.942570746
	H	-1.71623657	1.201987668	1.444658799
	H	-0.1847515152	2.097267845	1.466344765
	H	-0.7180129969	-1.238902929	2.941485242
	H	-0.1670132112	-2.087451334	1.466457192
	H	-1.723935286	-1.189952072	1.465569159

Table A.6.: Distorted structures for mode 12

$\Delta x / \text{\AA}$	atom	$x / \text{\AA}$	$y / \text{\AA}$	$z / \text{\AA}$
-0.04	O	-0.0006143311286	-0.00006342950906	-0.03821988123
	N	0.001723302736	-0.0008717422875	1.345250847
	C	1.413440678	-0.00050086029	1.848803245
	C	-0.7058370472	1.223887813	1.851287831
	C	-0.7055705787	-1.224196089	1.850533163
	H	1.431901243	0.008209679642	2.94072063
	H	1.895520272	0.8984794535	1.469982143
	H	1.890320494	-0.897161828	1.459042054
	H	-0.7198634594	1.224782765	2.942732919
	H	-1.721230773	1.211135941	1.45932039
	H	-0.1851258922	2.090052808	1.44782729
	H	-0.7298248267	-1.224605245	2.942155844
	H	-0.1761693451	-2.085087902	1.447916658
	H	-1.725077359	-1.205171982	1.469649709
-0.02	O	-0.0005251830668	-0.0001079082305	-0.0382197747
	N	0.0008712606859	-0.0004437406668	1.345250983
	C	1.413364624	-0.0002603373615	1.849200579
	C	-0.7061262666	1.223804949	1.850916926
	C	-0.7060350928	-1.223932625	1.850507016
	H	1.429145098	0.004068143846	2.94101397
	H	1.897616488	0.8948555757	1.464229578
	H	1.895088448	-0.8941362885	1.458676496
	H	-0.7167677426	1.229520791	2.942464607
	H	-1.721183823	1.205570028	1.458882408
	H	-0.181336202	2.09041868	1.453964304
	H	-0.7219389628	-1.2293631	2.942147536
	H	-0.176793067	-2.087912169	1.454107056
	H	-1.723083391	-1.202637308	1.463859738
0.02	O	-0.0003468869432	-0.0001968656735	-0.03821956164
	N	-0.0008328234139	0.0004122625748	1.345251255
	C	1.413212516	0.0002207084955	1.849995248
	C	-0.7067047054	1.223639222	1.850175117
	C	-0.706964121	-1.223405697	1.850454721
	H	1.423632808	-0.004214927746	2.941600649
	H	1.901808922	0.8876078199	1.452724446
	H	1.904624356	-0.8880852094	1.45794538
	H	-0.710576309	1.238996842	2.941927983
	H	-1.721089924	1.1944382	1.458006446
	H	-0.1737568215	2.091150424	1.466238332
	H	-0.706167235	-1.238878809	2.94213092
	H	-0.1780405108	-2.093560702	1.466487851
	H	-1.719095454	-1.19756796	1.452279794
0.04	O	-0.0002577388814	-0.0002413443949	-0.03821945512
	N	-0.001684865464	0.0008402641955	1.345251391
	C	1.413136462	0.000461231424	1.850392582
	C	-0.7069939247	1.223556358	1.849804212
	C	-0.7074286351	-1.223142232	1.850428573
	H	1.420876663	-0.008356463542	2.941893988
	H	1.903905138	0.8839839421	1.446971881
	H	1.90939231	-0.8850596699	1.457579822
	H	-0.7074805921	1.243734867	2.941659671
	H	-1.721042974	1.188872287	1.457568464
	H	-0.1699671313	2.091516296	1.472375346
	H	-0.6982813711	-1.243636663	2.942122613
	H	-0.1786642327	-2.096384969	1.472678248
	H	-1.717101485	-1.195033286	1.446489822

A. Additional data

Table A.7.: Distorted structures for mode 17

$\Delta x / \text{\AA}$	atom	$x / \text{\AA}$	$y / \text{\AA}$	$z / \text{\AA}$	
-0.04	O	-0.0003503157843	-0.0001409484535	-0.03821940751	
	N	-0.0009364319612	-0.0001422817971	1.345250911	
	C	1.409858561	0.000003503563629	1.848205247	
	C	-0.7069337538	1.224955588	1.851090328	
	C	-0.7074323693	-1.225568488	1.85134519	
	H	1.446745148	-0.0001505110582	2.940156341	
	H	1.913476922	0.8872736898	1.468691828	
	H	1.913472844	-0.8872106999	1.468540692	
	H	-0.7102767953	1.227111362	2.942642306	
	H	-1.719730388	1.194141981	1.454558682	
	H	-0.1740176214	2.08726979	1.456019899	
	H	-0.7082408464	-1.22299711	2.942848351	
	H	-0.1714862318	-2.08491718	1.453895447	
	H	-1.718897191	-1.191163753	1.451813587	
	-0.02	O	-0.0003931753947	-0.0001466677028	-0.03821953784
		N	-0.0004586066626	-0.00007901042154	1.345251015
C		1.4111573566	-0.000008155434685	1.84890158	
C		-0.7066746199	1.224338837	1.850818175	
C		-0.7069659881	-1.224618824	1.850913029	
H		1.436567051	-0.0001119515041	2.940731825	
H		1.906594813	0.8892526938	1.46358442	
H		1.906664623	-0.8891607245	1.463425815	
H		-0.7119744105	1.230685089	2.9424193	
H		-1.720433631	1.197073048	1.456501555	
H		-0.1757820666	2.089027171	1.458060608	
H		-0.7111469727	-1.228559032	2.94249379	
H		-0.1744515104	-2.087826808	1.45709645	
H		-1.719993306	-1.195633193	1.454941676	
0.02		O	-0.0004788946153	-0.0001581062012	-0.0382197985
		N	0.0004970439346	0.00004753232954	1.345251223
	C	1.415003575	-0.00003147343131	1.850294247	
	C	-0.7061563521	1.223105334	1.850273868	
	C	-0.7060332257	-1.222719497	1.850048708	
	H	1.416210856	-0.00003483239592	2.941882793	
	H	1.892830597	0.8932107018	1.453369604	
	H	1.893048181	-0.8930607735	1.453196061	
	H	-0.715369641	1.237832543	2.94197329	
	H	-1.721840116	1.20293518	1.460387299	
	H	-0.1793109569	2.092541933	1.462142027	
	H	-0.7169592252	-1.239682876	2.941784667	
	H	-0.1803820674	-2.093646063	1.463498456	
	H	-1.722185538	-1.204572074	1.461197855	
	0.04	O	-0.0005217542257	-0.0001638254505	-0.03821992883
		N	0.0009748692332	0.0001108037051	1.345251327
C		1.416718579	-0.00004313242963	1.85099058	
C		-0.7058972181	1.222488583	1.850001714	
C		-0.7055668445	-1.221769833	1.849616547	
H		1.406032758	0.000003727158151	2.942458277	
H		1.885948488	0.8951897058	1.448262196	
H		1.886239959	-0.895010798	1.448081183	
H		-0.7170672562	1.24140627	2.941750285	
H		-1.722543358	1.205866246	1.462330172	
H		-0.1810754021	2.094299314	1.464182737	
H		-0.7198653514	-1.245244798	2.941430106	
H		-0.183347346	-2.096555691	1.466699459	
H		-1.723281654	-1.209041515	1.464325944	

Table A.8.: Distorted structures for mode 18

$\Delta x / \text{\AA}$	atom	$x / \text{\AA}$	$y / \text{\AA}$	$z / \text{\AA}$
-0.04	O	-0.0004249597415	-0.0002380056067	-0.03821979388
	N	-0.0001072149655	0.000935812252	1.345251465
	C	1.412836997	-0.0002007707251	1.849414601
	C	-0.7080760523	1.22645824	1.851853492
	C	-0.7050288692	-1.221348118	1.849359013
	H	1.429069327	0.0006320705469	2.941155973
	H	1.901010136	0.8909415922	1.459955205
	H	1.902164108	-0.8903662902	1.459525184
	H	-0.703946199	1.217953702	2.943266929
	H	-1.717926946	1.187332976	1.448820061
	H	-0.1678191057	2.081423546	1.450583435
	H	-0.7225751125	-1.248006888	2.941218681
	H	-0.1858933401	-2.098861325	1.468424298
	H	-1.72382647	-1.210807271	1.46636543
-0.02	O	-0.0004304973733	-0.0001951962793	-0.03821973103
	N	-0.00004399816475	0.000460036603	1.345251292
	C	1.413062784	-0.0001102925791	1.849506257
	C	-0.7072457691	1.225090163	1.851199757
	C	-0.7057642381	-1.222508639	1.849919941
	H	1.42772914	0.0002793392985	2.941231641
	H	1.90036142	0.891086645	1.459216109
	H	1.901010255	-0.8907385196	1.458918061
	H	-0.7088091124	1.226106259	2.942731612
	H	-1.71953191	1.193668545	1.453632244
	H	-0.1726828087	2.086104049	1.455342377
	H	-0.7183141057	-1.241063921	2.941678954
	H	-0.1816550645	-2.09479888	1.464360876
	H	-1.722457946	-1.205454952	1.462217598
0.02	O	-0.0004415726367	-0.0001095776247	-0.03821960532
	N	0.00008243543675	-0.000491514695	1.345250946
	C	1.413514357	0.00007066371307	1.84968957
	C	-0.7055852028	1.222354008	1.849892286
	C	-0.7072349757	-1.224829682	1.851041796
	H	1.425048766	-0.0004261231985	2.941382977
	H	1.89906399	0.8913767506	1.457737915
	H	1.898702549	-0.8914829784	1.457703814
	H	-0.7185349392	1.242411373	2.941660978
	H	-1.722741837	1.206339683	1.46325661
	H	-0.1824102148	2.095465056	1.464860259
	H	-0.7097920921	-1.227177987	2.942599502
	H	-0.1731785133	-2.086673991	1.456234031
	H	-1.719720898	-1.194750315	1.453921933
0.04	O	-0.0004471102685	-0.00006676829732	-0.03821954246
	N	0.0001456522375	-0.000967290344	1.345250772
	C	1.413740144	0.0001611418591	1.849781226
	C	-0.7047549197	1.220985931	1.849238551
	C	-0.7079703446	-1.225990203	1.851602724
	H	1.42370858	-0.0007788544469	2.941458645
	H	1.898415275	0.8915218034	1.456998819
	H	1.897548695	-0.8918552077	1.457096691
	H	-0.7233978526	1.25056393	2.941125661
	H	-1.724346801	1.212675252	1.468068793
	H	-0.1872739178	2.100145559	1.4696192
	H	-0.7055310853	-1.220235021	2.943059776
	H	-0.1689402377	-2.082611546	1.452170609
	H	-1.718352374	-1.189397996	1.449774101

A. Additional data

Table A.9.: Distorted structures for mode 25

$\Delta x / \text{\AA}$	atom	$x / \text{\AA}$	$y / \text{\AA}$	$z / \text{\AA}$
-0.04	O	-0.000466425062	-0.0001444680882	-0.05333279963
	N	-0.00007222709247	-0.0001131552036	1.359271386
	C	1.410832762	-0.00005118037617	1.851687865
	C	-0.7051975093	1.221524937	1.852602443
	C	-0.7051913902	-1.221379982	1.852431419
	H	1.441317342	-0.00002091909366	2.94348491
	H	1.892676327	0.8900927104	1.452775235
	H	1.89315061	-0.8898920814	1.452687588
	H	-0.7210183277	1.247131116	2.944351082
	H	-1.716730801	1.194858667	1.452850347
	H	-0.1749632673	2.084069836	1.454410365
	H	-0.7212358295	-1.246570635	2.944188479
	H	-0.1749834184	-2.084199664	1.454763366
	H	-1.716654177	-1.194776069	1.45254056
-0.02	O	-0.0004512300335	-0.0001484275201	-0.0457762339
	N	-0.00002650422823	-0.00006444712482	1.352261252
	C	1.412060666	-0.00003549740458	1.850642889
	C	-0.7058064976	1.222623511	1.851574232
	C	-0.7058454986	-1.222524572	1.851456144
	H	1.433853147	-0.00004715552183	2.942396109
	H	1.896194516	0.8906622041	1.455626124
	H	1.896503506	-0.8905014152	1.455499263
	H	-0.7173451767	1.240694966	2.943273689
	H	-1.718933837	1.19743139	1.455647387
	H	-0.1762548895	2.087427194	1.457255841
	H	-0.7176444642	-1.240345795	2.943163854
	H	-0.1762001037	-2.08746805	1.45753041
	H	-1.7188718	-1.197439352	1.455305163
0.02	O	-0.0004208399765	-0.0001563463839	-0.03066310244
	N	0.00006494150023	0.00003296903282	1.338240985
	C	1.414516474	-0.000004131461417	1.848552938
	C	-0.7070244743	1.22482066	1.849517811
	C	-0.7071537152	-1.22481375	1.849505593
	H	1.418924759	-0.00009962837817	2.940218509
	H	1.903230894	0.8918011915	1.4613279
	H	1.903209298	-0.8917200827	1.461122613
	H	-0.7099988748	1.227822666	2.941118902
	H	-1.72333991	1.202576837	1.461241467
	H	-0.178838134	2.09414191	1.462946794
	H	-0.7104617336	-1.227896114	2.941114603
	H	-0.1786334741	-2.094004821	1.463064497
	H	-1.723307045	-1.202765916	1.460834369
0.04	O	-0.000405644948	-0.0001603058158	-0.02310653671
	N	0.0001106643645	0.00008167711164	1.331230852
	C	1.415744378	0.00001155151017	1.847507962
	C	-0.7076334627	1.225919234	1.8484896
	C	-0.7078078236	-1.225958339	1.848530317
	H	1.411460564	-0.0001258648063	2.939129709
	H	1.906749083	0.8923706852	1.464178789
	H	1.906562193	-0.8923294165	1.463934287
	H	-0.7063257239	1.221386516	2.940041508
	H	-1.725542946	1.205149561	1.464038507
	H	-0.1801297562	2.097499268	1.465792271
	H	-0.7068703683	-1.221671273	2.940089977
	H	-0.1798501594	-2.097273207	1.465831541
	H	-1.725524667	-1.205429198	1.463598971

Table A.10.: Thermodynamic data for mode 10 at 1 bar.

$\Delta x/\text{pm}$	Delta μ^{ex}/J	$\Delta G^{\text{sol}}/\text{J}$	$\Delta E^{\text{sol}}/\text{J}$
-4	0.	$4.945301679635806 \cdot 10^{-22}$	$2.123040660427613 \cdot 10^{-21}$
-2	$8.056923291999965 \cdot 10^{-22}$	0.	$8.22818163429425 \cdot 10^{-22}$
0	$1.6516061134711056 \cdot 10^{-21}$	$1.4979013082612314 \cdot 10^{-22}$	$1.26694509292296 \cdot 10^{-22}$
2	$2.493069836399994 \cdot 10^{-21}$	$8.645662916127524 \cdot 10^{-22}$	0.
4	$3.1770888468000018 \cdot 10^{-21}$	$2.075088325029313 \cdot 10^{-21}$	$5.265099709887211 \cdot 10^{-22}$

Table A.11.: Thermodynamic data for mode 10 at 100 bar.

$\Delta x/\text{pm}$	$\Delta\mu^{\text{ex}}/\text{J}$	$\Delta G^{\text{sol}}/\text{J}$	$\Delta E^{\text{sol}}/\text{J}$
-4	0.	$4.973508937608596 \cdot 10^{-22}$	$2.165650291180973 \cdot 10^{-21}$
-2	$8.169821791999932 \cdot 10^{-22}$	0.	$8.513172184872585 \cdot 10^{-22}$
0	$1.6823651812259137 \cdot 10^{-21}$	$1.556263233847572 \cdot 10^{-22}$	$1.4156053921142918 \cdot 10^{-22}$
2	$2.545169888800002 \cdot 10^{-21}$	$8.768704912062301 \cdot 10^{-22}$	0.
4	$3.2455435496000017 \cdot 10^{-21}$	$2.092346163463706 \cdot 10^{-21}$	$5.151020118496679 \cdot 10^{-22}$

Table A.12.: Thermodynamic data for mode 10 at 5 kbar.

$\Delta x/\text{pm}$	$\Delta\mu^{\text{ex}}/\text{J}$	$\Delta G^{\text{sol}}/\text{J}$	$\Delta E^{\text{sol}}/\text{J}$
-4	0.	$4.5378944158306075 \cdot 10^{-22}$	$2.61437493237752 \cdot -21$
-2	$1.0146969800000009 \cdot 10^{-21}$	0.	$1.1458885107919127 \cdot -21$
0	$2.11554210485 \cdot 10^{-21}$	$2.4312299437598356 \cdot 10^{-22}$	$2.8816637639285775 \cdot -22$
2	$3.2163775247999996 \cdot 10^{-21}$	$1.055792034105484 \cdot 10^{-21}$	0.
4	$4.1126804532000034 \cdot 10^{-21}$	$2.3448497381414377 \cdot 10^{-21}$	$3.9275477537766464 \cdot -22$

A. Additional data

Table A.13.: Thermodynamic data for mode 10 at 10 kbar.

$\Delta x/\text{pm}$	$\Delta\mu^{\text{ex}}/\text{J}$	$\Delta G^{\text{sol}}/\text{J}$	$\Delta E^{\text{sol}}/\text{J}$
-4	0.	$4.748476172311407 \cdot 10^{-22}$	$2.5865011612108923 \cdot 10^{-21}$
-2	$9.877263967999996 \cdot 10^{-22}$	0.	$1.1239201996934237 \cdot 10^{-21}$
0	$2.066292772529539 \cdot 10^{-21}$	$2.3207322561677016 \cdot 10^{-22}$	$2.77427054179348 \cdot 10^{-22}$
2	$3.1449492492 \cdot 10^{-21}$	$1.0333026527689649 \cdot 10^{-21}$	0.
4	$4.023056413199994 \cdot 10^{-21}$	$2.3126823499094923 \cdot 10^{-21}$	$4.012725331478704 \cdot 10^{-22}$

Table A.14.: Thermodynamic data for mode 11 at 1 bar.

$\Delta x/\text{pm}$	$\Delta\mu^{\text{ex}}/\text{J}$	$\Delta G^{\text{sol}}/\text{J}$	$\Delta E^{\text{sol}}/\text{J}$
-4	$1.1584428240000165 \cdot 10^{-22}$	$1.1820369987835957 \cdot 10^{-21}$	$1.072982320802841 \cdot 10^{-21}$
-2	0.	$2.7538909395629057 \cdot 10^{-22}$	$2.8217869848016364 \cdot 10^{-22}$
0	$6.78960387110319 \cdot 10^{-24}$	0.	0.
2	$2.3774687199996018 \cdot 10^{-23}$	$2.877002412449758 \cdot 10^{-22}$	$2.707151585683112 \cdot 10^{-22}$
4	$5.260027959999835 \cdot 10^{-23}$	$1.1803070463427535 \cdot 10^{-21}$	$1.1344963712722375 \cdot 10^{-21}$

Table A.15.: Thermodynamic data for mode 11 at 100 bar.

$\Delta x/\text{pm}$	$\Delta\mu^{\text{ex}}/\text{J}$	$\Delta G^{\text{sol}}/\text{J}$	$\Delta E^{\text{sol}}/\text{J}$
-4	$1.2220133640001634 \cdot 10^{-22}$	$1.1870112718592088 \cdot 10^{-21}$	$1.0713931545928165 \cdot 10^{-21}$
-2	0.	$2.751874049025766 \cdot 10^{-22}$	$2.8177062408655166 \cdot 10^{-22}$
0	$6.583218425917013 \cdot 10^{-24}$	0.	0.
2	$2.4365233200008958 \cdot 10^{-23}$	$2.878181418320722 \cdot 10^{-22}$	$2.700361276114805 \cdot 10^{-22}$
4	$6.118751320001574 \cdot 10^{-23}$	$1.1880464642456311 \cdot 10^{-21}$	$1.1334421700990124 \cdot 10^{-21}$

Table A.16.: Thermodynamic data for mode 11 at 5 kbar.

$\Delta x/\text{pm}$	Delta μ^{ex}/J	$\Delta G^{\text{sol}}/\text{J}$	$\Delta E^{\text{sol}}/\text{J}$
-4	$1.7702484799999897 \cdot 10^{-22}$	$1.2251688945048268 \cdot 10^{-21}$	$1.0541168911286908 \cdot 10^{-21}$
-2	0.	$2.7697434169698363 \cdot 10^{-22}$	$2.829541337616387 \cdot 10^{-22}$
0	$5.972840849997161 \cdot 10^{-24}$	0.	0.
2	$3.4112716000002985 \cdot 10^{-23}$	$2.9534379598179014 \cdot 10^{-22}$	$2.672039246768914 \cdot 10^{-22}$
4	$1.1009166960000064 \cdot 10^{-22}$	$1.2378482645119141 \cdot 10^{-21}$	$1.1337294395168902 \cdot 10^{-21}$

Table A.17.: Thermodynamic data for mode 11 at 10 kbar.

$\Delta x/\text{pm}$	Delta μ^{ex}/J	$\Delta G^{\text{sol}}/\text{J}$	$\Delta E^{\text{sol}}/\text{J}$
-4	$1.7705958600000008 \cdot 10^{-22}$	$1.2278051195414405 \cdot 10^{-21}$	$1.0578252424276636 \cdot 10^{-21}$
-2	0.	$2.762340332083267 \cdot 10^{-22}$	$2.833137419217405 \cdot 10^{-22}$
0	$7.079713329542853 \cdot 10^{-24}$	0.	0.
2	$3.5307703199999503 \cdot 10^{-23}$	$2.9670861034758503 \cdot 10^{-22}$	$2.6848061598260974 \cdot 10^{-22}$
4	$1.1762981560000051 \cdot 10^{-22}$	$1.2469874431214727 \cdot 10^{-21}$	$1.1364303888158402 \cdot 10^{-21}$

Table A.18.: Thermodynamic data for mode 12 at 1 bar.

$\Delta x/\text{pm}$	Delta μ^{ex}/J	$\Delta G^{\text{sol}}/\text{J}$	$\Delta E^{\text{sol}}/\text{J}$
-4	$4.894584199999913 \cdot 10^{23}$	$1.128220889291187 \cdot 10^{21}$	$1.1068588183900061 \cdot 10^{21}$
-2	$1.1977662399990712 \cdot 10^{23}$	$2.708592588037918 \cdot 10^{22}$	$2.864653676530585 \cdot 10^{22}$
0	$2.758377067110527 \cdot 10^{23}$	0.	0.
2	$6.504343119999544 \cdot 10^{23}$	$3.425237527374073 \cdot 10^{22}$	$3.0506409272426914 \cdot 10^{22}$
4	0.	$1.1773821066950836 \cdot 10^{21}$	$1.2049658779990254 \cdot 10^{21}$

Table A.19.: Thermodynamic data for mode 12 at 100 bar.

$\Delta x/\text{pm}$	Delta μ^{ex}/J	$\Delta G^{\text{sol}}/\text{J}$	$\Delta E^{\text{sol}}/\text{J}$
-4	$4.158138600000981 \cdot 10^{-23}$	$1.1304369648403125 \cdot 10^{-21}$	$1.1064229538072098 \cdot 10^{-21}$
-2	$2.132913199997599 \cdot 10^{-24}$	$2.7036577069288224 \cdot 10^{-22}$	$2.858002320866428 \cdot 10^{-22}$
0	$1.7567374025909746 \cdot 10^{-23}$	0.	0.
2	$6.263261399999529 \cdot 10^{-23}$	$3.490126026606583 \cdot 10^{-22}$	$3.039473632802527 \cdot 10^{-22}$
4	0.	$1.1878241409572193 \cdot 10^{-21}$	$1.2053915157890465 \cdot 10^{-21}$

Table A.20.: Thermodynamic data for mode 12 at 5 kbar.

$\Delta x/\text{pm}$	$\Delta \mu^{\text{ex}}/\text{J}$	$\Delta G^{\text{sol}}/\text{J}$	$\Delta E^{\text{sol}}/\text{J}$
-4	$6.266040439999675 \cdot 10^{-23}$	$1.1476823116622713 \cdot 10^{-21}$	$1.1028404098481864 \cdot 10^{-21}$
-2	0.	$2.70130955594821 \cdot 10^{-22}$	$2.8794251068416096 \cdot 10^{-22}$
0	$1.7811551249992617 \cdot 10^{-23}$	0.	0.
2	$9.969111239999039 \cdot 10^{-23}$	$3.8781635208588937 \cdot 10^{-22}$	$3.0593679475257317 \cdot 10^{-22}$
4	$3.885097919999289 \cdot 10^{-23}$	$1.2456295764508854 \cdot 10^{-21}$	$1.2245901522237378 \cdot 10^{-21}$

Table A.21.: Thermodynamic data for mode 12 at 10 kbar.

$\Delta x/\text{pm}$	$\Delta \mu^{\text{ex}}/\text{J}$	$\Delta G^{\text{sol}}/\text{J}$	$\Delta E^{\text{sol}}/\text{J}$
-4	$6.159047399999476 \cdot 10^{-23}$	$1.1479910907532365 \cdot 10^{-21}$	$1.1054232499063306 \cdot 10^{-21}$
-2	0.	$2.697727652149811 \cdot 10^{-22}$	$2.8880234579945516 \cdot 10^{-22}$
0	$1.902263772953776 \cdot 10^{-23}$	0.	0.
2	$1.0646502239999686 \cdot 10^{-22}$	$3.9624687564504353 \cdot 10^{-22}$	$3.0880448636992065 \cdot 10^{-22}$
4	$5.176656759999672 \cdot 10^{-23}$	$1.2602504116373816 \cdot 10^{-21}$	$1.2275064771158921 \cdot 10^{-21}$

Table A.22.: Thermodynamic data for mode 17 at 1 bar.

$\Delta x/\text{pm}$	$\Delta \mu^{\text{ex}}/\text{J}$	$\Delta G^{\text{sol}}/\text{J}$	$\Delta E^{\text{sol}}/\text{J}$
-4	$1.3594654528895428 \cdot 10^{-23}$	$1.1353699694465298 \cdot 10^{-21}$	$1.1217753156855508 \cdot 10^{-21}$
-2	$7.390447728900805 \cdot 10^{-24}$	$2.80071776233987 \cdot 10^{-22}$	$2.726813292935499 \cdot 10^{-22}$
0	0.	0.	0.
2	$3.236012212888732 \cdot 10^{-23}$	$3.0068530550245846 \cdot 10^{-22}$	$2.683182364594486 \cdot 10^{-22}$
4	$9.549991092889117 \cdot 10^{-23}$	$1.2411610746421219 \cdot 10^{-21}$	$1.1456542169336945 \cdot 10^{-21}$

A. Additional data

Table A.23.: Thermodynamic data for of mode 17 at 100 bar.

$\Delta x/\text{pm}$	$\Delta\mu^{\text{ex}}/\text{J}$	$\Delta G^{\text{sol}}/\text{J}$	$\Delta E^{\text{sol}}/\text{J}$
-4	$1.5072450774082135 \cdot 10^{-23}$	$1.1362590537492526 \cdot 10^{-21}$	$1.1211866037803416 \cdot 10^{-21}$
-2	$7.430090774090267 \cdot 10^{-24}$	$2.795227073502783 \cdot 10^{-22}$	$2.7209261738834066 \cdot 10^{-22}$
0	0.	0.	0.
2	$3.4803634774094624 \cdot 10^{-23}$	$3.0221356888958675 \cdot 10^{-22}$	$2.67409934913429 \cdot 10^{-22}$
4	$1.10643636374091 \cdot 10^{-22}$	$1.2552158609111397 \cdot 10^{-21}$	$1.1445722251768547 \cdot 10^{-21}$

Table A.24.: Thermodynamic data for mode 17 at 5 kbar.

$\Delta x/\text{pm}$	$\Delta\mu^{\text{ex}}/\text{J}$	$\Delta G^{\text{sol}}/\text{J}$	$\Delta E^{\text{sol}}/\text{J}$
-4	$2.2380314750004446 \cdot 10^{-23}$	$1.1484604428758899 \cdot 10^{-21}$	$1.1260801318147094 \cdot 10^{-21}$
-2	$7.116437550003749 \cdot 10^{-24}$	$2.7898914549981397 \cdot 10^{-22}$	$2.718796594565956 \cdot 10^{-22}$
0	0.	0.	0.
2	$4.900351795000553 \cdot 10^{-23}$	$3.146789668842353 \cdot 10^{-22}$	$2.656754526360537 \cdot 10^{-22}$
4	$1.7918069915000114 \cdot 10^{-22}$	$1.3282504356459534 \cdot 10^{-21}$	$1.1490697403036361 \cdot 10^{-21}$

Table A.25.: Thermodynamic data for mode 17 at 10 kbar.

$\Delta x/\text{pm}$	$\Delta\mu^{\text{ex}}/\text{J}$	$\Delta G^{\text{sol}}/\text{J}$	$\Delta E^{\text{sol}}/\text{J}$
-4	$2.3823211470460177 \cdot 10^{-23}$	$1.1493945060552761 \cdot 10^{-21}$	$1.1255782374047785 \cdot 10^{-21}$
-2	$5.412071470456789 \cdot 10^{-24}$	$2.7795009025875396 \cdot 10^{-22}$	$2.7253801436910045 \cdot 10^{-22}$
0	0.	0.	0.
2	$4.9967030270460174 \cdot 10^{-23}$	$3.1690528342563234 \cdot 10^{-22}$	$2.6693824874857224 \cdot 10^{-22}$
4	$1.8739750587046335 \cdot 10^{-22}$	$1.3428226375576428 \cdot 10^{-21}$	$1.15543207468706 \cdot 10^{-21}$

Table A.26.: Thermodynamic data for mode 18 at 1 bar.

$\Delta x/\text{pm}$	$\Delta\mu^{\text{ex}}/\text{J}$	$\Delta G^{\text{sol}}/\text{J}$	$\Delta E^{\text{sol}}/\text{J}$
-4	0.	$1.1123803611548183 \cdot 10^{-21}$	$1.1133131388853594 \cdot 10^{-21}$
-2	$4.6041745199991145 \cdot 10^{-23}$	$3.031794939637196 \cdot 10^{-22}$	$2.580774741408233 \cdot 10^{-22}$
0	$9.327770711027257 \cdot 10^{-25}$	0.	0.
2	$4.461748719999463 \cdot 10^{-23}$	$3.0225546312289555 \cdot 10^{-22}$	$2.5857770129323093 \cdot 10^{-22}$
4	$2.029393959999897 \cdot 10^{-23}$	$1.1259768143075221 \cdot 10^{-21}$	$1.1066156526076174 \cdot 10^{-21}$

Table A.27.: Thermodynamic data for mode 18 at 100 bar.

$\Delta x/\text{pm}$	$\Delta\mu^{\text{ex}}/\text{J}$	$\Delta G^{\text{sol}}/\text{J}$	$\Delta E^{\text{sol}}/\text{J}$
-4	$5.658619740910933 \cdot 10^{-25}$	$1.113255550067126 \cdot 10^{-21}$	$1.1126896888985431 \cdot 10^{-21}$
-2	$4.7851227574093346 \cdot 10^{-23}$	$3.0436037752085315 \cdot 10^{-22}$	$2.5650915062199085 \cdot 10^{-22}$
0	0.	0.	0.
2	$4.6941091974087705 \cdot 10^{-23}$	$3.039713117168286 \cdot 10^{-22}$	$2.5703022046559056 \cdot 10^{-22}$
4	$2.1304447974090254 \cdot 10^{-23}$	$1.1272827546034538 \cdot 10^{-21}$	$1.1059783074276013 \cdot 10^{-21}$

Table A.28.: Thermodynamic data for mode 18 at 5 kbar.

$\Delta x/\text{pm}$	$\Delta\mu^{\text{ex}}/\text{J}$	$\Delta G^{\text{sol}}/\text{J}$	$\Delta E^{\text{sol}}/\text{J}$
-4	$8.422586350000083 \cdot 10^{-24}$	$1.1249289216549561 \cdot 10^{-21}$	$1.1164993914688969 \cdot 10^{-21}$
-2	$6.854016915000781 \cdot 10^{-23}$	$3.1827087600271023 \cdot 10^{-22}$	$2.4973765834450165 \cdot 10^{-22}$
0	0.	0.	0.
2	$6.826226515000526 \cdot 10^{-23}$	$3.183403519687092 \cdot 10^{-22}$	$2.500780906765041 \cdot 10^{-22}$
4	$3.40661779499979 \cdot 10^{-23}$	$1.1419366466117529 \cdot 10^{-21}$	$1.107870472350308 \cdot 10^{-21}$

Table A.29.: Thermodynamic data for mode 18 at 10 kbar.

$\Delta x/\text{pm}$	$\Delta\mu^{\text{ex}}/\text{J}$	$\Delta G^{\text{sol}}/\text{J}$	$\Delta E^{\text{sol}}/\text{J}$
-4	$9.809902270458916 \cdot 10^{-24}$	$1.1272941903255663 \cdot 10^{-21}$	$1.1174842835202044 \cdot 10^{-21}$
-2	$6.833648467046137 \cdot 10^{-23}$	$3.1987885634810905 \cdot 10^{-22}$	$2.5154931468701948 \cdot 10^{-22}$
0	0.	0.	0.
2	$6.823921827046229 \cdot 10^{-23}$	$3.1933694361610204 \cdot 10^{-22}$	$2.510977206122035 \cdot 10^{-22}$
4	$3.5328437070456185 \cdot 10^{-23}$	$1.1442046487327493 \cdot 10^{-21}$	$1.1088762070928076 \cdot 10^{-21}$

Table A.30.: Thermodynamic data for mode 25 at 1 bar.

$\Delta x/\text{pm}$	$\Delta\mu^{\text{ex}}/\text{J}$	$\Delta G^{\text{sol}}/\text{J}$	$\Delta E^{\text{sol}}/\text{J}$
-4	0.	$5.78685752046287 \cdot 10^{-21}$	$7.462257365355164 \cdot 10^{-21}$
-2	$4.237758095999984 \cdot 10^{-22}$	$2.8591597231898566 \cdot 10^{-21}$	$4.1107698632113624 \cdot 10^{-21}$
0	$6.90634924271108 \cdot 10^{-22}$	$8.49594088509955 \cdot 10^{-22}$	$1.834352060876512 \cdot 10^{-21}$
2	$1.2355820268000029 \cdot 10^{-21}$	0.	$4.398108705187551 \cdot 10^{-22}$
4	$2.056517390400005 \cdot 10^{-21}$	$3.8112449334462997 \cdot 10^{-22}$	0.

Table A.31.: Thermodynamic data for mode 25 at 100 bar.

$\Delta x/\text{pm}$	$\Delta\mu^{\text{ex}}/\text{J}$	$\Delta G^{\text{sol}}/\text{J}$	$\Delta E^{\text{sol}}/\text{J}$
-4	0.	$5.788101140747289 \cdot 10^{-21}$	$7.523055812881734 \cdot 10^{-21}$
-2	$4.326478947999986 \cdot 10^{-22}$	$2.851301987589679 \cdot 10^{-21}$	$4.153608764948342 \cdot 10^{-21}$
0	$7.1428659722591015 \cdot 10^{-22}$	$8.434039853391072 \cdot 10^{-22}$	$1.8640720596231832 \cdot 10^{-21}$
2	$1.2803384660000048 \cdot 10^{-21}$	0.	$4.546162060714863 \cdot 10^{-22}$
4	$2.1265283556000023 \cdot 10^{-21}$	$3.915736835612521 \cdot 10^{-22}$	0.

Table A.32.: Thermodynamic data for mode 25 at 5 kbar.

$\Delta x/\text{pm}$	$\Delta\mu^{\text{ex}}/\text{J}$	$\Delta G^{\text{sol}}/\text{J}$	$\Delta E^{\text{sol}}/\text{J}$
-4	0.	$5.8161486019275216 \cdot 10^{-21}$	$8.058250283564628 \cdot 10^{-21}$
-2	$5.561623275999956 \cdot 10^{-22}$	$2.824435618423074 \cdot 10^{-21}$	$4.510374972189182 \cdot 10^{-21}$
0	$9.405848356499955 \cdot 10^{-22}$	$8.083936254323556 \cdot 10^{-22}$	$2.1099104676544597 \cdot 10^{-21}$
2	$1.661817286799998 \cdot 10^{-21}$	0.	$5.8029134239952275 \cdot 10^{-22}$
4	$2.7027136664000017 \cdot 10^{-21}$	$4.606119845996009 \cdot 10^{-22}$	0.

A. Additional data

Table A.33.: Thermodynamic data for mode 25 at 10 kbar.

$\Delta x/\text{pm}$	$\Delta\mu^{\text{ex}}/\text{J}$	$\Delta G^{\text{sol}}/\text{J}$	$\Delta E^{\text{sol}}/\text{J}$
-4	0.	$5.9242185199911704 \cdot 10^{-21}$	$7.967688317412968 \cdot 10^{-21}$
-2	$4.921610364000007 \cdot 10^{-22}$	$2.8869292803088784 \cdot 10^{-21}$	$4.4382380414895584 \cdot 10^{-21}$
0	$8.223527829295427 \cdot 10^{-22}$	$8.386751292576911 \cdot 10^{-22}$	$2.05979214838844 \cdot 10^{-21}$
2	$1.4883774004000006 \cdot 10^{-21}$	0.	$5.550923972057534 \cdot 10^{-22}$
4	$2.4755549368000075 \cdot 10^{-21}$	$4.32085139352583 \cdot 10^{-22}$	0.

A. Additional data

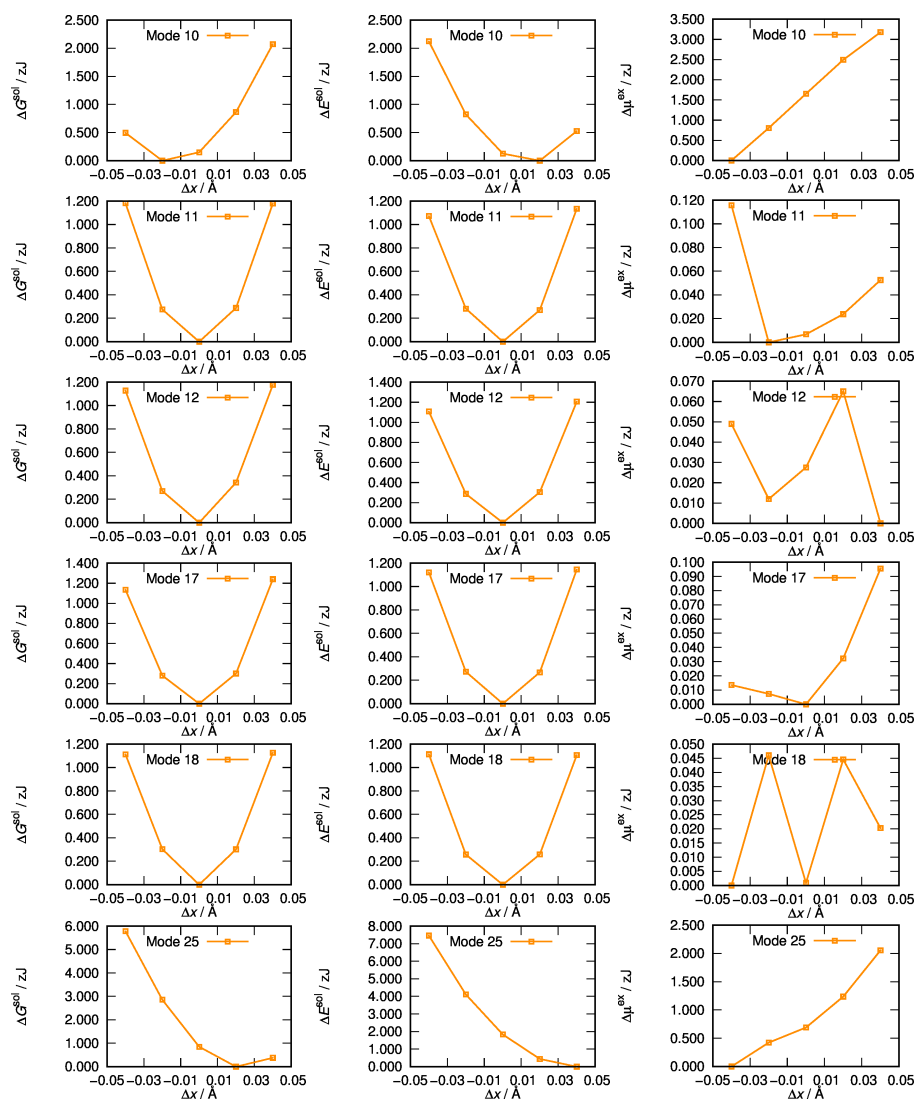


Figure A.1.: Gibbs energy (left column), solute electronic energy (center column) and chemical excess potential (right) column for the analyzed normal modes of vibration at 1 bar. Every plot is normalized to the lowest occurring value.

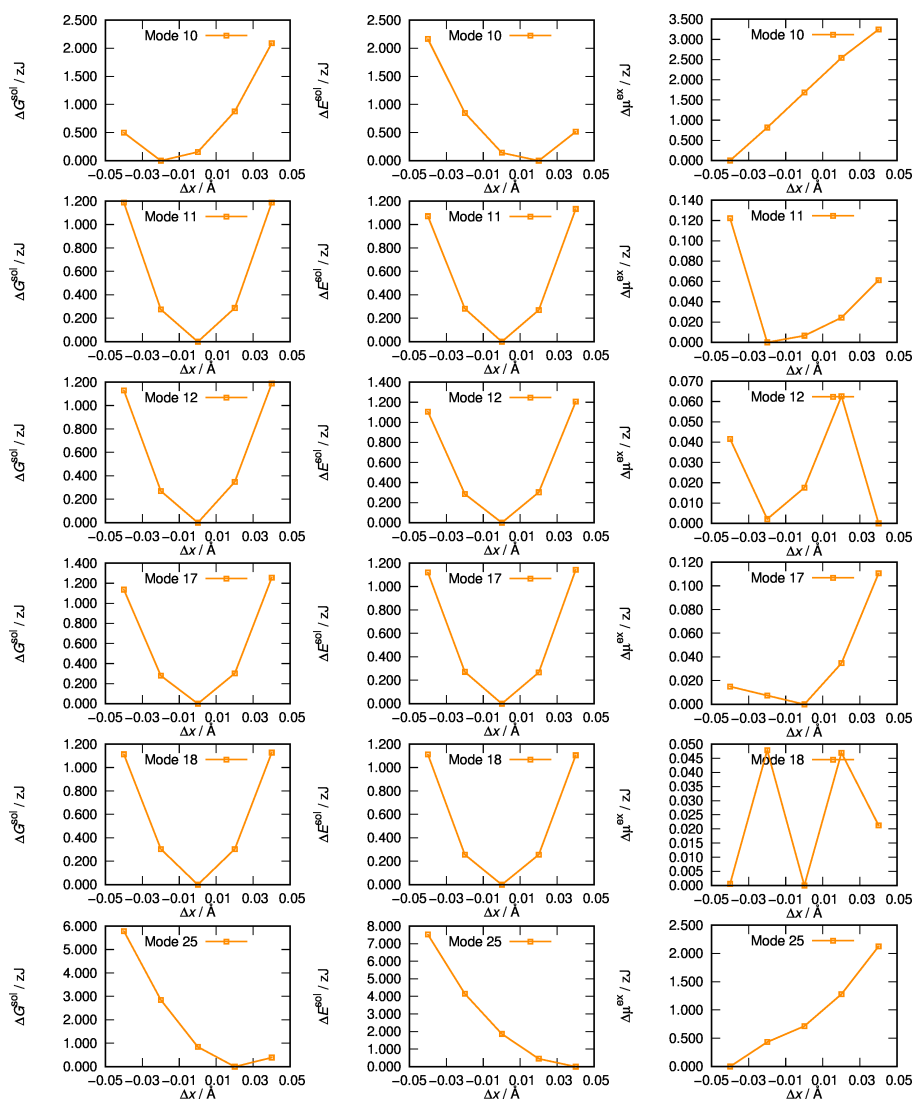


Figure A.2.: Gibbs energy (left column), solute electronic energy (center column) and chemical excess potential (right) column for the analyzed normal modes of vibration at 100 bar. Every plot is normalized on the lowest occurring value.

A. Additional data

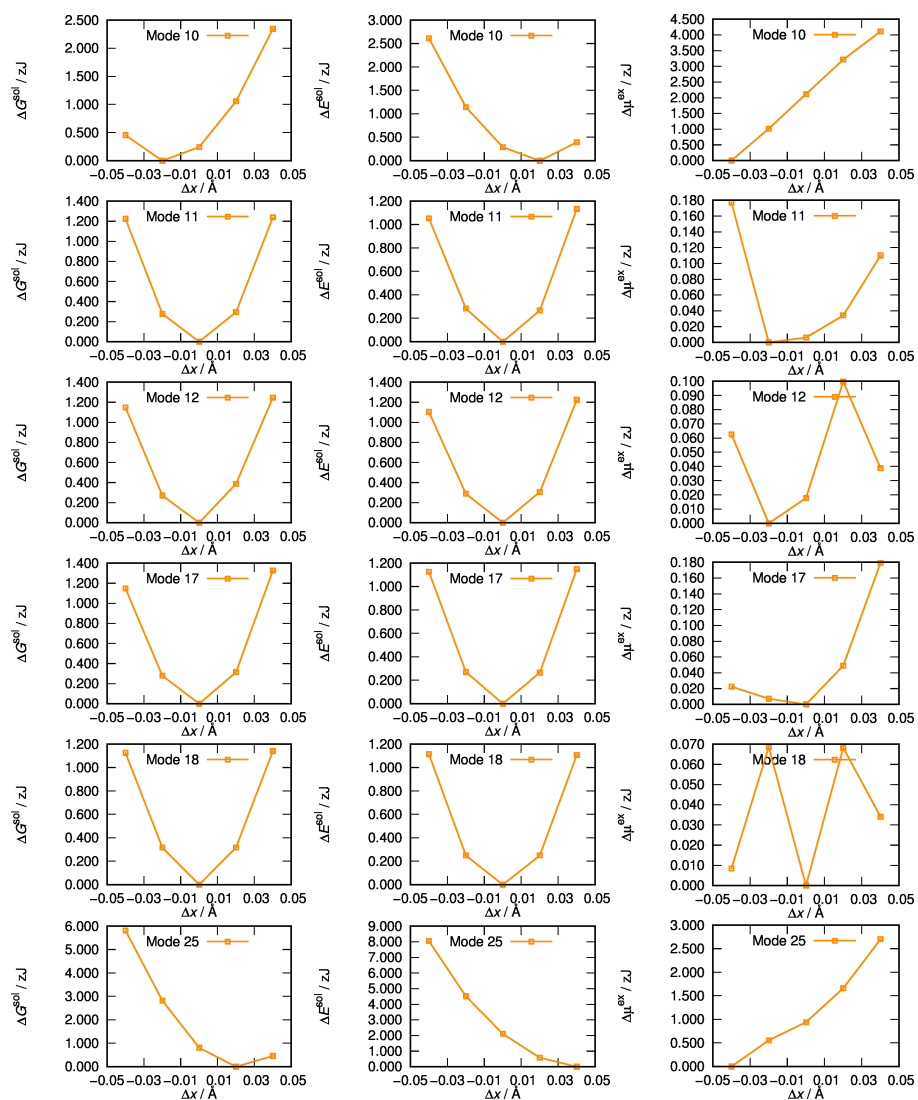


Figure A.3.: Gibbs energy (left column), solute electronic energy (center column) and chemical excess potential (right) column for the analyzed normal modes of vibration at 5 kbar. Every plot is normalized on the lowest occurring value.

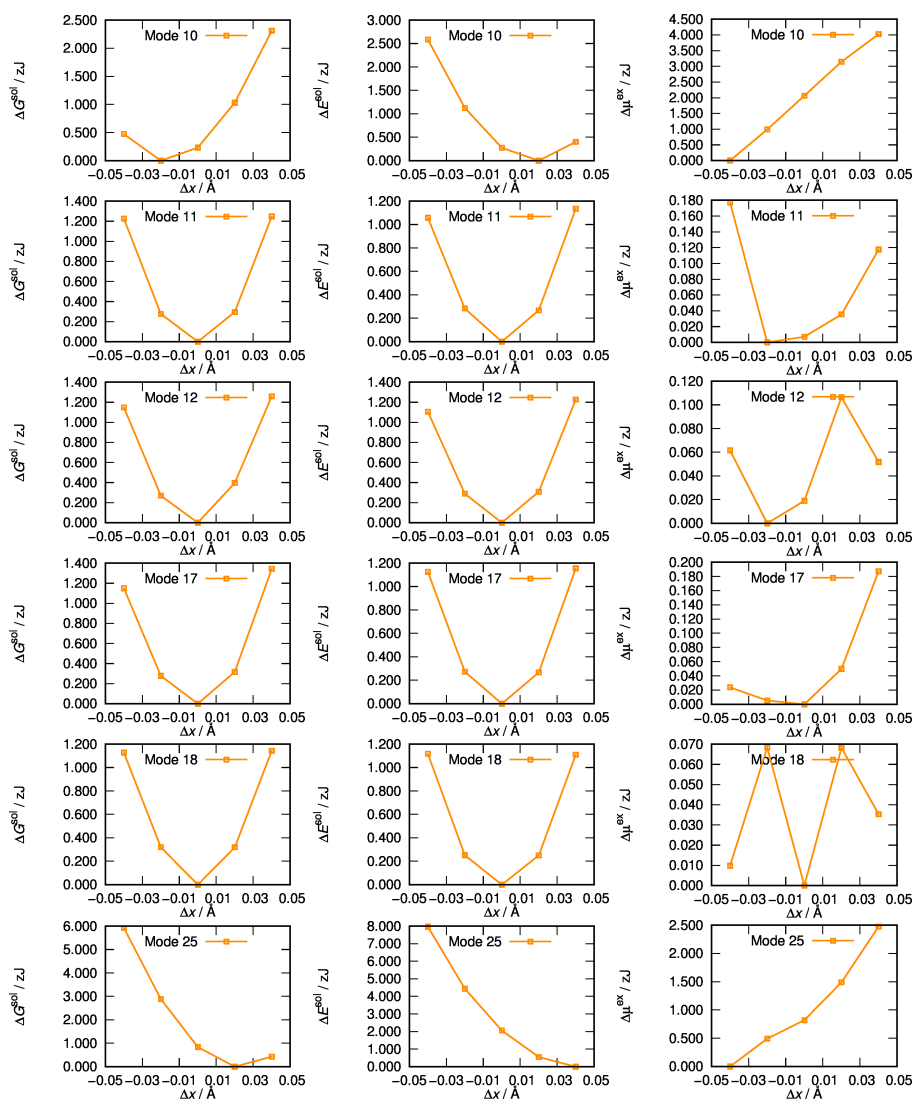


Figure A.4.: Gibbs energy (left column), solute electronic energy (center column) and chemical excess potential (right) column for the analyzed normal modes of vibration at 1 bar. Every plot is normalized on the lowest occurring value.

A. Additional data

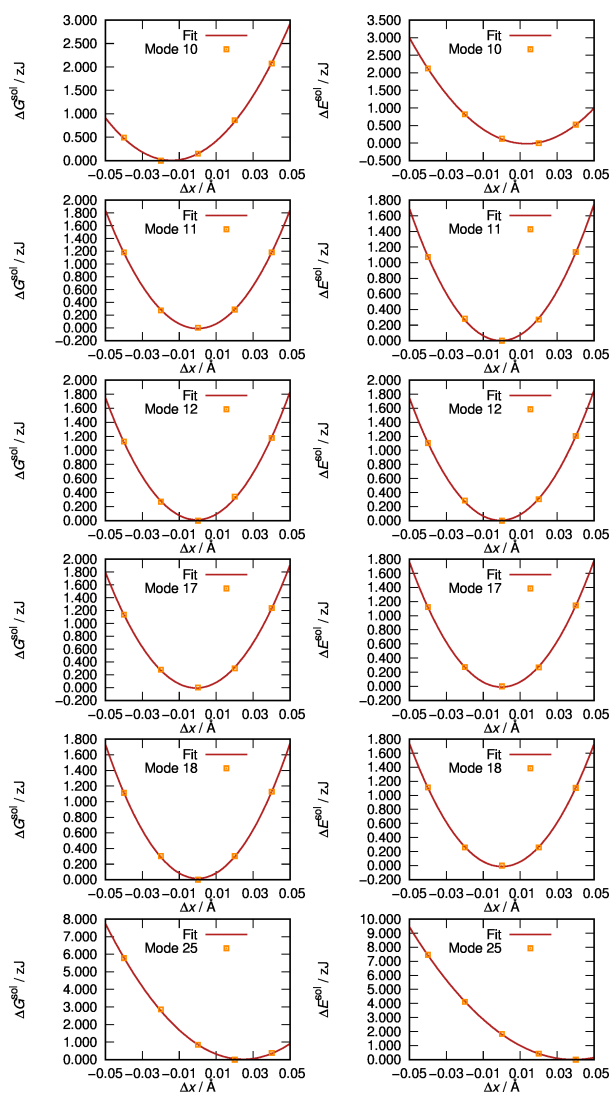


Figure A.5.: Gibbs energy (left) and solute electronic energy (right) from EC-RISM calculations on the distorted TMAO molecule at 1 bar. Calculated data points are shown as orange points, the red lines represent a fitted second order polynomial.

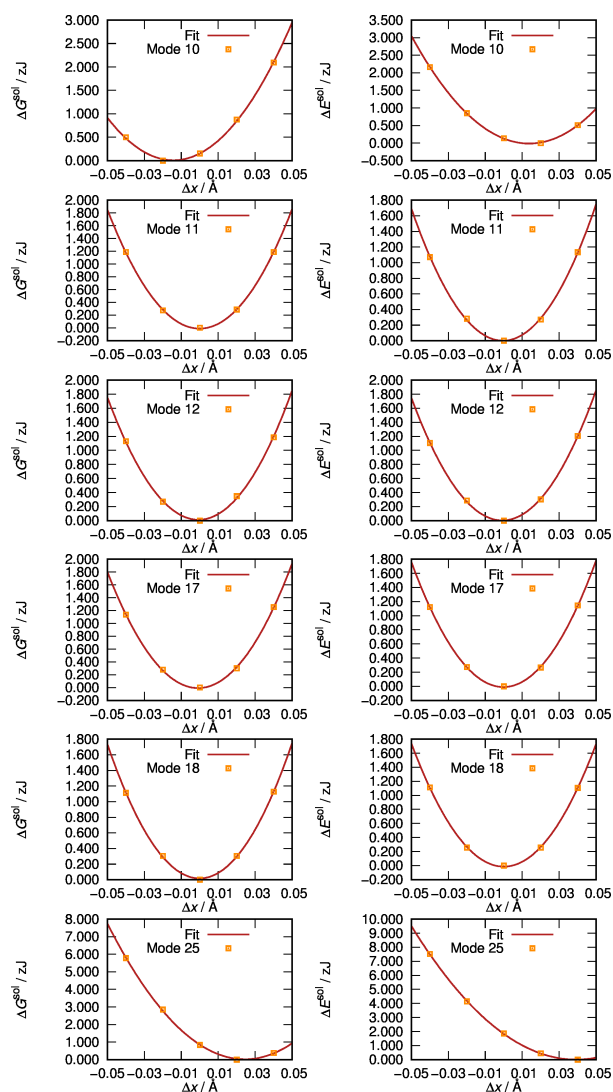


Figure A.6.: Gibbs energy (left) and solute electronic energy (right) from EC-RISM calculations on the distorted TMAO molecule at 100 bar. Calculated data points are shown as orange points, the red lines represent a fitted second order polynomial.

A. Additional data

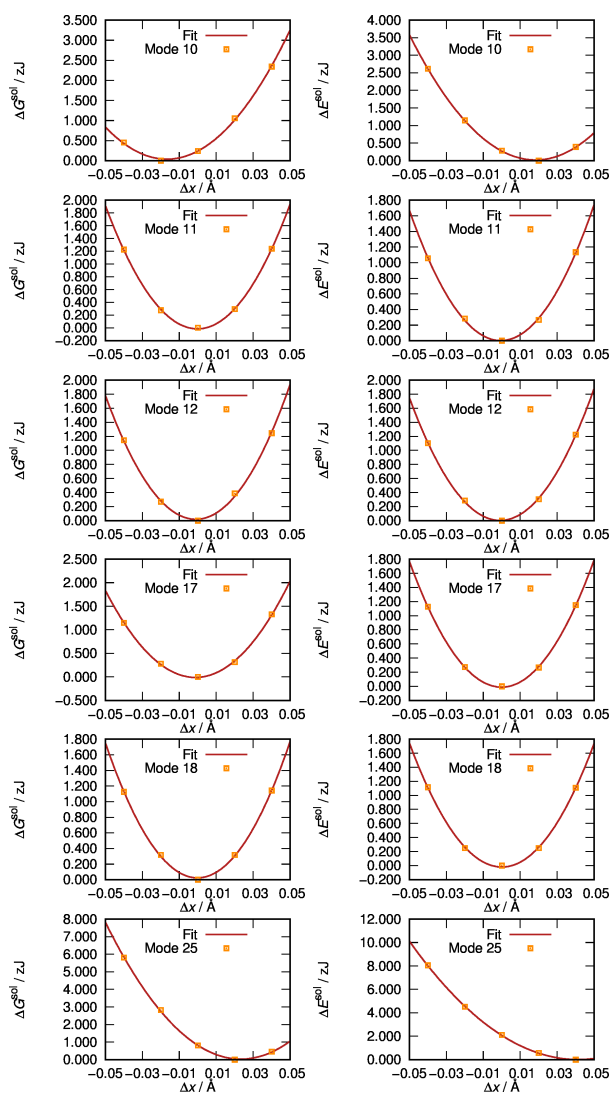


Figure A.7.: Gibbs energy (left) and solute electronic energy (right) from EC-RISM calculations on the distorted TMAO molecule at 5 kbar. Calculated data points are shown as orange points, the red lines represent a fitted second order polynomial.

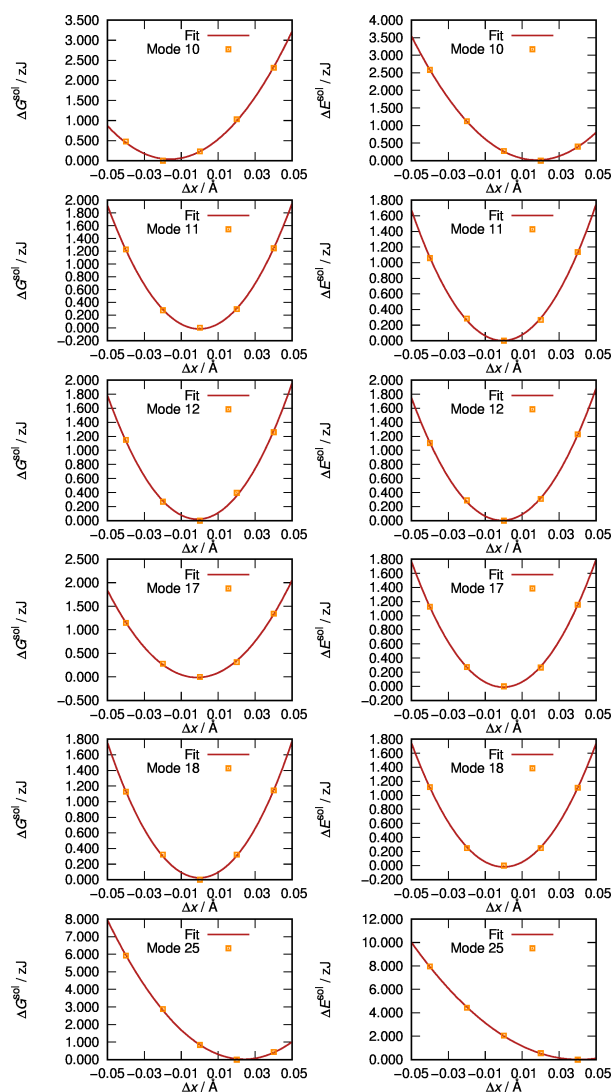


Figure A.8.: Gibbs energy (left) and solute electronic energy (right) from EC-RISM calculations on the distorted TMAO molecule at 10 kbar. Calculated data points are shown as orange points, the red lines represent a fitted second order polynomial.

A. Additional data

Table A.34.: Fit coefficients for TMAO modes at 1 bar obtained from Gibbs energies.

Mode	offset	x	x^2
Mode 10	$-1.088656 \cdot 10^{-15}$	$2.012841 \cdot 10^{-10}$	70.983758
Mode 11	$-1.088656 \cdot 10^{-15}$	$4.425622 \cdot 10^{-13}$	74.314263
Mode 12	$-1.088656 \cdot 10^{-15}$	$8.499346 \cdot 10^{-12}$	71.389696
Mode 17	$-1.088656 \cdot 10^{-15}$	$1.160979 \cdot 10^{-11}$	74.505447
Mode 18	$-1.088656 \cdot 10^{-15}$	$1.313444 \cdot 10^{-12}$	69.129989
Mode 25	$-1.088656 \cdot 10^{-15}$	$-6.835313 \cdot 10^{-10}$	138.886002

Table A.35.: Fit coefficients for TMAO modes at 100 bar obtained from Gibbs energies.

Mode	offset	x	x^2
Mode 10	$-1.088656 \cdot 10^{-15}$	$2.033431 \cdot 10^{-10}$	71.272696
Mode 11	$-1.088656 \cdot 10^{-15}$	$7.350561 \cdot 10^{-13}$	74.769820
Mode 12	$-1.088656 \cdot 10^{-15}$	$9.671059 \cdot 10^{-12}$	71.734711
Mode 17	$-1.088656 \cdot 10^{-15}$	$1.303022 \cdot 10^{-11}$	75.021671
Mode 18	$-1.088656 \cdot 10^{-15}$	$1.383267 \cdot 10^{-12}$	69.156159
Mode 25	$-1.088656 \cdot 10^{-15}$	$-6.822178 \cdot 10^{-10}$	139.664994

Table A.36.: Fit coefficients for TMAO modes at 5 kbar obtained from Gibbs energies.

Mode	offset	x	x^2
Mode 10	$-1.088568 \cdot 10^{-15}$	$2.418956 \cdot 10^{-10}$	72.415006
Mode 11	$-1.088568 \cdot 10^{-15}$	$2.186410 \cdot 10^{-12}$	77.744932
Mode 12	$-1.088568 \cdot 10^{-15}$	$1.567900 \cdot 10^{-11}$	73.726366
Mode 17	$-1.088568 \cdot 10^{-15}$	$1.976349 \cdot 10^{-11}$	77.852744
Mode 18	$-1.088568 \cdot 10^{-15}$	$1.704246 \cdot 10^{-12}$	69.591427
Mode 25	$-1.088568 \cdot 10^{-15}$	$-6.767754 \cdot 10^{-10}$	144.862470

Table A.37.: Fit coefficients for TMAO modes at 10 kbar obtained from Gibbs energies.

Mode	offset	x	x^2
Mode 10	$-1.088498 \cdot 10^{-15}$	$2.354486 \cdot 10^{-10}$	72.814479
Mode 11	$-1.088498 \cdot 10^{-15}$	$2.941961 \cdot 10^{-12}$	78.154330
Mode 12	$-1.088498 \cdot 10^{-15}$	$1.754964 \cdot 10^{-11}$	74.115417
Mode 17	$-1.088498 \cdot 10^{-15}$	$2.129057 \cdot 10^{-11}$	78.385338
Mode 18	$-1.088498 \cdot 10^{-15}$	$1.663950 \cdot 10^{-12}$	69.710391
Mode 25	$-1.088498 \cdot 10^{-15}$	$-6.935598 \cdot 10^{-10}$	145.505853

Table A.38.: Fit coefficients for TMAO modes at 1 bar obtained from electronic energies.

Mode	offset	x	x^2
Mode 10	$-1.088562 \cdot 10^{-15}$	$-2.007940 \cdot 10^{-10}$	75.408823
Mode 11	$-1.088562 \cdot 10^{-15}$	$5.578228 \cdot 10^{-12}$	68.965420
Mode 12	$-1.088562 \cdot 10^{-15}$	$1.074064 \cdot 10^{-11}$	72.002142
Mode 17	$-1.088562 \cdot 10^{-15}$	$2.169736 \cdot 10^{-12}$	71.318920
Mode 18	$-1.088562 \cdot 10^{-15}$	$-6.447372 \cdot 10^{-13}$	70.057186
Mode 25	$-1.088562 \cdot 10^{-15}$	$-9.297737 \cdot 10^{-10}$	119.736248

Table A.39.: Fit coefficients for TMAO modes at 100 bar obtained from electronic energies.

Mode	offset	x	x^2
Mode 10	$-1.088559 \cdot 10^{-15}$	$-2.076207 \cdot 10^{-10}$	75.483327
Mode 11	$-1.088559 \cdot 10^{-15}$	$5.618177 \cdot 10^{-12}$	68.890427
Mode 12	$-1.088559 \cdot 10^{-15}$	$1.080421 \cdot 10^{-11}$	72.033595
Mode 17	$-1.088559 \cdot 10^{-15}$	$2.104428 \cdot 10^{-12}$	71.285984
Mode 18	$-1.088559 \cdot 10^{-15}$	$-6.450846 \cdot 10^{-13}$	70.067797
Mode 25	$-1.088559 \cdot 10^{-15}$	$-9.372552 \cdot 10^{-10}$	119.816831

Table A.40.: Fit coefficients for TMAO modes at 5 kbar obtained from electronic energies.

Mode	offset	x	x^2
Mode 10	$-1.088534 \cdot 10^{-15}$	$-2.747189 \cdot 10^{-10}$	76.728091
Mode 11	$-1.088534 \cdot 10^{-15}$	$7.118858 \cdot 10^{-12}$	68.512802
Mode 12	$-1.088534 \cdot 10^{-15}$	$1.320843 \cdot 10^{-11}$	72.647368
Mode 17	$-1.088534 \cdot 10^{-15}$	$2.705395 \cdot 10^{-12}$	71.831149
Mode 18	$-1.088534 \cdot 10^{-15}$	$-8.833873 \cdot 10^{-13}$	70.537035
Mode 25	$-1.088534 \cdot 10^{-15}$	$-9.909261 \cdot 10^{-10}$	121.829677

A. Additional data

Table A.41.: Fit coefficients for TMAO modes at 10 kbar obtained from electronic energies.

Mode	offset	x	x^2
Mode 10	$-1.088534 \cdot 10^{-15}$	$-2.747189 \cdot 10^{-10}$	76.728091
Mode 11	$-1.088534 \cdot 10^{-15}$	$7.118858 \cdot 10^{-12}$	68.512802
Mode 12	$-1.088534 \cdot 10^{-15}$	$1.320843 \cdot 10^{-11}$	72.647368
Mode 17	$-1.088534 \cdot 10^{-15}$	$2.705395 \cdot 10^{-12}$	71.831149
Mode 18	$-1.088534 \cdot 10^{-15}$	$-8.833873 \cdot 10^{-13}$	70.537035
Mode 25	$-1.088534 \cdot 10^{-15}$	$-9.909261 \cdot 10^{-10}$	121.829677

A.2. Urea

A.2.1. Bonded urea parameters

Table A.42.: Rigid bond lengths of urea.

Type	r/nm
C-O	0.12290
C-N	0.13350
N-H	0.10100

Table A.43.: Harmonic angles of urea.

Type	$\phi/^\circ$	$k/\text{kJ mol}^{-1} \text{ rad}^{-2}$
C-N-H	120	390
H-N-H	120	445
O-C-N	121.4	730
N-C-N	117.2	670

Table A.44.: Dihedrals. $V_d = k(1 + \cos(n\theta - \theta_S))$

Type	$\phi/^\circ$	$k/\text{kJ mol}^{-1}$	n
O-C-N-H	0.0	8.36800	1
O-C-N-H	180.0	10.4600	2
N-C-N-H	180.0	10.4600	2
N-N-C-O	180.0	43.93200	2
C-H-N-H	180.0	4.18400	2

A.2.2. Non-bonded urea parameters

The following tables illustrate the non-bonded parameters for the urea V1, V2 and V3 force fields, which were optimized by Dr. Christoph Hölzl.

A. Additional data

Table A.45.: Urea V1 non-bonded parameters. Optimized by Dr. Christoph Hözl.

	σ/nm	$\epsilon/\text{kJ mol}^{-1}$	$q(1\text{bar})/e$	$q(10\text{kbar})/e$
C	0.35978	0.359820	0.6333	0.6627
H	0.11314	0.065689	0.4212	0.4336
N	0.34394	0.711280	-0.8495	-0.8685
O	0.31324	0.878640	-0.6191	-0.6601

Table A.46.: Urea V2 non-bonded parameters. Optimized by Dr. Christoph Hözl.

	σ/nm	$\epsilon/\text{kJ mol}^{-1}$	$q(1\text{bar})/e$	$q(10\text{kbar})/e$
C	0.35978	0.359820	0.6333	0.6627
H	0.11314	0.065689	0.4212	0.4336
N	0.34394	0.511140	-0.8495	-0.8685
O	0.31324	0.594320	-0.6191	-0.6601

Table A.47.: Urea V3 non-bonded parameters

	σ/nm	$\epsilon/\text{kJ mol}^{-1}$	$q(1\text{bar})/e$	$q(10\text{kbar})/e$
C	0.36039	0.359820	0.6068	0.6389
H ^{cis}	0.11333	0.065689	0.4026	0.4150
H ^{trans}	0.11333	0.065689	0.4421	0.4565
N	0.34452	0.511140	-0.8400	-0.8603
O	0.31377	0.594320	-0.6162	-0.6613

A.2.3. Force field modifications: Parameters

Table A.48.: Parameters of the modified urea force field V3-Mod1. Values in brackets denote the difference to the original V3 force field

Element	$\sigma/\text{\AA}$	ϵ / zJ
N	3.44524698 (+0.00)	0.848756280 (+0.00)
C	3.60391626 (+0.00)	0.597493600 (+0.00)
N	3.54524698 (+0.10)	0.848756280 (+0.00)
O	3.65772508 (+0.52)	1.136878020 (+0.15)
H	1.23332338 (+0.10)	0.209077322 (+0.10)
H	1.23332338 (+0.10)	0.209077322 (+0.10)
H	1.23332338 (+0.10)	0.209077322 (+0.10)
H	1.23332338 (+0.10)	0.209077322 (+0.10)

Table A.49.: Parameters of the modified urea force field V3-Mod2. Values in brackets denote the difference to the original V3 force field

Element	$\sigma/\text{\AA}$	ϵ / zJ
N	3.44524698 (0.0)	0.848756280(+0.000000)
C	3.60391626 (0.0)	0.855600600(+0.258107)
N	3.44524698 (0.0)	0.848756280(+0.000000)
O	3.13772508 (0.0)	0.786878020(-0.200000)
H	1.13332338 (0.0)	0.337586322(+0.228509)
H	1.13332338 (0.0)	0.337586322(+0.228509)
H	1.13332338 (0.0)	0.337586322(+0.228509)
H	1.13332338 (0.0)	0.337586322(+0.228509)

A. Additional data

Table A.50.: Parameters of the modified urea force field V3-Mod3. Values in brackets denote the difference to the original V3 force field

Element	$\sigma/\text{\AA}$	ϵ / zJ
N	3.44524698 (0.0)	0.84875628 (0.000000000)
C	3.60391626 (0.0)	0.47428800 (-0.123205600)
N	3.44524698 (0.0)	0.84875628 (0.000000000)
O	3.13772508 (0.0)	0.08235000 (-0.904528020)
H	1.13332338 (0.0)	0.00000000 (-0.109077322)
H	1.13332338 (0.0)	0.00000000 (-0.109077322)
H	1.13332338 (0.0)	0.00000000 (-0.109077322)
H	1.13332338 (0.0)	0.00000000 (-0.109077322)

Table A.51.: Parameters of the modified urea force field V3-Mod4. Values in brackets denote the difference to the original V3 force field

Element	$\sigma/\text{\AA}$	ϵ / zJ
N	3.44524698 (0.0)	0.84875628 (0.000000000)
C	3.60391626 (0.0)	1.37181000 (+0.774316400)
N	3.44524698 (0.0)	0.84875628 (0.000000000)
O	3.13772508 (0.0)	0.38687800 (-0.600000020)
H	1.13332338 (0.0)	0.79460500 (0.6855276780)
H	1.13332338 (0.0)	0.79460500 (0.6855276780)
H	1.13332338 (0.0)	0.79460500 (0.6855276780)
H	1.13332338 (0.0)	0.79460500 (0.6855276780)

Table A.52.: Parameters of the modified urea force field V3-Mod5. Values in brackets denote the difference to the original V3 force field

Element	$\sigma/\text{\AA}$	ϵ / zJ
N	3.44524698 (0.0)	0.848756 (0.000000000)
C	3.60391626 (0.0)	0.662020 (+0.064526400)
N	3.44524698 (0.0)	0.848756 (0.000000000)
O	3.13772508 (0.0)	0.936878 (-0.050000020)
H	1.13332338 (0.0)	0.166205 (+0.057127678)
H	1.13332338 (0.0)	0.166205 (+0.057127678)
H	1.13332338 (0.0)	0.166205 (+0.057127678)
H	1.13332338 (0.0)	0.166205 (+0.057127678)

Table A.53.: Parameters of the modified urea force field V3-Mod6. Values in brackets denote the difference to the original V3 force field

Element	$\sigma/\text{\AA}$	ϵ / zJ
N	3.44524698 (0.0)	0.848756 (0.000000000)
C	3.60391626 (0.0)	0.532967 (-0.064526600)
N	3.44524698 (0.0)	0.848756 (0.000000000)
O	3.13772508 (0.0)	1.036888 (+0.050009980)
H	1.13332338 (0.0)	0.051955 (-0.057122322)
H	1.13332338 (0.0)	0.051955 (-0.057122322)
H	1.13332338 (0.0)	0.051955 (-0.057122322)
H	1.13332338 (0.0)	0.051955 (-0.057122322)

Table A.54.: Parameters of the modified urea force field V3-Mod7. Values in brackets denote the difference to the original V3 force field

Element	$\sigma/\text{\AA}$	ϵ / zJ
N	3.44524698 (0.0)	0.7737560 (-0.075000280)
C	3.60391626 (0.0)	0.4334020 (-0.164091600)
N	3.44524698 (0.0)	0.7737560 (-0.075000280)
O	3.13772508 (0.0)	1.0868880 (+0.100009980)
H	1.13332338 (0.0)	0.0132123 (-0.095865022)
H	1.13332338 (0.0)	0.0132123 (-0.095865022)
H	1.13332338 (0.0)	0.0132123 (-0.095865022)
H	1.13332338 (0.0)	0.0132123 (-0.095865022)

Table A.55.: Parameters of the modified urea force field V3-Mod8. Values in brackets denote the difference to the original V3 force field

Element	$\sigma/\text{\AA}$	ϵ / zJ
N	3.34525 (-0.0999969)	0.7737560 (-0.09999698)
C	3.77859 (+0.1746737)	0.4334020 (+0.17467374)
N	3.34525 (-0.0999969)	0.7737560 (-0.09999698)
O	3.12773 (-0.0099950)	1.0868880 (-0.00999508)
H	1.34038 (+0.2070566)	0.0132123 (+0.20705662)
H	1.34038 (+0.2070566)	0.0132123 (+0.20705662)
H	1.34038 (+0.2070566)	0.0132123 (+0.20705662)
H	1.34038 (+0.2070566)	0.0132123 (+0.20705662)

A. Additional data

Table A.56.: Parameters of the modified urea force field V3-Mod9. Values in brackets denote the difference to the original V3 force field

Element	$\sigma/\text{\AA}$	ϵ / zJ
N	2.94525 (-0.49999698)	0.7737560 (-0.075000280)
C	4.44416 (+0.84024374)	0.4334020 (-0.164091600)
N	2.94525 (-0.49999698)	0.7737560 (-0.075000280)
O	3.08813 (-0.04959508)	1.0868880 (+0.100009980)
H	2.17191 (1.038586620)	0.0132123 (-0.095865022)
H	2.17191 (1.038586620)	0.0132123 (-0.095865022)
H	2.17191 (1.038586620)	0.0132123 (-0.095865022)
H	2.17191 (1.038586620)	0.0132123 (-0.095865022)

Table A.57.: Parameters of the modified urea force field V3-Mod10. Values in brackets denote the difference to the original V3 force field

Element	$\sigma/\text{\AA}$	ϵ / zJ
N	3.19525 (-0.24999698)	0.7737560 (-0.07500028)
C	4.02404 (+0.42012374)	0.4334020 (-0.164091600)
N	3.19525 (-0.24999698)	0.7737560 (-0.075000280)
O	3.11293 (-0.02479508)	1.0868880 (+0.100009980)
H	1.65262 (+0.51929662)	0.0132123 (-0.095865022)
H	1.65262 (+0.51929662)	0.0132123 (-0.095865022)
H	1.65262 (+0.51929662)	0.0132123 (-0.095865022)
H	1.65262 (+0.51929662)	0.0132123 (-0.095865022)

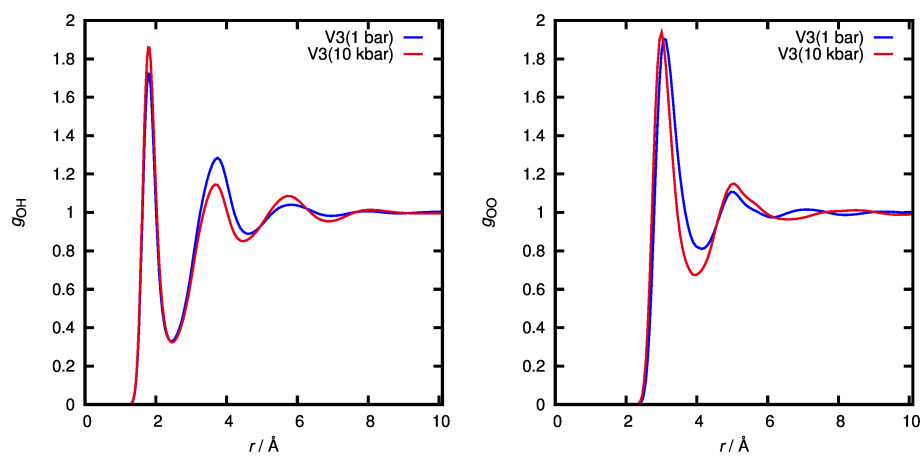
A.2.4. Force field modifications: Radial distribution functions

Figure A.9.: Radial distribution functions of the water sites around urea's oxygen, calculated with EC-RISM applying the V3 parameters.

A. Additional data

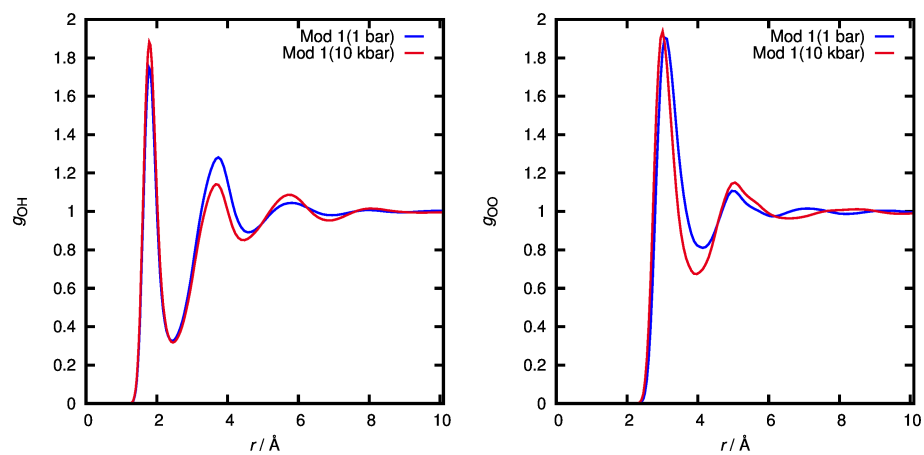


Figure A.10.: Radial distribution functions of the water sites around urea's oxygen, calculated with EC-RISM applying the V3 Mod 1 parameters.

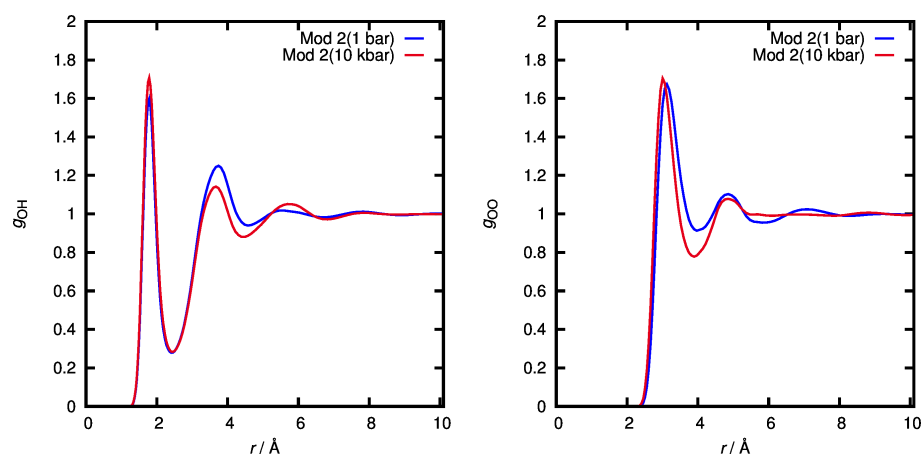


Figure A.11.: Radial distribution functions of the water sites around urea's oxygen, calculated with EC-RISM applying the V3 Mod 2 parameters.

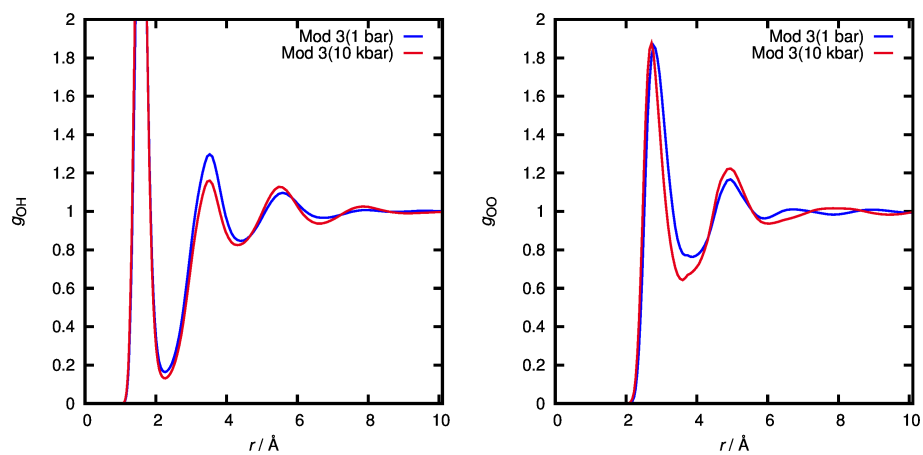


Figure A.12.: Radial distribution functions of the water sites around urea's oxygen, calculated with EC-RISM applying the V3 Mod 3 parameters.

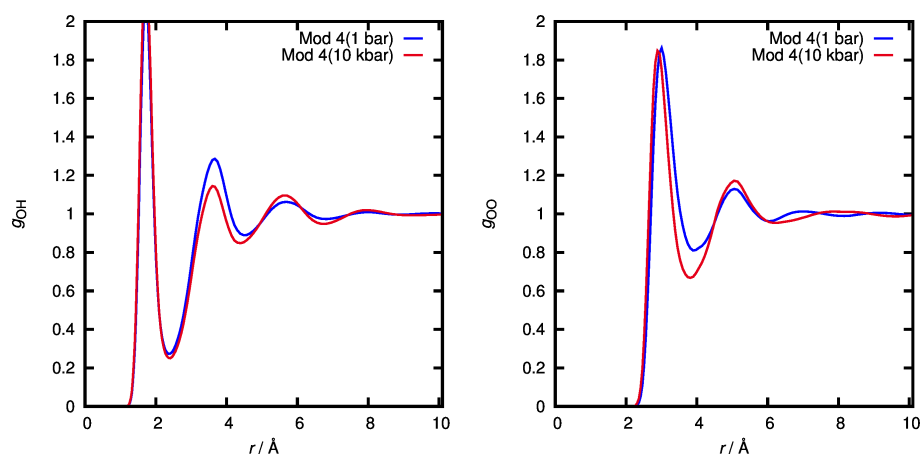


Figure A.13.: Radial distribution functions of the water sites around urea's oxygen, calculated with EC-RISM applying the V3 Mod 4 parameters.

A. Additional data

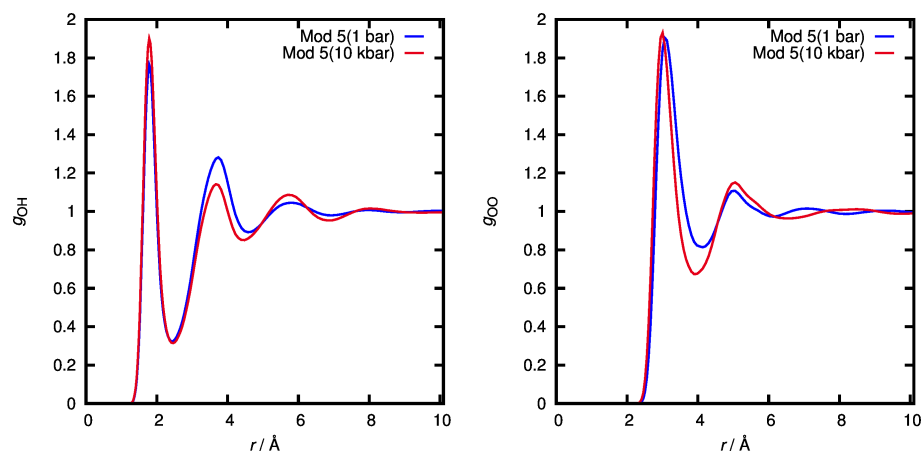


Figure A.14.: Radial distribution functions of the water sites around urea's oxygen, calculated with EC-RISM applying the V3 Mod 5 parameters.

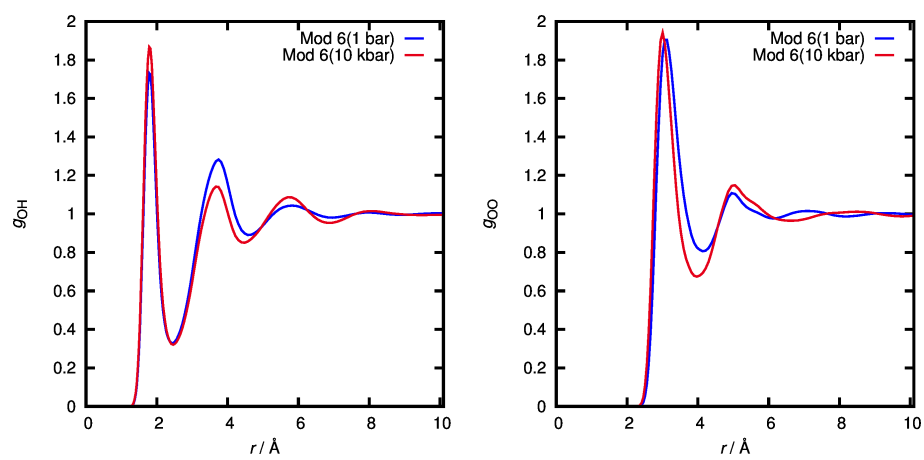


Figure A.15.: Radial distribution functions of the water sites around urea's oxygen, calculated with EC-RISM applying the V3 Mod 6 parameters.

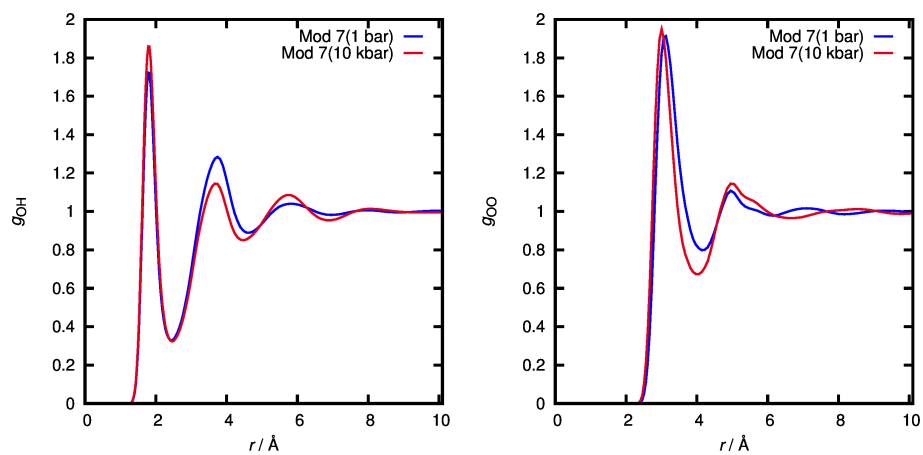


Figure A.16.: Radial distribution functions of the water sites around urea's oxygen, calculated with EC-RISM applying the V3 Mod 7 parameters.

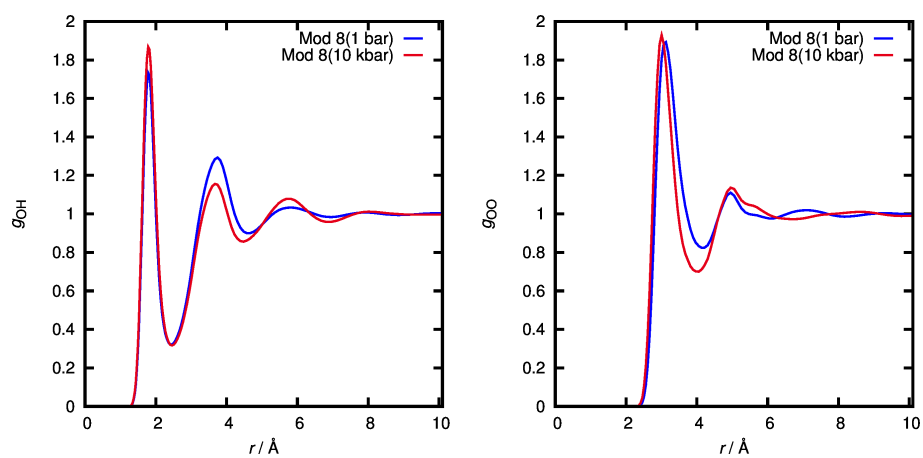


Figure A.17.: Radial distribution functions of the water sites around urea's oxygen, calculated with EC-RISM applying the V3 Mod 8 parameters.

A. Additional data

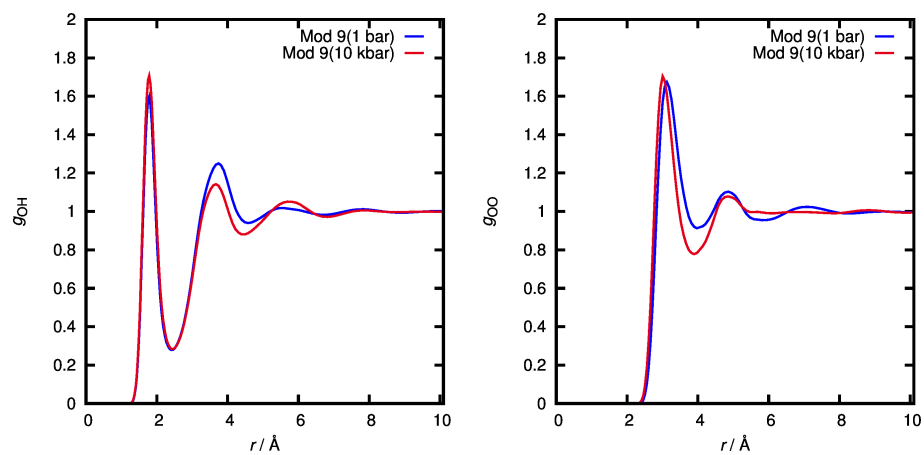


Figure A.18.: Radial distribution functions of the water sites around urea's oxygen, calculated with EC-RISM applying the V3 Mod 9 parameters.

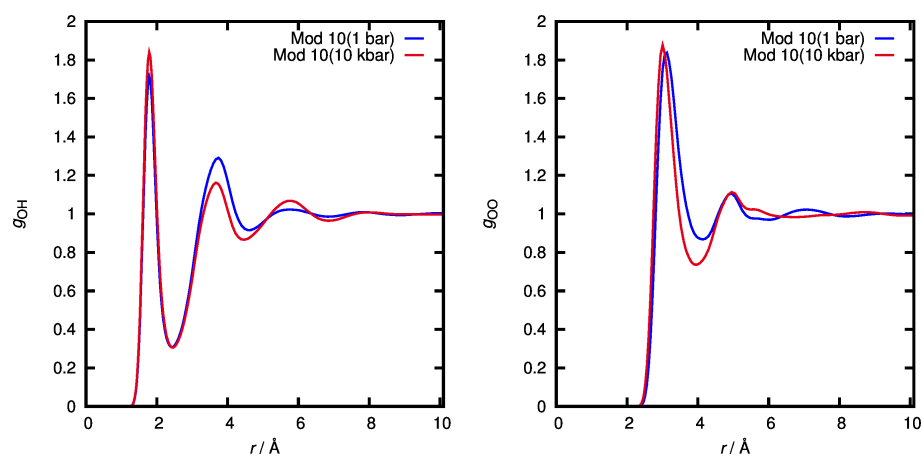


Figure A.19.: Radial distribution functions of the water sites around urea's oxygen, calculated with EC-RISM applying the V3 Mod 10 parameters.

A.3. New electrostatics model

A.3.1. Molecule geometries

Table A.58.: Cartesian coordinates of the optimized alanine anion.

Element	$x/\text{\AA}$	$y/\text{\AA}$	$z/\text{\AA}$
N	0.387345418374	1.082475321510	-0.816186574551
C	1.567298268806	0.386573143690	-0.272677360554
C	1.235883024947	-0.793820605157	0.688908275828
O	0.175876794798	-0.703359328088	1.364270793145
H	-0.116640430042	0.449639358455	-1.432553459150
H	2.125625598688	-0.025221082024	-1.118155535849
C	2.462383957254	1.395690768663	0.459394589256
H	2.770629485042	2.196109547008	-0.218447387459
H	1.920892619418	1.849271631753	1.296240202509
H	3.357644586195	0.911305544846	0.856664363445
H	-0.250385801829	1.254908385302	-0.040850563553
O	2.076236478349	-1.733572685958	0.736472656933

Table A.59.: Cartesian coordinates of the optimized alanine zwitterion.

Element	$x/\text{\AA}$	$y/\text{\AA}$	$z/\text{\AA}$
N	-0.107343555357	0.355845328975	-0.308311908542
C	1.404618953321	0.325875322901	-0.214189146032
C	1.746951565912	-0.853992601175	0.756060431496
O	0.749063191676	-1.499788016400	1.183009401966
H	-0.379871966899	-0.482387884148	0.261119592359
H	1.777548101668	0.064665540882	-1.204821545696
C	1.962421806367	1.672270761754	0.227114360666
H	1.719288314289	2.457015905495	-0.492810324494
H	1.573513914029	1.958026318250	1.208572170699
H	3.046736585251	1.596945483213	0.301103859637
H	-0.458246064082	0.273148296471	-1.261331083682
O	2.953188653732	-1.039550052120	0.989993746849
H	-0.515299499907	1.193005595903	0.108410444774

A. Additional data

Table A.60.: Cartesian coordinates of the optimized alanine cation.

Element	$x/\text{\AA}$	$y/\text{\AA}$	$z/\text{\AA}$
N	-0.101621751187	0.377143918193	-0.247735646176
C	1.404786276825	0.344223816164	-0.198094908394
C	1.776825028036	-0.814956732049	0.735379107823
O	0.984931096707	-1.276038411655	1.518796504081
H	-0.485026960062	0.196836963561	0.688007631576
H	1.747558903692	0.147031221170	-1.213733290741
C	1.946142910525	1.684875459412	0.306011856131
H	1.657058733528	2.483780617537	-0.378661003283
H	1.570689714088	1.910988818128	1.305624012322
H	3.035431185707	1.656936209805	0.342351488140
H	-0.446530888218	1.281164807580	-0.578969191406
O	3.028971918759	-1.266495956996	0.673341773655
H	3.552689298344	-0.854315789397	-0.029431430662
H	-0.479115466746	-0.342844941453	-0.869096903066

Table A.61.: Cartesian coordinates of the optimized nitrogen molecule.

Element	$x/\text{\AA}$	$y/\text{\AA}$	$z/\text{\AA}$
N	-0.547662996196	0.000000000000	0.000000000000
N	0.547662996196	0.000000000000	0.000000000000

Table A.62.: Cartesian coordinates of the shifted optimized nitrogen molecule.

Element	$x/\text{\AA}$	$y/\text{\AA}$	$z/\text{\AA}$
N	0.452337003804	0.000000000000	0.000000000000
N	1.547662996196	0.000000000000	0.000000000000

A.4. *hpCADD*

A.4.1. List of substances

A. Additional data

Table A.63.: Alkanes	
Name	Structure
1,3,5-Hexatriene	
1,3,5-Trimethylbenzene	
2-Methylprop-1-ene	
3,3-Dimethylbut-1-yne	
Benzene	
But-2-yne	
Buta-1,3-diene	
Butane	
Cyclohexane	
Cyclohexene	
E-But-2-ene	
Ethene	
Ethylbenzene	
Ethyne	
Naphthalene	
Prop-2-enylbenzene	
Propane	
Propene	
Propyne	
Toluene	
Z-But-2-ene	

Table A.64.: Alcohols

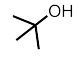
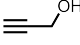
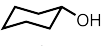
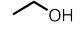
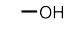
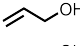
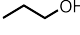
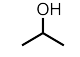
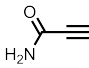
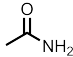
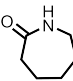
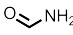
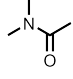
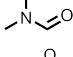
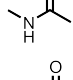
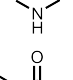

Name	Structure
2-Methylpropan-2-ol	
2-Propyn-1-ol	
Cyclohexanol	
Ethanol	
Methanol	
Prop-1-en-2-ol	
Propan-1-ol	
Propan-2-ol	

Table A.65.: Amides

Name	Structure
2-Propynamide	
Acetamide	
Azepan-2-one	
Formamide	
<i>N,N</i> -Dimethylacetamide	
<i>N,N</i> -Dimethylformamide	
<i>N,N</i> -Methylacetamide	
<i>N,N</i> -Methylformamide	
Prop-2-enamide	

A. Additional data

Table A.66.: Bromides


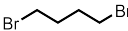

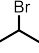


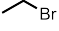
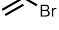
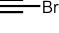



Name	Structure
1-Bromobutane	
1,4-Dibromobutane	
2-Bromo-2-methylpropane	
2-Bromopropane	
3-Bromoprop-1-ene	
Bromocyclohexane	
Bromoethane	
Bromoethene	
Bromoethyne	
Bromomethane	
Dibromomethane	
E-1,2-Dibromocyclohexane	

Table A.67.: Aldehydes and Ketones

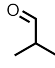
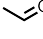
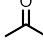
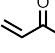

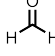
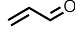
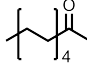
Name	Structure
2-Methylpropanal	
Acetaldehyde	
Acetone	
But-3-en-2-one	
Cyclohexanone	
Formaldehyde	
Prop-2-enal	
Undecan-2-one	

Table A.68.: Chlorides


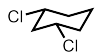
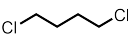
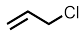


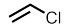
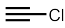
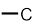

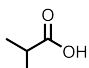
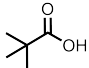
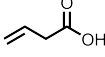
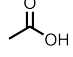
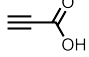
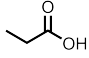
Name	Structure
1-Chlorobutane	
1,3-Dichlorocyclohexane	
1,4-Dichlorobutane	
3-Chloroprop-1-ene	
Chlorocyclohexane	
Chloroethane	
Chloroethene	
Chloroethyne	
Chloromethane	
Dichloromethane	

Table A.69.: Carboxylic acids

Name	Structure
2-Methylpropanoic acid	
2,2-Dimethylpropanoic acid	
3-Butenoic acid	
Acetic acid	
Prop-2-ynoic acid	
Propanoic acid	

A. Additional data

Table A.70.: Esters

Name	Structure
Ethenyl acetate	
Ethyl 2-methylpropanoate	
Ethyl 2,2-dimethylpropionate	
Ethyl acetate	
Ethyl prop-2-enoate	
Ethyl propanoate	
Ethynyl 2,2-dimethylpropionate	
Ethynyl prop-2-enoate	
Methyl 2-methylpropanoate	
Methyl 2,2-dimethylpropionate	
Methyl acetate	
Methyl prop-2-enoate	
Propan-2-yl 2-methylpropanoate	
Propan-2-yl 2,2-dimethylpropionate	
Propan-2-yl acetate	
Propan-2-yl prop-2-ynoate	
Propan-2-yl propionate	
<i>tert</i> -Butyl acetate	
<i>tert</i> -Butyl prop-2-ynoate	
<i>tert</i> -Butyl propionate	

Table A.71.: Ethers

Name	Structure
1,4-Dioxane	
Di- <i>tert</i> -butyl ether	
Diethyl ether	
Diisopropyl ether	
Dimethyl ether	
Ethyl methyl ether	
Ethynyl methyl ether	
Isobutyl methyl ether	
Methyl <i>tert</i> -butyl ether	
Oxane	
Tetrahydrofuran	

Table A.72.: Fluorides

Name	Structure
1-Fluoropropane	
1,4-Difluorocyclohexane	
2-Fluoropropane	
2,2-Difluoropropane	
3-Fluoroprop-1-ene	
Difluoromethane	
Fluorocyclohexane	
Fluoroethene	
Fluoroethyne	
Fluoromethane	

A. Additional data

Table A.73.: Conjugated systems

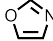
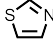
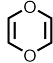
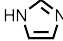
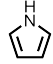
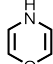
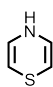
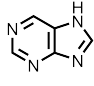
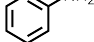
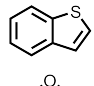
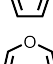
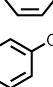
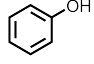
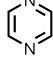
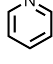
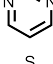

Name	Structure
1,3-Oxazole	
1,3-Thiazole	
1,4-Dioxin	
1 <i>H</i> -Imidazole	
1 <i>H</i> -Pyrrole	
4 <i>H</i> -1,4-Oxazine	
4 <i>H</i> -1,4-Thiazine	
9 <i>H</i> -Purine	
Aniline	
Benzo[<i>b</i>]thiophene	
Furan	
Oxepine	
Phenol	
Pyrazine	
Pyridine	
Pyrimidine	
Thiophene	

Table A.74.: Nitriles

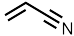
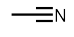
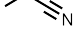
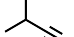

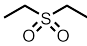
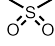
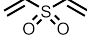
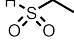
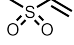
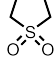
Name	Structure
Prop-2-enenitrile	
Acetonitrile	
Propanenitrile	
2-Methylpropanenitrile	
2,2-Dimethylpropanenitrile	

Table A.75.: Sulfones

Name	Structure
Diethyl sulfone	
Dimethyl sulfone	
Divinyl sulfone	
Ethyl sulfone	
Methyl vinyl sulfone	
Tetrahydrothiophene 1,1-dioxide	

A. Additional data

Table A.76.: Thioethers

Name	Structure
(Methylsulfanyl)methane	
1,4-Dithiane	
1,1-Thiobisethane	
(Methylsulfanyl)-2-propane	
(Methylsulfanyl)-2-ethyne	
Thiane	
terttert-Butyl methyl sulfide	
Di-tert-Butyl sulfide	
Ethyl methyl sulfide	
Thiolane	

Table A.77.: Thiols

Name	Structure
Propane-2-thiol	
Prop-2-yne-1-thiol	
Prop-2-ene-1-thiol	
Cyclohexanethiol	
Ethanethiol	
Methanethiol	
Propane-1-thiol	
2-Methylpropane-2-thiol	

Table A.78.: Thiones

Name	Structure
(1R,4S)-1,3,3-trimethylbicyclo[2.2.1]heptane-2-thione	
6,6-Dimethylhept-1-yne-4-thione	
Hept-1-ene-4-thione	
Methanethial	
Nonane-5-thione	
Pentanthial	
Propane-2-thione	

A. Additional data

A.4.2. Raw data

Table A.79.: Raw hpCADD EC-RISM results for the group of the Alkanes at 1 bar.

Name	$\mu^{\text{ex}}/\text{kcal mol}^{-1}$	$E^{\text{sol}}/\text{kcal mol}^{-1}$	$G^{\text{sol}}/\text{kcal mol}^{-1}$	μ^x/D	μ^y/D	μ^z/D	μ^{tot}/D
Ethyne	15.5590807270555	3.53037250597514	19.0894532330306	0.000	0.000	0.000	0
Prop-2-enylbenzene	2121.31713106907	15.8420013833652	2137.15913245244	0.850	1.040	0.592	1.46784331588899
Benzene	1644.01938765416	7.0137817626673	1651.03316941683	0.000	-0.000	0.000	0
Buta-1,3-diene	1504.59725095578	13.6779239913958	1518.27517494718	0.000	-0.000	0.000	0
Butane	-306.775462617591	14.5543718640057	-292.221090753585	0.000	0.000	-0.000	0
But-2-yne	-362.495533053298	11.0259830707457	-351.469549982553	-0.000	-0.000	0.000	0
Cyclohexane	-104.983214093929	17.4222956895315	-87.5609184043977	-0.000	0.000	-0.000	0
Cyclohexene	456.223011914436	15.0135599261472	471.236571840583	-0.000	0.357	-0.000	0.357
E-But-2-ene	264.331543907983	13.1804148838432	277.511958791826	-0.001	-0.000	0.000	0.001
Ethene	919.089840732792	6.91979580258126	926.009636535373	-0.000	0.000	-0.000	0
Ethylbenzene	1297.51532617591	16.731539416109	1314.24686559202	-0.255	0.001	-0.053	0.26045153099532
1,3,5-Hexatriene	2008.30497966946	17.6267152409178	2025.93169491037	-0.000	0.000	-0.000	0
1,3,5-Trimethylbenzene	724.586807072897	22.6063633685468	747.193170441444	-0.022	-0.008	0.010	0.0254558441227157
2-Methylprop-1-ene	283.097694057122	13.5218427593212	296.619536816444	0.000	0.187	-0.000	0.187
Naphtalene	2383.23676593929	16.1400864321224	2399.37685237141	0.000	-0.000	-0.000	0
Propane	-288.553659372849	11.8360451030115	-276.717614269837	-0.000	0.212	-0.000	0.212
Propene	587.718306603729	10.1175087973231	597.835815401052	-0.115	0.217	0.000	0.24558908770546
Propyne	-172.027585179254	7.22341182026769	-164.804173358987	0.707	-0.000	0.000	0.707
3,3-Dimethylbut-1-yne	-231.013726569312	16.5855214189771	-214.428205150335	-1.474	-0.002	0.003	1.47400440976274
Toluene	1333.9150121152	13.3127539849426	1347.22776610014	-0.774	-0.000	-0.001	0.774000645994563
z-But-2-ene	273.823040113528	10.8279168355641	284.650956949092	0.000	0.979	0.000	0.979

Table A.80.: Raw hpCADD EC-RISM results for the group of the Alcohols at 1 bar.

Name	$\mu^{\text{ex}}/\text{kcal mol}^{-1}$	$E^{\text{sol}}/\text{kcal mol}^{-1}$	$G^{\text{sol}}/\text{kcal mol}^{-1}$	μ^x/D	μ^y/D	μ^z/D	μ^{tot}/D
Cyclohexanol	293.427257988289	15.324109418499	308.751367406788	0.337	1.187	0.555	1.35298300063231
Ethanol	130.604623793977	7.1730555874761	137.777679381453	-0.522	1.286	-0.000	1.38790489587724
Propan-2-ol	105.343794396989	7.78112300693117	113.12491740392	0.000	-0.127	1.403	1.40873631315445
Methanol	146.55984464412	3.6844770458891	150.24432169001	-1.441	0.338	-0.000	1.48010979322481
Propan-1-ol	111.171111768881	9.92810847036329	121.099220239245	0.586	1.117	0.001	1.2613825747964
Prop-1-en-2-ol	943.443973867352	6.33932582265774	949.78329969001	-1.263	0.533	0.543	1.47448533393859
2-Propyn-1-ol	217.814064044694	0.509397194072658	218.323461238767	3.246	0.892	0.004	3.36633272271176
2-Methylpropan-2-ol	90.7890332404398	11.4124980126673	102.201531253107	-1.413	-0.000	0.394	1.46690320062368

Table A.81.: Raw hpCADD EC-RISM results for the group of the Amides at 1 bar.

Name	$\mu^{ex}/\text{kcal mol}^{-1}$	$E^{sol}/\text{kcal mol}^{-1}$	$G^{sol}/\text{kcal mol}^{-1}$	μ^x/D	μ^y/D	μ^z/D	μ^{tot}/D
Prop-2-enamide	-2168.13305723638	-17.8100042471319	-2185.94306148351	7.258	-5.560	0.000	9.14287504016106
Acetamide	-3008.40522531597	-15.3109478656788	-3023.71617318164	2.829	-6.890	0.012	7.44818669207479
Azepan-2-one	-3014.8925096685	2.90076876768642	-3011.99174090081	4.505	-3.358	0.079	5.61937985902359
<i>N,N</i> -Dimethylacetamide	-3354.81727595339	7.1893098585086	-3347.62796609488	-2.460	4.760	0.577	5.389074967005
<i>N,N</i> -Dimethylformamide	-3251.31068637667	4.55489643570746	-3246.75578994097	-5.780	0.459	0.001	5.79819644372282
<i>N,N</i> -Methylacetamide	-3186.37604426601	-5.97727816754302	-3192.35332243356	-1.195	-6.789	-0.004	6.8933708735277
<i>N,N</i> -Methylformamide	-3084.03866274116	-7.81364375979923	-3091.85230650096	-5.260	4.331	0.001	6.81360125044018
Formamide	-2905.79236684895	-18.0095053620937	-2923.80187221104	7.363	-0.791	0.008	7.40537061867939
propiolamide	-2961.6326735354	-44.8505677674474	-3006.48324132098	-9.431	7.844	0.002	12.2667070153322

Table A.82.: Raw hpCADD EC-RISM results for the group of the Bromides at 1 bar.

Name	$\mu^{ex}/\text{kcal mol}^{-1}$	$E^{sol}/\text{kcal mol}^{-1}$	$G^{sol}/\text{kcal mol}^{-1}$	μ^x/D	μ^y/D	μ^z/D	μ^{tot}/D
Bromoethyne	21.9775151018164	5.09188975095602	27.0694048527725	0.000	0.000	0.410	0.41
3-Bromoprop-1-ene	694.413875131453	10.5730538202677	704.986928951721	2.469	0.087	0.356	2.49605007962581
Bromoethane	-102.273654961042	10.827141333174	-91.4465136278681	2.210	0.423	0.000	2.25011755248476
Bromomethane	-76.771892043738	8.16946122657744	-68.6024308171606	-1.996	0.000	0.000	1.996
1-Bromobutane	-140.191372928298	16.0902299794455	-124.101142948853	2.777	0.523	0.000	2.82581988102568
Bromocyclohexane	56.3013311620459	19.4225209476577	75.7238521097036	2.916	-0.000	0.094	2.91751469576419
E-1,2-Dibromocyclohexane	221.49286701673	21.8028391295411	243.295706146271	-4.328	0.000	-0.000	4.328
1,4-Dibromobutane	28.2695239753824	18.1143067779637	46.3838307533461	0.000	-0.000	0.000	0
Dibromomethane	81.6665585884321	9.58247233723709	91.2490309256692	0.001	1.097	0.000	1.09700045578842
2-Bromopropane	-125.16299011783	14.1987745470841	-110.964215570746	2.046	0.000	0.230	2.05888707801084
2-Bromo-2-methylpropane	-147.348114274618	17.6608050150574	-129.68730925956	1.706	-0.000	-0.001	1.70600029308321
Bromoethene	716.372928325765	9.08375629206501	725.45668461783	1.229	-0.391	0.000	1.28969841435895

Table A.83.: Raw hpCADD EC-RISM results for the group of the Carbonyls at 1 bar.

Name	$\mu^{ex}/\text{kcal mol}^{-1}$	$E^{sol}/\text{kcal mol}^{-1}$	$G^{sol}/\text{kcal mol}^{-1}$	μ^x/D	μ^y/D	μ^z/D	μ^{tot}/D
2-Methylpropanal	-27.2422397875239	9.91101533891013	-17.3312244486138	4.704	-0.000	0.164	4.70685797533769
Acetaldehyde	20.3397176218929	5.38973705544933	25.7294546773423	3.802	0.850	0.007	3.89586357564019
Prop-2-enal	889.196266380019	3.0987663539675	892.295032733987	5.407	0.073	-0.009	5.40750025427646
Cyclohexanone	86.4055012237094	11.7568619536329	98.1623631773423	-5.195	0.001	1.225	5.33747608893942
Formaldehyde	134.237323641252	4.35211535325048	138.589438994503	2.788	-0.000	0.007	2.78800878764756
Acetone	-81.5273804799235	8.27920134751434	-73.2481791324092	-0.011	4.051	-0.066	4.0515525419276
Undecan-2-one	-240.323240530593	30.3832031221319	-209.940037408461	-1.458	-3.583	0.173	3.87215469732293
But-3-en-2-one	764.109008904637	7.93324751434034	772.042256418977	-0.487	-3.815	-0.000	3.84595813809771

Table A.84.: Raw hpCADD EC-RISM results for the group of the Chlorides at 1 bar.

Name	$\mu^{ex}/\text{kcal mol}^{-1}$	$E^{sol}/\text{kcal mol}^{-1}$	$G^{sol}/\text{kcal mol}^{-1}$	μ^x/D	μ^y/D	μ^z/D	μ^{tot}/D
Chloroethyne	12.3331421730402	6.21335288838432	18.5464950614245	0.000	0.000	-0.459	0.459
3-Chloroprop-1-ene	712.107783746176	9.89559138957935	722.003375135755	3.049	0.247	0.498	3.09926023431399
1-Chlorobutane	-145.660076042065	15.5138847526291	-130.146191289436	2.930	0.642	0.000	2.9995106267523
Chloroethane	-107.857074451721	10.3734708066444	-97.4836036450765	2.429	0.555	0.000	2.49159908492518
Chloromethane	-83.2372807425908	7.88678846988528	-75.3504922727056	2.213	0.000	0.000	2.213
Chlorocyclohexane	51.7728753489484	18.8132163831262	70.5860917320746	-3.046	-0.000	0.099	3.04760840660345
1,3-Dichlorocyclohexane	212.635424713432	20.8509820913002	233.486406804732	0.000	2.780	0.297	2.79581991551673
1,4-Dichlorobutane	17.9124269134799	17.0324693465583	34.9448962600382	0.000	-0.000	-0.000	0
Dichloromethane	85.1285037703155	9.98896015272467	95.1174639230402	-0.000	1.664	0.000	1.664
Chloroethene	728.102542537285	8.71634151720841	736.818884054493	2.101	-0.043	0.000	2.1014399824882

A. Additional data

Table A.85.: Raw hpCADD EC-RISM results for the group of the Acids at 1 bar.

Name	$\mu^{\text{ex}}/\text{kcal mol}^{-1}$	$E^{\text{sol}}/\text{kcal mol}^{-1}$	$G^{\text{sol}}/\text{kcal mol}^{-1}$	μ^x/D	μ^y/D	μ^z/D	μ^{tot}/D
3-Butenoic acid	-1126.87911257505	8.56491108628107	-1118.31420148877	-3.972	-1.796	0.596	4.39972908256861
Acetic acid	-1924.98289584273	5.3384857772467	-1919.64441006501	-3.181	-1.624	-0.000	3.5715734627752
2,2-Dimethylpropanoic acid	-2001.81690799665	8.63491464913958	-1993.18199334751	7.819	-1.116	0.002	7.89824163975755
Prop-2-ynoic acid	-1838.00818138862	4.57409057146271	-1833.43409081716	-1.640	-1.942	0.001	2.54184283542472
Propanoic acid	-1950.05938167997	8.20429617758126	-1941.85508550239	2.493	-2.605	0.000	3.60570020939068

Table A.86.: Raw hpCADD EC-RISM results for the group of the Esters at 1 bar.

Name	$\mu^{\text{ex}}/\text{kcal mol}^{-1}$	$E^{\text{sol}}/\text{kcal mol}^{-1}$	$G^{\text{sol}}/\text{kcal mol}^{-1}$	μ^x/D	μ^y/D	μ^z/D	μ^{tot}/D
Ethyl acetate	166.031686230163	10.493378792782	176.525065022945	-0.193	-3.266	0.000	3.27169757159796
Ethyl prop-2-enoate	963.360185731119	8.86823958054493	972.228425311663	-0.116	-3.423	-0.000	3.42496496332444
Ethyl 2-methylpropanoate	125.44319903848	17.1165041551147	142.559703193595	-0.261	2.788	-1.570	3.2102904852988
Ethyl 2,2-dimethylpropionate	105.032381023901	20.4937198587476	125.526100882648	-0.170	-3.239	-0.002	3.24345880195818
Ethyl propanoate	144.33885715153	13.6528242868069	157.991681438337	0.245	-3.066	0.000	3.07577323611478
Ethynyl prop-2-enoate	1064.92941575072	-29.6389164923518	1035.29049925837	-15.574	-3.557	0.002	15.9750345539532
Ethynyl 2,2-dimethylpropionate	217.78858468738	-3.01740219646272	214.771182490918	-12.559	-2.273	0.000	12.7630329467568
Propan-2-yl acetate	148.089510440966	14.1781426969407	162.267653137906	0.098	-2.451	1.842	3.06756727717584
Propan-2-yl 2-methylpropanoate	107.513486118308	21.3985435105163	128.912029628824	0.075	1.108	-2.789	3.00196768803397
Propan-2-yl 2,2-dimethylpropionate	86.9290436871415	25.0296029713193	111.958646658461	0.363	2.514	1.694	3.05312970572821
Propan-2-yl prop-2-ynoate	219.971821597514	-1.44484584560229	218.526975751912	11.016	-1.849	0.808	11.1992821644961
Propan-2-yl propionate	126.368787297562	17.3449312712715	143.713718568834	0.117	-2.258	1.735	2.84999614034826
Methyl acetate	184.20886162739	8.42222263647227	192.631084263862	3.091	0.394	0.000	3.11600978817461
Methyl prop-2-enoate	984.524365240201	5.9327049459847	990.457070186185	-2.835	-2.866	0.000	4.0312753565094
Methyl 2-methylpropanoate	143.574843450048	14.8113636159178	158.386207065966	1.748	2.071	-1.611	3.1527553029057
Methyl 2,2-dimethylpropionate	123.236815243069	18.3199726594168	141.556787902486	-1.500	-2.620	0.000	3.01900645908551
Methyl propanoate	162.280315434751	11.3208440908222	173.601159525574	0.062	-3.059	0.000	3.05962824539191
Methyl propiolate	267.135878850143	0.157337785611855	267.293216635755	6.722	-3.196	0.000	7.44309747349852
<i>tert</i> -Butyl acetate	129.28478898566	18.2153092521511	147.500098237811	-0.547	2.813	-0.002	2.86569049270852
<i>tert</i> -Butyl prop-2-ynoate	199.646518804971	2.05449730664436	201.701016111616	11.615	1.894	-0.002	11.7684096206752
<i>tert</i> -Butyl propionate	107.5871158174	21.227200905832	128.814335907983	-0.743	2.571	0.000	2.67620813839283

Table A.87.: Raw hpCADD EC-RISM results for the group of the Ethers at 1 bar.

Name	$\mu^{\text{ex}}/\text{kcal mol}^{-1}$	$E^{\text{sol}}/\text{kcal mol}^{-1}$	$G^{\text{sol}}/\text{kcal mol}^{-1}$	μ^x/D	μ^y/D	μ^z/D	μ^{tot}/D
1,4-Dioxane	-196.693139968929	11.8661295480402	-184.827010420889	-0.000	-0.000	0.000	0
Diethyl ether	-373.710715504302	14.7282745301147	-358.982440974187	0.000	0.000	-1.260	1.26
Diisopropyl ether	-408.223147966778	21.6801758119025	-386.542972154876	0.043	0.002	-0.974	0.974950767987799
Dimethyl ether	-330.934495618547	9.23819540129063	-321.696300217256	0.000	-0.000	-1.533	1.533
Di- <i>tert</i> -butyl ether	-441.324479792304	28.1200812323136	-413.20439855999	0.000	0.001	-0.255	0.255001960776775
Isobutyl methyl ether	-366.002189512189	15.1358550181644	-350.866334494025	0.045	0.749	0.827	1.11667139302482
Ethyl methyl ether	-345.72837972347	11.9291101517686	-333.799269571702	-0.092	1.231	0.000	1.23443306825441
Ethynyl methyl ether	-299.782276798279	7.18243082863289	-292.599845969646	-1.670	1.172	0.001	2.04021690023389
Methyl <i>tert</i> -butyl ether	-385.234430618786	18.532374792782	-366.702055826004	0.901	0.385	0.000	0.979809165092877
Tetrahydrofuran	-129.669726431405	11.1340186558317	-118.535707775574	-0.000	2.734	0.001	2.73400018288222
Oxane	-152.461268819073	14.4448711046845	-138.016397714388	-0.000	1.760	0.569	1.84969213654597

Table A.88.: Raw hpCADD EC-RISM results for the group of the Fluorides at 1 bar.

Name	$\mu^{\text{ex}}/\text{kcal mol}^{-1}$	$E^{\text{sol}}/\text{kcal mol}^{-1}$	$G^{\text{sol}}/\text{kcal mol}^{-1}$	μ^x/D	μ^y/D	μ^z/D	μ^{tot}/D
Fluoroethyne	117.159535373327	5.19494133269598	122.354476706023	-0.000	0.000	-1.941	1.941
3-Fluoroprop-1-ene	787.387449608509	10.1577018558795	797.545151464388	1.975	0.319	0.923	2.20325100703483
1,4-Difluorocyclohexane	316.643480256692	19.1725856591778	335.81606591587	0.000	-0.000	-0.000	0
Fluorocyclohexane	104.077490395554	18.1533281336042	122.230818529159	2.289	0.000	0.301	2.30870569800484
2,2-Difluoropropane	142.495828587476	14.0225350889101	156.518363676386	-0.000	2.577	-0.002	2.57700077609612
Difluoromethane	181.207254652247	8.01341157265774	189.220666224904	0.000	2.167	-0.000	2.167
Fluoromethane	-42.3126379020077	7.23740742041109	-35.0752304815966	-1.831	0.000	0.000	1.831
1-Fluoropropane	-79.7905175384799	12.4073771625239	-67.383140375956	1.876	-0.457	0.000	1.93086120681938
2-Fluoropropane	-79.2606070133843	12.917241374522	-66.3433656388623	0.000	-1.737	0.524	1.81431667577631
Fluoroethene	866.021650999283	5.44678076434034	871.468431763623	-2.784	0.795	0.001	2.89528616893046

Table A.89.: Raw hpCADD EC-RISM results for the group of the conjugated systems at 1 bar.

Name	$\mu^{ex}/\text{kcal mol}^{-1}$	$E^{sol}/\text{kcal mol}^{-1}$	$G^{sol}/\text{kcal mol}^{-1}$	μ^x/D	μ^y/D	μ^z/D	μ^{tot}/D
Aniline	-1603.92355196343	-7.62650633126195	-1611.55005829469	-9.117	0.002	2.644	9.49265131562305
1,4-Dioxin	1509.50652044049	10.3833027428298	1519.88982318332	-0.000	0.000	0.000	0
Furan	1309.72203984417	1.35048631285851	1311.07252615703	0.000	2.721	0.008	2.7210117603568
1H-Imidazole	-2493.65176810349	-15.5692522629063	-2509.2210203664	-2.081	-0.020	0.000	2.08109610542137
4H-1,4-Oxazine	-1923.54811988743	-15.202792416109	-1938.75091230354	5.560	-0.000	-2.609	6.14170017177654
1,3-Oxazole	860.800068685946	-21.1146425549713	839.685426130975	-1.435	4.805	-0.004	5.014704976367
Oxepine	1757.52180688337	4.14045270315488	1761.66225958652	1.938	0.001	-1.751	2.61186638249356
9H-Purine	-2679.26300739747	-67.1962331003824	-2746.45924049785	5.233	-0.567	-0.001	5.26362793137965
Pyrazine	708.705424210325	-39.232242623566	669.473181586759	0.000	-0.000	0.000	0
Pyridine	1184.03772819981	-4.54787878441683	1179.48984941539	-0.001	-4.031	0.000	4.0310001240387
Pyrimidine	821.1163782155883	4.70214403035373	825.818522245937	1.193	-0.000	0.000	1.193
1H-Pyrrole	-2044.92280298757	-2.91875941491396	-2047.84156240249	3.484	-0.000	0.000	3.484
4H-1,4-Thiazine	-2125.48389589364	-8.56401623398662	-2134.04791212763	7.590	-0.000	1.094	7.66843765052569
1,3-Thiazole	630.58184507696	-12.5382239063098	618.04362117065	5.750	-1.252	-0.002	5.88472667164755

Table A.90.: Raw hpCADD EC-RISM results for the group of the Nitriles at 1 bar.

Name	$\mu^{ex}/\text{kcal mol}^{-1}$	$E^{sol}/\text{kcal mol}^{-1}$	$G^{sol}/\text{kcal mol}^{-1}$	μ^x/D	μ^y/D	μ^z/D	μ^{tot}/D
Prop-2-enitrile	-21.7305338080784	-4.92534091921606	-26.6558747272945	-1.081	4.150	-0.000	4.28848003376488
Acetonitrile	-861.561805894837	-1.04629586998088	-862.608101764818	-0.000	-0.000	1.148	1.148
Propanenitrile	-881.301243174952	3.08355928800191	-878.21768388695	1.213	-0.179	-0.000	1.22613620776813
2-Methylpropanenitrile	-901.474521019121	7.1629164543499	-894.311604564771	-0.055	-1.235	0.000	1.23622408971836
2,2-Dimethylpropanenitrile	-937.462686910612	10.3279034512428	-927.134783459369	1.552	-0.002	-0.001	1.55200161082391

Table A.91.: Raw hpCADD EC-RISM results for the group of the Sulfones at 1 bar.

Name	$\mu^{ex}/\text{kcal mol}^{-1}$	$E^{sol}/\text{kcal mol}^{-1}$	$G^{sol}/\text{kcal mol}^{-1}$	μ^x/D	μ^y/D	μ^z/D	μ^{tot}/D
Diethyl sulfone	-804.217867581979	-1.39008589794455	-805.607953479924	-0.000	6.474	-0.001	6.474000077232
Dimethyl sulfone	-764.285824022706	-10.425061582696	-774.710885605402	-0.001	7.334	-0.002	7.33400034087809
Divinyl sulfone	907.0409808891	-13.4858641226099	893.5551249663	-0.000	-7.947	0.001	7.94700006291682
Msulfonylthen	73.1063464130019	-10.9216666407744	62.1846797722275	3.594	6.699	-0.485	7.6176546259331
Tetrahydrothiophene 1,1-dioxide	-574.443608572658	-13.7913715948853	-588.234980167543	9.674	0.001	-0.003	9.67400051684927

Table A.92.: Raw hpCADD EC-RISM results for the group of the Thioethers at 1 bar.

Name	$\mu^{ex}/\text{kcal mol}^{-1}$	$E^{sol}/\text{kcal mol}^{-1}$	$G^{sol}/\text{kcal mol}^{-1}$	μ^x/D	μ^y/D	μ^z/D	μ^{tot}/D
(Methylsulfanyl)methane	-230.89063146271	10.0426976773423	-220.946365468929	-0.000	-0.974	0.000	0.974
1,4-Dithiane	-28.8763197045889	14.8078053269598	-14.0685143776291	-0.000	0.000	0.000	0
1,1-Thioisethane	-283.505605662285	15.5913914777725	-267.914214184512	-0.000	0.648	0.000	0.648
(Methylsulfanyl)-2-propane	-283.623695630497	16.0498983107075	-267.57379731979	-0.212	0.596	0.390	0.743141978359452
(Methylsulfanyl)-2-ethyne	-162.296146917065	2.29536609536329	-160.000780821702	4.399	0.435	-0.000	4.42045540640328
Thiane	-68.9675163874283	15.8253975332218	-53.1421188542065	-1.826	0.000	0.001	1.82600027382254
terttert-Butyl methyl sulfide	-310.088315267447	19.1763885807839	-290.911926686663	-0.304	0.407	-0.001	0.508001968500123
Di-tert-Butyl sulfide	-391.420711106836	28.5037753656788	-362.916935741157	-0.001	-0.203	0.001	0.203004926048606
Ethyl methyl sulfide	-257.069574563097	12.844345539914	-244.225229023184	-0.526	0.890	0.000	1.03381623125196
Thiophene	-46.1487911089866	13.6963317832218	-32.4524593257648	-2.599	-0.001	-0.000	2.59900019238168

Table A.93.: Raw hpCADD EC-RISM results for the group of the Thiones at 1 bar.

Name	$\mu^{ex}/\text{kcal mol}^{-1}$	$E^{sol}/\text{kcal mol}^{-1}$	$G^{sol}/\text{kcal mol}^{-1}$	μ^x/D	μ^y/D	μ^z/D	μ^{tot}/D
(1R,4S)-1,3,3-trimethylbicyclo[2.2.1]heptane-2-thione	441.90034495913	27.3116553793021	469.212000338432	0.766	-5.545	0.858	5.66303319785431
6,6-Dimethylhept-1-yne-4-thione	74.815846626195	24.8705518467973	99.6863984729924	-1.551	4.791	0.787	5.09692564199244
Hept-1-ene-4-thione	861.236410189053	19.2454002347036	880.481810423757	-0.610	-2.221	0.051	2.30381032205345
Methanethial	757.099583694073	4.28180787045889	761.381391564532	1.388	-0.000	0.001	1.3880003602305
Nonane-5-thione	22.2869926051625	29.4634393979445	51.7504320031071	0.005	-2.220	0.027	2.2201698133251
Pentanthial	338.771821211998	13.6457992621893	352.417620474187	-6.795	0.830	0.317	6.85283984928876
Propane-2-thione	96.9456379440727	13.5877212131931	110.533359157266	-4.104	0.000	0.000	4.104

A. Additional data

Table A.94.: Raw hpCADD EC-RISM results for the group of the Alkanes at 10 kbar.

Name	$\mu^{\text{ex}}/\text{kcal mol}^{-1}$	$E^{\text{sol}}/\text{kcal mol}^{-1}$	$G^{\text{sol}}/\text{kcal mol}^{-1}$	μ^x/D	μ^y/D	μ^z/D	μ^{tot}/D
Ethyne	13.9575256049235	16.0830203773901	30.0405459823136	-0.000	-0.000	-0.000	0
Prop-2-enylbenzene	2117.34347091826	54.3228486704111	2171.66631958867	1.448	1.360	0.847	2.15956315026905
Benzene	1639.3407738413	29.8346156328872	1669.17538947419	0.000	-0.000	0.000	0
Buta-1,3-diene	1504.11365646845	37.9771511491396	1542.09080761759	0.000	0.000	0.000	0
Butane	-305.729935351338	42.9347061328872	-262.795229218451	0.000	-0.000	0.000	0
But-2-yne	-362.017324380258	35.9205178073614	-326.096806572897	-0.000	0.000	0.000	0
Cyclohexane	-103.882962169933	52.1175608231358	-51.7654013467973	0.000	0.000	0.000	0
Cyclohexene	456.747752443117	47.0706705040631	503.81842294718	-0.000	0.659	-0.001	0.659000758724905
e-But-2-ene	264.873431193356	39.3649842191683	304.238415412524	-0.001	-0.000	0.000	0.001
Ethene	918.261019257887	21.0396992705545	939.300718528442	-0.000	-0.000	-0.000	0
Ethylbenzene	1295.10008670076	53.8754105198375	1348.9754972206	-0.421	0.001	0.007	0.421059378235422
1,3,5-Hexatriene	2007.90134115464	50.6771541453155	2058.57849529995	-0.000	0.000	-0.000	0
1,3,5-Trimethylbenzene	725.026657064293	68.1934112351816	793.220068299474	-0.020	0.004	0.006	0.0212602916254693
2-Methylprop-1-ene	283.65881892304	39.5575668410612	323.216385764101	0.000	0.384	-0.000	0.384
Naphtalene	2378.97936673781	54.0179961532027	2432.99736289101	0.000	-0.000	0.000	0
Propane	-287.686511433317	34.5861521728011	-253.100359260516	-0.000	0.236	-0.000	0.236
Propene	587.471727380497	30.2495097765296	617.721237157027	-0.222	0.331	0.000	0.398553635035487
Propyne	-172.996135990201	25.8296746288241	-147.166461361377	0.873	-0.001	0.000	0.873000572737498
3,3-Dimethylbut-1-yne	-231.63530476434	51.5011706465105	-180.13413411783	-1.772	-0.003	0.002	1.77200366816776
Toluene	1331.23999213002	44.6142430059751	1375.85423513599	-1.007	-0.000	-0.003	1.00700446870905
z-But-2-ene	273.765920149618	35.4371142256214	309.203034375239	0.000	1.443	0.000	1.443

Table A.95.: Raw hpCADD EC-RISM results for the group of the Alcohols at 10 kbar.

Name	$\mu^{\text{ex}}/\text{kcal mol}^{-1}$	$E^{\text{sol}}/\text{kcal mol}^{-1}$	$G^{\text{sol}}/\text{kcal mol}^{-1}$	μ^x/D	μ^y/D	μ^z/D	μ^{tot}/D
Cyclohexanol	292.654269880258	50.6041400487572	343.258409929015	0.613	1.302	0.528	1.53289171176571
Ethanol	129.896239662524	24.9379122409178	154.834151903442	-0.759	1.259	-0.000	1.4700891129452
Propan-2-ol	103.600416032027	30.1363583475143	133.736774379541	0.000	0.115	1.661	1.66497627610726
Methanol	145.564581037046	15.3192312863289	160.883812323375	-1.570	0.112	0.000	1.57398983478293
Propan-1-ol	110.540933457696	33.3526515339388	143.893584991635	0.840	1.081	0.001	1.36900036523005
Prop-1-en-2-ol	940.943969258843	25.6971729316444	966.641142190488	-1.569	0.281	0.494	1.66875941944907
2-Propyn-1-ol	212.746947919216	16.9703403647228	229.717288283939	4.066	0.833	0.004	4.15045310779438
2-Methylpropan-2-ol	89.6714398953155	39.6381049008126	129.309544796128	-1.571	-0.001	0.658	1.70323398275164

Table A.96.: Raw hpCADD EC-RISM results for the group of the Amides at 10 kbar.

Name	$\mu^{\text{ex}}/\text{kcal mol}^{-1}$	$E^{\text{sol}}/\text{kcal mol}^{-1}$	$G^{\text{sol}}/\text{kcal mol}^{-1}$	μ^x/D	μ^y/D	μ^z/D	μ^{tot}/D
Prop-2-enamide	-2180.52486713575	-4.33053908389101	-2184.85540621965	8.222	-5.942	-0.000	10.144389976731
Acetamide	-3018.00157781501	-2.01170382146271	-3020.01328163647	2.983	-7.256	0.013	7.84525295959283
Azepan-2-one	-3020.14736634871	36.9184720743308	-2983.22889427438	4.793	-3.562	0.056	5.97192004300125
N,N-Dimethylacetamide	-3359.06836470411	35.9506977143881	-3323.11766698972	-2.638	5.079	0.632	5.75801259116373
N,N-Dimethylformamide	-3255.16857745053	27.9732209072658	-3227.19535654326	-6.144	0.477	0.001	6.16248862067915
N,N-Methylacetamide	-3193.781726951	15.0493787184512	-3178.73234823255	-1.253	-7.192	-0.004	7.30033485533369
N,N-Methylformamide	-3091.05428709178	7.68104065511472	-3083.37324643666	-5.568	4.519	0.001	7.17105194514724
Formamide	-2915.44050363097	-10.5503726598948	-2925.99087629087	7.706	-0.858	0.008	7.75362263719353
propiolamide	-2983.76945610588	-42.6041788924474	-3026.37363499833	-11.084	7.993	0.002	13.6653982378853

Table A.97.: Raw hpCADD EC-RISM results for the group of the Bromides at 10 kbar.

Name	$\mu^{ex}/\text{kcal mol}^{-1}$	$E^{sol}/\text{kcal mol}^{-1}$	$G^{sol}/\text{kcal mol}^{-1}$	μ^x/D	μ^y/D	μ^z/D	μ^{tot}/D
Bromoethyne	20.9192099844646	23.3813662375717	44.3005762220363	0.000	0.000	0.616	0.616
3-Bromoprop-1-ene	694.136714463671	35.6259872755736	729.762701739245	2.642	-0.130	0.482	2.68875212691687
Bromoethane	-101.712015249761	33.5513882382887	-68.1606270114723	2.249	0.397	0.000	2.28377100428217
Bromomethane	-76.2843529299713	25.1147441622849	-51.1696087676864	-2.006	0.000	0.000	2.006
1-Bromobutane	-139.320970106119	49.9525815341778	-89.3683885719407	2.848	0.486	0.000	2.88916943082264
Bromocyclohexane	57.106600286807	59.8141859388145	116.920785967495	3.011	0.000	0.056	3.01152071219841
E-1,2-Dibromocyclohexane	222.113283972992	67.6574142571702	289.770698230163	-4.477	-0.000	-0.000	4.477
1,4-Dibromobutane	29.212578540392	57.6467734858987	86.8593520262906	0.000	-0.000	0.000	0
Dibromomethane	82.7567521919216	32.0816416935946	114.838393885516	0.001	1.002	0.000	1.00200049900187
2-Bromopropane	-124.369624861616	42.6425216144837	-81.7271032471319	2.068	0.000	0.208	2.07843402589546
2-Bromo-2-methylpropane	-146.250949026769	51.5633240910612	-94.6876249357074	1.699	-0.000	0.000	1.699
Bromoethene	715.69877531979	29.0823962428298	744.78117156262	1.338	-0.476	0.000	1.42014787962381

Table A.98.: Raw hpCADD EC-RISM results for the group of the Carbonyls at 10 kbar.

Name	$\mu^{ex}/\text{kcal mol}^{-1}$	$E^{sol}/\text{kcal mol}^{-1}$	$G^{sol}/\text{kcal mol}^{-1}$	μ^x/D	μ^y/D	μ^z/D	μ^{tot}/D
2-Methylpropanal	-29.0753210664436	37.3251749631931	8.24985389674952	4.927	-0.000	0.162	4.92966256451697
Acetaldehyde	18.376463915153	21.9999377382887	40.3764016534417	3.978	0.884	0.008	4.07504650280215
Prop-2-enal	884.957781252151	20.4803083683078	905.438089620459	6.089	-0.215	-0.010	6.09280280330818
Cyclohexanone	84.1580090164914	45.535181709847	129.693190726338	-5.494	0.001	1.277	5.64045796013054
Formaldehyde	132.622492215583	15.5141819414436	148.136674157027	2.913	-0.000	0.008	2.91301098521787
Acetone	-83.4664599201721	30.7139088833652	-52.7525510368069	-0.011	4.247	-0.069	4.24757471976656
Undecan-2-one	-240.553066933795	97.8177615200765	-142.735305413719	-1.365	-3.770	0.190	4.01400361235513
But-3-en-2-one	760.759541422801	32.3192366577438	793.078778080545	-0.649	-4.194	-0.000	4.24391764764586

Table A.99.: Raw hpCADD EC-RISM results for the group of the Chlorides at 10 kbar.

Name	$\mu^{ex}/\text{kcal mol}^{-1}$	$E^{sol}/\text{kcal mol}^{-1}$	$G^{sol}/\text{kcal mol}^{-1}$	μ^x/D	μ^y/D	μ^z/D	μ^{tot}/D
Chloroethyne	11.5160941761472	23.7719536450765	35.2880478212237	-0.000	0.000	-0.418	0.418
3-Chloroprop-1-ene	711.298846601577	33.5371602717495	744.836006873327	3.351	0.040	0.593	3.40329986924455
1-Chlorobutane	-145.174181758604	48.0421160740918	-97.1320656845124	3.050	0.633	0.000	3.11499422150347
Chloroethane	-107.686828445746	31.7160210800669	-75.9708073656788	2.526	0.551	0.000	2.58539687475637
Chloromethane	-83.147878459847	23.5071110131453	-59.6407674467017	2.285	0.000	-0.000	2.285
Chlorocyclohexane	52.2166133190727	57.8522533130975	110.06886663217	-3.190	-0.000	0.070	3.19076793264568
1,3-Dichlorocyclohexane	212.814988181166	64.2952741199809	277.110262301147	0.000	2.903	0.246	2.91340436602954
1,4-Dichlorobutane	18.0117274115679	53.8594650308317	71.8711924423996	0.000	-0.000	-0.000	0
Dichloromethane	85.7099490265296	30.2905794249522	116.000528451482	0.000	1.663	0.000	1.663
Chloroethene	726.900468108748	27.3023823164436	754.202850425191	2.375	-0.042	0.000	2.37537133939096

Table A.100.: Raw hpCADD EC-RISM results for the group of the Acids at 10 kbar.

Name	$\mu^{ex}/\text{kcal mol}^{-1}$	$E^{sol}/\text{kcal mol}^{-1}$	$G^{sol}/\text{kcal mol}^{-1}$	μ^x/D	μ^y/D	μ^z/D	μ^{tot}/D
3-Butenoic acid	-1129.49440777271	35.5615762956501	-1093.93283147706	-4.435	-1.793	0.599	4.82108649580154
Acetic acid	-1927.47240545363	23.8298588833652	-1903.64254657027	-3.331	-1.739	-0.000	3.75761653179246
2-Methylpropanoic acid	-1972.69452076673	41.0242458501434	-1931.67027491659	3.513	1.883	-1.291	4.18969438026212
2,2-Dimethylpropanoic acid	-2005.20204103705	42.3712328236138	-1962.83080821343	8.110	-1.142	0.002	8.19001025640383
Prop-2-ynoic acid	-1841.35694308724	24.9077255767208	-1816.44921751052	-1.704	-2.129	0.001	2.72695031124515
Propanoic acid	-1952.10412180234	32.372801581979	-1919.73132022036	2.599	-2.767	0.000	3.79619414677384

A. Additional data

Table A.101.: Raw hpCADD EC-RISM results for the group of the Esters at 10 kbar.

Name	$\mu^{\text{ex}}/\text{kcal mol}^{-1}$	$E^{\text{sol}}/\text{kcal mol}^{-1}$	$G^{\text{sol}}/\text{kcal mol}^{-1}$	μ^x/D	μ^y/D	μ^z/D	μ^{tot}/D
Ethyl acetate	163.937043176864	40.479693457935	204.416736634799	-0.127	-3.514	-0.000	3.51629421408391
Ethyl prop-2-enoate	958.815288825287	39.7631056156788	998.578394440966	-0.711	-3.936	-0.000	3.9970211390798
Ethyl 2-methylpropanoate	124.026349760038	58.2861596524857	182.312509412524	-0.288	2.981	-1.686	3.4368446284363
Ethyl 2,2-dimethylpropionate	104.011532682122	66.7209023458413	170.732435027964	-0.230	-3.471	-0.002	3.4786125107577
Ethyl propanoate	142.578469130736	49.342349	191.920818130736	0.320	-3.293	0.000	3.30851159889156
Ethynyl prop-2-enoate	1036.00050512763	-22.9168632476099	1013.08364188002	-18.728	-4.305	0.002	19.2164256041544
Ethynyl 2,2-dimethylpropionate	197.206739269598	23.4775774208891	220.684316690488	-15.584	-2.547	-0.000	15.7907651809531
Propan-2-yl acetate	146.298893626912	49.7407324698853	196.039626096797	0.032	-2.631	1.988	3.29777637204223
Propan-2-yl 2-methylpropanoate	106.379277033222	68.4381627440249	174.817439777247	0.099	1.177	-2.994	3.21856582968253
Propan-2-yl 2,2-dimethylpropionate	86.1877196108987	77.0841300217495	163.271849632648	0.429	2.694	1.815	3.27656863196851
Propan-2-yl prop-2-ynoate	209.757852949331	28.6495203360421	238.407373285373	12.822	-1.708	0.672	12.952703655994
Propan-2-yl propionate	124.913787040153	58.6602470112333	183.574034051386	0.194	-2.416	1.869	3.06069485574763
Methyl acetate	182.273496471797	32.7325025996654	215.005999071463	3.322	0.551	0.000	3.36738548431866
Methyl prop-2-enoate	979.803404628824	30.6617518205067	1010.46515644933	-3.814	-3.220	0.000	4.99149236200958
Methyl 2-methylpropanoate	142.348244105641	50.4171643491874	192.765408454828	1.936	2.183	-1.708	3.38095385948995
Methyl 2,2-dimethylpropionate	122.467452750956	59.1860617595602	181.653514510516	-1.626	-2.766	0.000	3.20852489471408
Methyl propanoate	160.717412414436	41.3582096324092	202.075622046845	-0.033	-3.307	0.000	3.3071646466422
Methyl propiolate	259.42050167065	21.7922074055927	281.212709076243	8.201	-3.339	0.000	8.85467797268766
<i>tert</i> -Butyl acetate	128.08992003131	59.1819271759082	187.271847207218	-0.717	3.019	-0.002	3.10297502406964
<i>tert</i> -Butyl prop-2-ynoate	188.71186261066	36.5113409906788	225.223203601338	13.628	1.713	-0.003	13.7352379666317
<i>tert</i> -Butyl propionate	106.701318794455	67.9498853185946	174.65120411305	-0.928	2.755	0.000	2.9070963176338

Table A.102.: Raw hpCADD EC-RISM results for the group of the Ethers at 10 kbar.

Name	$\mu^{\text{ex}}/\text{kcal mol}^{-1}$	$E^{\text{sol}}/\text{kcal mol}^{-1}$	$G^{\text{sol}}/\text{kcal mol}^{-1}$	μ^x/D	μ^y/D	μ^z/D	μ^{tot}/D
1,4-Dioxane	-196.256198160612	39.6908965329828	-156.565301627629	-0.000	0.000	0.000	0
Diethyl ether	-372.576840441444	45.0369146192639	-327.53992582218	0.000	0.000	-1.193	1.193
Diisopropyl ether	-406.795921628107	63.2435875929732	-343.552334035134	0.011	0.002	-0.899	0.899069519002841
Dimethyl ether	-330.034511604207	28.1147265975143	-301.919785006692	-0.000	-0.000	-1.495	1.495
Di- <i>tert</i> -butyl ether	-439.547724010755	79.8563393092734	-359.691384701482	0.000	0.001	-0.131	0.131003816738292
Isobutyl methyl ether	-364.750083118786	45.4330050394359	-319.31707807935	0.089	0.699	0.778	1.04966947178624
Ethyl methyl ether	-344.605757542782	36.620157708413	-307.985599834369	-0.143	1.161	0.000	1.16977348234605
Ethynyl methyl ether	-301.178251282505	27.5703847237094	-273.607866558795	-2.043	1.105	0.001	2.32268702153347
Methyl <i>tert</i> -butyl ether	-383.897565977533	54.1918287657744	-329.705737211759	0.824	0.405	0.000	0.918150859064021
Tetrahydrofuran	-129.56723084608	37.0662551173518	-92.5009757287285	-0.000	2.856	0.001	2.85600017507002
Oxane	-151.640105249283	45.6576382110421	-105.982467038241	-0.000	1.823	0.496	1.88927102343735

Table A.103.: Raw hpCADD EC-RISM results for the group of the Fluorides at 10 kbar.

Name	$\mu^{\text{ex}}/\text{kcal mol}^{-1}$	$E^{\text{sol}}/\text{kcal mol}^{-1}$	$G^{\text{sol}}/\text{kcal mol}^{-1}$	μ^x/D	μ^y/D	μ^z/D	μ^{tot}/D
Fluoroethyne	115.812888050669	19.8428361187859	135.655724169455	-0.000	0.000	-2.038	2.038
3-Fluoroprop-1-ene	786.66587439173	31.4658513876673	818.131725779398	2.155	0.152	0.932	2.35281809751625
1,4-Difluorocyclohexane	316.531388689054	57.0383219216061	373.56971061066	0.000	-0.000	-0.000	0
Fluorocyclohexane	104.504237680927	54.4161781422084	158.920415823136	2.360	0.000	0.292	2.37799579478182
2,2-Difluoropropane	142.287972312381	40.0757453788241	182.363717691205	-0.000	2.649	-0.002	2.64900075500178
Difluoromethane	180.700513230402	22.410908958652	203.111422189054	0.000	2.195	-0.000	2.195
Fluoromethane	-42.3090507378107	20.0366683941205	-22.2723823436902	-1.855	0.000	0.000	1.855
1-Fluoropropane	-79.5549489937858	36.582053292065	-42.9728957017208	1.907	-0.434	0.000	1.95576199983536
2-Fluoropropane	-78.9069787124761	37.2370507172562	-41.6699279952199	-0.000	-1.774	0.527	1.85062286811765
Fluoroethene	863.304134955545	20.3167412172562	883.620876172801	-3.047	0.885	0.001	3.17292215473371

Table A.104.: Raw hpCADD EC-RISM results for the group of the conjugated systems at 10 kbar.

Name	$\mu^{ex}/\text{kcal mol}^{-1}$	$E^{sol}/\text{kcal mol}^{-1}$	$G^{sol}/\text{kcal mol}^{-1}$	μ^x/D	μ^y/D	μ^z/D	μ^{tot}/D
Aniline	-1613.74708347849	15.7356404713193	-1598.01144300717	-10.228	0.003	2.698	10.5778635366505
1,4-Dioxin	1508.46653735899	34.984806583413	1543.4513439424	-0.000	0.000	0.000	0
Furan	1303.58554455569	17.3234323130975	1320.90897686879	0.000	3.433	0.001	3.4330001456452
1 <i>H</i> -Imidazole	-2501.84412731047	-2.32263032313576	-2504.1667576336	-1.690	-0.066	0.000	1.69128826638158
4 <i>H</i> -1,4-Oxazine	-1937.33735687906	-2.6872917375717	-1940.02464861663	6.380	-0.000	-2.856	6.9900741054727
1,3-Oxazole	847.045324448853	-14.2304957559751	832.814828692878	-1.990	5.437	-0.004	5.78973963145149
Oxepine	1749.55177810349	26.2281444608031	1775.77992256429	2.570	0.000	-2.118	3.33028887635893
9 <i>H</i> -Purine	-2706.17802881119	-63.5300834531549	-2769.70811226434	6.116	-0.832	-0.002	6.17233213623505
Pyrazine	691.226813436902	-34.4038133217017	656.823000115201	0.000	0.000	0.000	0
Pyridine	1176.59978921319	14.070302375717	1190.67009158891	-0.001	-4.247	0.000	4.24700011773016
Pyrimidine	817.90760934369	27.0172453871893	844.92485473088	1.228	-0.000	0.000	1.228
1 <i>H</i> -Pyrrole	-2049.53188511185	16.0178290394359	-2033.51405607242	3.409	0.000	0.000	3.409

Table A.105.: Raw hpCADD EC-RISM results for the group of the Nitriles at 10 kbar.

Name	$\mu^{ex}/\text{kcal mol}^{-1}$	$E^{sol}/\text{kcal mol}^{-1}$	$G^{sol}/\text{kcal mol}^{-1}$	μ^x/D	μ^y/D	μ^z/D	μ^{tot}/D
Prop-2-enenitrile	-28.0393109137189	10.018341667782	-18.0209692459369	-1.260	4.710	-0.000	4.87562303711023
Acetonitrile	-864.074436179254	13.9880566577438	-850.08637952151	-0.000	0.000	1.298	1.298
Propanenitrile	-883.244169520076	24.0225098704589	-859.221659649618	1.373	-0.290	-0.000	1.40329220050565
2-Methylpropanenitrile	-902.844282940488	33.8013764239962	-869.042906516491	-0.143	-1.448	0.000	1.45504398558944
2,2-Dimethylpropanenitrile	-938.358304237572	42.0757873613767	-896.282516876195	1.817	-0.002	-0.000	1.81700110071513

Table A.106.: Raw hpCADD EC-RISM results for the group of the Sulfones at 10 kbar.

Name	$\mu^{ex}/\text{kcal mol}^{-1}$	$E^{sol}/\text{kcal mol}^{-1}$	$G^{sol}/\text{kcal mol}^{-1}$	μ^x/D	μ^y/D	μ^z/D	μ^{tot}/D
Diethyl sulfone	-812.967253303298	30.9059339407266	-782.061319362572	-0.000	6.917	-0.001	6.91700007228567
Dimethyl sulfone	-774.927688109943	9.05997794192161	-765.867710168021	-0.001	7.834	-0.002	7.83400031912177
Divinyl sulfone	893.906184465344	10.6731415303537	904.579325995698	-0.000	-8.685	0.001	8.68500005757052
Ethyl sulfone	has	not	finished.				
Msulfonylethen	61.8361525798279	11.5572065210325	73.3933591008604	3.899	7.211	-0.645	8.22294028921529
Tetrahydrothiophene 1,1-dioxide	-586.247891862572	11.6466533530115	-574.60123850956	10.357	0.001	-0.003	10.3570004827653

Table A.107.: Raw hpCADD EC-RISM results for the group of the Thioethers at 10 kbar.

Name	$\mu^{ex}/\text{kcal mol}^{-1}$	$E^{sol}/\text{kcal mol}^{-1}$	$G^{sol}/\text{kcal mol}^{-1}$	μ^x/D	μ^y/D	μ^z/D	μ^{tot}/D
(Methylsulfanyl)methane	-229.181678601577	31.5470954079828	-197.634583193595	-0.000	-0.686	0.000	0.686
1,4-Dithiane	-26.4841466998088	48.194188708652	21.7100420088432	-0.000	-0.000	-0.000	0
1,1-Thioisethane	-281.677638791348	48.7247041907266	-232.952934600621	0.000	0.330	0.000	0.33
(Methylsulfanyl)-2-propane	-281.592930039197	48.9579959928298	-232.634934046367	-0.249	0.333	0.223	0.471825179489183
(Methylsulfanyl)-2-ethyne	-168.617787830306	19.2472081909656	-149.37057963934	6.026	0.029	-0.000	6.02606978054519
Thiane	-67.2619034242352	49.8500343659178	-17.4118690583174	-1.681	0.000	-0.164	1.68898105377177
tert-tert-Butyl methyl sulfide	-307.965290123566	57.283122417782	-250.682167705784	-0.352	0.098	-0.001	0.365388833983744
Di-tert-Butyl sulfide	-389.022493300908	82.7942009371415	-306.228292363767	-0.001	-0.606	0.001	0.60600165016277
Ethyl methyl sulfide	-255.187534624761	40.2161515599904	-214.971383064771	-0.635	0.595	0.000	0.870201126177161
Thiophene	-44.6527985640535	42.8713192268164	-1.78147933723709	-2.534	-0.002	-0.001	2.53400098658229

Table A.108.: Raw hpCADD EC-RISM results for the group of the Thiones at 10 kbar.

Name	$\mu^{ex}/\text{kcal mol}^{-1}$	$E^{sol}/\text{kcal mol}^{-1}$	$G^{sol}/\text{kcal mol}^{-1}$	μ^x/D	μ^y/D	μ^z/D	μ^{tot}/D
(1 <i>R</i> ,4 <i>S</i>)-1,3,3-trimethylbicyclo[2.2.1]heptane-2-thione	442.042709709369	82.4592640578394	524.501973767208	0.808	-5.918	0.932	6.04518089059376
6,6-Dimethylhept-1-ene-4-thione	73.5227937808317	77.741508875956	151.264302656788	-1.621	5.316	1.067	5.65915064298522
Hept-1-ene-4-thione	860.304299770555	62.8770864615201	923.181386232075	-0.901	-2.027	-0.004	2.218230337577254
Methanethial	757.347488772705	17.6650713028203	775.012560075526	1.261	-0.000	0.001	1.26100039651064
Nonane-5-thione	23.6660199952199	88.9139940554493	112.580014050669	0.005	-2.158	0.030	2.15821430817238
Pentanthial	337.594975113528	49.0500178183556	386.644992931883	-7.348	0.858	0.354	7.40638805356565
Propane-2-thione	96.9770893537285	40.098873373805	137.075962727533	-4.250	0.000	0.000	4.25

A. Additional data

Table A.109.: Raw MP2 EC-RISM results for the group of the Carbonyls at 1 bar.

Name	$\mu^{ex}/\text{kcal mol}^{-1}$	$E^{sol}/\text{kcal mol}^{-1}$	$G^{sol}/\text{kcal mol}^{-1}$	μ^x/D	μ^y/D	μ^z/D	μ^{tot}/D
2-Methylpropanal	-145447.680557652	5.41219928202677	-145442.26835837	4.6904	-0.0011	1.5038	4.9255728407973
Acetaldehyde	-96263.6779930884	-1.14398376888145	-96264.8219768573	4.1262	1.9403	0.0111	4.55965061600119
Prop-2-enal	-120091.267951044	0.0344959005736138	-120091.233455143	5.4696	1.6860	-0.0089	5.72356526738361
Cyclohexanone	-193891.877159882	6.49213762213193	-193885.38502226	-5.3350	-0.0002	1.9748	5.6887661298387
Formaldehyde	-71667.6568759052	-3.07301151338432	-71670.7298874186	3.9772	-0.0003	0.0103	3.97721334856454
Acetone	-120860.914163912	1.01527403513384	-120859.898889877	-0.0131	5.0520	-0.0817	5.05267755749365
Undecan-2-one	-317587.473871473	26.7380673795411	-317560.735804093	-0.4331	-4.9766	0.2020	4.99949269126378
But-3-en-2-one	-144686.367265317	3.12504691515296	-144683.242218402	-0.8769	-4.6316	-0.0000	4.71388079717763

Table A.110.: Raw MP2 EC-RISM results for the group of the Chlorides at 1 bar.

Name	$\mu^{ex}/\text{kcal mol}^{-1}$	$E^{sol}/\text{kcal mol}^{-1}$	$G^{sol}/\text{kcal mol}^{-1}$	μ^x/D	μ^y/D	μ^z/D	μ^{tot}/D
Chloroethyne	-336435.90159745	5.83700370172084	-336430.064593748	0.0000	-0.0000	-0.6674	0.6674
3-Chloroprop-1-ene	-361810.144798204	9.66588276625239	-361800.478915438	2.6050	1.5619	0.3794	3.06096405892
1-Chlorobutane	-387167.232493637	14.6239765592734	-387152.608517078	3.0661	1.4930	0.0003	3.41028126406019
Chloroethane	-337985.655273857	8.34372098804971	-337977.311552869	2.9690	1.2661	0.0003	3.22768807352879
Chloromethane	-313392.73789724	5.18444956190249	-313387.553447678	2.9058	-0.0000	-0.0004	2.90580002573114
Chlorocyclohexane	-435612.7298486	17.7656837473709	-435594.964164852	-3.7761	-0.0000	0.6663	3.8344436506612
1,3-Dichlorocyclohexane	-723683.511988174	16.8180769918738	-723666.693911183	-0.0000	3.7430	1.4237	4.00461866973623
1,4-Dichlorobutane	-675233.745151104	12.5298794027247	-675221.215271701	0.0000	-0.0000	0.0001	0.0001
Dichloromethane	-601456.333821911	6.5134132583652	-601449.820408653	-0.0000	2.5458	0.0002	2.54580000785608
Chloroethene	-337218.747045995	8.59588020363289	-337210.151165792	2.1899	0.5825	0.0004	2.26604687065383

Table A.111.: Raw MP2 EC-RISM results for the group of the Acids at 1 bar.

Name	$\mu^{ex}/\text{kcal mol}^{-1}$	$E^{sol}/\text{kcal mol}^{-1}$	$G^{sol}/\text{kcal mol}^{-1}$	μ^x/D	μ^y/D	μ^z/D	μ^{tot}/D
3-Butenoic acid	-191810.742306247	0.919658558795411	-191809.822647688	-0.0361	-2.6780	0.4062	2.70887165624361
Acetic acid	-143395.566092797	-3.82451016539197	-143399.380602963	-1.2483	-2.5069	-0.0005	2.80050008926977
2-Methylpropanoic acid	-192578.647900346	3.48055804110899	-192575.167342305	0.9162	2.2496	-1.5006	2.85515725661477
2,2-Dimethylpropanoic acid	-217164.472263589	2.27803247036329	-217162.194231118	5.2962	-4.5028	0.0008	6.9516144110559
Prop-2-ynoic acid	-166440.663919645	-5.02221518021032	-166445.686134826	-1.4733	-2.2966	0.0004	2.7285499097506
Propanoic acid	-167986.397316077	-0.35333266873805	-167986.750648746	0.2256	-2.7168	0.0003	2.72615070933358

Table A.112.: Raw MP2 EC-RISM results for the group of the Esters at 1 bar.

Name	$\mu^{ex}/\text{kcal mol}^{-1}$	$E^{sol}/\text{kcal mol}^{-1}$	$G^{sol}/\text{kcal mol}^{-1}$	μ^x/D	μ^y/D	μ^z/D	μ^{tot}/D
Ethyl acetate	-192568.756551978	7.22622664866157	-192561.530325329	-1.2615	-2.8270	0.0000	3.0956923700523
Ethyl prop-2-enoate	-216394.568086859	9.70671054708413	-216384.861376312	0.2012	-2.5953	-0.0002	2.60308731509337
Ethyl 2-methylpropanoate	-241752.150477255	14.725405414675	-241737.42507184	0.6998	2.6320	-1.4072	3.06551070459372
Ethyl 2,2-dimethylpropanoate	-266346.107624773	18.5633518470363	-266327.544272926	-0.5342	-3.2304	-0.0001	3.27427149301948
Ethyl propanoate	-217159.634791432	10.8368813460803	-217148.797910086	-1.0056	-2.7950	0.0001	2.97039666879695
Ethynyl prop-2-enoate	-214839.192241558	5.08605178561185	-214834.106189772	-3.3534	-2.1860	0.0014	4.00298507616504
Ethynyl 2,2-dimethylpropanoate	-264792.057687589	13.955461209608	-264778.102226379	-3.0125	-2.4689	0.0009	3.89494855806851
Propan-2-yl acetate	-217163.776712626	11.3137537875239	-217152.462958838	1.1352	-2.3050	1.5458	2.99853325477641
Propan-2-yl 2-methylpropanoate	-266347.532996908	19.3356574452677	-266328.197339463	-0.7040	1.0080	-2.7169	2.98215117155385
Propan-2-yl 2,2-dimethylpropanoate	-290941.561211089	23.4841227289675	-290918.077088361	0.4933	2.6872	1.6652	3.19957493583132
Propan-2-yl prop-2-ynoate	-240210.330161536	10.2982515054971	-240200.031910031	0.8316	-2.5533	1.2204	2.94962296065107
Propan-2-yl propionate	-241754.713687281	14.9238812277725	-241739.789806054	-0.9706	-2.2460	1.4964	2.86806438560922
Methyl acetate	-167975.63426994	4.09009569144359	-167971.544174249	2.6739	-1.8663	0.0000	2.925243391583
Methyl prop-2-enoate	-191801.358355482	6.51576208914914	-191794.842593393	-0.5347	-2.4608	0.0004	2.51822177140934
Methyl 2-methylpropanoate	-217158.935348405	11.4647450941683	-217147.47060331	0.1130	2.3275	-1.7481	2.91305318523366
Methyl 2,2-dimethylpropanoate	-241752.794493037	15.0943097177342	-241737.700183319	-0.4440	-3.0726	0.0001	3.10451393457978
Methyl propanoate	-192566.429882742	7.60743998087954	-192558.822442762	1.7716	-2.2042	0.0000	2.82790809610213
Methyl propionate	-191021.85463927	3.19566039818356	-191018.658978872	-0.2764	-2.8050	0.0001	2.81858510071986
<i>tert</i> -Butyl acetate	-241757.359084981	15.6052473164436	-241741.753837665	1.3047	2.7571	-0.0000	3.05022007402745
<i>tert</i> -Butyl prop-2-ynoate	-264804.17178228	14.2792152641013	-264789.892567016	1.0861	2.8090	-0.0000	3.01165971019304
<i>tert</i> -Butyl propionate	-266348.423313373	19.2399823018642	-266329.183331072	1.1710	2.6659	0.0002	2.91174584227401
Ethynyl acetate	-191794.249480554	1.82381187356597	-191792.42566868	-3.3129	5.3830	0.1479	6.32248921074603

Table A.113.: Raw MP2 EC-RISM results for the group of the Ethers at 1 bar.

Name	$\mu^{ex}/\text{kcal mol}^{-1}$	$E^{sol}/\text{kcal mol}^{-1}$	$G^{sol}/\text{kcal mol}^{-1}$	μ^x/D	μ^y/D	μ^z/D	μ^{tot}/D
1,4-Dioxane	-192540.402833258	3.74440436472275	-192536.658428893	0.0000	0.0000	-0.0000	0
Diethyl ether	-146189.453609853	10.4535408042543	-146179.000069048	0.0001	0.0003	-2.4852	2.4852000201191
Diisopropyl ether	-195377.521590079	17.5829935516252	-195359.938596528	0.8059	0.0020	-2.4257	2.55607106708714
Dimethyl ether	-97005.238236453	4.3771271792543	-97000.8611092738	-0.0000	-0.0000	-2.2761	2.2761
Di- <i>tert</i> -butyl ether	-244610.84363052	24.4782474046367	-244586.365383116	0.0001	0.0005	-2.5164	2.5164000516611
Isobutyl methyl ether	-146192.113812789	10.9467430162524	-146181.167069773	-0.0313	1.7657	1.6140	2.3924197323408
Ethyl methyl ether	-121598.715269073	7.86413554349904	-121590.85113353	0.2840	2.2372	0.0003	2.25515408121042
Ethynyl methyl ether	-120051.915480395	4.45422224043977	-120047.461258154	-1.8449	1.8760	0.0009	2.63116567703366
Methyl <i>tert</i> -butyl ether	-170786.217113617	14.3202141046845	-170771.896899513	2.1878	1.0747	0.0000	2.43750875485607
Tetrahydrofuran	-145444.421553219	6.34897506716061	-145438.072578152	0.0005	3.0297	0.0007	3.0297001221243
Oxane	-170040.420343676	10.1304021410134	-170030.289941535	0.0000	2.3016	1.3726	2.67981217998575

Table A.114.: Raw MP2 EC-RISM results for the group of the Fluorides at 1 bar.

Name	$\mu^{ex}/\text{kcal mol}^{-1}$	$E^{sol}/\text{kcal mol}^{-1}$	$G^{sol}/\text{kcal mol}^{-1}$	μ^x/D	μ^y/D	μ^z/D	μ^{tot}/D
Fluoroethyne	-110518.653857862	5.52425994622371	-110513.129597916	0.0000	0.0000	-1.1830	1.183
3-Fluoroprop-1-ene	-135901.21681322	8.38157271821224	-135892.835240502	2.2379	1.1888	1.3554	2.87376947753295
1,4-Difluorocyclohexane	-271866.600607299	14.221947998327	-271852.378659301	0.0009	-0.0000	0.0001	0.000905538513813742
Fluorocyclohexane	-209704.09039049	16.481795831262	-209687.608594659	3.2097	0.0000	0.6997	3.28508054391365
2,2-Difluoropropane	-198844.192965303	11.1615444916348	-198833.031420811	0.0000	3.4691	-0.0003	3.46910001297166
Difluoromethane	-149649.91980201	4.16221402198853	-149645.757587988	-0.0000	2.7686	-0.0000	2.7686
Fluoromethane	-87484.1949966085	4.18234012978011	-87480.0126564787	-2.6437	-0.0001	-0.0001	2.64370000378258
1-Fluoropropane	-136668.058489371	10.377667624283	-136657.680821746	2.7251	-1.0269	-0.0001	2.91216305003686
2-Fluoropropane	-136672.79598072	10.3972642841778	-136662.398716436	0.0000	-2.8262	0.9384	2.97791890420139
Fluoroethene	-111311.575066583	7.54709744383365	-111304.027969139	-1.8265	1.0469	0.0009	2.10525596306007

Table A.115.: Raw MP2 EC-RISM results for the group of the conjugated systems at 1 bar.

Name	$\mu^{ex}/\text{kcal mol}^{-1}$	$E^{sol}/\text{kcal mol}^{-1}$	$G^{sol}/\text{kcal mol}^{-1}$	μ^x/D	μ^y/D	μ^z/D	μ^{tot}/D
Aniline	-179942.584498024	5.4406221749522	-179937.143875849	-1.1205	0.0016	1.7357	2.06595675172546
Benzo[<i>b</i>]thiophene	-442531.522667565	15.8795981106597	-442515.643069454	-0.4154	1.1717	0.0001	1.24315649055137
1,4-Dioxin	-191014.856646662	6.85098585569656	-191008.005660805	0.0000	0.0000	0.0026	0.0026
Furan	-143944.135821386	7.84104798996176	-143936.294773396	0.0001	1.1534	0.0002	1.15340002167505
1 <i>H</i> -Imidazole	-141558.91674416	-7.78142331763862	-141566.698167478	-2.9744	5.1417	0.0002	5.94004497373547
4 <i>H</i> -1,4-Oxazine	-178565.613240293	1.82179914483748	-178563.791441148	2.7878	-0.0000	-1.9789	3.41875328884668
1,3-Oxazole	-154007.196902919	1.98156163121415	-154005.215341288	-0.8243	-2.1082	0.0010	2.26362071248697
Oxepine	-192348.717938917	10.3266308018642	-192338.391309015	0.8612	0.0001	-2.1041	2.2735219946154
Phenol	-192397.386317424	5.48585967710325	-192391.900457747	0.3218	2.0820	0.0008	2.10672254461759
9 <i>H</i> -Purine	-257799.30097577	-15.5984622939771	-257814.899438064	-5.2181	7.7713	0.0009	9.36064485545734
Pyrazine	-165399.538932151	3.41507537786807	-165396.123856773	0.0000	0.0000	0.0000	0
Pyridine	-155344.668353294	4.74760338360421	-155339.920749911	0.0002	3.8453	0.0000	3.84530000520115
Pyrimidine	-165400.39254061	0.898960069072658	-165399.493580541	-3.7574	0.0005	0.0000	3.75740003326768
1 <i>H</i> -Pyrrole	-131499.83260988	3.41602139651052	-131496.416588483	2.7899	-0.0002	0.0000	2.78990000716872
4 <i>H</i> -1,4-Thiazine	-381017.787971076	2.67497271391013	-381015.112998362	4.6602	-0.0000	1.7797	4.98846631040042
1,3-Thiazole	-356454.097858693	3.6573297540631	-356450.440528938	-2.2772	1.5070	0.0005	2.73069388434515
Thiophene	-346392.800169567	10.061171460086	-346382.738998107	-0.8367	-0.0000	-0.0006	0.836700215130844

Table A.116.: Raw MP2 EC-RISM results for the group of the Nitriles at 1 bar.

Name	$\mu^{ex}/\text{kcal mol}^{-1}$	$E^{sol}/\text{kcal mol}^{-1}$	$G^{sol}/\text{kcal mol}^{-1}$	μ^x/D	μ^y/D	μ^z/D	μ^{tot}/D
Prop-2-enitrile	-106891.18069444	0.854205555688336	-106890.326488884	1.6512	-6.0460	0.0000	6.2674219133548
Acetonitrile	-83067.411136381	-1.68169064770554	-83069.0928270287	0.0000	-0.0002	-5.7597	5.7597000034724
Propanenitrile	-107657.675782433	1.78923039555449	-107655.886552037	-5.6108	2.0092	0.0007	5.95969477154661
2-Methylpropanenitrile	-132250.077545961	5.3696400291587	-132244.707905932	1.8784	5.7901	-0.0000	6.08717048964459
2,2-Dimethylpropanenitrile	-156843.271680846	9.04475810946463	-156834.226922736	-6.0237	-0.0002	-0.0007	6.02370004399289

A. Additional data

Table A.117.: Raw MP2 EC-RISM results for the group of the Sulfones at 1 bar.

Name	$\mu^{\text{ex}}/\text{kcal mol}^{-1}$	$E^{\text{sol}}/\text{kcal mol}^{-1}$	$G^{\text{sol}}/\text{kcal mol}^{-1}$	μ^x/D	μ^y/D	μ^z/D	$\mu^{\text{tot}}/\text{D}$
Diethyl sulfone	-442809.958146458	-1.06941466778203	-442811.027561126	-0.0000	7.5601	-0.0002	7.56010000264547
Dimethyl sulfone	-393624.486539157	-9.49211180114723	-393633.978650958	-0.0001	7.6063	-0.0003	7.6063000065735
Divinyl sulfone	-441272.870844255	-0.552309646510516	-441273.423153902	-0.0001	-7.5191	-0.0002	7.51910000332487

Table A.118.: Raw MP2 EC-RISM results for the group of the Thioethers at 1 bar.

Name	$\mu^{\text{ex}}/\text{kcal mol}^{-1}$	$E^{\text{sol}}/\text{kcal mol}^{-1}$	$G^{\text{sol}}/\text{kcal mol}^{-1}$	μ^x/D	μ^y/D	μ^z/D	$\mu^{\text{tot}}/\text{D}$
(Methylsulfanyl)methane	-299455.149024355	6.65355796223709	-299448.495466392	0.0000	-2.8037	0.0000	2.8037
1,4-Dithiane	-597439.024430775	9.10976578656788	-597429.914664988	-0.0001	-0.0000	0.0003	0.000316227766016838
1,1-Thiobisethane	-348637.909722928	13.1561752574092	-348624.75354767	-0.0000	2.9964	0.0006	2.99640006007209
(Methylsulfanyl)-2-propane	-348640.175425907	13.0342263224187	-348627.141199585	-0.4743	2.5188	1.6319	3.03848836430222
(Methylsulfanyl)-2-ethyne	-322507.626740728	6.96231590105162	-322500.664424827	1.1739	2.1155	-0.0002	2.41937626259332
Thiane	-372489.499827484	12.5551545776769	-372476.944672906	-3.0764	-0.0000	1.2613	3.32492325475341
tert-tert-Butyl methyl sulfide	-373234.885460553	16.328862248805	-373218.556598305	0.7890	2.9723	-0.0006	3.07523798266085
Di-tert-Butyl sulfide	-447011.349520262	25.9866651314532	-446985.362855131	0.0001	3.2099	-0.0001	3.20990000311536
Ethyl methyl sulfide	-324046.540819596	9.88865215129063	-324036.652167445	-0.0282	2.9086	-0.0000	2.90873670173153
Thiophene	-347896.309398434	9.28535587332696	-347887.024042561	-3.5936	0.0001	0.0014	3.59360027409839

Table A.119.: Raw MP2 EC-RISM results for the group of the Thiones at 1 bar.

Name	$\mu^{\text{ex}}/\text{kcal mol}^{-1}$	$E^{\text{sol}}/\text{kcal mol}^{-1}$	$G^{\text{sol}}/\text{kcal mol}^{-1}$	μ^x/D	μ^y/D	μ^z/D	$\mu^{\text{tot}}/\text{D}$
(1R,4S)-1,3,3-trimethylbicyclo[2.2.1]heptane-2-thione	-493951.77545869	24.5585383840822	-493927.216920306	1.2775	-5.8167	1.2057	6.07615977653649
6,6-Dimethylhept-1-yne-4-thione	-469303.132271837	21.1208721424474	-469282.011399694	-3.2545	2.8731	-2.5505	5.03502970299084
Hept-1-ene-4-thione	-420890.039824307	17.5578738499044	-420872.481950457	1.1475	-4.9387	0.5886	5.10430836646847
Methanethial	-274100.774928774	2.91243826218929	-274097.862490512	3.4466	0.0000	0.0002	3.44660000580282
Nonane-5-thione	-470833.610067774	28.8133126070746	-470804.796755167	-0.0003	-4.5522	-0.0314	4.55230830348736
Pentaanthial	-372468.817081938	14.0654748575526	-372454.75160708	-4.2507	1.9404	1.5628	4.92706266349435
Propane-2-thione	-323291.563497903	6.4623390207935	-323285.101158882	-5.4002	-0.0000	0.0000	5.4002

Table A.120.: Raw MP2 EC-RISM results for the group of the Alkanes at 10 kbar.

Name	$\mu^{\text{ex}}/\text{kcal mol}^{-1}$	$E^{\text{sol}}/\text{kcal mol}^{-1}$	$G^{\text{sol}}/\text{kcal mol}^{-1}$	μ^x/D	μ^y/D	μ^z/D	$\mu^{\text{tot}}/\text{D}$
Ethyne	-48374.1232993341	14.6557877131931	-48359.4675116209	0.0000	-0.0000	-0.0000	0
Prop-2-enylbenzene	-218301.901488061	62.5874521065966	-218239.314035954	0.0782	-0.2492	-0.1602	0.306398302867363
Benzene	-145291.157342015	40.3651142155832	-145250.792227799	-0.0000	0.0000	0.0003	0.0003
Buta-1,3-diene	-97572.7353070202	35.2585979510038	-97537.4767090692	-0.0000	-0.0000	-0.0002	0.0002
Butane	-99100.0934388226	46.1468975172084	-99053.9465413054	0.0000	0.0000	0.0000	0
But-2-yne	-97564.2284759906	32.0431732174952	-97532.1853027731	-0.0000	0.0000	-0.0000	0
Cyclohexane	-147540.807377394	55.5492630198375	-147485.258114374	0.0000	-0.0000	0.0000	0
Cyclohexene	-146776.203247769	49.6748300913002	-146726.528417678	0.0002	-0.6253	-0.0001	0.625300039980808
n-But-2-ene	-98332.1842614961	40.9773111140057	-98291.2069503821	-0.0000	0.0001	0.0008	0.000806225774829855
Ethene	-49150.7895977875	22.3024799101338	-49128.4871178773	-0.0000	-0.0000	-0.0000	0
Ethylbenzene	-194476.326080472	58.6872655040631	-194417.638814968	0.7106	-0.0000	-0.0531	0.712581202390296
1,3,5-Hexatriene	-145995.975104405	48.241942415153	-145947.73316199	-0.0000	0.0000	0.0002	0.0002
1,3,5-Trimethylbenzene	-219071.538795831	67.8420462289675	-219003.696749602	0.0001	0.0017	0.0571	0.0571253884013054
2-Methylprop-1-ene	-98337.6942759623	39.782976626912	-98297.9112993354	-0.0001	-1.0795	-0.0000	1.07950000463177
Naphthalene	-241423.749235735	58.9081509280593	-241364.841084807	0.0001	-0.0001	0.0000	0.00014142135623731
Propane	-74509.4515925158	37.2065252244264	-74472.2450672914	-0.0000	0.1086	0.0000	0.1086
Propene	-73741.5184058014	31.3279603025813	-73710.1904454988	0.6678	0.0279	0.0003	0.668382629935877
Propyne	-72969.6268660061	23.1055894053537	-72946.5212766008	1.2365	-0.0005	-0.0001	1.23650010513546
3,3-Dimethylbut-1-yne	-146747.351510516	50.2896478998566	-146697.061862616	-1.4043	-0.0013	-0.0005	1.40430069073543
Toluene	-169884.750389508	49.4630923778681	-169835.28729713	0.6383	-0.0001	0.0552	0.640682401818561
z-But-2-ene	-98334.2375373323	13.9540780155354	-98320.2834593167	0.0000	-0.5122	0.0003	0.512200087856299

Table A.121.: Raw MP2 EC-RISM results for the group of the Alcohols at 10 kbar.

Name	$\mu^{ex}/\text{kcal mol}^{-1}$	$E^{sol}/\text{kcal mol}^{-1}$	$G^{sol}/\text{kcal mol}^{-1}$	μ^x/D	μ^y/D	μ^z/D	μ^{tot}/D
Cyclohexanol	-194642.590788287	43.7886745982314	-194598.802113689	-1.5555	2.0587	1.4255	2.947859594689
Ethanol	-97016.7589609914	16.5646004337954	-97000.1943605576	0.2785	2.7240	0.0000	2.7381998192243
Propan-2-ol	-121610.506165681	25.1731563128585	-121585.333009368	-0.0002	-2.4160	1.5740	2.88349302756223
Methanol	-72423.8892689306	7.79114866945507	-72416.0981202612	-2.1529	1.5999	-0.0000	2.68228604365754
Propan-1-ol	-121606.9883044	25.5372074612811	-121581.451096938	-0.4752	2.6126	0.0015	2.65546531703956
Prop-1-en-2-ol	-120839.773823256	20.3453866720841	-120819.428436583	-0.4491	2.3190	1.4954	2.79565251238418
2-Propyn-1-ol	-120062.710959279	12.5004556331262	-120050.210503646	1.4430	2.7572	0.0027	3.11197816991058
2-Methylpropan-2-ol	-146206.143569553	34.2596233066444	-146171.883946246	-2.1705	0.0004	-1.9636	2.92690884210629

Table A.122.: Raw MP2 EC-RISM results for the group of the Amides at 10 kbar.

Name	$\mu^{ex}/\text{kcal mol}^{-1}$	$E^{sol}/\text{kcal mol}^{-1}$	$G^{sol}/\text{kcal mol}^{-1}$	μ^x/D	μ^y/D	μ^z/D	μ^{tot}/D
Prop-2-enamide	-154755.549681599	9.50680834918738	-154746.04287325	0.0207	-6.2448	-0.0000	6.2448343076498
Acetamide	-130929.123513219	2.95251904732314	-130926.170994172	-0.5463	-6.6549	0.0081	6.67729011725565
Azapan-2-one	-228544.009411163	33.1386676441205	-228510.870743519	6.9226	-1.6784	1.8342	7.3555222085179
<i>N,N</i> -Dimethylacetamide	-180099.627637139	27.6400686880975	-180071.987568451	-3.0006	6.0966	0.0807	6.79548706201042
<i>N,N</i> -Dimethylformamide	-155506.211537086	18.4351785678776	-155487.776358518	-6.7499	-1.2053	0.0002	6.85666815151499
<i>N,N</i> -Methylacetamide	-155514.011723809	14.138097791826	-155499.873626018	-0.7441	-6.8212	-0.0038	6.86166661169136
<i>N,N</i> -Methylformamide	-130918.762058205	5.43009347155832	-130913.331964733	-4.4691	5.0401	0.0008	6.73613119379366
Formamide	-106334.084253274	-5.62513292112811	-106339.709386195	6.2061	1.9204	0.0049	6.496432665702
propiolamide	-153979.082275657	6.31935016395793	-153972.762925493	2.0821	6.2631	0.0020	6.60011863681252

Table A.123.: Raw MP2 EC-RISM results for the group of the Bromides at 10 kbar.

Name	$\mu^{ex}/\text{kcal mol}^{-1}$	$E^{sol}/\text{kcal mol}^{-1}$	$G^{sol}/\text{kcal mol}^{-1}$	μ^x/D	μ^y/D	μ^z/D	μ^{tot}/D
Bromoethyne	-1662287.03566617	23.9533237306405	-1662263.08234244	0.0000	0.0000	-0.3983	0.3983
3-Bromoprop-1-ene	-1687660.71705289	35.1148611704111	-1687625.60219172	2.8546	1.5597	0.0627	3.25351141691558
Bromoethane	-1663835.78930317	30.636663082696	-1663805.15264009	3.3098	1.1924	0.0004	3.51803836818191
Bromomethane	-1639242.77473545	21.3966734837476	-1639221.37806197	-3.1231	-0.0013	-0.0006	3.12310032819953
1-Bromobutane	-1713017.80173515	48.4982237387667	-1712969.30351141	3.3567	1.5011	0.0003	3.67705536944985
Bromocyclohexane	-1761463.66308366	58.3075456431644	-1761405.35553802	4.1062	0.0000	0.6932	4.16430122349477
<i>E</i> -1,2-Dibromocyclohexane	-3375384.17033038	62.1362236570268	-3375322.03410672	-5.9942	-0.0000	-0.0000	5.9942
1,4-Dibromobutane	-3326934.89265309	50.9512043092734	-3326883.94144878	0.0000	0.0000	-0.0002	0.0002
Dibromomethane	-3253156.16194932	28.2146186630019	-3253127.94733066	0.0018	2.5729	0.0002	2.57290063741296
2-Bromopropane	-1688430.32654498	39.7520882036329	-1688390.57445678	3.7458	0.0000	0.7470	3.81955843521211
2-Bromo-2-methylpropane	-1713026.12903435	48.7558167335086	-1712977.37321761	4.0398	-0.0002	0.0005	4.0398003589287
Bromoethene	-1663068.21949122	28.8605910896272	-1663039.35890013	2.3695	0.4570	0.0000	2.41316788682429

Table A.124.: Raw MP2 EC-RISM results for the group of the Carbonyls at 10 kbar.

Name	$\mu^{ex}/\text{kcal mol}^{-1}$	$E^{sol}/\text{kcal mol}^{-1}$	$G^{sol}/\text{kcal mol}^{-1}$	μ^x/D	μ^y/D	μ^z/D	μ^{tot}/D
2-Methylpropanal	-145445.313988976	31.5003401309751	-145413.813648845	4.9065	-0.0013	1.6441	5.17463126705662
Acetaldehyde	-96261.0938171682	13.2107115322658	-96247.883105636	4.3732	2.1072	0.0119	4.85441156990216
Prop-2-enal	-120088.549804181	17.797015042304	-120070.752789139	5.8140	1.8436	-0.0094	6.09930695407273
Cyclohexanone	-193889.285279671	38.9999828252868	-193850.285296846	-5.5970	-0.0002	2.1198	5.98497795150492
Formaldehyde	-71665.1768078623	5.27195838695029	-71659.9048494753	4.2557	-0.0003	0.0110	4.25571422677792
Acetone	-120858.222332725	21.1970597258604	-120837.025272999	-0.0141	5.3914	-0.0867	5.39211550877761
Undecan-2-one	-317584.56294349	93.1097559060707	-317491.453187584	-0.4291	-5.3389	0.2169	5.36050609830826
But-3-en-2-one	-144683.5051196	26.4486845975143	-144657.056435003	-0.9646	-4.9523	-0.0000	5.04536702827455

A. Additional data

Table A.125.: Raw MP2 EC-RISM results for the group of the Chlorides at 10 kbar.

Name	$\mu^{ex}/\text{kcal mol}^{-1}$	$E^{sol}/\text{kcal mol}^{-1}$	$G^{sol}/\text{kcal mol}^{-1}$	μ^x/D	μ^y/D	μ^z/D	μ^{tot}/D
Chloroethyne	-336435.401072891	23.2500563369981	-336412.151016554	0.0000	0.0000	-0.6662	0.6662
3-Chloroprop-1-ene	-361809.300295257	33.7155425375239	-361775.58475272	2.6906	1.6712	0.3953	3.191942964716
1-Chlorobutane	-387166.62340038	47.1544970702677	-387119.46890331	3.1425	1.5997	0.0003	3.5262368527153
Chloroethane	-337985.03087463	29.2383380437381	-337955.792536586	3.0984	1.3649	0.0003	3.38571036268609
Chloromethane	-313392.151193018	20.0759897014818	-313372.075203317	3.0595	-0.0001	-0.0009	3.05950013400882
Chlorocyclohexane	-435612.125865758	56.9153367803537	-435555.210528978	-3.8820	-0.0000	0.7283	3.94972719184503
1,3-Dichlorocyclohexane	-723682.408779424	59.3309657349426	-723623.077813689	-0.0000	3.8756	1.5484	4.17346593612551
1,4-Dichlorobutane	-675232.562694414	48.2713762428298	-675184.291317897	-0.0000	0.0000	0.0001	0.0001
Dichloromethane	-601455.640523594	25.6317176926386	-601430.008805902	0.0000	2.7008	0.0003	2.70080001666173
Chloroethene	-337218.243355941	27.6478195368069	-337190.595536404	2.2831	0.6157	0.0004	2.36466324452341

Table A.126.: Raw MP2 EC-RISM results for the group of the Acids at 10 kbar.

Name	$\mu^{ex}/\text{kcal mol}^{-1}$	$E^{sol}/\text{kcal mol}^{-1}$	$G^{sol}/\text{kcal mol}^{-1}$	μ^x/D	μ^y/D	μ^z/D	μ^{tot}/D
3-Butenoic acid	-191808.597427661	25.7696905769598	-191782.827737084	-0.0112	-2.8634	0.4281	2.89524689966158
Acetic acid	-143393.515063651	11.9278306586998	-143381.587232992	-1.2960	-2.6692	-0.0006	2.9671948031769
2-Methylpropanoic acid	-192576.64274508	30.6923218532505	-192545.950423226	0.9376	2.3943	-1.6218	3.04006603382229
2,2-Dimethylpropanoic acid	-217161.943808166	34.1854197875239	-217127.758388378	5.4788	-4.7608	0.0008	7.25826885145487
Prop-2-ynoic acid	-166438.648007211	12.7513885889101	-166425.896618622	-1.5488	-2.4258	0.0004	2.87807005474155
Propanoic acid	-167984.357681184	21.1822063537285	-167963.17547483	0.2000	-2.9136	0.0003	2.92045630852441

Table A.127.: Raw MP2 EC-RISM results for the group of the Esters at 10 kbar.

Name	$\mu^{ex}/\text{kcal mol}^{-1}$	$E^{sol}/\text{kcal mol}^{-1}$	$G^{sol}/\text{kcal mol}^{-1}$	μ^x/D	μ^y/D	μ^z/D	μ^{tot}/D
Ethyl acetate	-192566.962342871	36.2227635131453	-192530.739579357	-1.3118	-2.9632	0.0000	3.24058227483889
Ethyl prop-2-enoate	-216392.598446187	42.0016907184512	-216350.596755469	0.1508	-2.7362	-0.0002	2.74035237150261
Ethyl 2-methylpropanoate	-21650.318130515	54.9303752041109	-241695.387755311	0.7369	2.7646	-1.4966	3.22890791599884
Ethyl 2,2-dimethylpropionate	-246344.3017174	63.8556150535373	-266280.446102347	-0.5266	-3.3764	-0.0001	3.41721882969177
Ethyl propanoate	-217157.744981883	45.4296825504302	-217112.315299332	-1.0583	-2.9643	0.0001	3.14755037926321
Ethynyl prop-2-enoate	-214837.162961908	33.8821347327916	-214803.280827175	-3.4368	-2.3374	0.0015	4.1563247286515
Ethynyl 2,2-dimethylpropionate	-264790.35527083	56.2285655607075	-264734.12670527	-0.0270	-2.6242	0.0010	4.00613974294457
Propan-2-yl acetate	-217162.01473957	46.0457634077438	-217115.968976162	1.1905	-2.4204	1.6206	3.14673970483737
Propan-2-yl 2-methylpropanoate	-266345.758930788	65.5641625647706	-266280.194768224	-0.7412	1.0304	-2.8778	3.1452876561612
Propan-2-yl 2,2-dimethylpropionate	-290939.823782024	74.8867041641969	-290864.937077859	0.4888	2.8173	1.7276	3.34076435714942
Propan-2-yl prop-2-ynoate	-240208.683817928	47.2372018484704	-240161.44661608	0.7840	-2.6885	1.2791	3.07876356026246
Propan-2-yl propionate	-241752.863452187	55.2732585635755	-241697.590193623	-1.0274	-2.3880	1.5844	3.04440767966447
Methyl acetate	-167973.85634512	27.0302609658222	-167946.825373546	2.8335	-1.2563	-0.0000	3.09951801736698
Methyl prop-2-enoate	-191799.450142125	32.8440449311664	-191766.606097194	-0.5957	-2.6215	0.0004	2.68833050423492
Methyl 2-methylpropanoate	-217157.130318131	45.7173036637189	-217111.413014467	0.1083	2.4697	-1.8814	3.10657575796889
Methyl 2,2-dimethylpropionate	-241751.045385051	54.6068525236616	-241696.438532527	-0.4901	-3.2405	0.0002	3.2775233076946
Methyl propanoate	-192564.563588241	36.2230517294455	-192528.340536511	1.9079	-2.3599	-0.0000	3.03466809058256
Methyl propiolate	-191020.208361132	28.2231754048757	-190991.985185727	-0.3473	-2.9589	0.0001	2.97921239759773
tert-Butyl acetate	-241755.68130486	55.7339315712237	-241699.947373288	1.3929	2.8971	-0.0000	3.2145542179282
tert-Butyl prop-2-ynoate	-264802.558154075	56.6006673778681	-264745.957486697	1.0549	2.9725	-0.0000	3.15413542195005
tert-Butyl propionate	-266346.642649907	64.9587234562619	-266281.68392645	1.2513	2.8382	0.0002	3.10179479817734
Ethenyl acetate	-191791.920479757	27.9220360203155	-191763.998443736	-3.4671	5.6423	0.1749	6.62472050051925

Table A.128.: Raw MP2 EC-RISM results for the group of the Ethers at 10 kbar.

Name	$\mu^{ex}/\text{kcal mol}^{-1}$	$E^{sol}/\text{kcal mol}^{-1}$	$G^{sol}/\text{kcal mol}^{-1}$	μ^x/D	μ^y/D	μ^z/D	μ^{tot}/D
1,4-Dioxane	-192538.32396748	28.1333310967973	-192510.190636383	0.0000	-0.0000	-0.0000	0
Diethyl ether	-146187.962934972	38.953319082457	-146149.009615889	0.0001	0.0003	-2.7141	2.71410001842231
Diisopropyl ether	-195375.91113862	57.2969431094646	-195318.614195511	0.8475	0.0022	-2.6668	2.79822860574328
Dimethyl ether	-97003.9438863681	21.3507398080784	-96982.59314656	0.0000	-0.0000	-2.4730	2.473
Di-tert-butyl ether	-244610.84363052	24.4782474046367	-244586.365383116	0.0001	0.0005	-2.5164	2.5164000516611
Isobutyl methyl ether	-146190.565735113	39.3118774043977	-146151.253857709	-0.0379	1.9254	1.7849	2.62573219883521
Ethyl methyl ether	-121597.285526322	30.7087149560229	-121566.576811366	0.3167	2.4587	0.0003	2.47901284183846
Ethynyl methyl ether	-120051.040353868	24.4164122007648	-120026.623941668	-1.8760	1.9683	0.0010	2.71911417377057
Methyl tert-butyl ether	-147078.702522568	48.0880845050191	-147073.614438063	2.3957	1.1706	0.0000	2.66639885426018
Tetrahydrofuran	-145442.903903028	30.624089083413	-145412.279813944	0.0005	3.2292	0.0008	3.22920013780503
Oxane	-170038.99772521	39.7666170901052	-169999.231155431	-0.0000	2.4382	1.5212	2.87382474761423

Table A.129.: Raw MP2 EC-RISM results for the group of the Fluorides at 10 kbar.

Name	$\mu^{ex}/\text{kcal mol}^{-1}$	$E^{sol}/\text{kcal mol}^{-1}$	$G^{sol}/\text{kcal mol}^{-1}$	μ^x/D	μ^y/D	μ^z/D	μ^{tot}/D
Fluoroethyne	-110518.286988566	20.2569408816922	-110498.030047684	-0.0000	0.0000	-1.2161	1.2161
3-Fluoroprop-1-ene	-135900.364108384	29.4105803119025	-135870.953528072	2.3070	1.2656	1.4256	2.9927124352333
1,4-Difluorocyclohexane	-271865.512668086	50.6768970380019	-271814.835771048	0.0009	-0.0000	0.0001	0.000905538513813742
Fluorocyclohexane	-209703.492097683	52.5700642112811	-209650.922033471	3.2983	0.0000	0.7518	3.38289611575644
2,2-Difluoropropane	-198843.609303105	36.5834989228011	-198807.025804182	0.0000	3.6042	-0.0003	3.60420001248543
Diffuoromethane	-149649.241847986	17.3349735222275	-149631.906874463	-0.0000	2.8819	-0.0000	2.8819
Fluoromethane	-87483.6367585026	16.1231928704589	-87467.5135656321	-2.7542	0.0001	0.0001	2.75420000363082
1-Fluoropropane	-136667.483394788	34.140840543738	-136633.342554245	2.8014	-1.0954	-0.0001	3.00794666342341
2-Fluoropropane	-136672.174896797	34.100791418499	-136638.074105379	0.0000	-2.9490	1.0060	3.11586857874333
Fluoroethene	-111311.06995935	23.6095680279637	-111287.460391322	-1.8919	1.0936	0.0010	2.18523398518328

Table A.130.: Raw MP2 EC-RISM results for the group of the conjugated systems at 10 kbar.

Name	$\mu^{ex}/\text{kcal mol}^{-1}$	$E^{sol}/\text{kcal mol}^{-1}$	$G^{sol}/\text{kcal mol}^{-1}$	μ^x/D	μ^y/D	μ^z/D	μ^{tot}/D
Aniline	-179940.203204144	32.691967790392	-179907.511236354	-1.1202	0.0017	1.9151	2.21866151992592
Benzo[b]thiophene	-442530.320161999	54.0367925702677	-442476.283369429	-0.4067	1.2049	0.0001	1.27168742621762
1,4-Dioxin	-191013.86726028	29.969096956979	-190983.898163323	-0.0000	0.0000	0.0028	0.0028
Furan	-143943.234952566	29.1764239060707	-143914.05852866	0.0001	1.2039	0.0002	1.20390002076584
1H-Imidazole	-141555.139163872	7.59405517160612	-141547.5451087	-3.2024	5.5419	0.0002	6.40062664197811
4H-1,4-Oxazine	-178563.642984623	23.7506249390535	-178539.892359684	2.9278	-0.0000	-2.1209	3.61527725769408
1,3-Oxazole	-154005.390891679	20.1350987222753	-153985.255792956	-0.8553	-2.3030	0.0010	2.4566945455225
Oxepine	-192347.209209917	39.2499556620459	-192307.959254255	0.9152	0.0001	-2.2548	2.43345722995084
Phenol	-192395.730873216	32.9584722024379	-192362.772401014	0.3357	2.2105	0.0008	2.23584556264515
9H-Purine	-257793.571615781	7.87021605258126	-257785.701399728	-5.4820	8.3007	0.0010	9.94755977564347
Pyrazine	-165397.621549049	25.5750429280593	-165372.046506121	0.0000	0.0000	0.0000	0
Pyridine	-155342.212462747	28.5672584340344	-155313.645204313	0.0002	4.1816	0.0000	4.18160000478286
Pyrimidine	-165397.546121806	22.3441109610421	-165375.202010845	-4.0488	0.0005	0.0000	4.04880003087334
1H-Pyrrrole	-131498.197808279	23.5105783009082	-131474.687229978	2.9908	-0.0002	0.0000	2.99080000668717
4H-1,4-Thiazine	-381015.516445569	27.5282414629541	-380987.988204106	4.9080	-0.0000	1.9449	5.27930866780869
1,3-Thiazole	-356451.969489367	24.6803520062141	-356427.289137361	-2.5583	1.6158	0.0006	3.02584019571424
Thiophene	-346391.990525318	34.3887267454589	-346357.601798572	-0.8310	0.0000	-0.0006	0.83100021660647

Table A.131.: Raw MP2 EC-RISM results for the group of the Nitriles at 10 kbar.

Name	$\mu^{ex}/\text{kcal mol}^{-1}$	$E^{sol}/\text{kcal mol}^{-1}$	$G^{sol}/\text{kcal mol}^{-1}$	μ^x/D	μ^y/D	μ^z/D	μ^{tot}/D
Prop-2-enenitrile	-106889.29509482	19.6824536046845	-106869.612641215	1.7311	-6.3701	0.0000	6.601127268837
Acetonitrile	-83065.5919901079	13.4525229517208	-83052.1394671562	0.0000	-0.0012	-6.0546	6.05460011891785
Propanenitrile	-107655.952976941	22.9328922894359	-107633.020084652	-5.8538	2.1414	0.0007	6.23318288597407
2-Methylpropanenitrile	-132248.498557561	32.3484030752868	-132216.150154486	1.9919	6.0194	-0.0000	6.34041339109683
2,2-Dimethylpropanenitrile	-156841.951720044	41.5259653862333	-156800.425754658	-6.2451	-0.0002	0.0001	6.24510000400314

Table A.132.: Raw MP2 EC-RISM results for the group of the Sulfones at 10 kbar.

Name	$\mu^{ex}/\text{kcal mol}^{-1}$	$E^{sol}/\text{kcal mol}^{-1}$	$G^{sol}/\text{kcal mol}^{-1}$	μ^x/D	μ^y/D	μ^z/D	μ^{tot}/D
Diethyl sulfone	-442806.340487606	31.8641480475621	-442774.476339558	-0.0000	7.9852	-0.0002	7.98520000250463
Dimethyl sulfone	-393620.867137936	11.3486257533461	-393609.518512183	-0.0001	7.9830	-0.0003	7.98300000626331
Divinyl sulfone	-441269.815616663	29.4301098912524	-441240.385506772	-0.0001	-7.8641	-0.0002	7.864100003179
Ethyl sulfone	-393610.424697739	7.74386135301147	-393602.680836386	6.4768	-2.7546	3.2109	7.73606089751108
Msulfonylethen	-417445.141016808	20.6166540913002	-417424.524362716	3.4781	7.1741	-0.2318	7.9761282374345
Tetrahydrothiophene 1,1-dioxide	-442058.934870909	22.93484241587	-442036.000028493	9.0753	0.0007	-0.0027	9.07530042863596

A. Additional data

Table A.133.: Raw MP2 EC-RISM results for the group of the Thioethers at 10 kbar.

Name	$\mu^{ex}/\text{kcal mol}^{-1}$	$E^{sol}/\text{kcal mol}^{-1}$	$G^{sol}/\text{kcal mol}^{-1}$	μ^x/D	μ^y/D	μ^z/D	μ^{tot}/D
(Methylsulfanyl)methane	-299453.64243945	27.1312719524379	-299426.511167497	-0.0000	-3.0633	0.0000	3.0633
1,4-Dithiane	-597436.625516609	40.160334082935	-597396.465182526	-0.0001	-0.0000	0.0003	0.000316227766016838
1,1-Thiobisethane	-348636.201589138	45.4815609894837	-348590.720028149	-0.0000	3.2874	0.0006	3.28740005475452
(Methylsulfanyl)-2-propane	-348638.468347466	44.898403582935	-348593.569943884	-0.4640	2.7425	1.8062	3.31646810477653
(Methylsulfanyl)-2-ethyne	-322506.637127844	30.3321811952677	-322476.304946649	1.2243	2.2153	-0.0002	2.53109948836469
Thiane	-372487.859992304	45.4980972390057	-372442.361895065	-3.2657	-0.0000	1.4323	3.56598931293968
terttert-Butyl methyl sulfide	-373233.15088191	53.4187854608031	-373179.732096449	0.8042	3.2503	-0.0005	3.34831121313417
Di-tert-Butyl sulfide	-447009.232291152	78.9666595788719	-446930.265631573	0.0001	3.5212	-0.0000	3.52120000141997
Ethyl methyl sulfide	-324044.92237655	36.2489540991874	-324008.673422451	0.0160	3.1870	-0.0001	3.18704016447863
Thiophene	-347894.738089367	37.0784578955545	-347857.659631472	-3.8476	0.0001	0.0016	3.84760033397441

Table A.134.: Raw MP2 EC-RISM results for the group of the Thiones at 10 kbar.

Name	$\mu^{ex}/\text{kcal mol}^{-1}$	$E^{sol}/\text{kcal mol}^{-1}$	$G^{sol}/\text{kcal mol}^{-1}$	μ^x/D	μ^y/D	μ^z/D	μ^{tot}/D
(1R,4S)-1,3,3-trimethylbicyclo[2.2.1]heptane-2-thione	-493949.364342934	79.0425342743786	-493870.321808659	1.3898	-6.2256	1.3160	6.51317859420422
6,6-Dimethylhept-1-yne-4-thione	-469300.58623468	73.6789896909656	-469226.907244989	-3.4470	3.0295	-2.7798	5.36534875753664
Hept-1-ene-4-thione	-420887.14613479	61.6080866412524	-420825.538048148	1.1754	-5.3937	0.6505	5.55848136634459
Methanethial	-274098.802844447	15.9148929380975	-274082.887951509	3.7689	0.0000	0.0002	3.76890000530659

A.4.3. Scatter plots

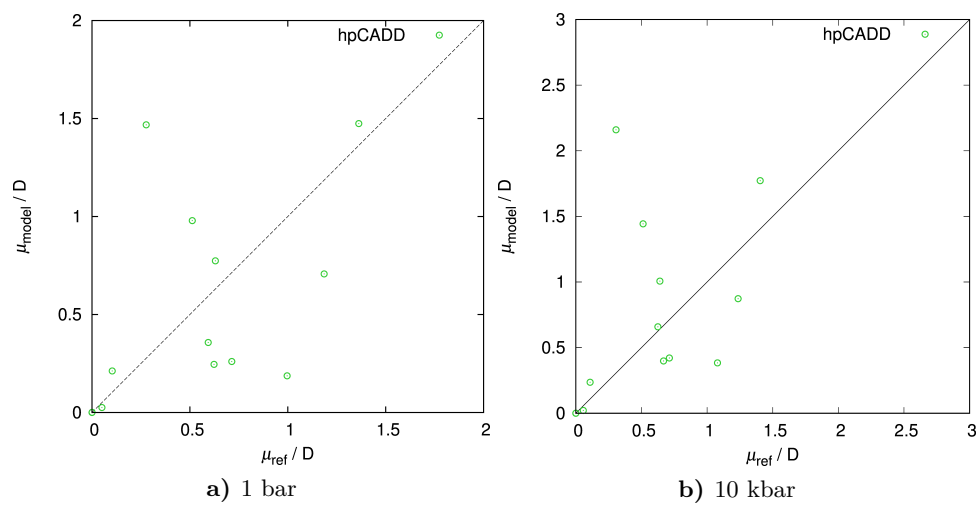


Figure A.20.: Scatter plots of the dipole moments of the hpCADD-Hamiltonians vs. the MP2/aug-cc-pVDZ-reference. Data for the group of hydrocarbons is shown, 1 bar on the left, and 10 kbar on the right hand side.

A. Additional data

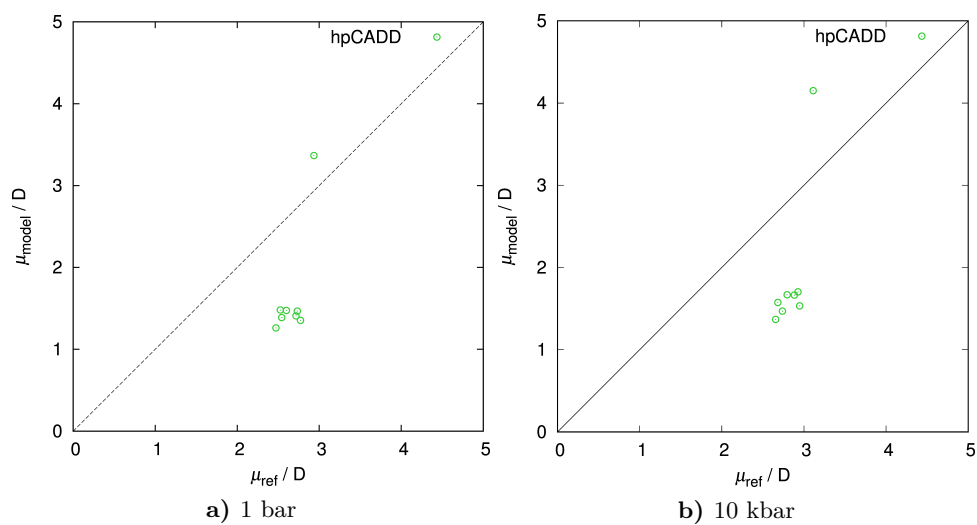


Figure A.21.: Scatter plots of the dipole moments of the hpCADD-Hamiltonians vs. the MP2/aug-cc-pVDZ-reference. Data for the group of alcohols is shown, 1 bar on the left, and 10 kbar on the right hand side.

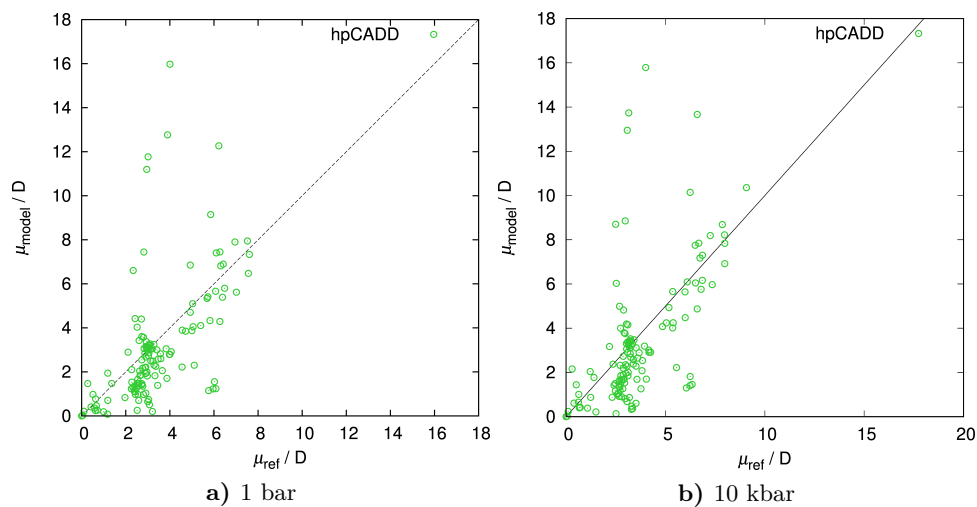


Figure A.22.: Scatter plots of the dipole moments of the hpCADD-Hamiltonians vs. the MP2/aug-cc-pVDZ-reference. Data for all molecules is shown, 1 bar on the left, and 10 kbar on the right hand side.

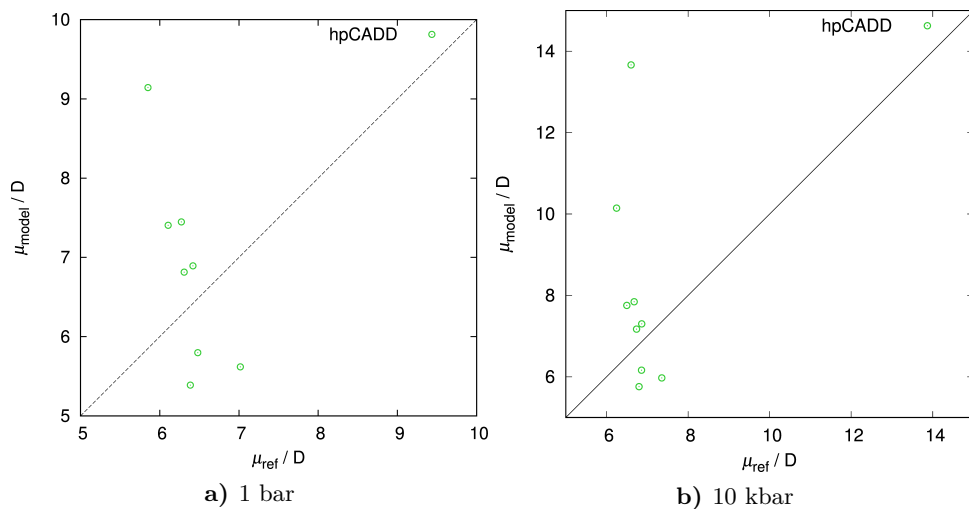


Figure A.23.: Scatter plots of the dipole moments of the hpCADD-Hamiltonians vs. the MP2/aug-cc-pVDZ-reference. Data for the group of amides is shown, 1 bar on the left, and 10 kbar on the right hand side.

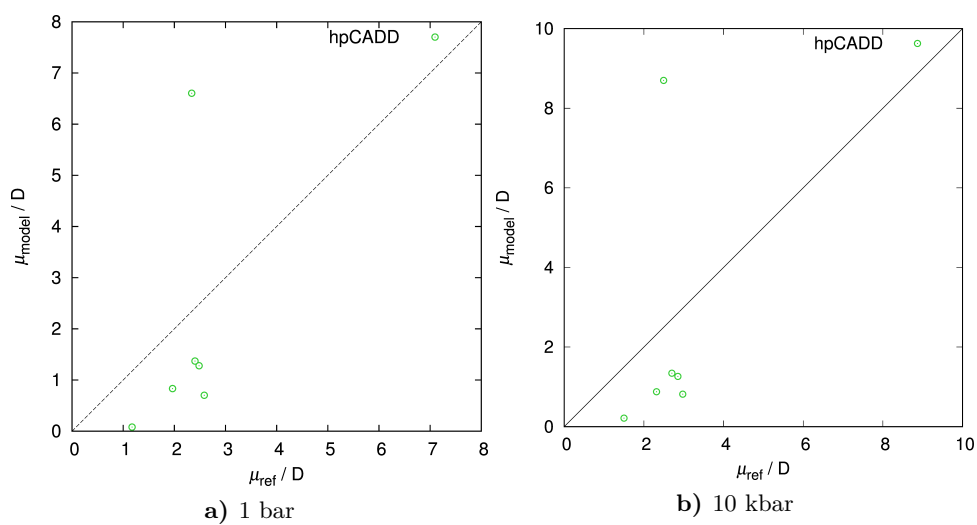


Figure A.24.: Scatter plots of the dipole moments of the hpCADD-Hamiltonians vs. the MP2/aug-cc-pVDZ-reference. Data for the group of amines is shown, 1 bar on the left, and 10 kbar on the right hand side.

A. Additional data

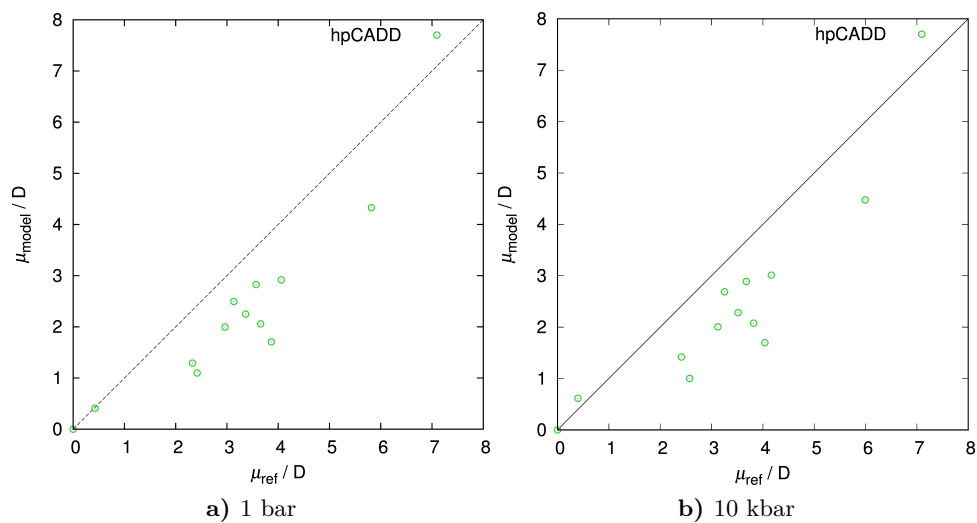


Figure A.25.: Scatter plots of the dipole moments of the hpCADD-Hamiltonians vs. the MP2/aug-cc-pVDZ-reference. Data for the group of bromides is shown, 1 bar on the left, and 10 kbar on the right hand side.

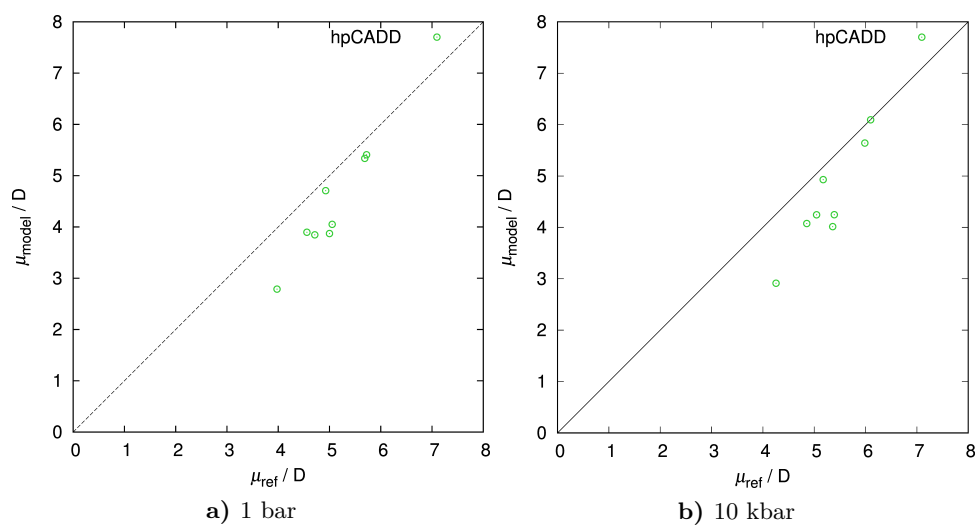


Figure A.26.: Scatter plots of the dipole moments of the hpCADD-Hamiltonians vs. the MP2/aug-cc-pVDZ-reference. Data for the group of aldehydes and ketones is shown, 1 bar on the left, and 10 kbar on the right hand side.

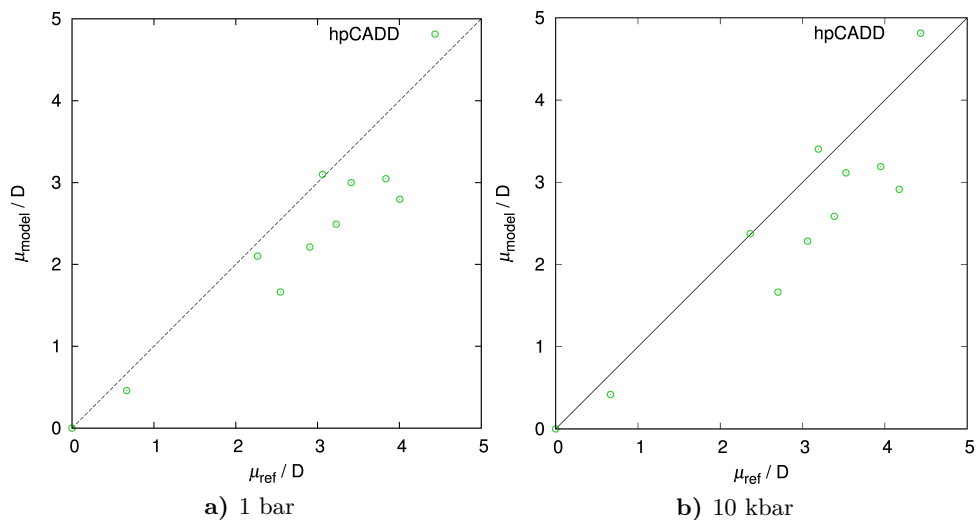


Figure A.27.: Scatter plots of the dipole moments of the hpCADD-Hamiltonians vs. the MP2/aug-cc-pVDZ-reference. Data for the group of chlorides is shown, 1 bar on the left, and 10 kbar on the right hand side.

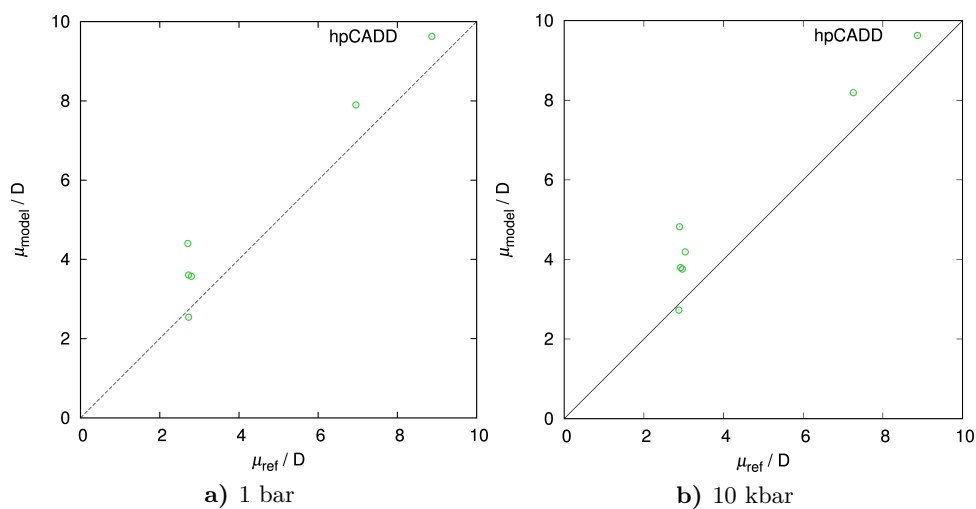


Figure A.28.: Scatter plots of the dipole moments of the hpCADD-Hamiltonians vs. the MP2/aug-cc-pVDZ-reference. Data for the group of carboxylic acids is shown, 1 bar on the left, and 10 kbar on the right hand side.

A. Additional data

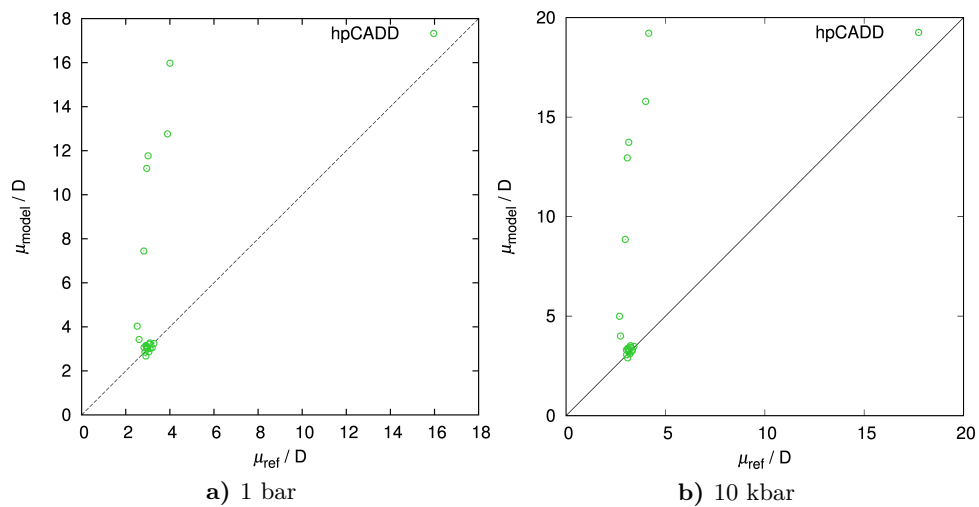


Figure A.29.: Scatter plots of the dipole moments of the hpCADD-Hamiltonians vs. the MP2/aug-cc-pVDZ-reference. Data for the group of esters is shown, 1 bar on the left, and 10 kbar on the right hand side.

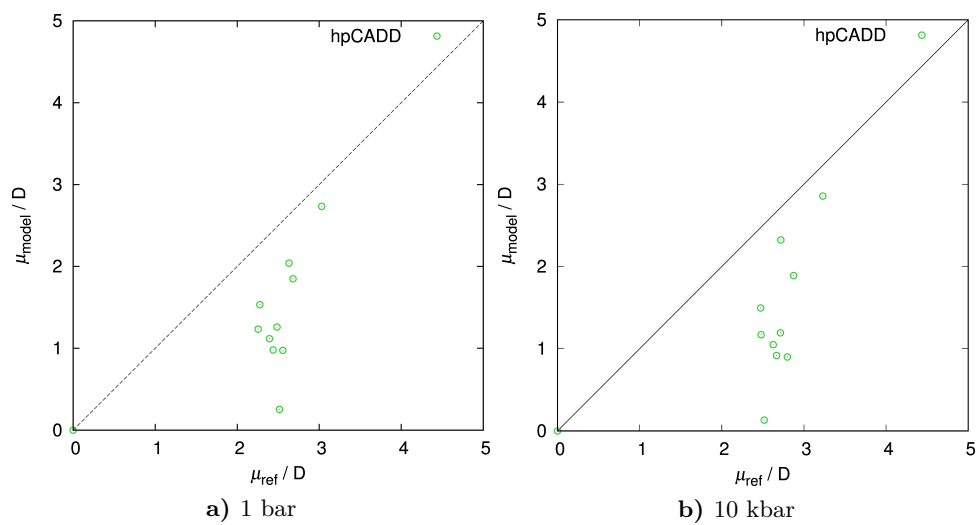


Figure A.30.: Scatter plots of the dipole moments of the hpCADD-Hamiltonians vs. the MP2/aug-cc-pVDZ-reference. Data for the group of ethers is shown, 1 bar on the left, and 10 kbar on the right hand side.

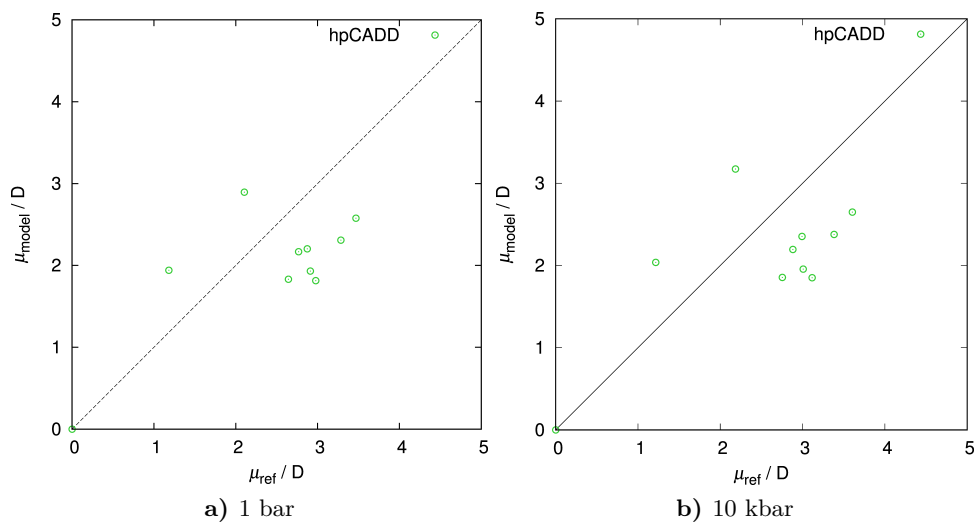


Figure A.31.: Scatter plots of the dipole moments of the hpCADD-Hamiltonians vs. the MP2/aug-cc-pVDZ-reference. Data for the group of fluorides is shown, 1 bar on the left, and 10 kbar on the right hand side.

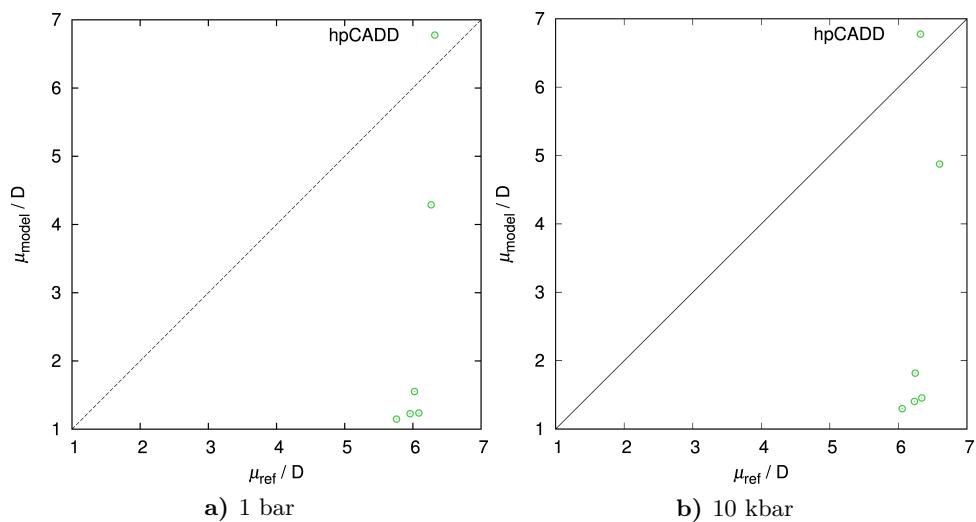


Figure A.32.: Scatter plots of the dipole moments of the hpCADD-Hamiltonians vs. the MP2/aug-cc-pVDZ-reference. Data for the group of nitriles is shown, 1 bar on the left, and 10 kbar on the right hand side.

A. Additional data

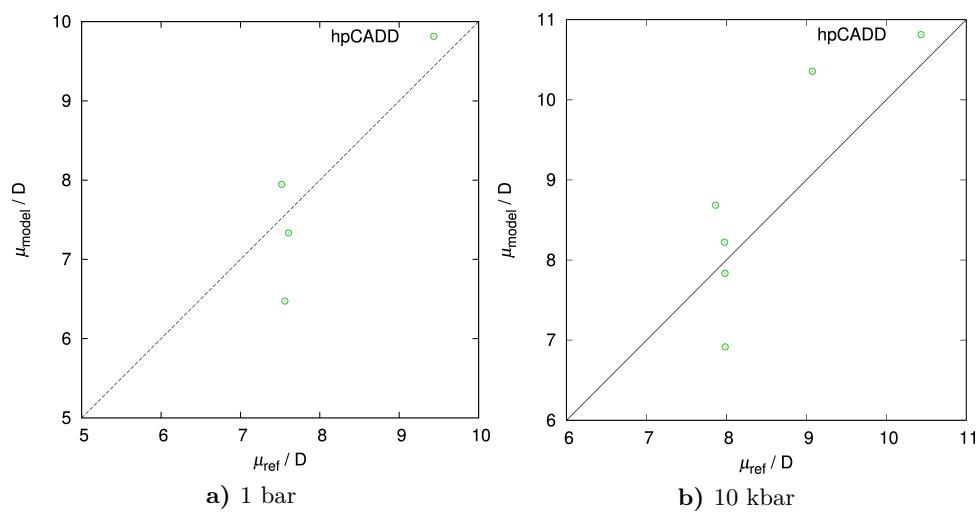


Figure A.33.: Scatter plots of the dipole moments of the hpCADD-Hamiltonians vs. the MP2/aug-cc-pVDZ-reference. Data for the group of sulfones is shown, 1 bar on the left, and 10 kbar on the right hand side.

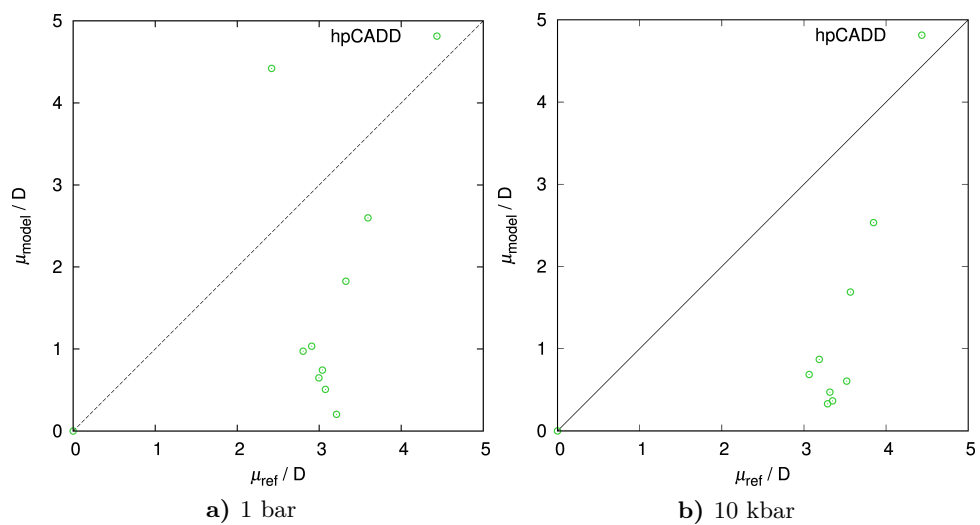


Figure A.34.: Scatter plots of the dipole moments of the hpCADD-Hamiltonians vs. the MP2/aug-cc-pVDZ-reference. Data for the group of thioethers is shown, 1 bar on the left, and 10 kbar on the right hand side.

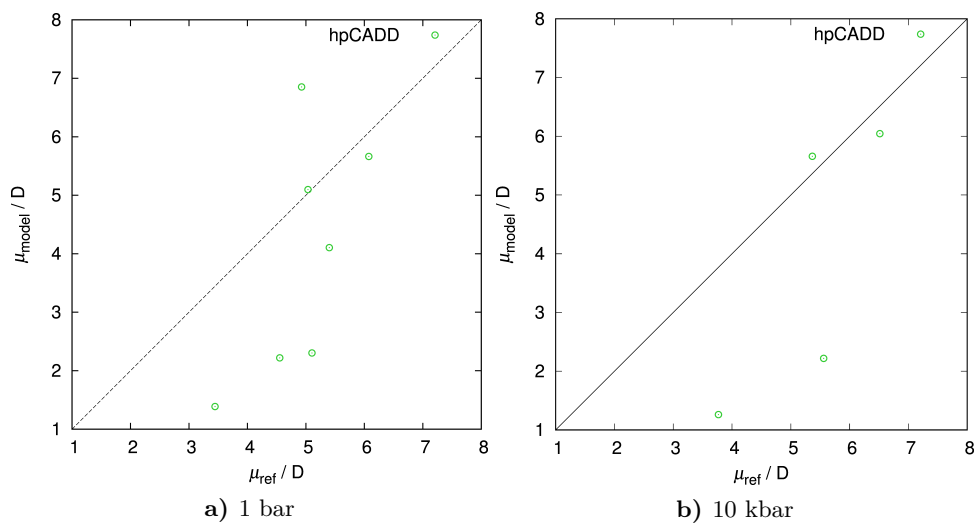


Figure A.35.: Scatter plots of the dipole moments of the hpCADD-Hamiltonians vs. the MP2/aug-cc-pVDZ-reference. Data for the group of thiones is shown, 1 bar on the left, and 10 kbar on the right hand side.

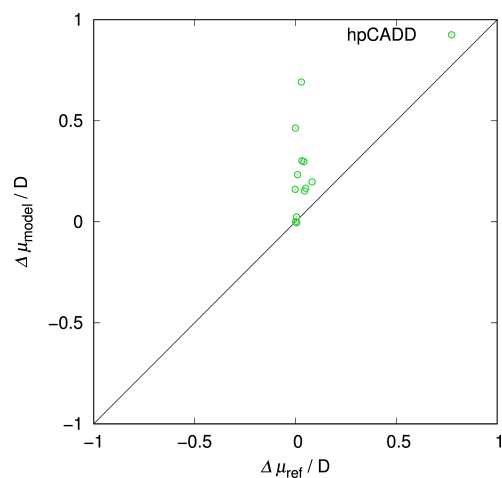


Figure A.36.: Scatter plots of the dipole moment difference between 10 kbar and 1 bar of the hpCADD-Hamiltonians vs. the MP2/aug-cc-pVDZ-reference. Datapoints for the alkanes are shown.

A. Additional data

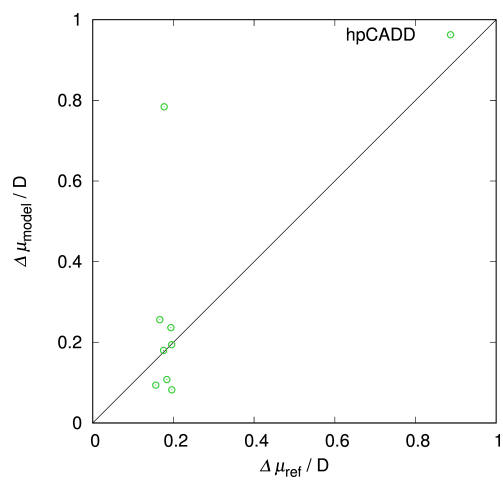


Figure A.37.: Scatter plots of the dipole moment difference between 10 kbar and 1 bar of the hpCADD-Hamiltonians vs. the MP2/aug-cc-pVDZ-reference. Datapoints for the alcohols are shown.

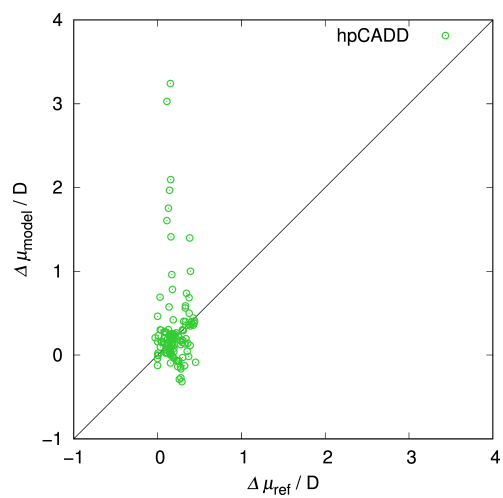


Figure A.38.: Scatter plots of the dipole moment difference between 10 kbar and 1 bar of the hpCADD-Hamiltonians vs. the MP2/aug-cc-pVDZ-reference. The whole dataset is shown.

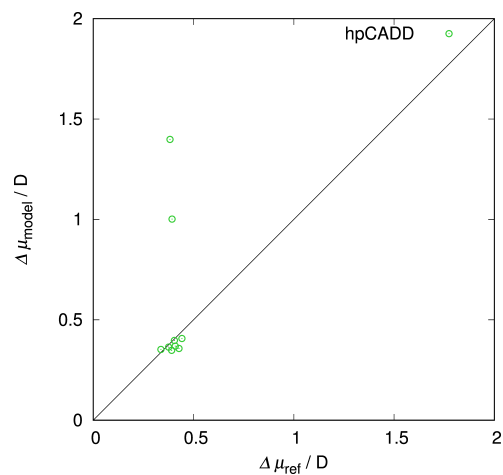


Figure A.39.: Scatter plots of the dipole moment difference between 10 kbar and 1 bar of the hpCADD-Hamiltonians vs. the MP2/aug-cc-pVDZ-reference. Datapoints for the amides are shown.

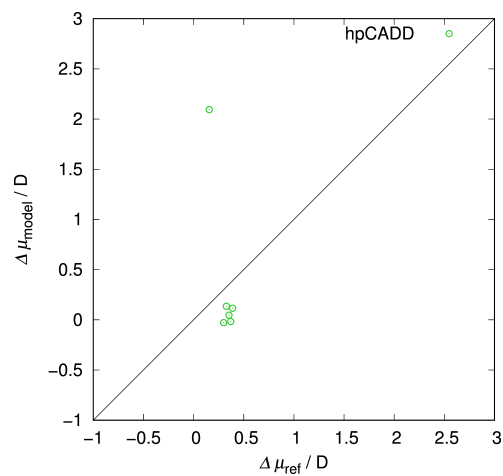


Figure A.40.: Scatter plots of the dipole moment difference between 10 kbar and 1 bar of the hpCADD-Hamiltonians vs. the MP2/aug-cc-pVDZ-reference. Datapoints for the amines are shown.

A. Additional data

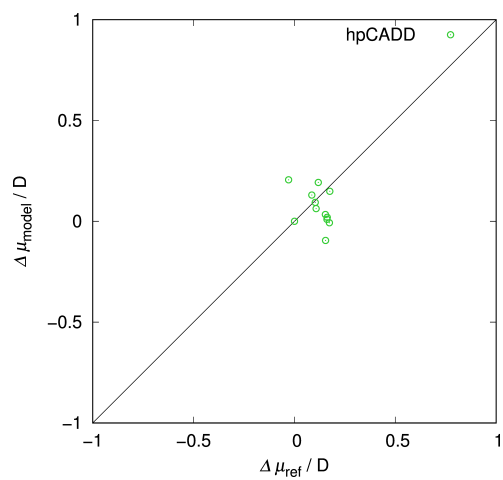


Figure A.41.: Scatter plots of the dipole moment difference between 10 kbar and 1 bar of the hpCADD-Hamiltonians vs. the MP2/aug-cc-pVDZ-reference. Datapoints for the bromides are shown.

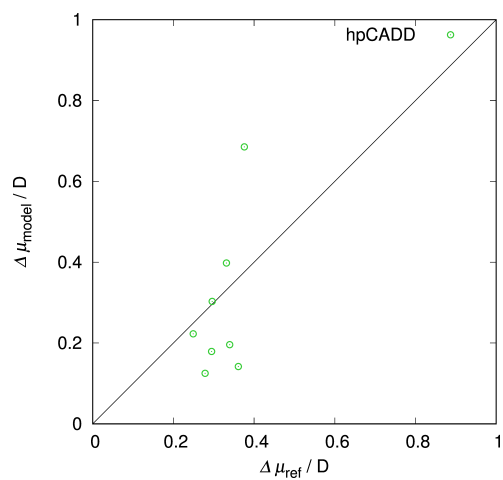


Figure A.42.: Scatter plots of the dipole moment difference between 10 kbar and 1 bar of the hpCADD-Hamiltonians vs. the MP2/aug-cc-pVDZ-reference. Datapoints for the aldehydes and ketones are shown.

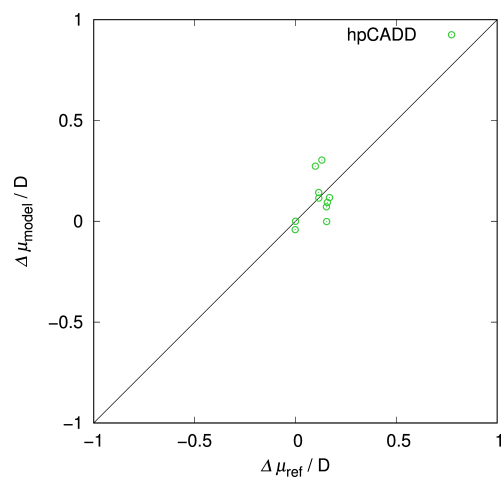


Figure A.43.: Scatter plots of the dipole moment difference between 10 kbar and 1 bar of the hpCADD-Hamiltonians vs. the MP2/aug-cc-pVDZ-reference. Datapoints for the chlorides are shown.

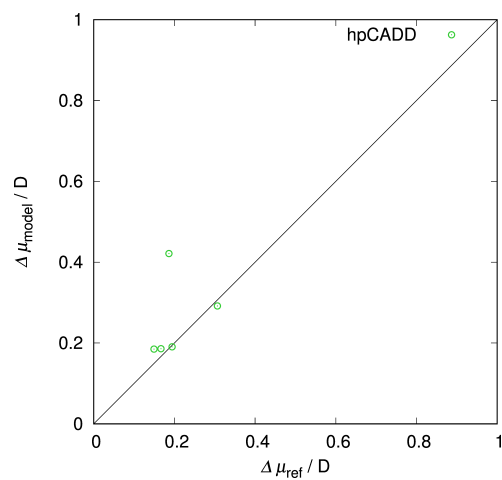


Figure A.44.: Scatter plots of the dipole moment difference between 10 kbar and 1 bar of the hpCADD-Hamiltonians vs. the MP2/aug-cc-pVDZ-reference. Datapoints for the carboxylic acids are shown.

A. Additional data

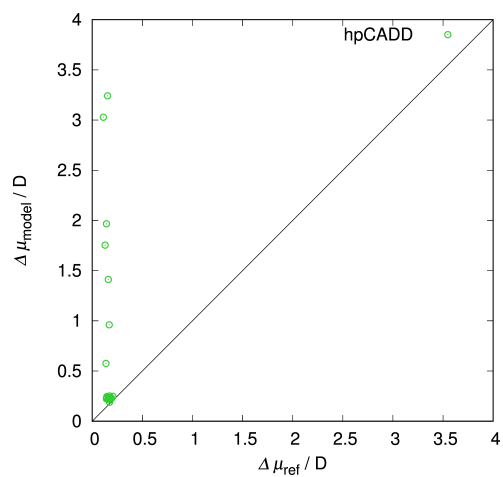


Figure A.45.: Scatter plots of the dipole moment difference between 10 kbar and 1 bar of the hpCADD-Hamiltonians vs. the MP2/aug-cc-pVDZ-reference. Datapoints for the esters are shown.

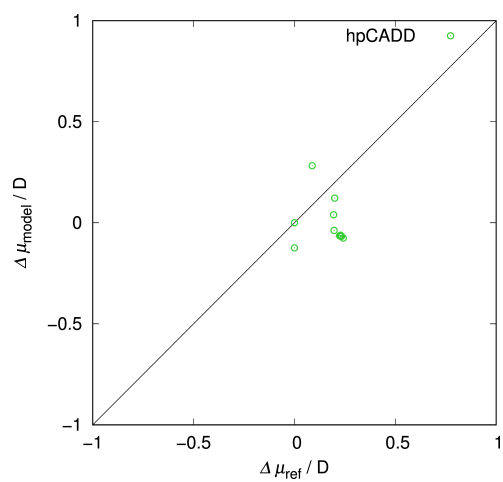


Figure A.46.: Scatter plots of the dipole moment difference between 10 kbar and 1 bar of the hpCADD-Hamiltonians vs. the MP2/aug-cc-pVDZ-reference. Datapoints for the ethers are shown.

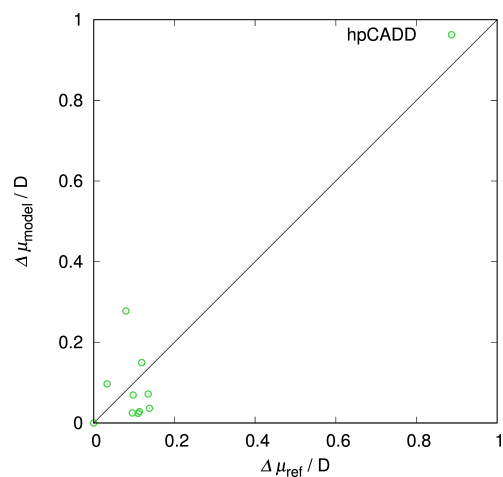


Figure A.47.: Scatter plots of the dipole moment difference between 10 kbar and 1 bar of the hpCADD-Hamiltonians vs. the MP2/aug-cc-pVDZ-reference. Datapoints for the fluorides are shown.

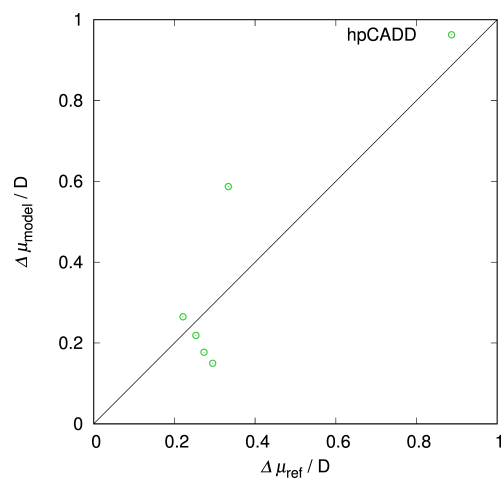


Figure A.48.: Scatter plots of the dipole moment difference between 10 kbar and 1 bar of the hpCADD-Hamiltonians vs. the MP2/aug-cc-pVDZ-reference. Datapoints for the nitriles are shown.

A. Additional data

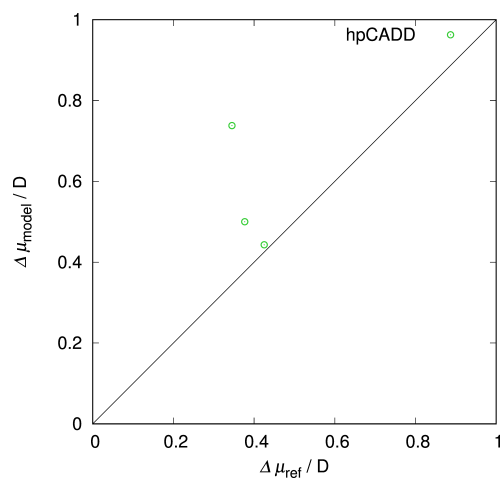


Figure A.49.: Scatter plots of the dipole moment difference between 10 kbar and 1 bar of the hpCADD-Hamiltonians vs. the MP2/aug-cc-pVDZ-reference. Datapoints for the sulfones are shown.

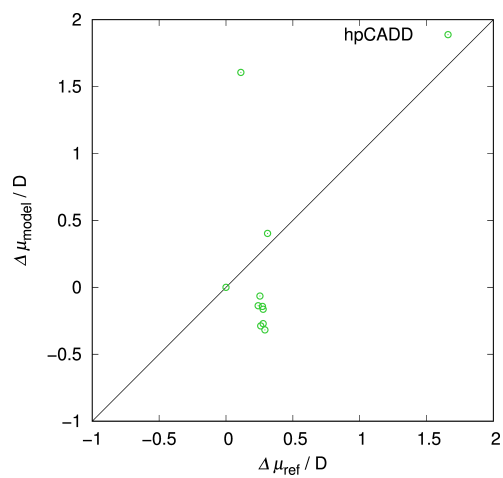


Figure A.50.: Scatter plots of the dipole moment difference between 10 kbar and 1 bar of the hpCADD-Hamiltonians vs. the MP2/aug-cc-pVDZ-reference. Datapoints for the thioethers are shown.

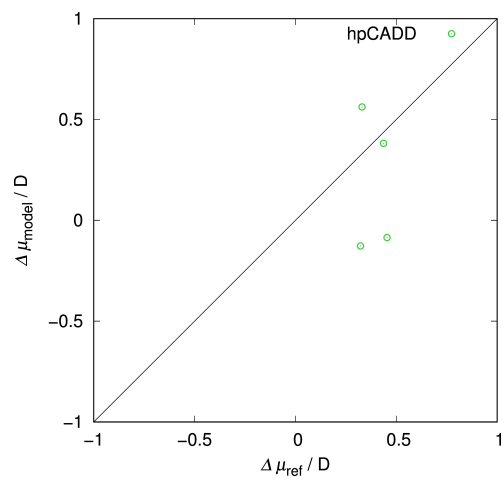


Figure A.51.: Scatter plots of the dipole moment difference between 10 kbar and 1 bar of the hpCADD-Hamiltonians vs. the MP2/aug-cc-pVDZ-reference. Datapoints for the thiones are shown.

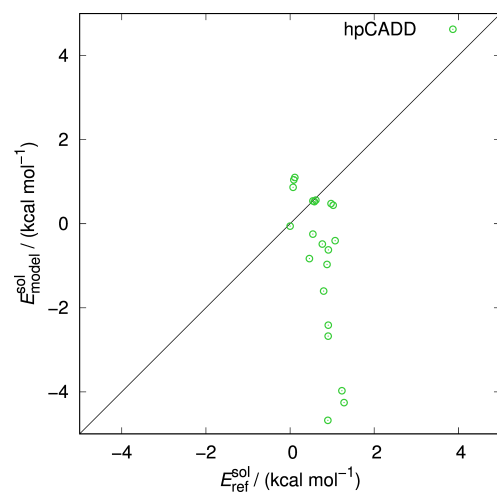


Figure A.52.: Scatter plot of the difference in solute electronic energy in solution between 10 kbar and 1 bar of the hpCADD-Hamiltonians vs. the MP2/aug-cc-pVDZ-reference. Datapoints for the hydrocarbons are shown.

A. Additional data

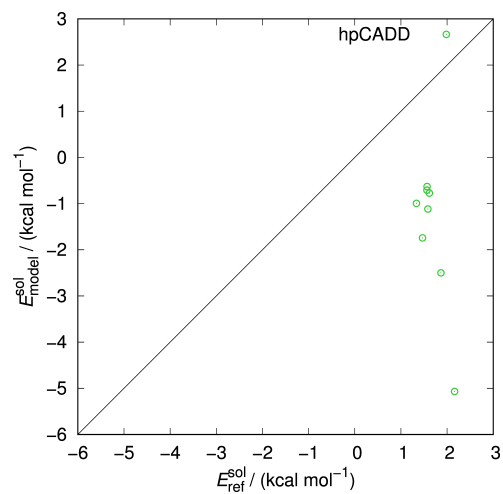


Figure A.53.: Scatter plot of the difference in solute electronic energy in solution between 10 kbar and 1 bar of the hpCADD-Hamiltonians vs. the MP2/aug-cc-pVDZ-reference. Datapoints for the alcohols are shown.

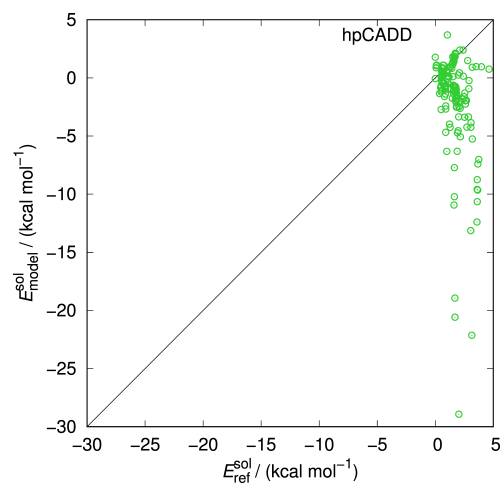


Figure A.54.: Scatter plot of the difference in solute electronic energy in solution between 10 kbar and 1 bar of the hpCADD-Hamiltonians vs. the MP2/aug-cc-pVDZ-reference. Datapoints for the whole data set are shown.

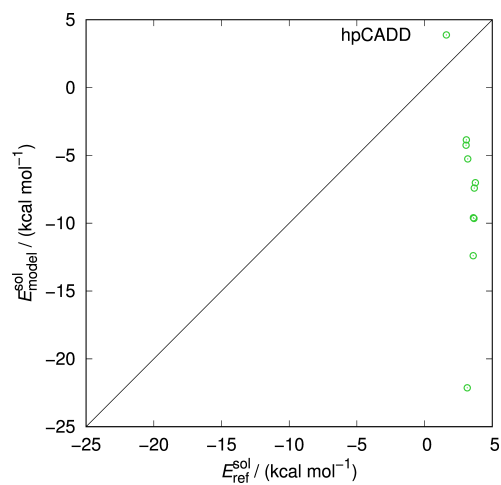


Figure A.55.: Scatter plot of the difference in solute electronic energy in solution between 10 kbar and 1 bar of the hpCADD-Hamiltonians vs. the MP2/aug-cc-pVDZ-reference. Datapoints for the amides are shown.

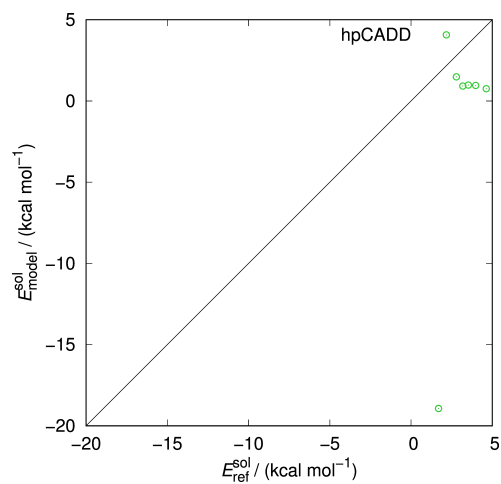


Figure A.56.: Scatter plot of the difference in solute electronic energy in solution between 10 kbar and 1 bar of the hpCADD-Hamiltonians vs. the MP2/aug-cc-pVDZ-reference. Datapoints for the amines are shown.

A. Additional data

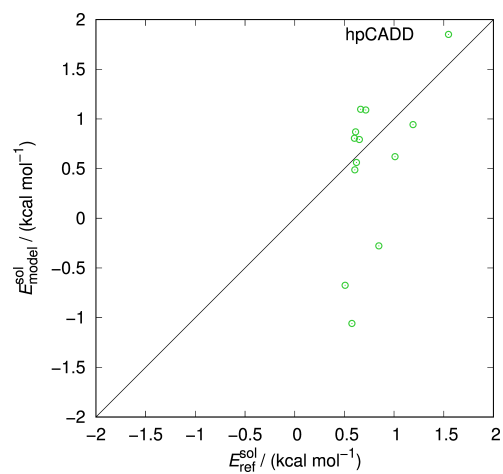


Figure A.57.: Scatter plot of the difference in solute electronic energy in solution between 10 kbar and 1 bar of the hpCADD-Hamiltonians vs. the MP2/aug-cc-pVDZ-reference. Datapoints for the bromides are shown.

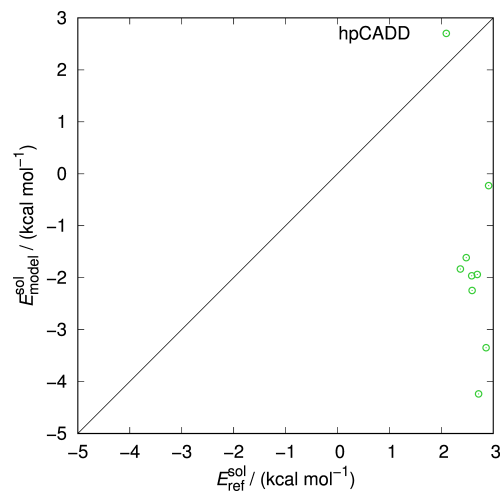


Figure A.58.: Scatter plot of the difference in solute electronic energy in solution between 10 kbar and 1 bar of the hpCADD-Hamiltonians vs. the MP2/aug-cc-pVDZ-reference. Datapoints for aldehydes and ketones are shown.

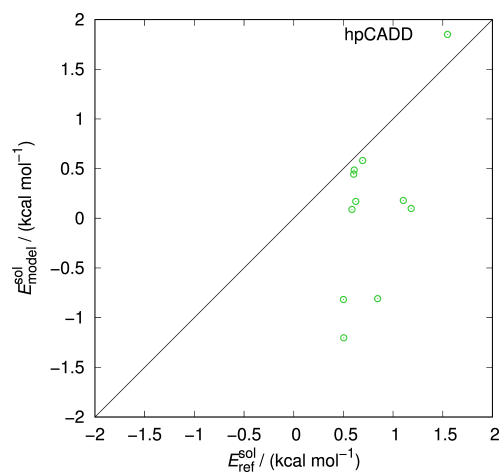


Figure A.59.: Scatter plot of the difference in solute electronic energy in solution between 10 kbar and 1 bar of the hpCADD-Hamiltonians vs. the MP2/aug-cc-pVDZ-reference. Datapoints for the chlorides are shown.

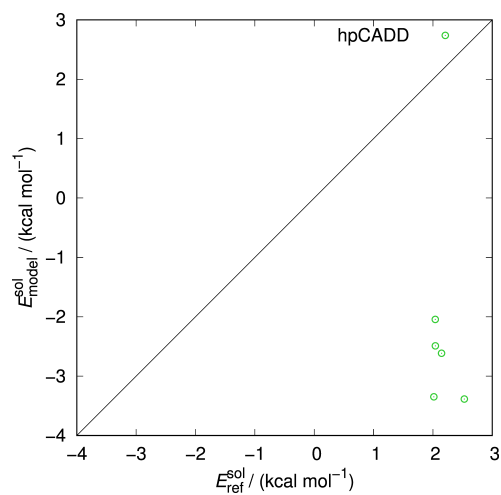


Figure A.60.: Scatter plot of the difference in solute electronic energy in solution between 10 kbar and 1 bar of the hpCADD-Hamiltonians vs. the MP2/aug-cc-pVDZ-reference. Datapoints for the carboxylic acids are shown.

A. Additional data

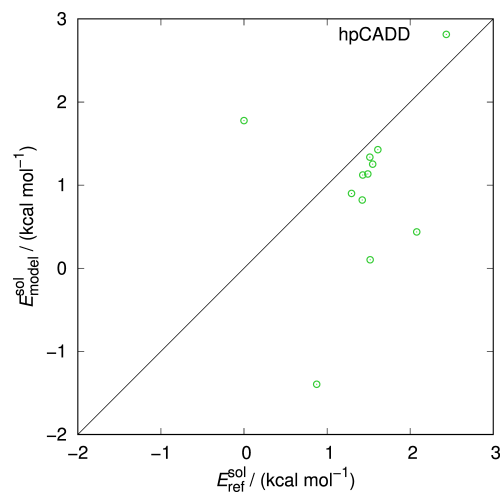


Figure A.61.: Scatter plot of the difference in solute electronic energy in solution between 10 kbar and 1 bar of the hpCADD-Hamiltonians vs. the MP2/aug-cc-pVDZ-reference. Datapoints for the ethers are shown.

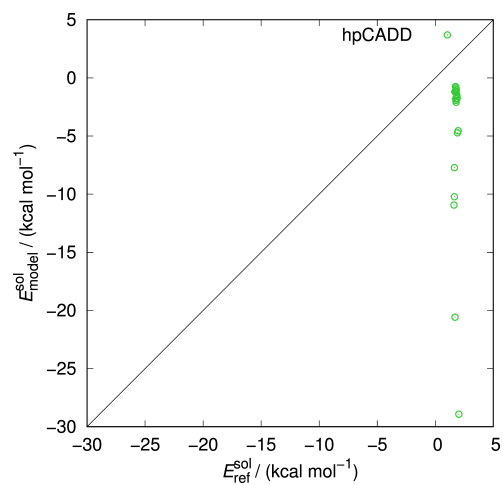


Figure A.62.: Scatter plot of the difference in solute electronic energy in solution between 10 kbar and 1 bar of the hpCADD-Hamiltonians vs. the MP2/aug-cc-pVDZ-reference. Datapoints for the esters are shown.

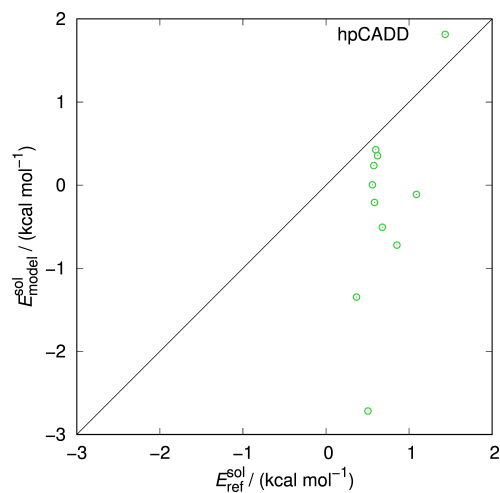


Figure A.63.: Scatter plot of the difference in solute electronic energy in solution between 10 kbar and 1 bar of the hpCADD-Hamiltonians vs. the MP2/aug-cc-pVDZ-reference. Datapoints for the fluorides are shown.

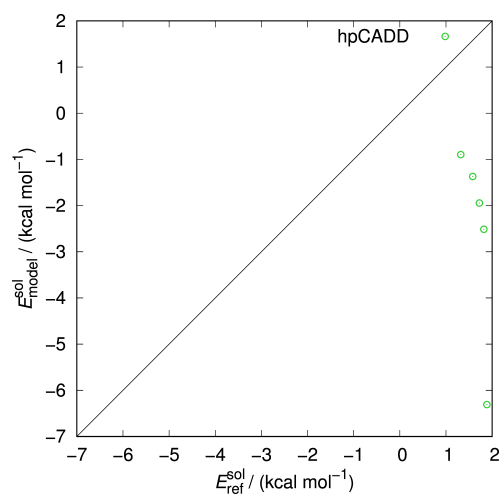


Figure A.64.: Scatter plot of the difference in solute electronic energy in solution between 10 kbar and 1 bar of the hpCADD-Hamiltonians vs. the MP2/aug-cc-pVDZ-reference. Datapoints for the nitriles are shown.

A. Additional data

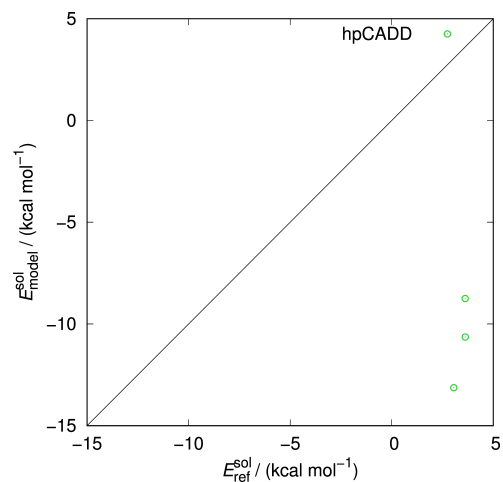


Figure A.65.: Scatter plot of the difference in solute electronic energy in solution between 10 kbar and 1 bar of the hpCADD-Hamiltonians vs. the MP2/aug-cc-pVDZ-reference. Datapoints for the sulfones are shown.

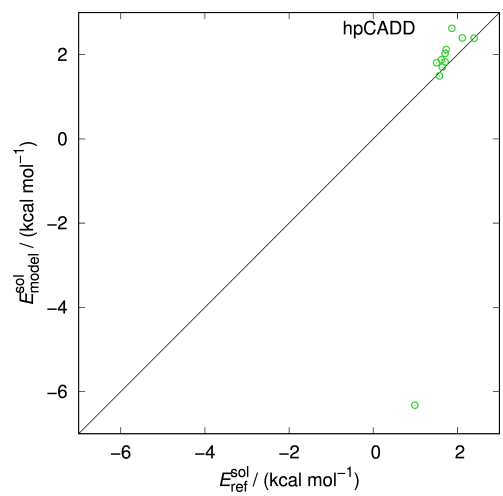


Figure A.66.: Scatter plot of the difference in solute electronic energy in solution between 10 kbar and 1 bar of the hpCADD-Hamiltonians vs. the MP2/aug-cc-pVDZ-reference. Datapoints for the thioethers are shown.

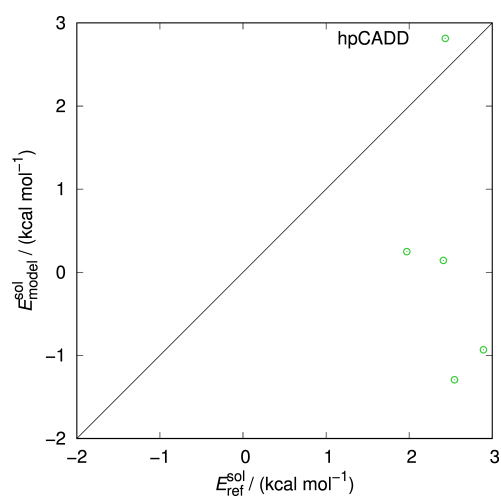


Figure A.67.: Scatter plot of the difference in solute electronic energy in solution between 10 kbar and 1 bar of the hpCADD-Hamiltonians vs. the MP2/aug-cc-pVDZ-reference. Datapoints for the thiones are shown.

A. Additional data

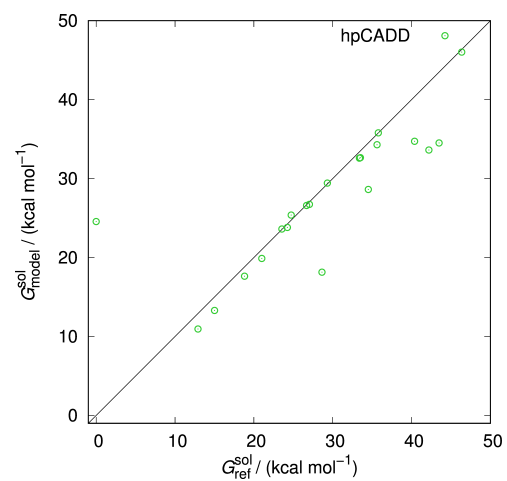


Figure A.68.: Scatter plot of the difference in solutes Gibbs energy in solution between 10 kbar and 1 bar of the hpCADD-Hamiltonians vs. the MP2/aug-cc-pVDZ-reference. Datapoints for the hydrocarbons are shown.

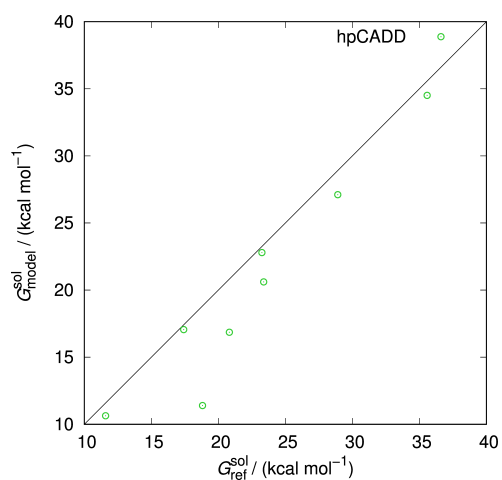


Figure A.69.: Scatter plot of the difference in solutes Gibbs energy in solution between 10 kbar and 1 bar of the hpCADD-Hamiltonians vs. the MP2/aug-cc-pVDZ-reference. Datapoints for the alcohols are shown.

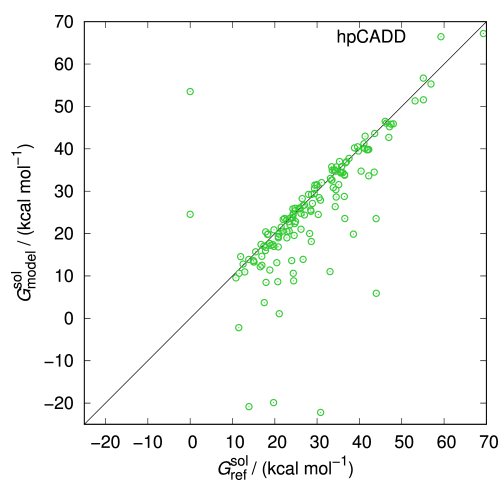


Figure A.70.: Scatter plot of the difference in solutes Gibbs energy in solution between 10 kbar and 1 bar of the hpCADD-Hamiltonians vs. the MP2/aug-cc-pVDZ-reference. Datapoints for the whole data set are shown.

A. Additional data

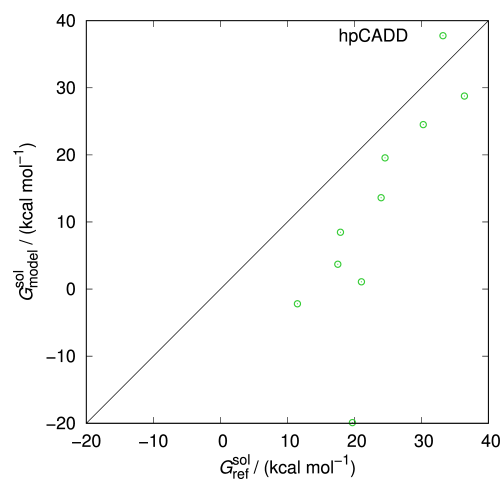


Figure A.71.: Scatter plot of the difference in solutes Gibbs energy in solution between 10 kbar and 1 bar of the hpCADD-Hamiltonians vs. the MP2/aug-cc-pVDZ-reference. Datapoints for the amides are shown.

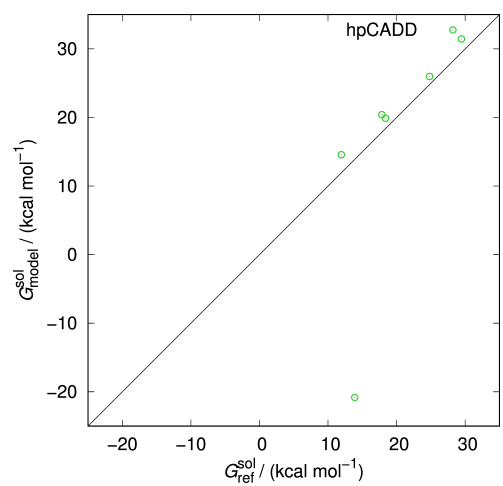


Figure A.72.: Scatter plot of the difference in solutes Gibbs energy in solution between 10 kbar and 1 bar of the hpCADD-Hamiltonians vs. the MP2/aug-cc-pVDZ-reference. Datapoints for the amines are shown.

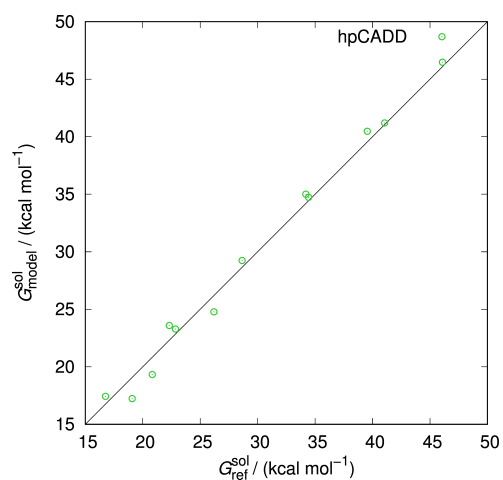


Figure A.73.: Scatter plot of the difference in solutes Gibbs energy in solution between 10 kbar and 1 bar of the hpCADD-Hamiltonians vs. the MP2/aug-cc-pVDZ-reference. Datapoints for the bromides are shown.

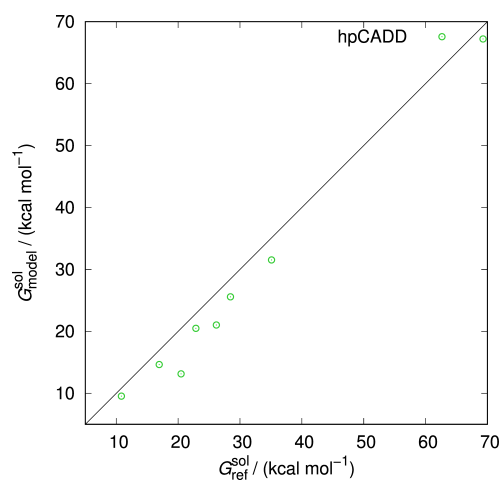


Figure A.74.: Scatter plot of the difference in solutes Gibbs energy in solution between 10 kbar and 1 bar of the hpCADD-Hamiltonians vs. the MP2/aug-cc-pVDZ-reference. Datapoints for aldehydes and ketones are shown.

A. Additional data

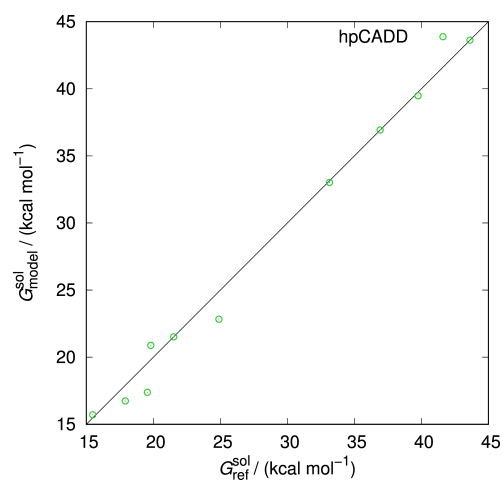


Figure A.75.: Scatter plot of the difference in solutes Gibbs energy in solution between 10 kbar and 1 bar of the hpCADD-Hamiltonians vs. the MP2/aug-cc-pVDZ-reference. Datapoints for the chlorides are shown.

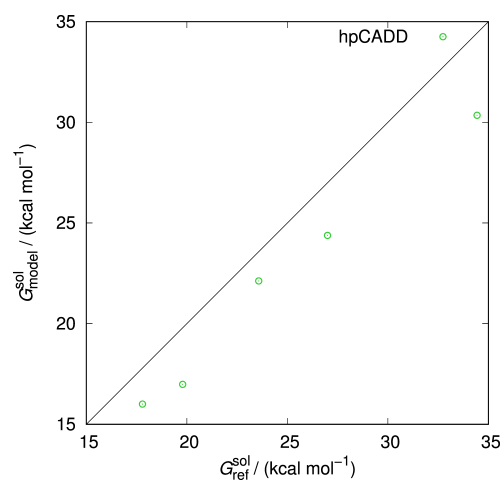


Figure A.76.: Scatter plot of the difference in solutes Gibbs energy in solution between 10 kbar and 1 bar of the hpCADD-Hamiltonians vs. the MP2/aug-cc-pVDZ-reference. Datapoints for the carboxylic acids are shown.

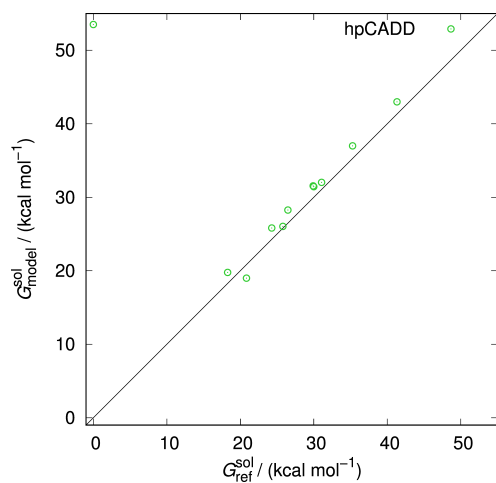


Figure A.77.: Scatter plot of the difference in solutes Gibbs energy in solution between 10 kbar and 1 bar of the hpCADD-Hamiltonians vs. the MP2/aug-cc-pVDZ-reference. Datapoints for the ethers are shown.

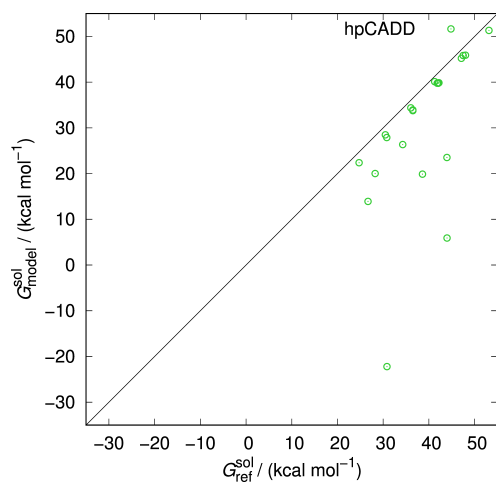


Figure A.78.: Scatter plot of the difference in solutes Gibbs energy in solution between 10 kbar and 1 bar of the hpCADD-Hamiltonians vs. the MP2/aug-cc-pVDZ-reference. Datapoints for the esters are shown.

A. Additional data

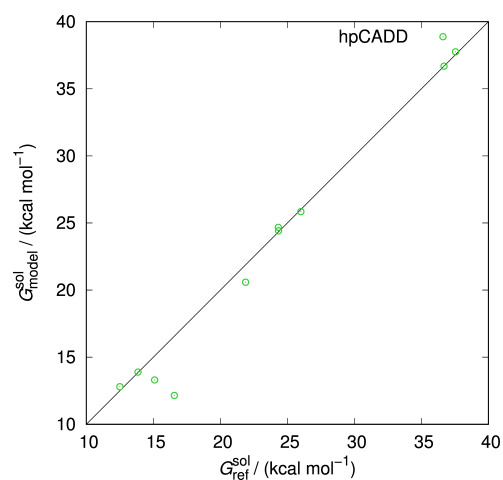


Figure A.79.: Scatter plot of the difference in solutes Gibbs energy in solution between 10 kbar and 1 bar of the hpCADD-Hamiltonians vs. the MP2/aug-cc-pVDZ-reference. Datapoints for the fluorides are shown.

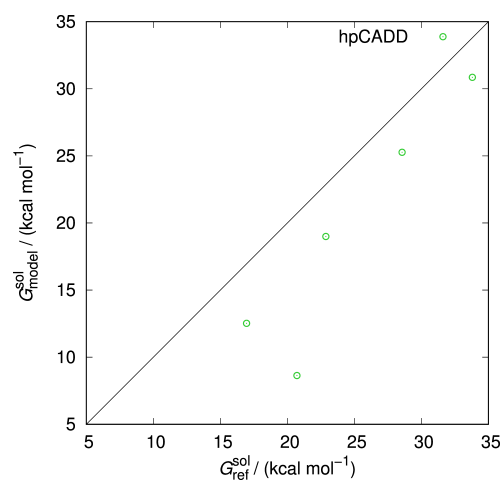


Figure A.80.: Scatter plot of the difference in solutes Gibbs energy in solution between 10 kbar and 1 bar of the hpCADD-Hamiltonians vs. the MP2/aug-cc-pVDZ-reference. Datapoints for the nitriles are shown.

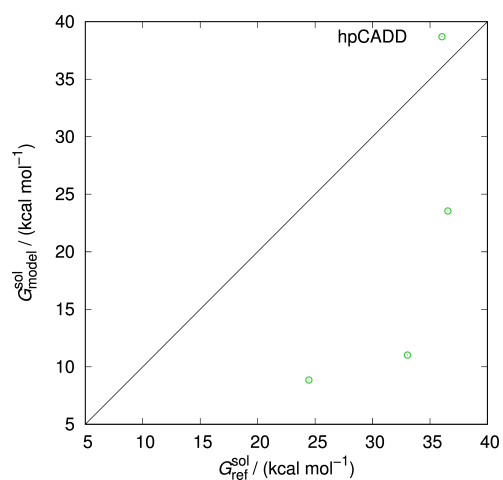


Figure A.81.: Scatter plot of the difference in solutes Gibbs energy in solution between 10 kbar and 1 bar of the hpCADD-Hamiltonians vs. the MP2/aug-cc-pVDZ-reference. Datapoints for the sulfones are shown.

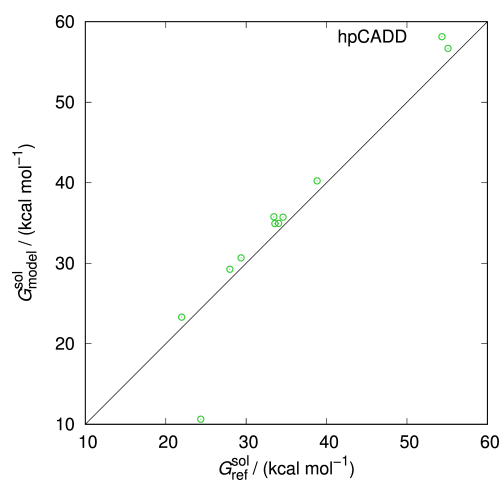


Figure A.82.: Scatter plot of the difference in solutes Gibbs energy in solution between 10 kbar and 1 bar of the hpCADD-Hamiltonians vs. the MP2/aug-cc-pVDZ-reference. Datapoints for the thioethers are shown.

A. Additional data

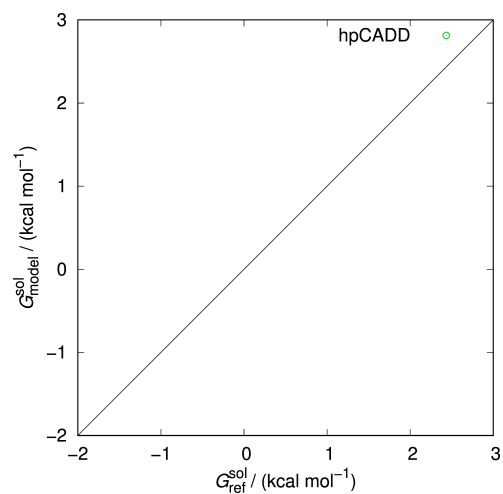


Figure A.83.: Scatter plot of the difference in solutes Gibbs energy in solution between 10 kbar and 1 bar of the hpCADD-Hamiltonians vs. the MP2/aug-cc-pVDZ-reference. Datapoints for the thiones are shown.

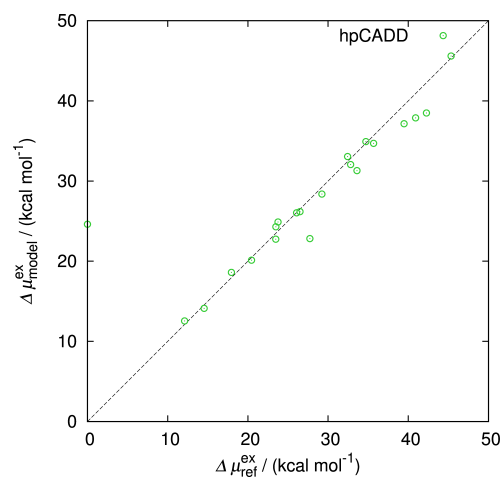


Figure A.84.: Scatter plot of the difference in solutes excess chemical potential in solution between 10 kbar and 1 bar of the hpCADD-Hamiltonians vs. the MP2/aug-cc-pVDZ-reference. Datapoints for the hydrocarbons are shown.

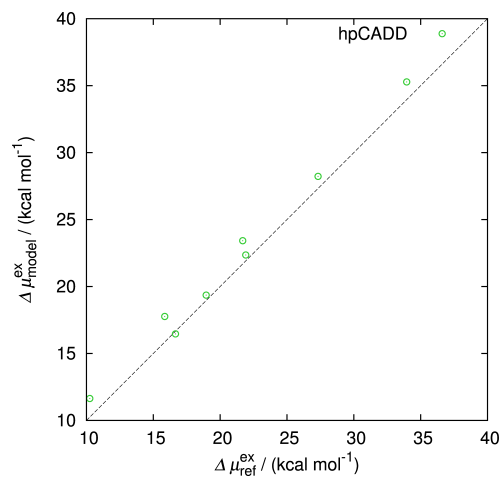


Figure A.85.: Scatter plot of the difference in solutes excess chemical potential in solution between 10 kbar and 1 bar of the hpCADD-Hamiltonians vs. the MP2/aug-cc-pVDZ-reference. Datapoints for the alcohols are shown.

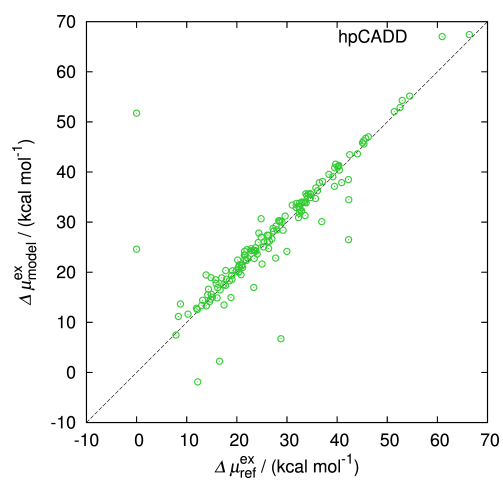


Figure A.86.: Scatter plot of the difference in solutes excess chemical potential in solution between 10 kbar and 1 bar of the hpCADD-Hamiltonians vs. the MP2/aug-cc-pVDZ-reference. Datapoints for the whole data set are shown.

A. Additional data

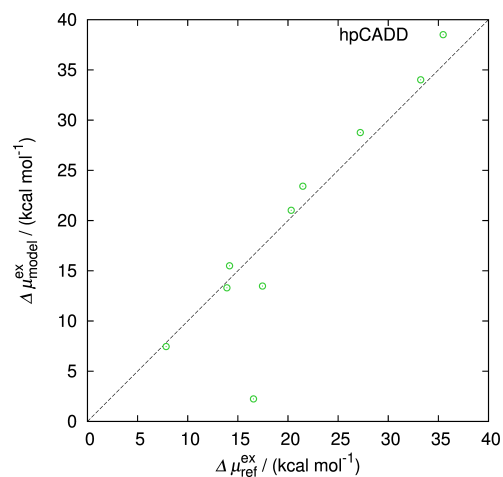


Figure A.87.: Scatter plot of the difference in solutes excess chemical potential in solution between 10 kbar and 1 bar of the hpCADD-Hamiltonians vs. the MP2/aug-cc-pVDZ-reference. Datapoints for the amides are shown.

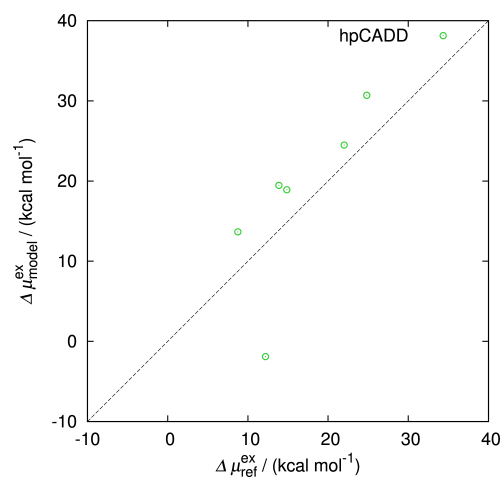


Figure A.88.: Scatter plot of the difference in solutes excess chemical potential in solution between 10 kbar and 1 bar of the hpCADD-Hamiltonians vs. the MP2/aug-cc-pVDZ-reference. Datapoints for the amines are shown.

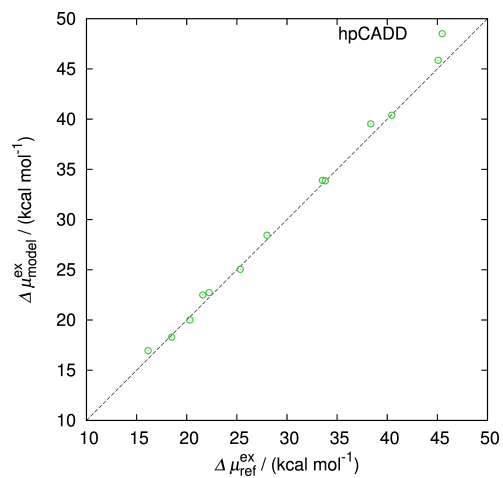


Figure A.89.: Scatter plot of the difference in solutes excess chemical potential in solution between 10 kbar and 1 bar of the hpCADD-Hamiltonians vs. the MP2/aug-cc-pVDZ-reference. Datapoints for the bromides are shown.

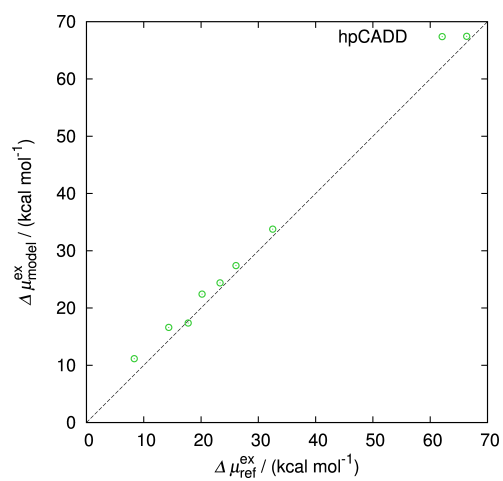


Figure A.90.: Scatter plot of the difference in solutes excess chemical potential in solution between 10 kbar and 1 bar of the hpCADD-Hamiltonians vs. the MP2/aug-cc-pVDZ-reference. Datapoints for aldehydes and ketones are shown.

A. Additional data

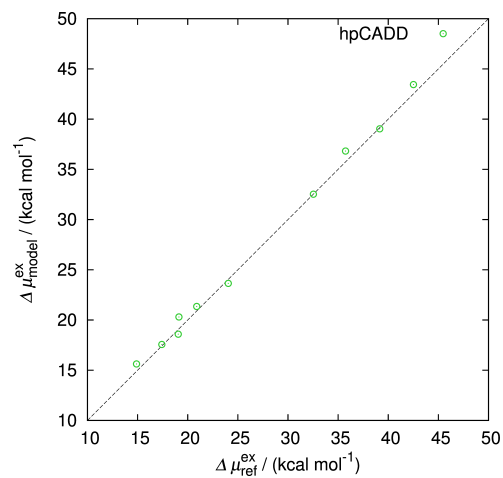


Figure A.91.: Scatter plot of the difference in solutes excess chemical potential in solution between 10 kbar and 1 bar of the hpCADD-Hamiltonians vs. the MP2/aug-cc-pVDZ-reference. Datapoints for the chlorides are shown.

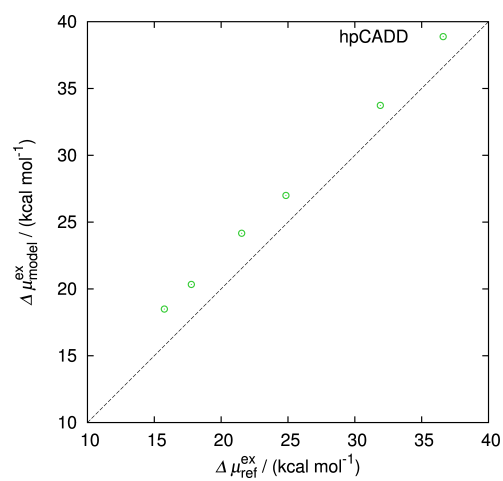


Figure A.92.: Scatter plot of the difference in solutes excess chemical potential in solution between 10 kbar and 1 bar of the hpCADD-Hamiltonians vs. the MP2/aug-cc-pVDZ-reference. Datapoints for the carboxylic acids are shown.

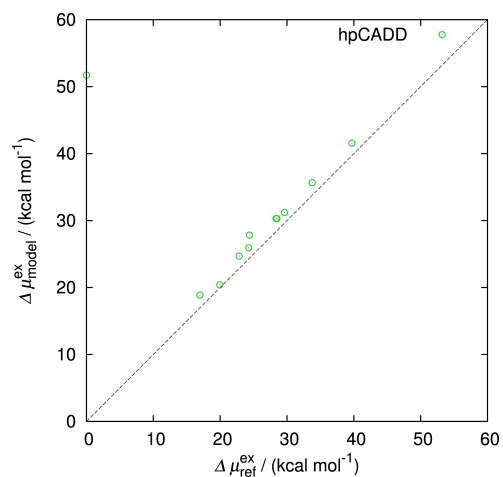


Figure A.93.: Scatter plot of the difference in solutes excess chemical potential in solution between 10 kbar and 1 bar of the hpCADD-Hamiltonians vs. the MP2/aug-cc-pVDZ-reference. Datapoints for the ethers are shown.

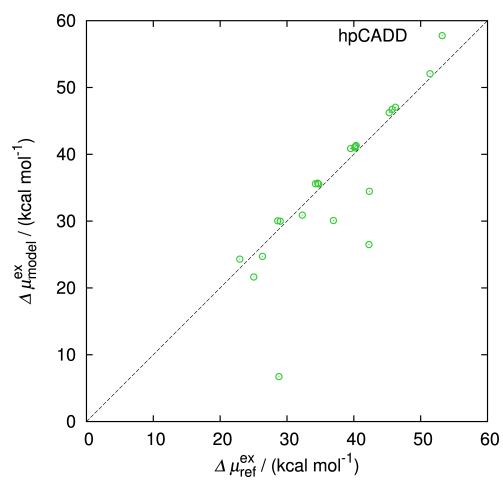


Figure A.94.: Scatter plot of the difference in solutes excess chemical potential in solution between 10 kbar and 1 bar of the hpCADD-Hamiltonians vs. the MP2/aug-cc-pVDZ-reference. Datapoints for the esters are shown.

A. Additional data

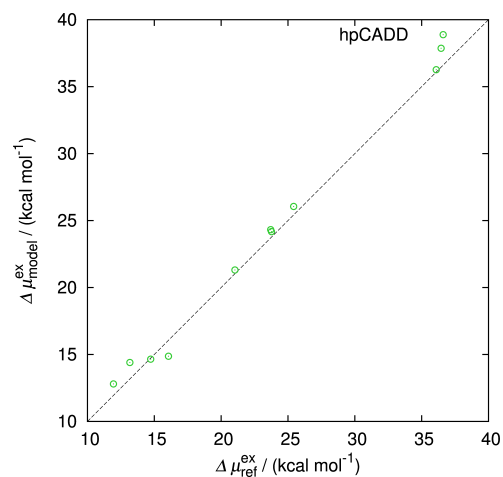


Figure A.95.: Scatter plot of the difference in solutes excess chemical potential in solution between 10 kbar and 1 bar of the hpCADD-Hamiltonians vs. the MP2/aug-cc-pVDZ-reference. Datapoints for the fluorides are shown.

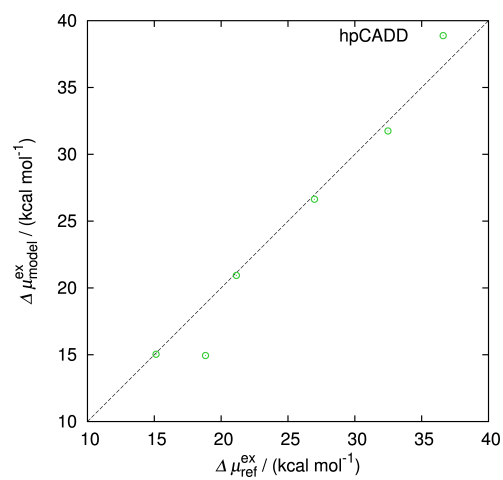


Figure A.96.: Scatter plot of the difference in solutes excess chemical potential in solution between 10 kbar and 1 bar of the hpCADD-Hamiltonians vs. the MP2/aug-cc-pVDZ-reference. Datapoints for the nitriles are shown.

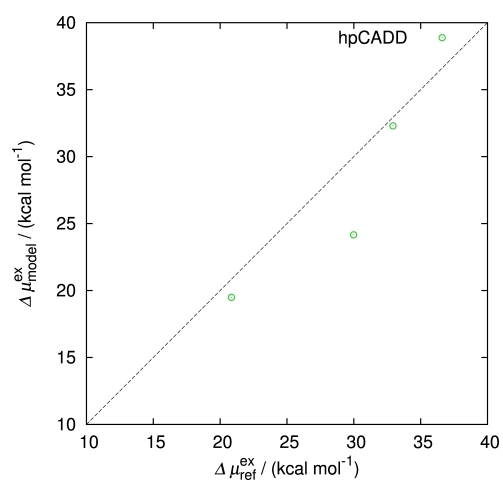


Figure A.97.: Scatter plot of the difference in solutes excess chemical potential in solution between 10 kbar and 1 bar of the hpCADD-Hamiltonians vs. the MP2/aug-cc-pVDZ-reference. Datapoints for the sulfones are shown.

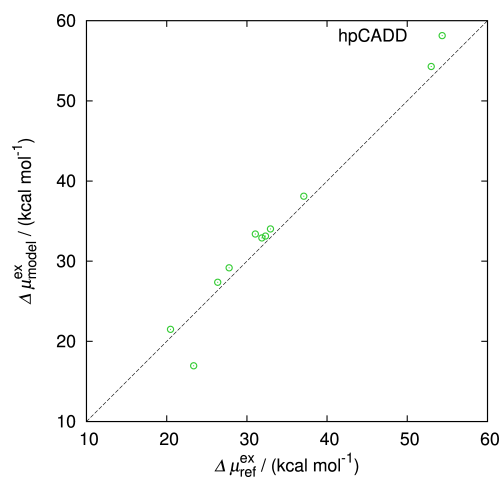


Figure A.98.: Scatter plot of the difference in solutes excess chemical potential in solution between 10 kbar and 1 bar of the hpCADD-Hamiltonians vs. the MP2/aug-cc-pVDZ-reference. Datapoints for the thioethers are shown.

A. Additional data

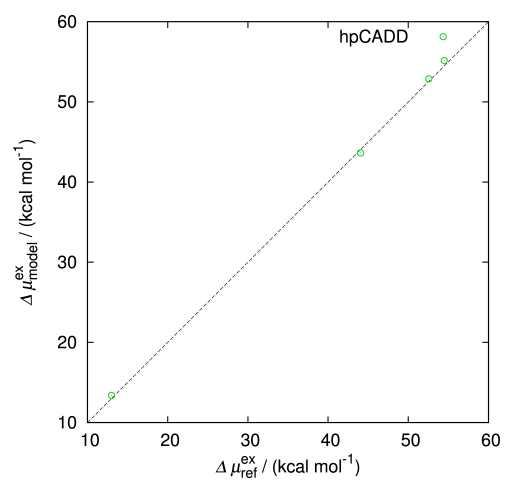


Figure A.99.: Scatter plot of the difference in solutes excess chemical potential in solution between 10 kbar and 1 bar of the hpCADD-Hamiltonians vs. the MP2/aug-cc-pVDZ-reference. Datapoints for the thiones are shown.

B. Conventions

B.1. Mathematical nomenclature

The asterisk symbol $*$ denotes convolution, the centered dot \cdot the scalar product. Vectorial products are denoted with the times symbol \times .

The temporal derivative of a

$$\frac{da}{dt} = \dot{a} \quad (\text{B.1})$$

is abbreviated with the overdot. Multiple dots mean higher order derivatives like

$$\frac{d^2a}{dt^2} = \ddot{a}. \quad (\text{B.2})$$

The ∇ symbol denotes vectorial partial derivatives

$$\nabla = \left(\frac{\partial}{\partial x_1}, \dots, \frac{\partial}{\partial x_n} \right). \quad (\text{B.3})$$

B.2. Constants and unit conversions used in this thesis

Symbol	Meaning	value	unit
c	speed of light	299792458	m s^{-1}
h	Planck constant	$6.62606957 \cdot 10^{-34}$	Js
k_B	Boltzmann constant	$1.3806488 \cdot 10^{-23}$	J K^{-1}
N_A	Avogadro's number	$6.02214129 \cdot 10^{23}$	mol^{-1}
1 u	Atomic mass unit	$1.66053878 \cdot 10^{-27}$	kg
1 kcal mol^{-1}	Energy	$6.9476 \cdot 10^{-21}$	J

C. Software

For running tasks in parallel the really useful script GNU `parallel` - the command line power tool - was used extensively on machines without queuing system¹³⁷.

Most scripts used for this thesis were written in Perl 5¹³⁸.

Thousands of lines of source code were produced with with what still is the simplest editor: `vim`.

This thesis was written with L^AT_EX applying KOMA `script`¹³⁹, `AMSMath`¹⁴⁰ and `mhchem`¹⁴¹ extensively.

2D molecular graphics were drawn with ChemBioDraw®.

Some tools were written in Python2.7¹⁴² - and the `python` interpreter makes a great calculator, too.

Tricky evaluations were done with `Mathematica`.

Three dimensional molecule graphics were created with `VMD`¹⁴³ or `MolCAD II`.

Molecular dynamics simulations were mostly performed with the Groningen Machine for Chemical simulations (`GROMACS`).¹¹⁶

EC-RISM calculations were performed with the in-house code `rismnblues.pl`⁵

3D-RISM calculations were performed with both in-house codes `3drism` and `RISMpar`.

1D-RISM calculations were performed with a `Mathematica` based in-house code.

Quantum chemistry calculations were performed with `Gaussian 03`⁹⁷ and `Gaussian 09`⁶⁵. Both versions were modified in order to suppress the calculation of the self-interaction energy of the EC-RISM point charge cluster.

Eidesstattliche Versicherung (Affidavit)

Kibies, Patrick Jascha

Name, Vorname
(Surname, first name)

124848

Matrikel-Nr.
(Enrolment number)

Belehrung:

Wer vorsätzlich gegen eine die Täuschung über Prüfungsleistungen betreffende Regelung einer Hochschulprüfungsordnung verstößt, handelt ordnungswidrig. Die Ordnungswidrigkeit kann mit einer Geldbuße von bis zu 50.000,00 € geahndet werden. Zuständige Verwaltungsbehörde für die Verfolgung und Ahndung von Ordnungswidrigkeiten ist der Kanzler/die Kanzlerin der Technischen Universität Dortmund. Im Falle eines mehrfachen oder sonstigen schwerwiegenden Täuschungsversuches kann der Prüfling zudem exmatrikuliert werden, § 63 Abs. 5 Hochschulgesetz NRW.

Die Abgabe einer falschen Versicherung an Eides statt ist strafbar.

Wer vorsätzlich eine falsche Versicherung an Eides statt abgibt, kann mit einer Freiheitsstrafe bis zu drei Jahren oder mit Geldstrafe bestraft werden, § 156 StGB. Die fahrlässige Abgabe einer falschen Versicherung an Eides statt kann mit einer Freiheitsstrafe bis zu einem Jahr oder Geldstrafe bestraft werden, § 161 StGB.

Die oben stehende Belehrung habe ich zur Kenntnis genommen:

Official notification:

Any person who intentionally breaches any regulation of university examination regulations relating to deception in examination performance is acting improperly. This offence can be punished with a fine of up to EUR 50,000.00. The competent administrative authority for the pursuit and prosecution of offences of this type is the chancellor of the TU Dortmund University. In the case of multiple or other serious attempts at deception, the candidate can also be unenrolled, Section 63, paragraph 5 of the Universities Act of North Rhine-Westphalia.

The submission of a false affidavit is punishable.

Any person who intentionally submits a false affidavit can be punished with a prison sentence of up to three years or a fine, Section 156 of the Criminal Code. The negligent submission of a false affidavit can be punished with a prison sentence of up to one year or a fine, Section 161 of the Criminal Code.

I have taken note of the above official notification.

Ort, Datum
(Place, date)

Unterschrift
(Signature)

Titel der Dissertation:
(Title of the thesis):

Integral equation-based calculations of the electronic
structure of small molecules under high pressure

Ich versichere hiermit an Eides statt, dass ich die vorliegende Dissertation mit dem Titel selbstständig und ohne unzulässige fremde Hilfe angefertigt habe. Ich habe keine anderen als die angegebenen Quellen und Hilfsmittel benutzt sowie wörtliche und sinngemäße Zitate kenntlich gemacht.

Die Arbeit hat in gegenwärtiger oder in einer anderen Fassung weder der TU Dortmund noch einer anderen Hochschule im Zusammenhang mit einer staatlichen oder akademischen Prüfung vorgelegen.

I hereby swear that I have completed the present dissertation independently and without inadmissible external support. I have not used any sources or tools other than those indicated and have identified literal and analogous quotations.

The thesis in its current version or another version has not been presented to the TU Dortmund University or another university in connection with a state or academic examination.*

*Please be aware that solely the German version of the affidavit ("Eidesstattliche Versicherung") for the PhD thesis is the official and legally binding version.

Ort, Datum
(Place, date)

Unterschrift
(Signature)